2013

Geophysical Investigation of the Pagosa Springs Geothermal System
-Upper San Juan Basin, Archuleta County, Colorado

Abstract

Pagosa Springs, Colorado, is situated above a unique and relatively unexplored geothermal reservoir. This resource manifests itself on the surface through the town's popular hot springs and a geothermal well downtown that is used to heat several public and private buildings. The mechanisms controlling the area's geothermal plumbing system are not well known, and invasive drilling investigations have negatively affected the reservoir's output in the past. As a result, non-invasive geophysical techniques are currently the most effective tools to further explore the reservoir. As part of their respective field investigation courses, the Colorado School of Mines and Imperial College London have conducted a geophysical field camp in the area since the summer of 2012. This exercise has the dual purpose of exposing students to geophysical field work and further characterizing the geothermal reservoir beneath Pagosa Springs. In 2012, students used a variety of geophysical field methods to build a basic model of the region's structural geology; this year, building off of the previous field camp's work, students continued to conduct geophysical surveys with the hope of refining the geologic model of the area. Among the geophysical methods utilized are deep seismic, shallow seismic, magnetic, gravitational, electromagnetic (EM), direct current (DC) resistivity, self-potential (SP), and ground penetrating radar (GPR), along with geologic field investigation and satellite remote sensing. Surveys were conducted at several locations in and around Pagosa Springs. A main survey line was set up just south of downtown that crossed several known and proposed faults, including one discovered during the 2012 field session; the presence of these faults was verified using deep seismic imaging, DC resistivity, gravity, magnetics, and SP. Further surveys were conducted at more localized sites along the main survey line; these sites included an igneous dike just east of the San Juan River, where DC, SP, magnetics, and gravity were used to locate the fault proposed in 2012, and GPR was used to image the dike. At the Mill Creek site, EM surveys were used to map groundwater, and DC/SP surveys found two possible faults. In downtown Pagosa Springs, time-lapse EM surveys were conducted to find areas where pipes in the geothermal heat exchange system may be leaking; a GPR survey mapped travertine deposits near the Mother Spring. An additional, student-chosen site was located at Shahan's Ranch, approximately 40km south of Pagosa Springs; here, DC and EM surveys mapped the subterranean propagation of water from an uncapped geothermal well. Additionally, DC and shallow seismic were used to characterize the geology of the area. Ultimately, using data from both the 2012 and 2013 field sessions, a revised geologic cross section is made, and a new mechanism is proposed to explain how the geothermal reservoir at Pagosa Springs is recharged

Acknowledgements

Finally, all the students who participated in the field camp:

CSM Students (last name, first name):

Deema Albeesh
Rami AlGhamdi
Mohammed AlManaa
Ghadeer Alselemi
Guillaume Barnier
Thomas Blitz
Jennifer Brush
Thu Thao Bui
Yuting Duan
Michael Dunham
Elena Dutcher
Jarred Eppeheimer
Paul Geimer
Spencer Haich
Nickolas Huebner
David Huffington
Joseph Jennings
Colton Kohnke
Max Kosmicki
Kritti Kreeprasertkul
Alyson Lozier
Simon Luo
Brennan Malcolm
Ibrahim Meer
Staci Mueller
Stevie Newbill
Chris Pacher
Natalya Patrikeeva
Elizabeth Pettinger
Steven Plescia
Linus Sebelin
Karyn Stanley
Ian Stone
Elijah Thomas
Andrew Yanke
Junwei Zhang

Imperial Students (last name, first name):

Aly Abdelgawad
Anthony Ayaa O'Biale
Samuel Coe
Caroline Colle
Laurent Olivier Feuilleaubois
Nur Azimah Haji Ashari
Dinara Kazyyeva
Baskoro Kurniawan
Jiayun Lai
Ivan Lim Chen Ning
Yalin Luan
Stephane Mangeon
Leanne Connie Mearns
Richard Metcalfe
Nurlan Nurmanov
Rapapasra Pacharakittiwich
Daniel Sprague
Xi Wang
Zuo Xu
Aidar Yermukhan

Disclaimer

The content of this report is derived from a summer field camp for undergraduate and graduate students in Geophysics at the Colorado School of Mines and Imperial College London. The main objective of this field camp was to introduce students to the many different geophysical methods that are used in exploration. All the data has been acquired, processed, and interpreted primarily by the students from the Colorado School of Mines and Imperial College London. Therefore, the content of this report should be regarded appropriately. The aforementioned schools do not guarantee the accuracy or validity of the data obtained or the subsequent interpretations and conclusions presented in this document.

Table of Contents

Table of Figures

Table of Tables

1. Introduction

1.1   Background

The town of Pagosa Springs in South Central Colorado is situated above a complex geothermal reservoir. This valuable natural resource not only feeds the town's popular hot springs, but is also the backbone of a geothermal heat exchange system that has heated many of the town's government, retail, and residential buildings since the 1980s [1]. Studies conducted in the 1980s and 1990s were able to characterize the geochemical nature of the geothermal system and to identify possible heat sources, though they were unable to create a detailed profile of the reservoir itself [1, 2]. Further, wells drilled in the area for exploration and energy purposes have diverted water away from the town's springs and heating system [1]. As a result, there is a need for a non-invasive geophysical investigation of the area to build upon the body of information compiled in previous studies.

In 2012, the Colorado School of Mines and Imperial College London conducted a field geophysics course in the Pagosa Springs area with the dual purpose of studying the geothermal reservoir and exposing students to a relevant field work experience. Students gathered data using a wide variety of geophysical methods, ultimately creating a report to detail their experience and the results of their data analysis. This year, both schools returned to Pagosa Springs to continue the research initiated in 2012. Again, students were tasked with conducting predetermined and student designed surveys in the area over a two week period (May 10th - 24th, 2013); two more weeks were spent at the Colorado School of Mines processing and analyzing the acquired data. Methods utilized in this year's study include satellite remote sensing, deep seismic, near-surface seismic, direct current (DC) resistivity, self-potential (SP), gravity, magnetic, electromagnetic (EM), and ground penetrating radar (GPR). This collection of methods not only allows for extensive cross-correlation of multiple data sets, but also provides students with a means to apply the knowledge and theory they acquire as part of their geophysics education.

The following report details each of the geophysical methods used in this survey, the processing associated with each method, and the interpretations of each data set. Wherever relevant, interpretations were made considering the data collected during the 2012 field session. Ultimately, it is hoped that the combined research from both field sessions will contribute significantly to the body of knowledge characterizing the geothermal reservoir beneath the Pagosa Springs area.

1.2 Locations

Figure 1.1: Regional map of the Pagosa Springs area including the location of Shahan's Ranch.

Geophysical data was collected in and around the town of Pagosa Springs (Figure 1.1); survey locations were chosen based on their geophysical value and their accessibility to different methods. The main survey location was a line just south of Pagosa Springs extending from the southwest to the northeast; 13 different surveys were conducted on and near this line. A student survey site was located at Shahan's Ranch near the Colorado/New Mexico border, wherein a number of geophysical surveys of varying method were conducted to better understand the geothermal system at the site. The final main site was downtown Pagosa Springs, where GPR and EM surveys were conducted along a subterranean geothermal pipeline.

1.2.1   Main Survey Line
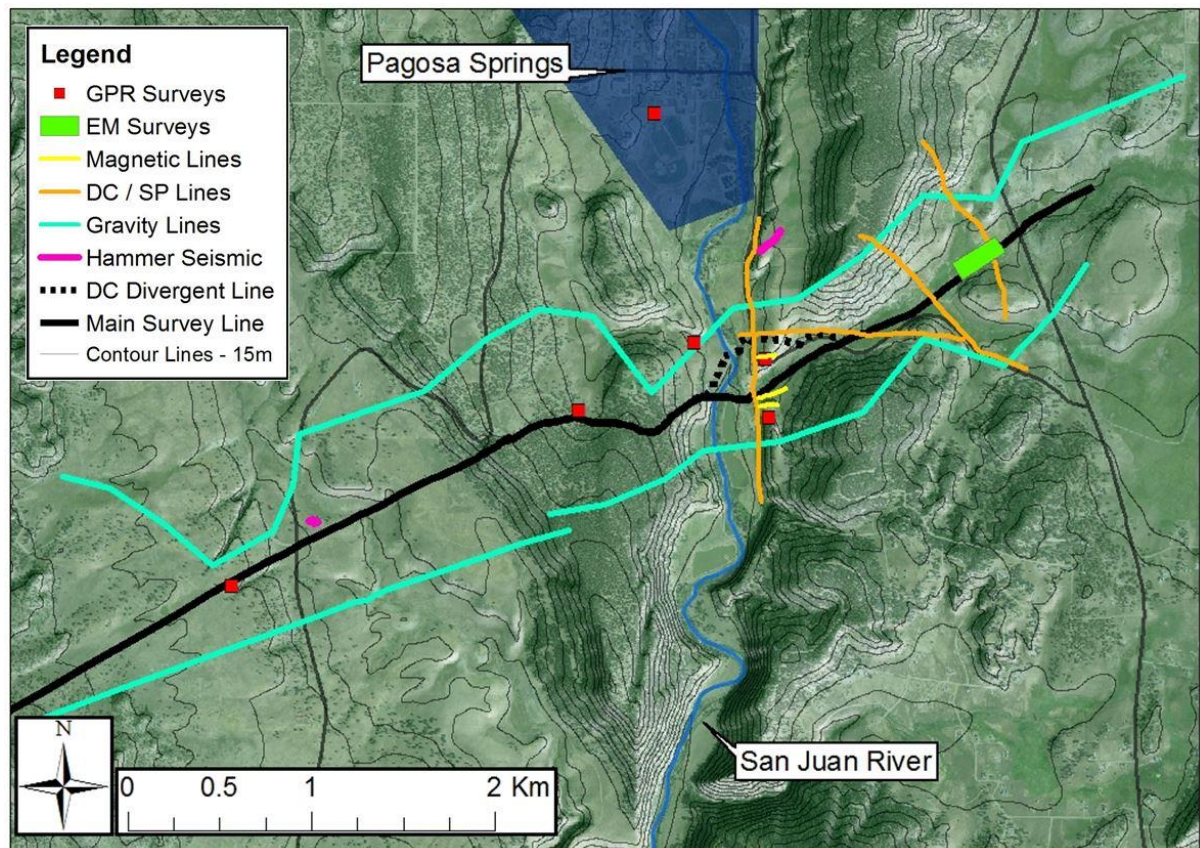
Figure 1.2: Map of the Main Survey Line with each survey method and location denoted on the map.

The main survey line began just east of S. Pagosa Boulevard and extended northeast 6.74 km (Figure 1.1). This line ran through rough terrain, including over a steep, 60 m slope on the west bank of the San Juan River. Many points along this slope could not be measured, along with the portion of the line spanning the San Juan River. This particular line was chosen in an effort to image areas with known faults (including the Eightmile Mesa Fault [1]), and points of geologic interest; the line was also chosen because it was largely accessible by vibroseis vehicles. All methods were performed in at least one location along the main survey line, with a few method performed along the entirety of the line. These methods include deep seismic, gravity, magnetics, DC resistivity, and SP.

1.2.2   Hairpin Turn Dike

The Hairpin Turn Dike was a survey location based around an igneous dike outcropping along Light Plant Road, just south of Pagosa Springs. The location was surveyed using DC, SP, magnetic, and GPR methods to identify the extent of the dike and possibly verify the location of the 2012 report's proposed fault. GPR grid surveying was performed south of the outcrop, while standard profile surveys were performed for every other method in this area.

1.2.3 Mill Creek

The Mill Creek survey site was a large, flat field that resided along the main survey line to the east of the hairpin turn dike. Mill Creek was chosen as a survey location because of its accessibility and its proximity to the main survey line. Several EM grid surveys were performed at this location.

1.2.4 Shahan's Ranch

The second main location was Shahan's Ranch, about 40km South of Pagosa Springs. This survey location was on a ranch property belonging to the Shahan family. A well drilled on site spills geothermally heated water into the surrounding pasture; the surveys developed for this site focused around developing a geologic and geothermal model or idea of the area (Figure 1.3).
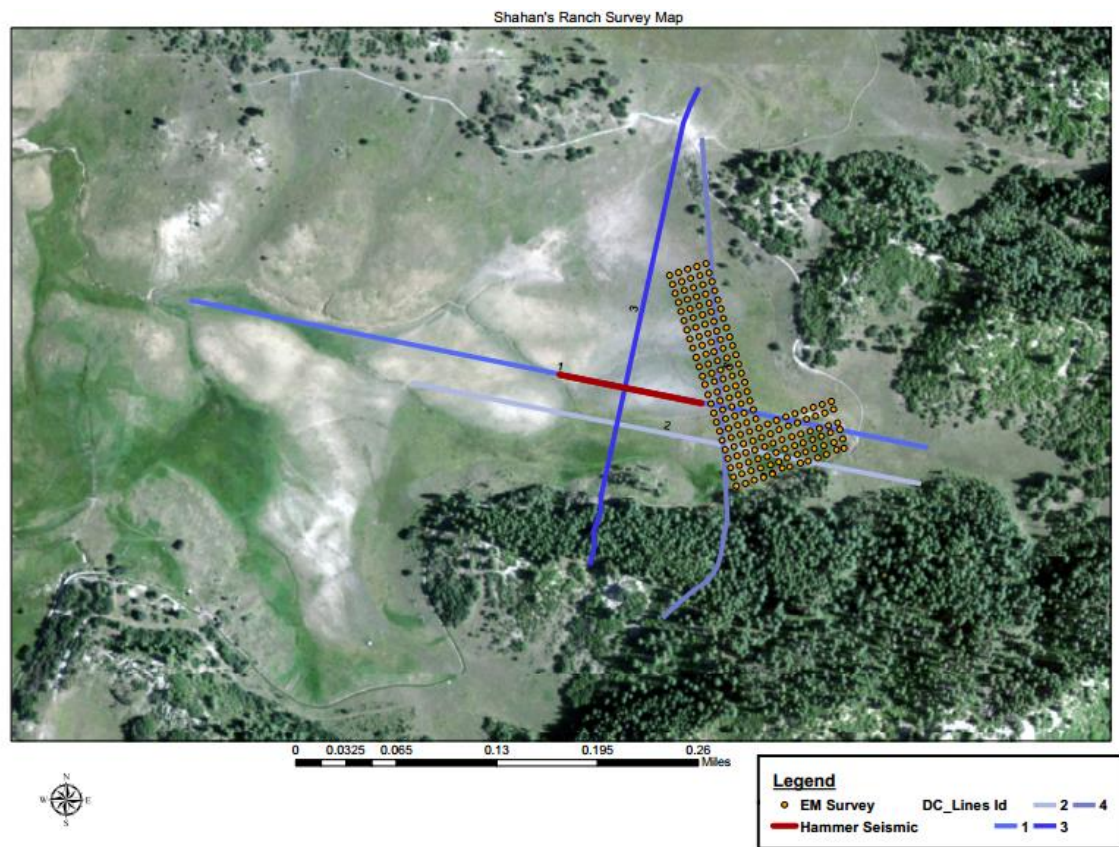
Figure 1.3: Survey layouts for Shahan's Ranch.

DC lines were laid out to cover a large area while maintaining a relative correlation to one another. It was hoped that DC line 4 would provide an image that illustrated the change in lithology along an easting profile from DC line 3. DC line 2 was designed to show a change in lithology along a southing profile from DC line 1. The interpretations from these lines should illuminate lithological trends that may correspond to geothermal water flow in the subsurface. The hammer seismic line and EM survey grid were set up with the intent to provide an image of the subsurface relative to the nearby geothermal well.

1.2.5 Downtown Pagosa Springs

The main survey in downtown Pagosa Springs was conducted over a geothermal pipeline buried 2m beneath the surface. The pipeline, which carries heated water to public, residential, and commercial buildings, traverses the center of downtown and doubles back on itself as part of a heat exchange loop. EM surveys were conducted over the course of the pipeline with the purpose of identifying the location of a leak (Figure 1.4). Additionally, a GPR survey was conducted near the Mother Spring, which is located near downtown. This survey sought to image the extent of a travertine deposit in the subsurface.

Figure 1.4: Survey layout for downtown Pagosa Springs.

2. Geology

2.1 Geological History and Overview

Pagosa Springs is located on the north-east edge of the San Juan Basin, north of the Colorado and New Mexico border (Figure 2.1).

Figure 2.1: Map View of Pagosa Springs Location [3].

In the San Juan Basin, the main sedimentary units are deposited on a crystalline Pre-Cambrian basement [4]. This basement consists of igneous and metamorphic crystalline rock, specifically including: granite (45%), schist and gneiss (30%), quartzite and phyllite (15%) and greenstone (10%) [5]. The basement does not appear as an outcrop at Pagosa Springs. However, wells drilled in the region encounter the formation at shallow depths which suggests major uplift of the basement throughout geological time.

A large time gap exists between the Pre-Cambrian basement and the layer directly above, the Upper Jurassic Entrada Formation (refer to Figure 2.2 for a diagram of unconformities). This disconformity is believed to be due to regional uplift during the Triassic period, which led to a period of major erosion and little to no deposition [6]. The Entrada Formation consists of a light grey, fine- to coarse-grained, poorly-sorted sandstone [7]. Due to its well-rounded, spherical grains and well-developed

cross-bedding, this formation is considered aeolian sandstone [7, 8]. The sandstone is highly cemented, with calcium carbonate and clays, so reducing much of the sandstone's primary porosity.
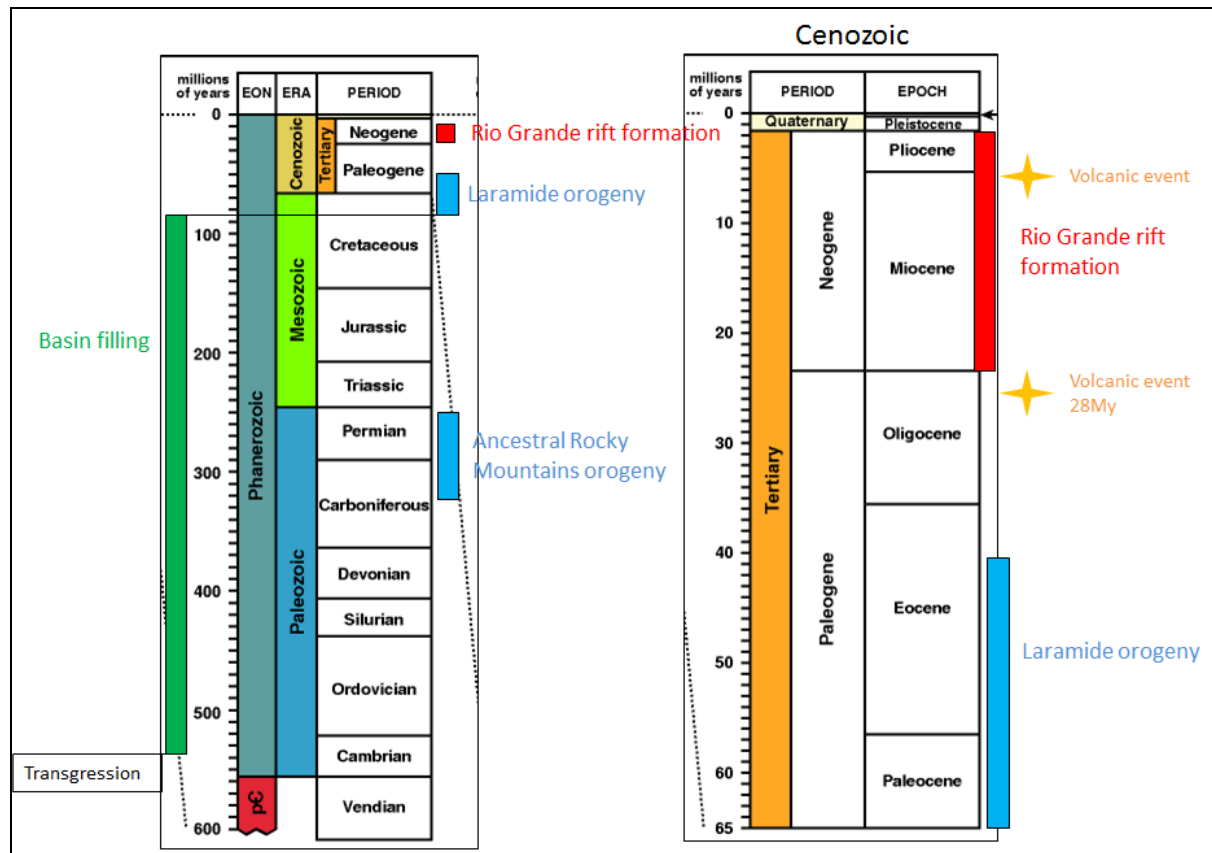
Figure 2.2: San Juan Basin Formation [9].

Above the Jurassic Entrada, the Wanakah Formation was conformably deposited. This is characterized by dark grey, finely laminated limestone, which approximately consists of 40% anhydrite nodules and the remainder thin sandstone beds [7]. The Wanakah Formation was deposited after a period of subsidence, in which the region was flooded with a highly saline, stagnant body of seawater [8].

Regression of this seaway then led to the deposition of the Jurassic Morrison Formation, which conformably overlies the Wanakah Formation [6]. The Morrison Formation consists of two main members: a massive light grey sandstone (upper member) and red-brown shales interbedded with thin sandstones (lower member) [7]. Neither the Entrada nor the Wanakah formations outcrop at Pagosa Springs. However the Morrison Formation is exposed at a few sites across the region.

After a period of uplift and erosion during the Lower Cretaceous period, the Upper Cretaceous Dakota Sandstone was unconformably deposited on top of the Morrison Formation [6]. The Dakota Sandstone is a 60 meter thick sequence of marine sediments and can be divided into three members, all of which were deposited due to the transgression of the Cretaceous seaway [8]. The lower member

consists of massive, cross-bedded conglomerates; the middle member is composed of a carbonaceous silty shale unit; while the upper member consists of massive, cross-bedded sandstones [7]. The Dakota Sandstone is heavily fractured and quartz-cemented, which can be seen at various outcrops around Pagosa Springs, especially along recognized fault planes.

The depositional history and seaway regression-transgression cycles are presented below in Figure 2.3. Note that the ocean arrived in the area 100 million years ago and departed 70 million years ago. This means that the marine sedimentation (Mancos shale) occurred during a period of 30 million years.
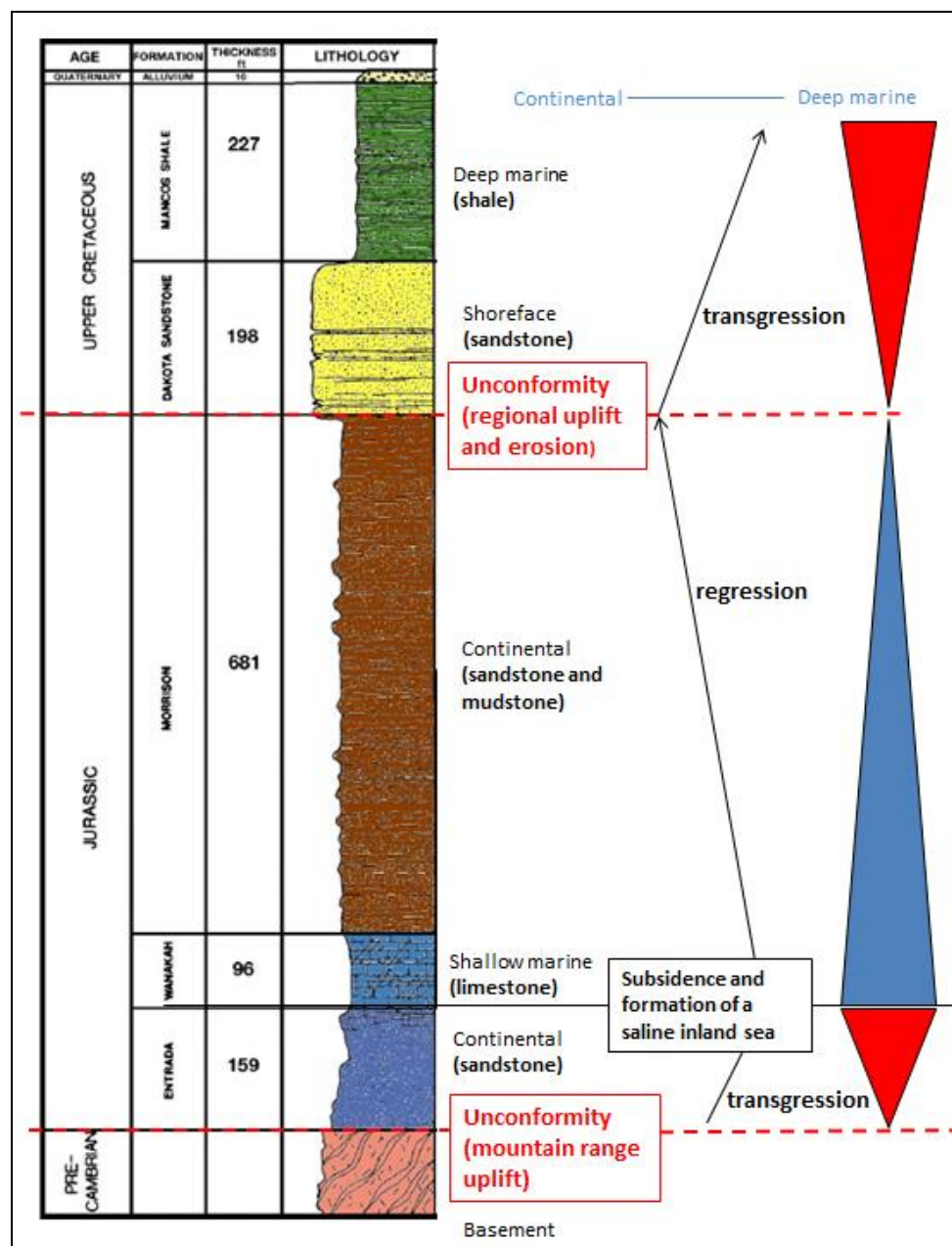
Figure 2.3: Stratigraphic Column of P1 Well & Associated Regression-Transgression Cycles [Modified from 7].

Conformably overlying the Dakota Sandstone is the Mancos Shale. Deposition of the Mancos shale occurred during the Upper Cretaceous, in a deep sea environment, after transgression of the Cretaceous seaway. The formation in its entirety is approximately 650 to 700 meters thick, yet erosion has thinned it to 70 meters at the P-1 well location in Pasgosa Springs. The shale is mainly dark grey to black, with massive to fissile shales interbedded with some sandstones and fossiliferous limestones (equivalent to the Niobrara in the Denver Basin) [7]. This formation outcrops at many of the survey locations around Pagosa Springs [7]. The Mancos Shale can be divided into several members of slightly differing composition. The most notable member within this layer is composed of predominantly limestone, which occurs approximately 30 meters above the Dakota Sandstone and Mancos Shale boundary [8]. Where this limestone layer outcrops and the Dakota Sandstone does not, this boundary can be approximated for mapping structure contours.

Interbedded with the Mancos Shale is the Mesa Verde Formation, also deposited in the Upper Cretaceous. This is composed of brittle sandstones with grey shales interspersed throughout. It is approximately 100 meters at its thickest [7]; however, it pinches out and eventually becomes indistinguishable from the surrounding Mancos Shale. This layer was rarely visible in the context of the Pagosa Springs surveys, but some was seen approximately 40 meters above the survey plane at Shahan's Ranch along the range of hills to the west. The Lewis Shale, again Upper Cretaceous in age, overlies the Mesa Verde Formation and the Mancos Shale. It is so similar in composition to the Mancos Shale that when the Mesa Verde is not evident, these are referred to as one unit [6]. In this area, the deposition of the Lewis Shale represents the end of sedimentation. Significant erosion and further uplift with folding have made it so there is prominent missing time above the marine shales.

Near the end of the Cretaceous, the Laramide orogeny produced the current Rocky Mountains and formed the Archuleta anticlinorium that Pagosa Springs is situated upon. The majority of the extensional faulting in the area likely occurred during this time due to the down-warping of the San Juan Basin. Later regional uplift and formation of the Rio Grande Rift created additional faults trending north-northeast, along with the Stinking Springs anticline (Figure 2.4). The Eight Mile Mesa fault was mapped during the 2012 Colorado School of Mines Field Camp and the purple and blue faults are those identified during the 2013 study [10, 7].
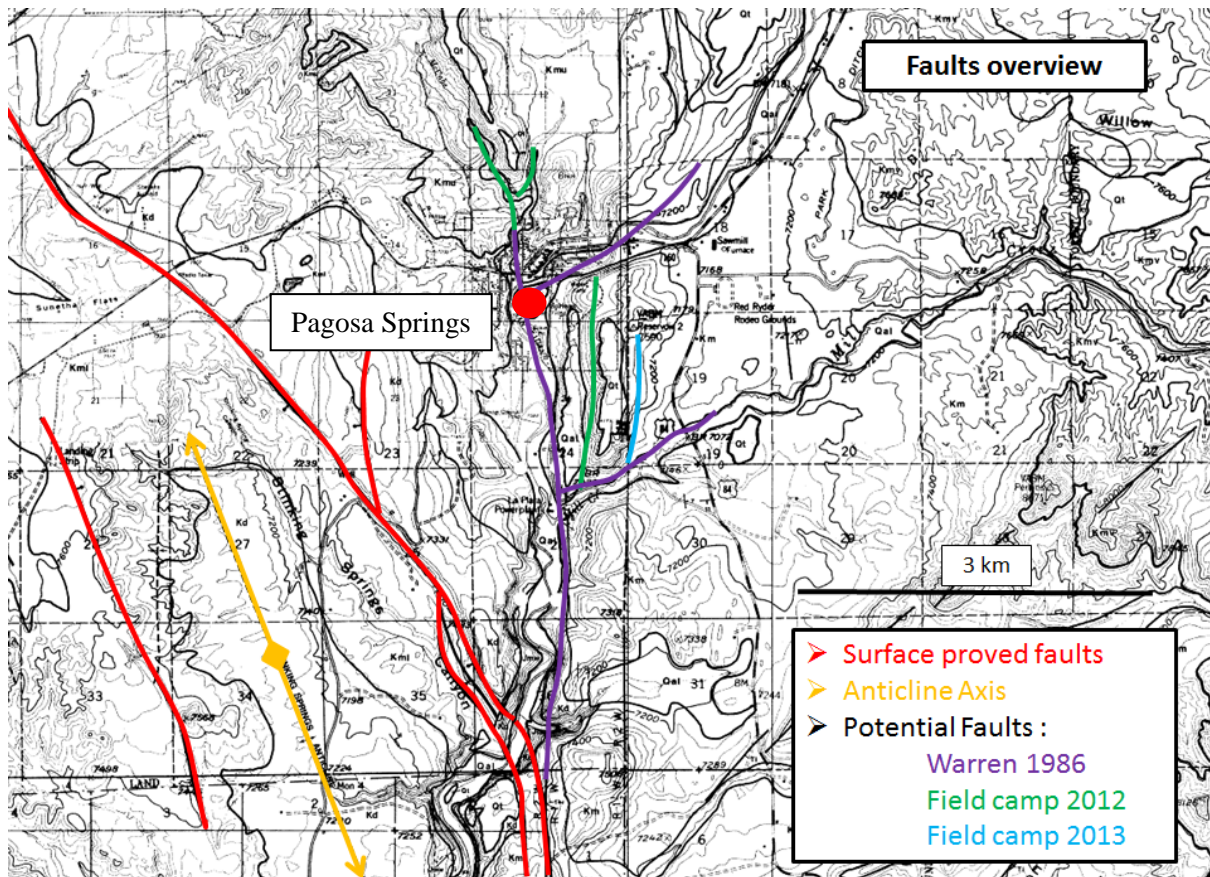
Figure 2.4: Identified Faults in the Pagosa Springs Area [7].
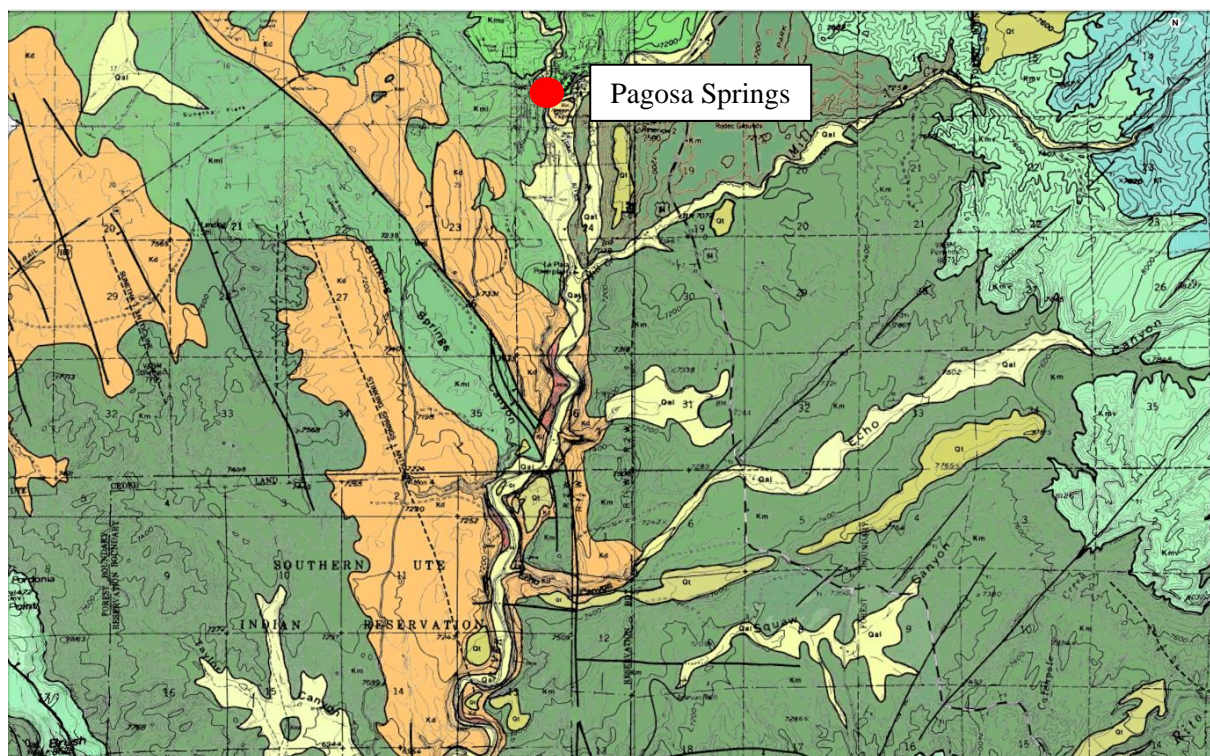
Figure 2.5: Geologic Map of the Pagosa Springs Area [3].

The Mancos Shale and Dakota Sandstone are the primary units exposed on the surface of the Pagosa Springs locations. Along the crest of some of the hills however, there are igneous fluvial cobbles that were deposited during erosion. It is likely that the hills on either side of the San Juan River were connected at one time. Regional uplift (up to ~3 kilometers of elevation) and later erosion by the river left the small valley where the town of Pagosa Springs is located. The igneous cobbles range from 2 to 6 inches in diameter and are well-rounded, indicating these were deposited while the river was at its previous elevated position. These are the youngest sedimentary deposits in the area of investigation [8].

The more modern events that are deforming the landscape are volcanic activity, faulting and folding, and active deposition of travertine. The San Juan Mountains were formed by the volcanic activity that was active until 28 million years ago. Volcanic tuffs comprise the majority of the high San Juan mountainsides to the north of Pagosa Springs, which contribute much of the layering that is visible along the ridges at Wolf Creek Pass [8]. This activity also formed many igneous dikes across the region, including a dike outcropping at the hairpin dike location. Isostatic rebound continues today, continuing the folding that deforms the subsurface in the area. Simultaneously, travertine is deposited at locations where current and ancient hot springs are located. The water from the hot springs carries high amounts of dissolved calcium carbonate (see Table 2.4 in Section 2.6) which precipitates out at surface temperature and pressure conditions, creating the hard travertine deposits seen at these springs.

2.2   Field Observations

Considerable geologic scouting was done prior to planning and executing any of the surveys in order to formulate a preliminary cross section of the area. To begin, the San Juan Mountains were analyzed from a vantage point at Wolf Creek Pass. Along the sides of the mountains, volcanic tuffs are visible with many layered facies differentiating the environment of deposition. Ancient and modern debris flows have also altered the landscape at many locations due to the clay rich soils and more recent rapid snowmelt. The Mesa Verde Formation was visible at these high vantage points, but had been eroded away at the remainder of the surveying locations.
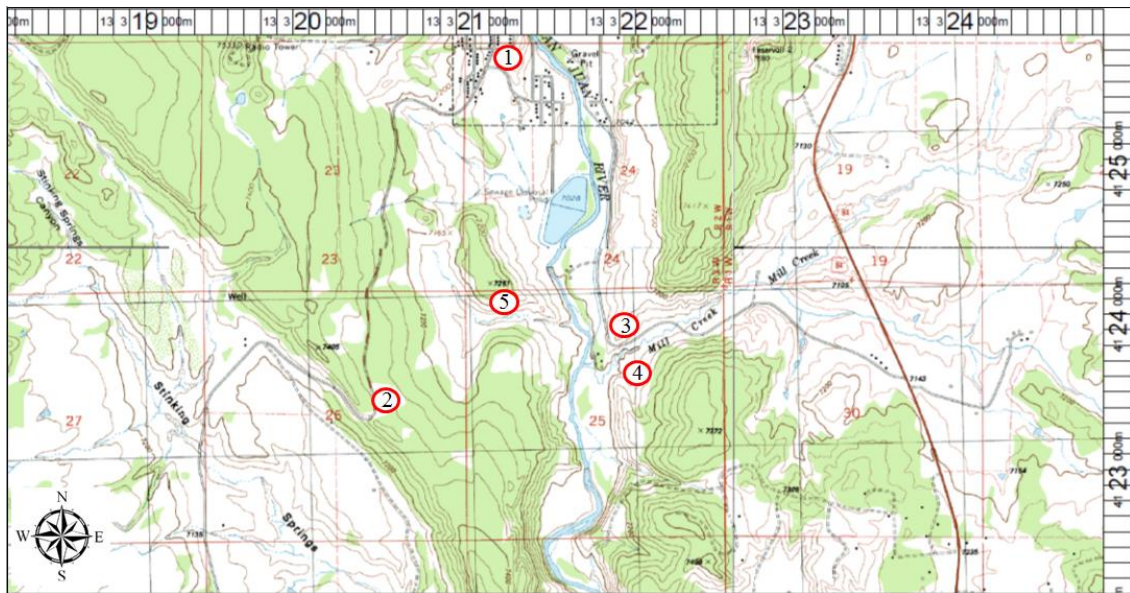
Figure 2.6: Map of Scouting Locations [11].

Once within the town of Pagosa Springs, much of the older rock layers, such as the Mancos Shale and Dakota Sandstone, were visible on the surface. The general trend of the Mancos Shale throughout the town was characterized by southward dip at approximately 5 – 10 degrees. Along several points on the San Juan River, localized sections of travertine can be seen. It is likely that these are locations of ancient hot springs because the spring water in downtown Pagosa has high concentrations of calcium carbonate (Table 2.4). The modern spring location is to the east of the river at a location named the Mother Spring (see Stop #1 on Figure 2.6). Previous surveying indicated that this natural spring is in excess of 1000 feet deep [10], however this depth has not been proven in this study.

The location for the main seismic line (Figure 1.2) was laid out across several plots of land to the south of downtown Pagosa Springs. One of the central locations that this line passed through was near a recycling plant that was determined to be on the edge of a probable fault (see Stop #2 on Figure 2.6). At the surface, the top of the Dakota Sandstone is visible. The Dakota Formation is rough and tightly compacted to the point where it appears to be quartzarenite at locations. Travelling down the hill, the sandstone can be seen in the road cuts (Figure 2.7). With this view, it can be seen that several facies associated with ocean transgression and regression are present. The presence of slickensides on this cliff face is evidence that a large fault cuts through the area. Slickensides form due to scraping that occurs during faulting. This fault location was supported by previous studies conducted in the area [10]. After field observations were made, a structure map was generated of the Top Dakota Sandstone using topography and outcrop locations (Figure 2.8).

Figure 2.7: Dakota Cliffs Outcrop at Stop #2; Photos Courtesy of Leanne Mearns and Nadine Young.
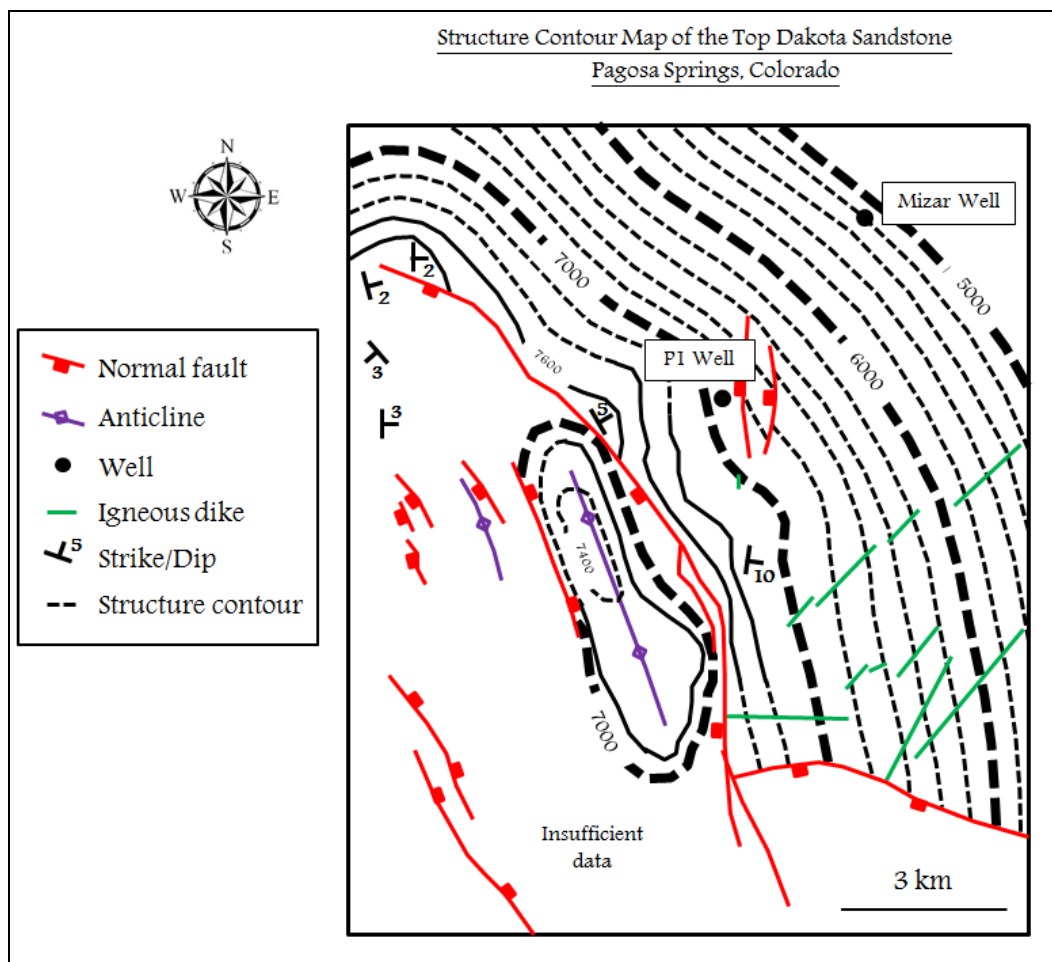
Figure 2.8: Structure Map of the Top Dakota Sandstone Constructed by Students.

Directly south of Pagosa Springs, the seismic line goes through a second location that was analyzed called the Hairpin Dike (see Stop #3 on Figure 2.6). At this point, there is a vertical dike penetrating through the Mancos Shale, which is visible from the road (Figure 2.9). The dike is yellow-orange in color and has baked approximately 1 meter of shale on either side of it. Contrary to many of the dikes indicated in Figure 2.5, this dike is striking north/south as opposed to northeast/southwest. It is likely that this area was faulted previously, which made it an area of weakness for the magma to inject into. Further evidence of the faulting in this area can be seen approximately 300 meters to the south (see Stop #4 on Figure 2.6). Within a small ravine, there are several normal faults striking east/west with approximately 1 meter of throw. It is suspected that these small, normal fault blocks are part of the plumbing for the hot water system in the area. Hot springs are typically formed at the intersection of several faults.

Figure 2.9: Hairpin Dike Outcrop at Stop #3; Photos Courtesy of Leanne Mearns and André Revil.

The Niobrara-equivalent member of the Mancos Shale was seen outcropping at several locations to the south of Pagosa Springs. These locations were toured and measured so that the boundary between the Dakota Sandstone and Mancos Shale could be approximated for mapping. It was estimated that there are 30 to 35 meters between the top of the Dakota Sandstone and the bottom of the limestone layer at a location to the northwest of the hairpin dike (see Stop #5 in Figure 2.6). At this same location, a normal fault through the Dakota Sandstone was seen striking north/south with approximately 5 meters of throw. At several locations slightly south of this outcrop, there were remnant springs visible with travertine deposits and some sulfuric odor (Figure 2.10). This is further evidence that faults in the Dakota Sandstone are part of the transport system for the hot water.

Figure 2.10: Limestone Layer (left) and Travertine Deposits (right) Near Stop #5; Photos Courtesy of Leanne Mearns and Nadine Young.

Once field observations and a structure map of the Top Dakota Sandstone were made, several rough cross sections along the main survey area were made. Previous findings regarding fault locations and thicknesses of the layers at Pagosa Springs were used to construct the following (Figure 2.11). For a complete interpreted cross-section following all of the data reduction, see Figure 13.1.7.
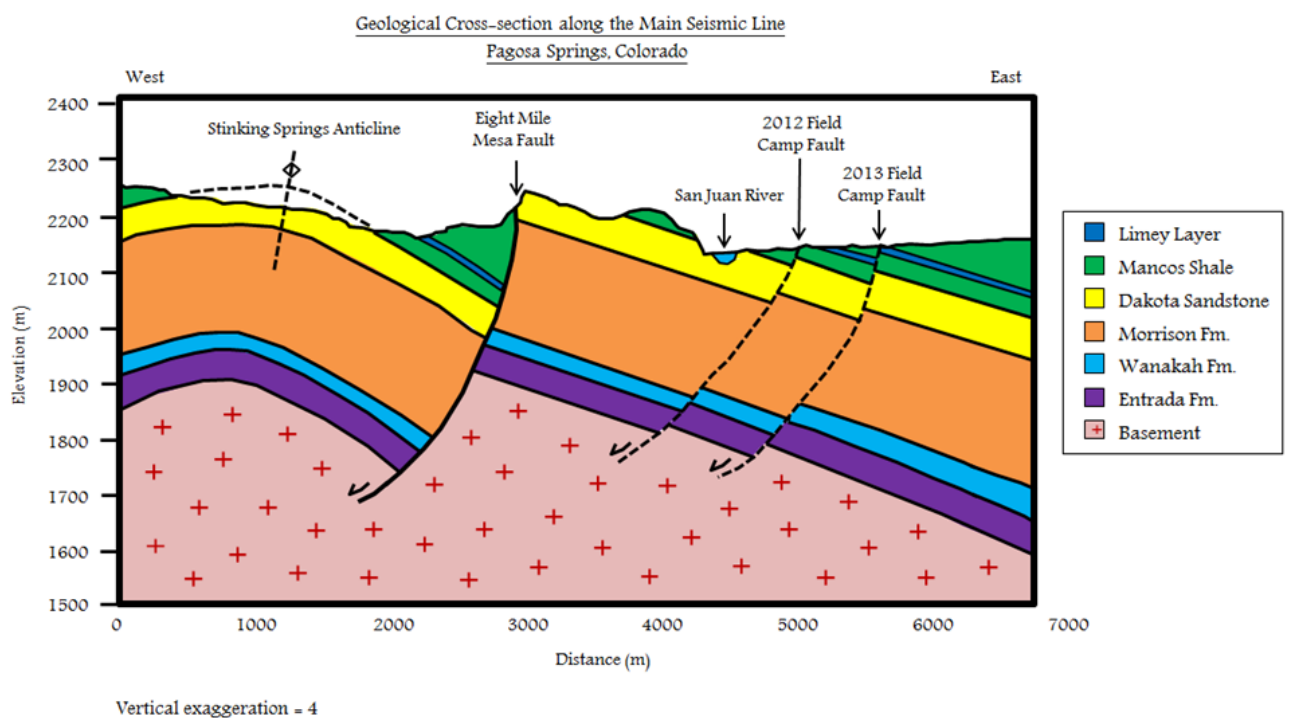
Figure 2.11: Initial Interpretation of Main Seismic Line.
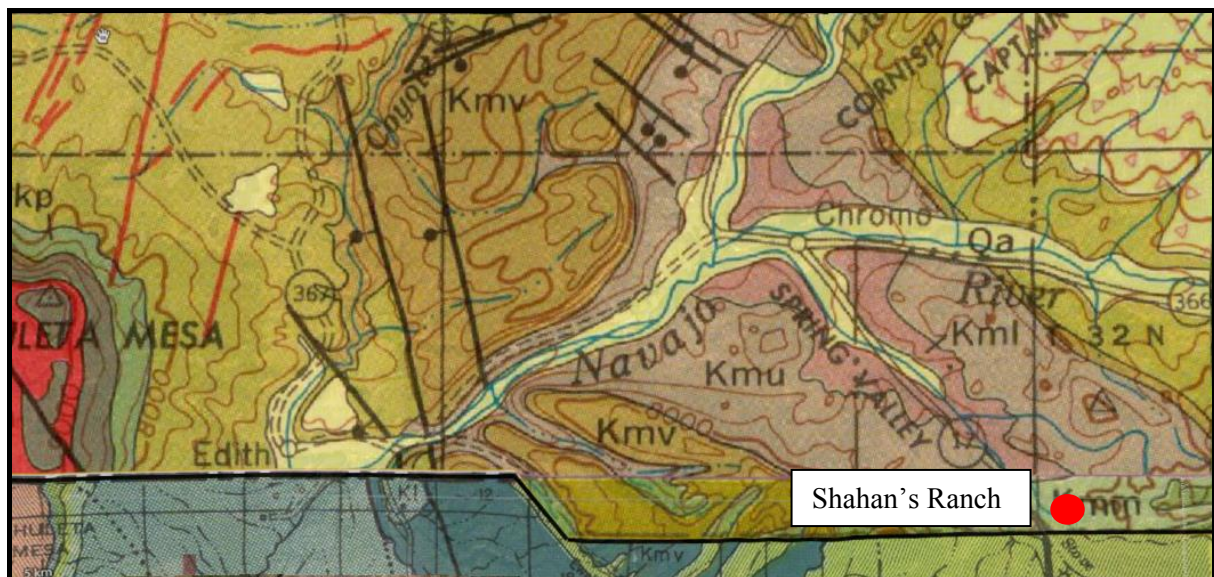
Figure 2.12: Map View of Shahan's Ranch (top) and Surface Geology Map (bottom) [3].

A secondary survey site called Shahan's Ranch was scouted by students due to the hot water well that is present on the property. Shahan's Ranch lies south of Pagosa Springs near the New Mexico border (Figure 2.12). After geochemical analysis, it was determined that this well is not of the same composition as the well in Pagosa Springs; however, analyzing the reservoir system can still be a valuable asset in understanding geothermal resources. The well at Shahan's Ranch was initially drilled for petroleum exploration, but was abandoned when the drillers reached an abundant supply of

hot water. Geologic surveys of the area revealed that the site lies in the middle of the Mancos Shale succession and that there were no Dakota Sandstone outcrops visible.

2.3   Mineralogy

Several rock samples were taken from various locations in the field (Figure 2.13) and were analyzed at the Colorado School of Mines. In order to estimate the mineralogy of the different rocks, both a hand lens and a stereo binocular microscope were used.

Figure 2.13: Location of the Samples Taken.

2.3.1   Mancos Shale

Shale Component

The Mancos Shale is black in color, very fragile, and breaks along fracture planes (Figure 2.14). An alternation between dark and lighter layers can be observed at a macroscopic scale on the order of several millimeters. This stratification is likely linked to the environment of deposition with the color being related to the percentage of organic matter. Some white patches approximately one millimeter thick are also visible in the shale. They have the same orientation as the bedding and are likely calcite intrusions formed during diagenesis. While not present in the samples analyzed, a few marine fossils were observed in the field and used to deduce the environment of deposition.
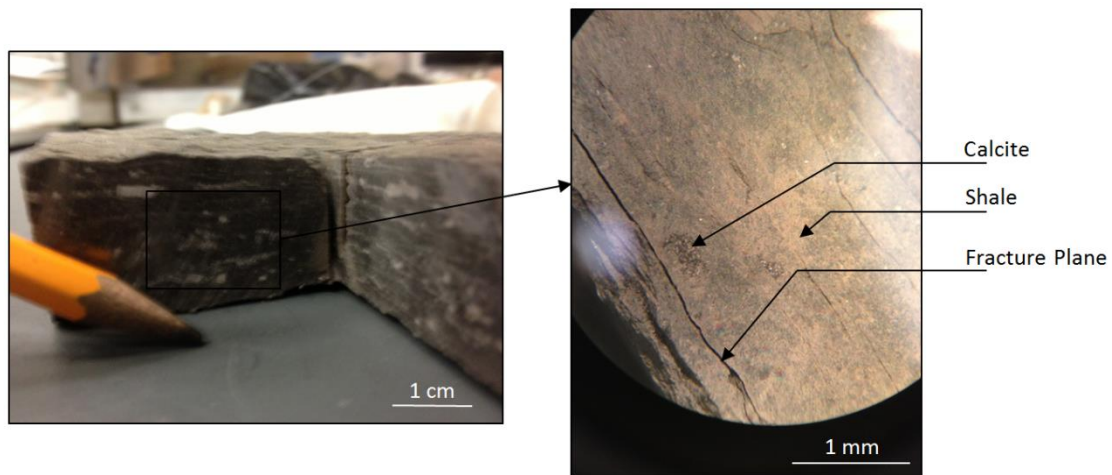
Figure 2.14: Mancos Shale Sample (Macroscopic and Stereo Binocular Microscopic x12).

While the grains were not visible when using the stereo binocular microscope, the stratification associated with deposition was even more obvious. A few calcite crystals are visible upon magnification and correspond to the white patches observed earlier. The composition of this rock is approximately 90 % shale and 10 % calcite. The mineralogy suggests the depositional environment is deep marine.

Limestone Component

The Mancos Shale also contains a hard, fractured layer which is much more resistant to erosion than the rest of the formation and is located approximately 30 meters above the base of the formation (Figure 2.15). This layer is much lighter in color than the surrounding Mancos Shale. Several calcite veins are visible with two different orientations approximately normal to each other. The majority of the rock is made of a grey and compact muddy limestone, with very few visible grains.
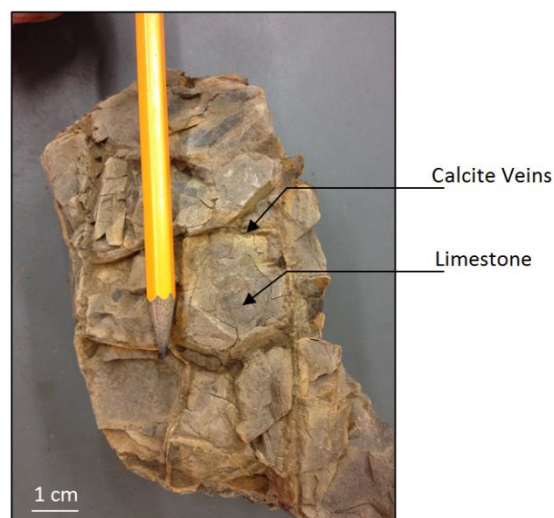
Figure 2.15: Sample from the limestone layer of the Mancos Shale.

It was not possible to look at this limestone with a microscope in order to determine the nature of the grains. Limestones are typically formed by precipitation of calcium carbonate rich sediments in a very calm, shallow marine environment, such as a lagoon. This implies that the depth of the inland sea was shallower at this point than during the deposition of the rest of the Mancos Shale. The calcite veins were likely formed after diagenesis.

2.3.2 Dakota Sandstone

As previously mentioned, the Dakota Sandstone can be split into different members. Looking at the mineralogy of samples from this formation helps to characterize the differences between the top and base of the formation.

Top Member

The top Dakota member is a nonhomogeneous yellow-brown rock that is highly fractured (Figure 2.16), as seen on the outcrop near the recycling center. There are two, orthogonal fracture planes that characterize the joints through this outcrop.

Figure 2.16: Sample of the top of the Dakota Sandstone.

The rock is massive, dense, fine-grained, and has a low porosity due to cementation. Ophiomorpha bioturbations (tubes about 1 cm of diameter) and symmetric mega-ripples can be observed, suggesting a shoreface depositional environment.

Base Member

The base member is similar to the top member; however, the fracture system is less dense and penetrates much deeper (Figure 2.17).

Figure 2.17: Sample of the Base of the Dakota Sandstone.

Comparison Between Top and Base

Upon closer inspection of the two samples with the stereo binocular microscope, more detailed differences can be observed (Figure 2.18). As expected, the majority of the grains are quartz (approximately 90 %), categorizing the Dakota Sandstone as a quartzarenite. In terms of cementation, the top member has a higher presence of shale and quartz cementation, as opposed to the base member, which is much cleaner. This matrix indicates that the top formation has been chemically altered.
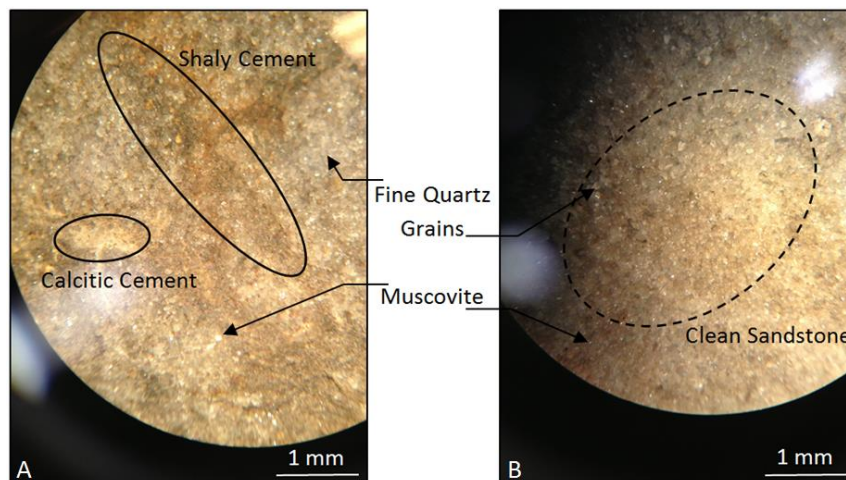
Figure 2.18: Comparison between the Top (A) and Base (B) of the Dakota Sandstone using a Stereo Binocular Microscope (x12).

Regarding the characteristics of these rocks, the porosity is estimated to be lower than 5% in both members. This suggests that the Dakota Sandstone is not an ideal reservoir rock; however, the fractures have made it so that it is the predicted reservoir in the area. Even rocks that are not very permeable or porous can store large amounts of water if they are fractured enough and can allow flow throughout.

2.3.3 Top Morrison

The Top Morrison Formation differs from the Dakota Sandstone above in that the grains are much coarser, the matrix contains more shale, and it is not as consolidated (Figure 2.19). This rock was deposited in a high energy environment, evidenced by the coarser sand grains. The shale rich matrix is likely to be formed afterwards during diagenesis.
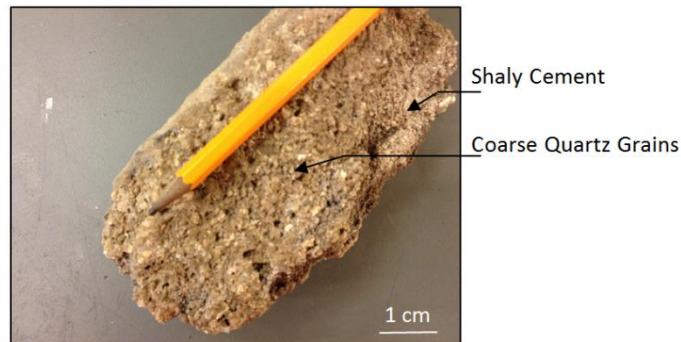
Figure 2.19: Top Morrison Formation Sample.

2.3.4 Dike

A sample was collected from the dike at the hairpin turn near the power plant station. As seen on Figure 2.20, this igneous rock is dark colored and closer investigation using the stereo binocular microscope identified elongated feldspar crystals suspended in volcanic glass. A few of the small crystals are visible, suggesting rapid cooling of the rock at the time of its intrusion.
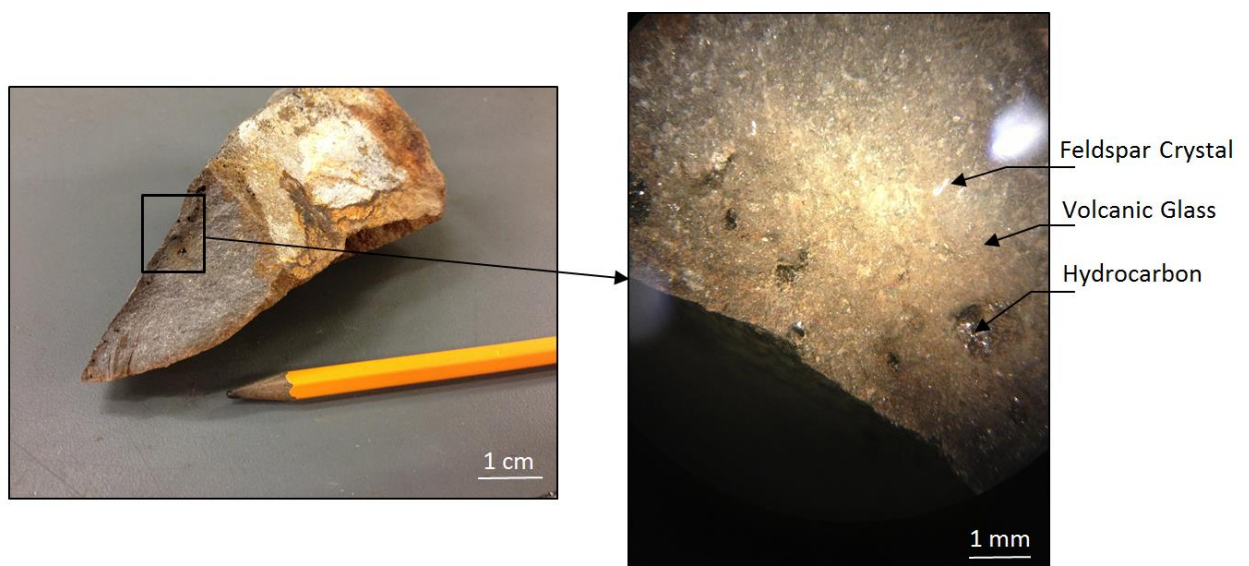
Figure 2.20: Sample from the Hairpin Turn Dike (Macroscopic and Stereo Binocular Microscope x12 scales).

It is possible that this dike intruded through a pre-existing fracture plane because of its different orientation when compared to other dikes in the area. Additionally, the edge of the dike is in contact

21

with shale containing small patches of hydrocarbons that were likely formed during the baking of the shale at the time of intrusion.

2.3.5 Travertine

A sample of travertine (Figure 2.21) from the Mother Spring was analyzed and was composed of 100% aragonite and calcite. This is a result of the precipitation of dissolved aragonite from saturated water at surface conditions. Deposits of this rock indicate the presence of the hot springs water.
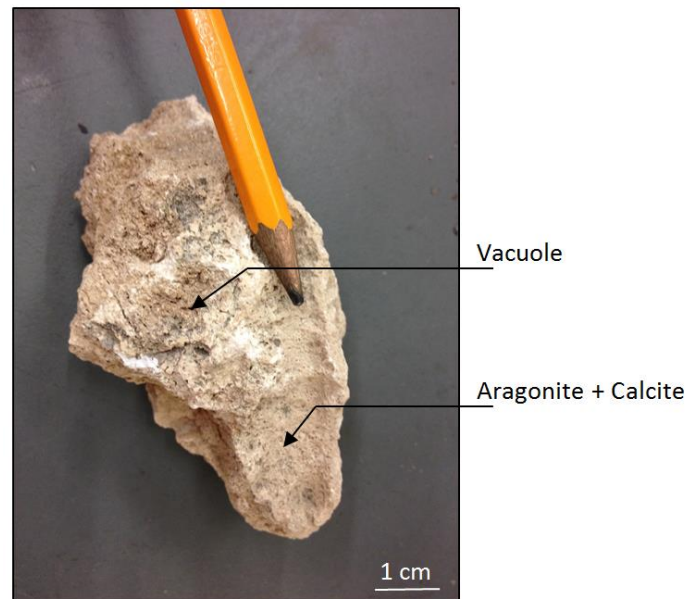
Figure 2.21: Travertine samples at the Mother Spring.

2.4 Petrophysics

In order to accurately interpret the surveys undertaken in the field, a good understanding of the petrophysical properties of the units of interest is required. The two main rock units of interest in this study are the Mancos Shale and Dakota Sandstone, as these two units are believed to be the reservoir-seal pair of the hydrothermal system in the area (see section 2.5).

A petrophysical study was carried out on the 'Adios Dineros 2' and 'Mizar' wells using the available gamma ray, resistivity, neutron porosity (NPHI) and density porosity logs (Figure 2.22). The logs start at the surface and go down to a depth of 340 meters; thus, only the Mancos Shale, the Dakota Sandstone and the Morrison Formation can be observed.
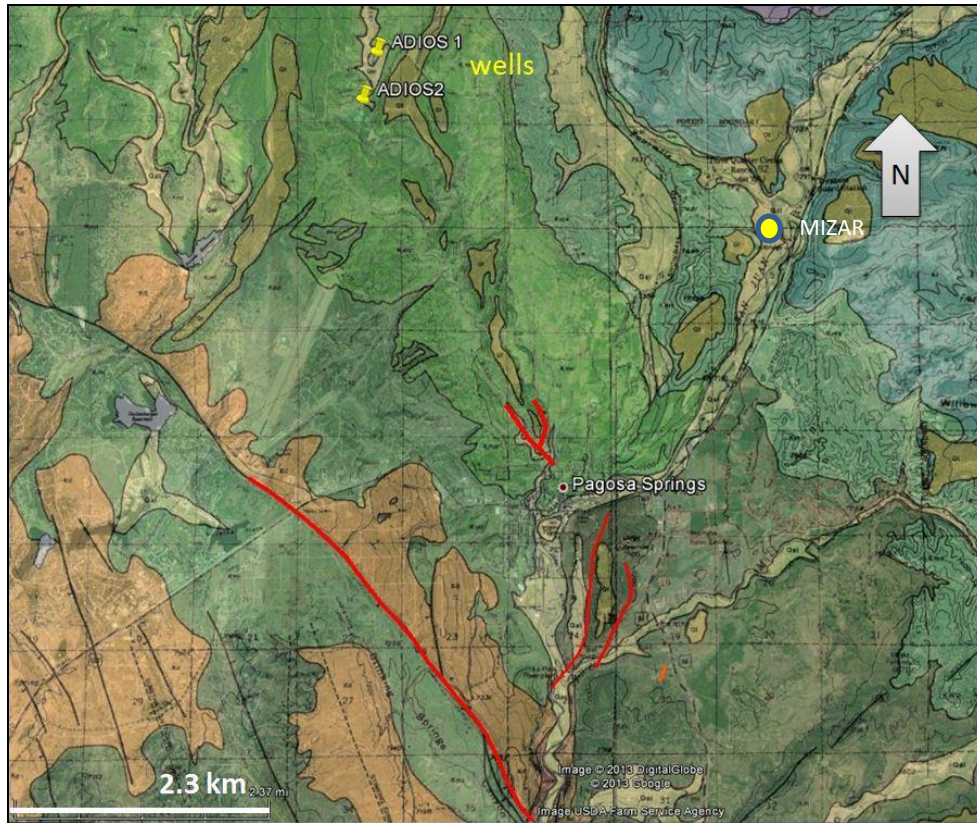
Figure 2.22: Location of the Adios Dineros 2 Well [3].

Adios Dineros 2

The top of the Dakota Sandstone was identified at 89 meters and the top of the Morrison Formation at 143 meters, according to their relative shale content.

In order to calculate the shale content and the porosity, the values of density and porosity from the logs were plotted on a neutron-density cross-plot. The pure shale values of neutron porosity and density has been taken in a clean shale interval of the Mancos Shale. The results obtained are presented in Table 2.1 below.

Table 2.1: Neutron Porosity and Density Values Extracted from the Adios Dineros 2 Log.

Layer	Neutron Porosity (NPHI) (%)	Density Porosity (RHOB) (g.cm-3)
Mancos shale	27	2.55
Dakota Sandstones	11	2.61
Morrison	20	2.54

These three points are plotted in a neutron-density cross-plot (Figure 2.23). A triangle is built, where one corner is water (100% porosity), the second corner is pure shale (100% shale) and the last one is pure sandstone (0% porosity and 0% shale). The projection of the point on the [Sandstone, Water] axis gives the porosity, and the projection of the point on the axis [Sandstone, Shale] gives the shale content.

23
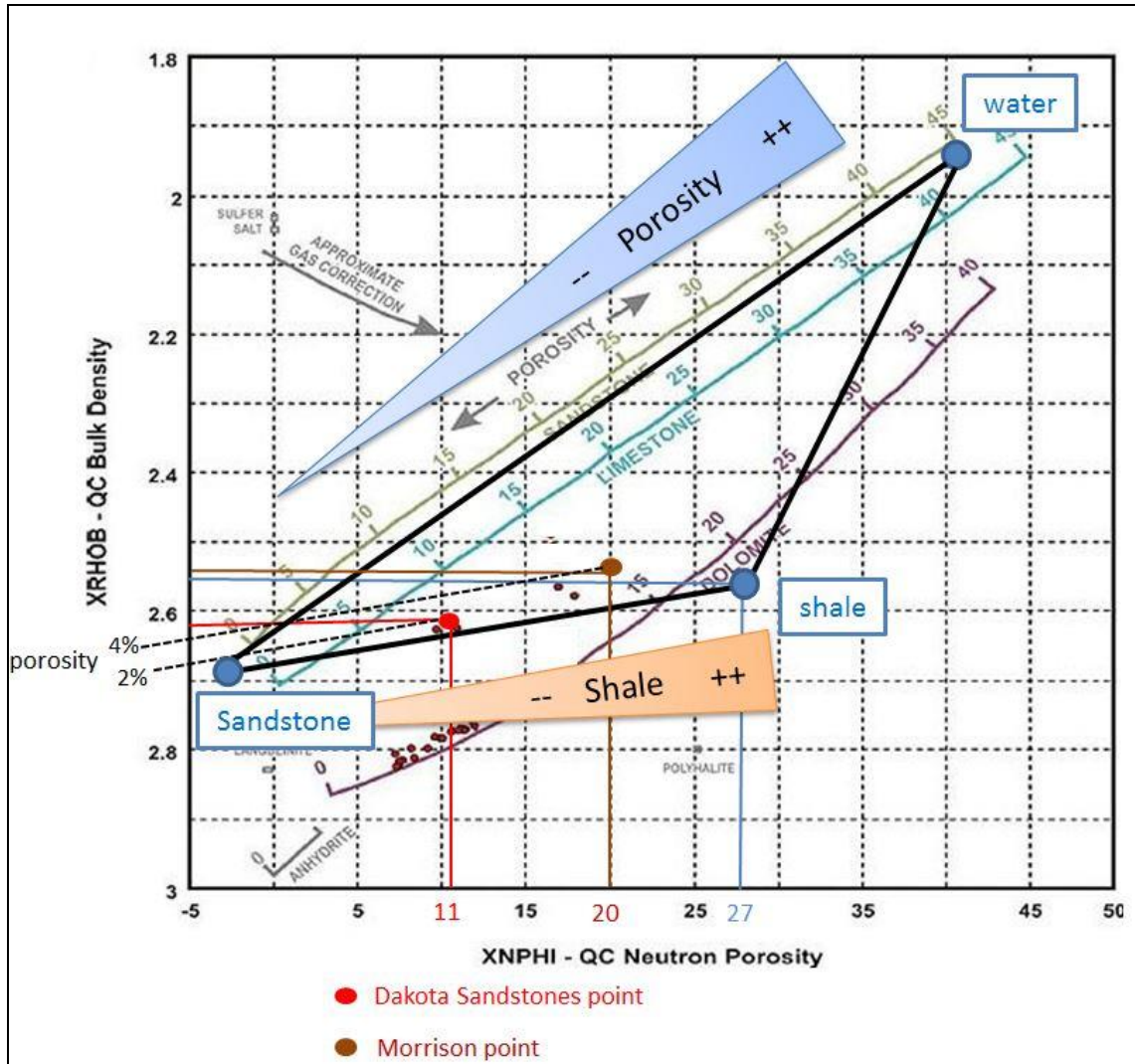
Figure 2.23: Neutron-Density Crossplot with Interpretations [12].

Finally, the effective densities for each of the three layers have been calculated with the formula:

$$\Phi_{eff} = [\Phi\, \rho_{air}] + [(1 - \Phi)\, \rho_{bulk}]$$

Equation 2.1: Effective Density Formula.

where Φ is the porosity and ρ the density. The results are summarized in Table 2.3.

Mizar

The Mizar well logging begins at 189 meters and ends at 701 meters. This means that this log cannot provide any information about the Mancos Shale or Dakota Sandstone, but is likely to provide some data for the Morrison, Wanakah, and Entrada formations as well as the Precambrian basement according to the depths found at the P1 well. Using this stratigraphic column, the tops of the

24

Wanakah, Entrada, and basement were identified at 288, 324 and 378 meter depth, respectively. The values extracted from the log are presented in Table 2.2 below.

Table 2.2: Neutron Porosity and Density Extracted from the Mizar Log.

Layer	Neutron porosity (NPHI) (%)	Density porosity (RHOB) (g.cm-3)
Morrison	0.28	2.6
Wanakah	0.27	2.6
Entrada	0.28	2.58
Precambrian Basement	0.22	2.6

The same protocol was used to get the results presented in Table 2.3; however, the Wanakah Formation had to be evaluated separately as the fact that it is a limestone had to take into consideration. It is possible that since the well logs are older and have not been updated, the information for the Wanakah layer is incorrect and has not been evaluated. The interpretation is shown in Figure 2.24.
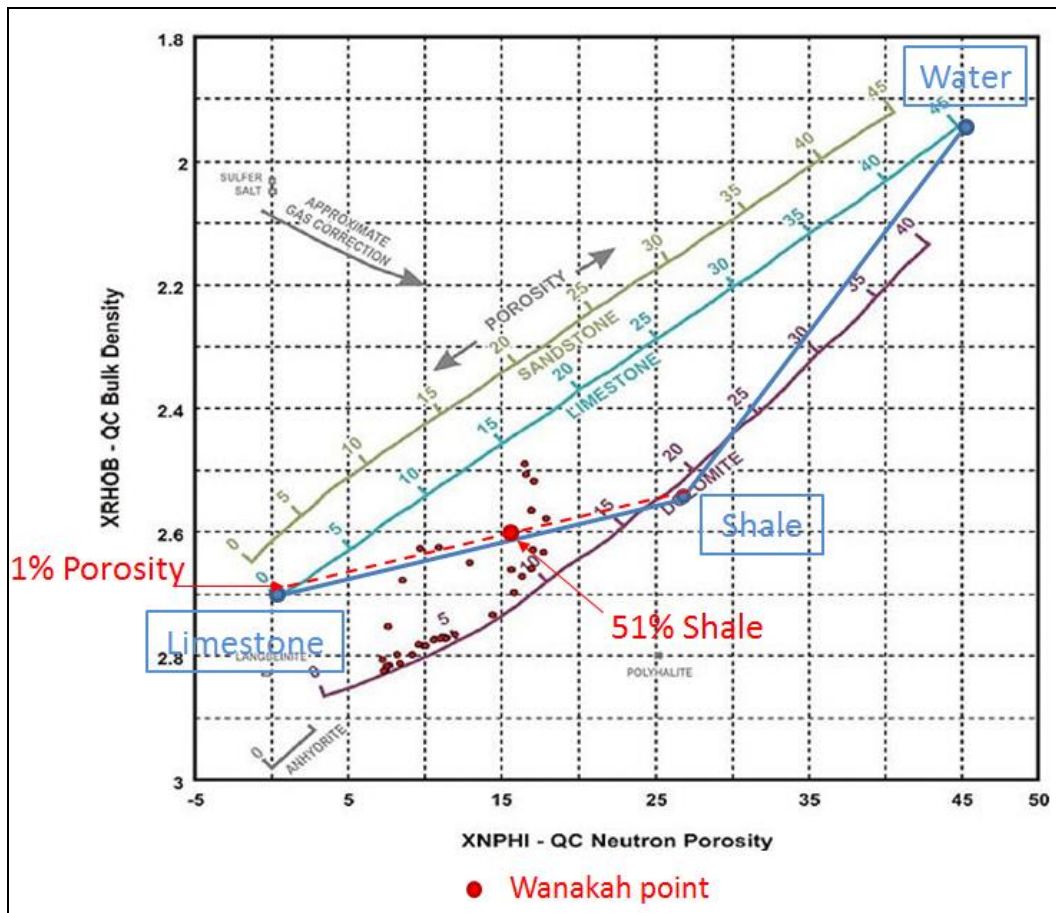
Figure 2.24: Neutron-Density Crossplot with interpretation for the Wanakah Formation [12].

Unfortunately, the result from the well log for the Precambrian basement was determined to be incorrect because the NPHI value was not equal to zero as expected. The values used in Table 2.3 are from reference [13].

Table 2.3: Petrophysics Results for the Layers at Pagosa Springs [13].

Layer	Porosity	Volume Shale	Density (g.cm^{-3})
Mancos Shale	0%	100%	2.55
Dakota Sandstone	2-3%	40%	2.61
Morrison Formation	4%	60%	2.50
Wanakah	1%	53%	2.63
Entrada	2%	55%	2.50
Precambrian Basement	0%	0%	2.80

The Dakota sandstone has a low porosity because it is quartz cemented. Therefore it is relatively dense and resistive to erosion. These density values are of great importance for interpretation of gravity data.

2.5 Reservoir Formation

Hot springs are found in areas in which geothermally heated water escapes to the surface of the Earth. The existence of a hot spring depends on five geological factors: a heat source, an aquifer (reservoir), a recharge mechanism, a cap rock and a migration route. A generalized view of this type of system can be seen below in Figure 2.25.
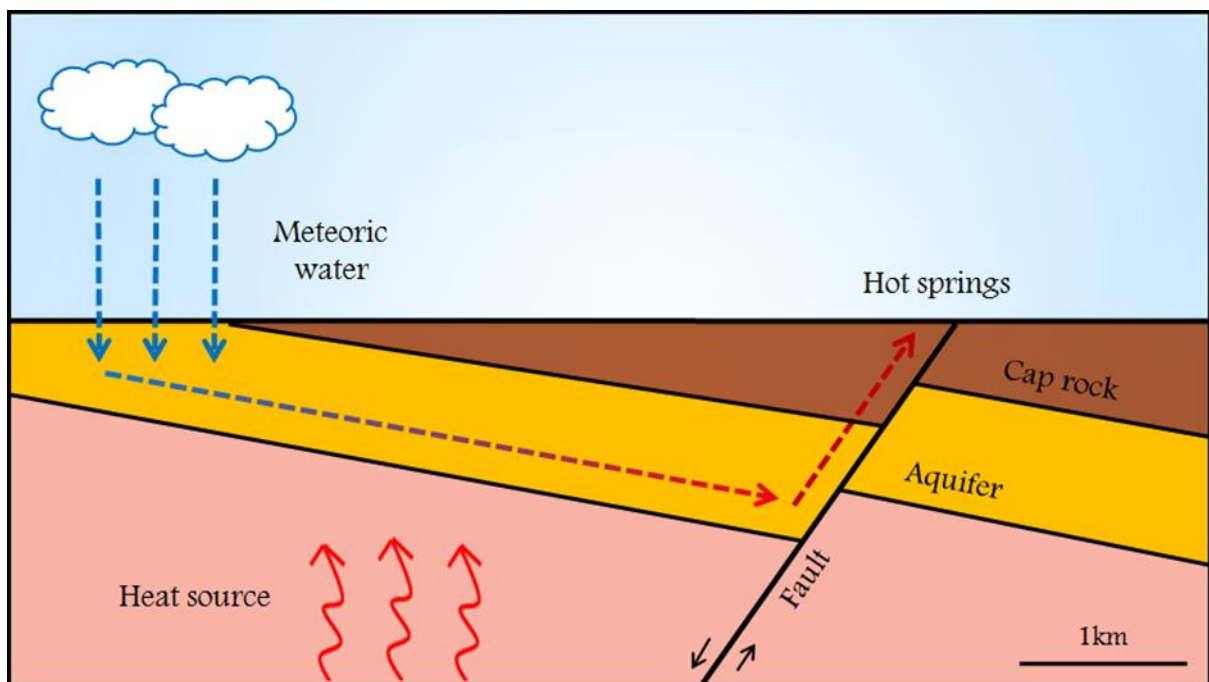
Figure 2.25: Generalized Reservoir System, Created by Leanne Mearns.

2.5.1 Heat Source

One of the most important elements in a hot spring system is a heat source. In general, as water percolates deeper into the subsurface, it warms up due to the Earth's geothermal gradient. However, in some areas, localized volcanism or increased tectonic activity can lead to temperature anomalies, in which the temperature is greater than usual. In Pagosa Springs, the heat source is not fully understood. However, visible igneous intrusions and volcanic tuffs, along with an abnormally high geothermal gradient, suggest that there could be a cooling magma chamber in the subsurface below the region [14].

2.5.2 Aquifer (Reservoir)

An aquifer is a subsurface reservoir in which geothermal water accumulates. In order for a hot spring to form, there must be an aquifer present to feed the spring with hot water. Aquifers need to be highly porous rock, so that water can be stored and easily transported through the rock. In Pagosa Springs, the Dakota Sandstone is believed to be the main aquifer for the hot springs. Most temperature logs from local wells show that the Dakota Sandstone's water has higher temperatures than in the surrounding rock units. However, a dynamic system is present, such that the water is constantly cycling and is never stored in the aquifer. The water only passes through the aquifer on its way to the surface. This whole cycle is believed to take around 10,000 years to complete [14].

2.5.3 Recharge Mechanism

The existence of a hot spring depends on whether the spring, in particular the aquifer, is consistently recharged with groundwater. In Pagosa Springs, rainwater and the San Juan River recharge the Dakota Sandstone aquifer with water. The rivers are fed by snow melt from the nearby Rocky Mountains; therefore the amount of water being fed into the hot spring system depends on the yearly precipitation [14].

2.5.4 Cap Rock

A cap rock is an impermeable rock that lies on top of the aquifer, preventing the water from escaping. Cap rocks act like a seal; hence they reduce heat loss and evaporation from the hot water stored in the aquifer. In Pagosa Springs, the cap rock is believed to be the Mancos Shale, due to its impermeable properties and its position above the Dakota Sandstone aquifer.

2.5.5 Migration Route

In general, meteoric rain water and snow melt percolate into porous rocks in the ground. As the water sinks deeper into the ground, it heats up due to the increasing internal temperature of the Earth. Because hot water is less dense than cold water, the hot water rises and tries to find a pathway to the surface. This pathway is usually along fault planes or fractures, as the layers above the reservoir tend

to be impermeable. Consequently, hot springs are usually found in areas in which the surface of the Earth is breached by fault systems. Pagosa Springs lies to the northeast of a large fault, known as the Eight Mile Mesa Fault. Knowing the fault system is key to understanding the migration pathway of the hot springs water.

2.6   Geochemistry

The geochemical signature of the water in Pagosa Springs was characterized previously at the Mother Spring (Figure 2.26). This data was provided by Paul Morgan of the Colorado Geologic Survey. Temperature, conductivity, pH, and the concentration in milligrams per liter (mg/L) of many different elements were measured on six separate occasions ranging from 1920 to 1993 [15].

Figure 2.26: Location of the Mother Spring [3].

The Mother Spring is approximately 8 to 10 meters in diameter and previous studies suggest that it is in excess of 1,000 feet deep [7]. The spring water is slightly acidic, with an average measured pH of 6.6 and an average of 3,206 total dissolved solids in milligrams per liter. The hot water from the subsurface is able to dissolve minerals from the surrounding rocks in much higher quantities than in a typical cooler groundwater system. In the water, there are relatively high quantities of dissolved calcium carbonate, bicarbonate, sodium, and sulfate, yet only small quantities of calcium, chlorine, potassium, and magnesium are found. Table 2.4 below has the specific values of the relevant dissolved solids. Any values that were either unreliable or deemed to be insignificant were not

included for ease of viewing. It should be noted that the variation in the data between dates could be due to seasonal variations since the time of year is inconsistent between measurements.

Within the Mancos Shale, there are pyrite clusters and small calcite veins that are contributing to the high amounts of dissolved sulphate and calcium carbonate respectively [7, 16]. The dissolved sodium could be from the water filtering through the plagioclase within the basement rock or from andesitic minerals in other layers. Biotite from the Precambrian basement could have contributed to the high quantities of potassium and magnesium. These signatures of near surface, as well as basement minerals, are characteristic of meteoric water that has originated from the surface, filtered through the deep layers, and returned to the surface via a faulting system [7]. This differs slightly from the reservoir system shown in Figure 2.25, as the water in Pagosa Springs percolates all the way down to the basement instead of circulating through only the Dakota Sandstone. Additionally, the high presence of sulfates implies that the water is not originating within the crystalline basement and only filters through it [7]. An updated diagram that more closely approximates the reservoir system in the area is shown below in Figure 2.27.

Table 2.4: Mother Spring Values Provided by Paul Morgan [15].

	Date	Unknown-1920	August-1975	October-1975	January-1976	April-1976	June-1993
Well Log Data at Mother Spring	pH	-	6.5	6.9	6.6	6.5	6.6
	Temp (0C)	65	58	57	55	54	52
	TDS (mg/L)	-	3200	-	3310	3040	3272
	CaCO3 (mg/L)	-	701	705	707	702	-
	HCO3 (mg/L)	636	855	859	862	856	771
	Ca (mg/L)	247.1	230.0	210.0	240.0	230.0	378.0
	Mg (mg/L)	16.8	25.0	23.0	2.6	24.0	42.0
	Na (mg/L)	525.0	790.0	780.0	800.0	730.0	574.0
	K (mg/L)	370.0	90.0	97.0	97.0	95.0	67.0
	Cl (mg/L)	180.0	180.0	180.0	190.0	180.0	175.0
	SiO2 (mg/L)	69	54	-	58	59	83
	F (mg/L)	-	4.3	-	5.0	4.8	4.4
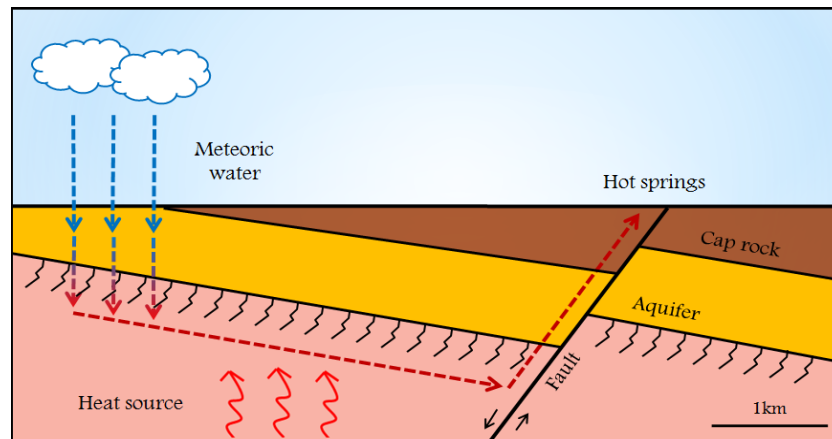
Figure 2.27: Revised Reservoir System: Created by Leanne Mearns.

2.7   Hydrology

The San Juan River is the main river running through the San Juan Basin, covering four states – Colorado, New Mexico, Arizona and Utah. The river runs east-west and is fed by many tributary rivers, most of which flow from northeast to southwest due to the regional topography (Figure 2.28). Pagosa Springs lies to the far east of the San Juan Basin, near the edge of the watershed cut-off and so groundwater tends to flow from northeast to southwest. However, this is not necessarily the direction of subsurface flow, as this depends on many factors, including the porosity, fracture systems and the dip of the strata. The subsurface flow direction is imaged using the self-potential (SP) method which is explained in detail in Section 11.
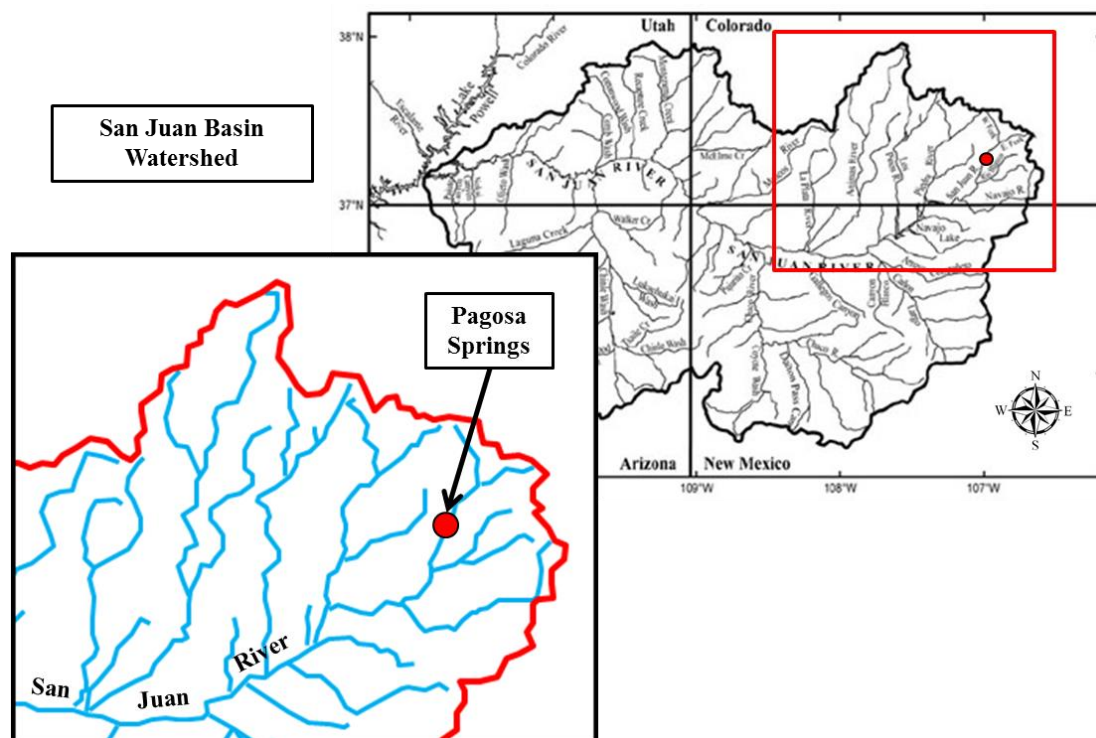
Figure 2.28: Tributaries and River System of San Juan Basin [17].

2.8 Heat Flow Analysis

2.8.1 Introduction

The geothermal system in Pagosa Springs, CO and surrounding areas (including Shahan's Ranch) has yet to be developed to its full potential. However, insights into the geothermal system can be obtained through the study of heat flow. Heat flow is the transfer of thermal energy from a hot area to a cool area [8]. The heat flow can be characterized by radiation from the sun, conduction, or advection [8]. Advective heat transfer is the transfer of heat by moving cold water to a warmer location and vice versa [18]. Heat flow is found using the thermal conductivity and gradient found from well temperature data. The thermal conductivity is the property of the rock's ability to transmit heat [7]. The geothermal gradient describes the change in temperature over the change in depth. The goal of the heat flow analysis is to determine the local heat source and pattern in Pagosa Springs, CO. Thermal buoyancy and hydraulic pressure can also be utilized to examine the driving force and effects of heat flow. Thermal buoyancy is a naturally occurring effect in the Earth to equilibrate a columnar water system of varying densities [8]. Hydraulic pressure is an effect caused by large amounts of pressure put on the system which forces the ground water to the surface through weaknesses in the subsurface geologic structure, such as faults and joints [8]. Thermal buoyancy is suspected to be the prominent effect of the water flow found in Shahan's Ranch.

2.8.2 Pagosa Springs Geothermal System

A heat flow analysis was conducted over Pagosa Springs using existing well data. The well locations are shown in Figure 2.29. The G well's heat flow data were obtained directly from a study performed in 1980 [7]. Table 2.5 presents the G wells heat flow data.

Table 2.5: G well heat flow data over various formations and depths [7].

Well (refer to Figure 2.29)	Depth (m)	Formation	Heat Flow (mW/m^2)
G1	48	Dakota Sandstone	4.76
G2	87	Mancos Shale	4.17
G3	86	Dakota Sandstone	3.59
G4	84	Dakota Sandstone	2.97
G5	88	Mancos Shale	3.05
G6	87	Mancos Shale	2.15
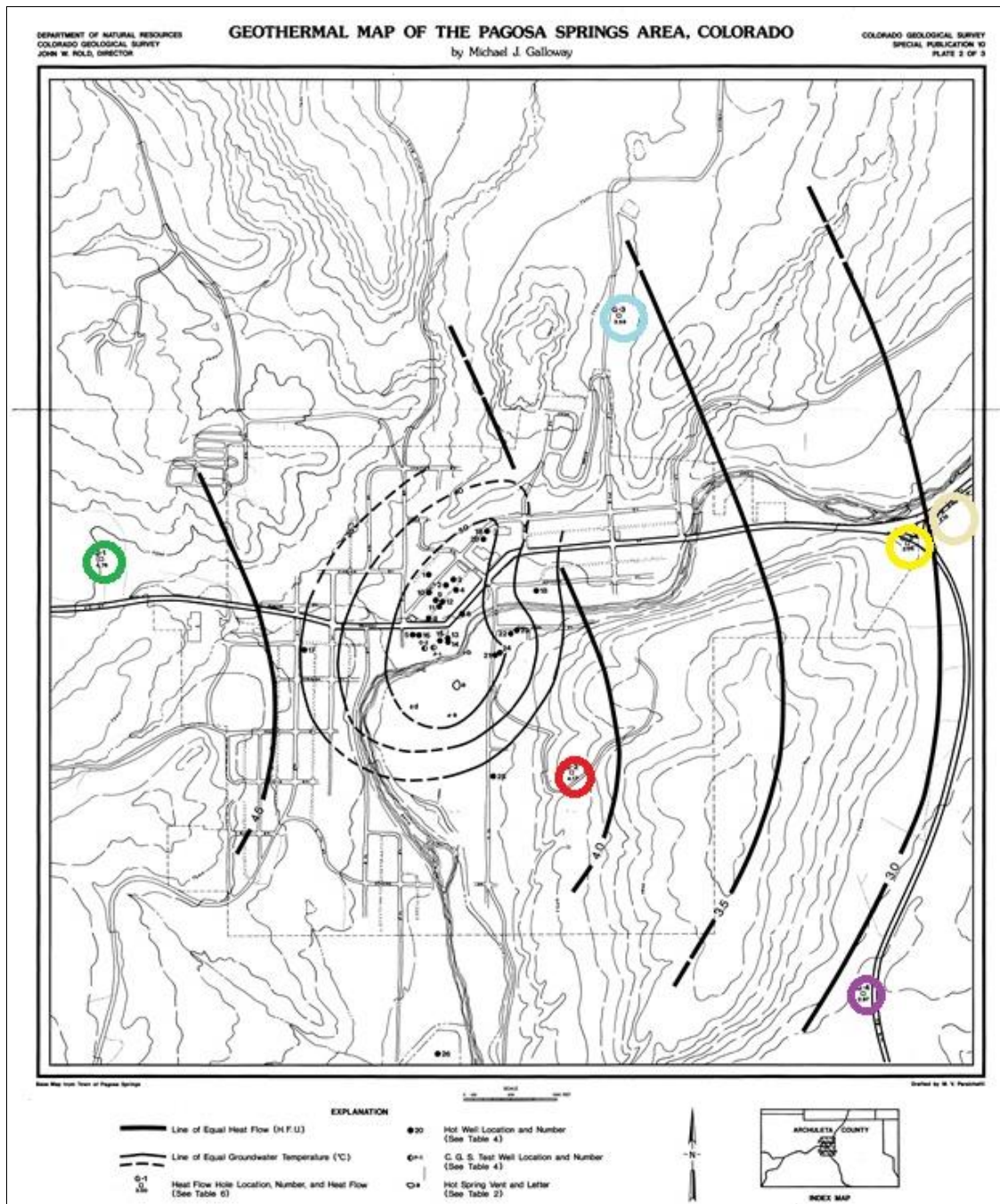
Figure 2.29: Geothermal Map of the Pagosa Springs Area, Colorado. Well G1 is circled in green, G2 in red, G3 in cyan, G4 in purple, G5 in yellow, G6 in nude, P1 in dark blue, and O2 in orange [8].

While the G wells are spread widely throughout the area, the P1 and O2 wells are much closer to the Mother Spring, and closely reflect the attributes of the Mother Spring. Insight was gained from this connection into the origin and processes of the Mother Spring. The thicknesses and temperatures associated with the P1 and O2 wells were taken from Galloway's data [7]. These values were used to calculate the geothermal gradient and the heat flow of the individual layers using Equation 2.2 [18], assuming heat flow through each individual layer.

$$Q = K \frac{dT}{dZ}$$

Equation 2.2: Heat Flow Equation.

Where Q is the heat flow (W/m^2), K is the thermal conductivity (W/m*K), dT is the change in temperature (K), and dZ is the change in thickness (m). Differentiating thermal conductivities and thermal gradients between the Mancos Shale, Dakota Sandstone, and Morrison Sandstone [19], it became necessary to determine the heat flow of each individual layer. All calculations performed in this section are assuming a static system, not a dynamic system. The values used to calculate heat flow and the calculated heat flow can be found in Table 2.6.

Table 2.6: P1 and O2 Heat Flow Values.

Well	Formation	Thermal Conductivity - K (W/m*K)	Thickness – dZ (m)	Temperature Change - dT (K)	Geothermal Gradient –dT/dZ (K/m)	Heat Flow – Q (mW/m^2)
P1	Mancos Shale	1.3	73.15	293.15	4.007	218.038
P1	Dakota Sst.	3.8	60.96	290.15	4.759	756.96
P1	Morrison Fm.	2.8	315.47	286.15	1.067	125.072
O2	Mancos Shale	1.3	73.15	288.65	3.946	214.69
O2	Dakota Sst.	3.8	60.96	273.65	4.489	714.014
O2	Morrison Fm.	2.8	103.63	277.15	2.626	307.782

Examining Table 2.5, Table 2.6 and Figure 2.29, the highest heat flow is located west of downtown Pagosa Springs and gradually decreases heading east. It can also be seen that the subsurface temperature decreases radially outward from downtown Pagosa Springs. The Dakota Sandstone exhibits a higher thermal conductivity and therefore a higher temperature gradient. The geothermal gradient and heat flow in the Dakota Sandstone is greater than in the other formations, which suggests the Dakota Sandstone facilitates the flow of hot water. The discrepancies between the G well and P1 and O2 heat flow results could be due to assumptions of a static versus a dynamic system, or a consistent thermal conductivity value for the layers [18].

2.8.3 Shahan's Ranch Geothermal System

Thermal buoyancy was the focus at Shahans's Ranch. This location can be seen in Figure 2.12. Temperature data was acquired using a temperature probe which provided information to find the thermal gradient [18]. That was then used in Equation 2.3 to find the approximate depth of water circulation.

$$Z_{circ} = \frac{Th}{\left(\frac{dT}{dZ}\right)}$$

Equation 2.3: Depth of Water Equation.

Where Z_{circ} is the depth of the water circulation (m), Th is the temperature (341.55 K) of the hot springs (K), dT is the change in temperature (300.15 K), and dZ is the change in thickness (1000 m). Next, the height of the hot water column was calculated using Equation 2.4, Equation 2.5, Equation 2.6, and Equation 2.7 [20].

$$\rho_{norm} = \frac{\rho\_s}{1 + \frac{\beta(Th - Ts)}{2}}$$

Equation 2.4: Average Density of a Column of Non-Thermal Water.

Where ρ_{norm} is the average density of a column of non-thermal water (kg/m^3), ρ_s is the density of water at the surface (999.941 kg/m^3), β is the volumetric temperature expansion coefficient (0.3128*10^{-3} 1/K), Th is the temperature of the hot springs (341.55 K), and Ts is the surface temperature (K).

$$W_{norm} = \rho_{norm} * g * Z_{circ}$$

Equation 2.5: Weight of Unit Column of Non-Thermal Water.

Where W_{norm} is the weight of a unit column of non-thermal water (Kg*m/s^2), ρ_{norm} is the average density of a column of non-thermal water (kg/m^3), g is the gravitational acceleration on Earth (9.81 m/s^2), and Z_{circ} is the depth of the water circulation (m).

$$\rho_{hot} = \frac{\rho\_s}{1 + \beta * Th}$$

Equation 2.6: Density of Hot Water.

Where ρ_{hot} is the density of the hot water (kg/m³), ρ_s is the density of water at the surface (999.941 kg/m³), β is the volumetric temperature expansion coefficient ($5.6036*10^{-3}$ 1/K), and Th is the temperature of the hot springs (341.55 K).

$$h_{hot} = \frac{W_{norm}}{\rho_{hot} * g}$$

Equation 2.7: Height of a Static Column of Hot Spring Water.

Where h_{hot} is the height of a static column of hot spring water (m), W_{norm} is the weight of a unit column of non-thermal water (Kg*m/s²), ρ_{hot} is the density of the hot water (kg/m³), and g is the gravitational acceleration on Earth (9.81 m/s²). Finally, the difference between the water circulation depth and the water column height was calculated. This calculation is represented by Equation 2.8 [19].

$$x = h_{hot} - Z_{circ}$$

Equation 2.8: Estimate of the Rising Height of the Hot Springs.

Where h_{hot} the height of a static column of hot-spring is water (m), and Z_{circ} is the depth of the water circulation (m). This difference gives an estimate of the height the hot springs can raise by thermal buoyancy above the local groundwater table. The values calculated from Equation 2.3 – 2.7 can be seen in Table 2.7[18].

Table 2.7: Thermal Buoyancy Values.

Well	Z_{circ} (m)	ρ_{norm} (kg/m³)	W_{norm} (Kg*m/s²)	ρ_{hot} (kg/m³)	h_{hot} (m)	$h_{hot} - Z_{circ}$ (m)
Shahan's Ranch	2530	949.9417	2.3577^7	343.1621	2998.436	468.4364

The calculated values carry the assumption of a static columnar geothermal system. The estimated height above ground level that the hot-water spring can be at is a reasonable result. It is expected to be a positive number because hot water is less dense than cold water and therefore more is needed to

balance out the mass of the columns which leads to a higher elevation [20]. The temperature data at Shahan's well is seen in Figure 2.30. Figure 2.30 is the temperature versus depth graph at Shahan's well which shows a linear increase in temperature with depth.
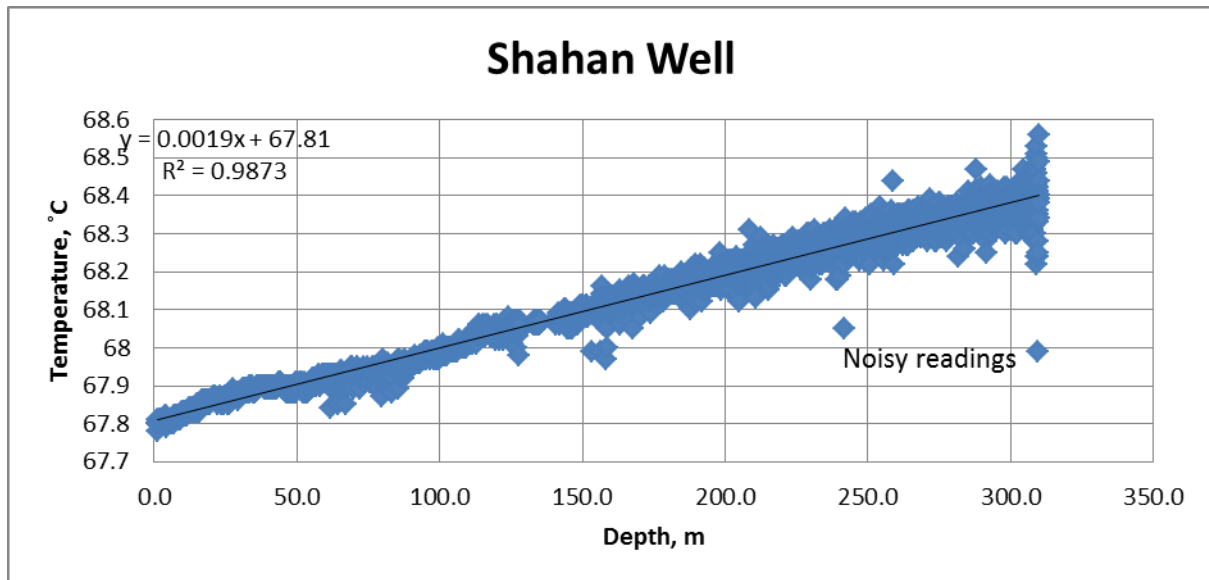
Figure 2.30: Temperature data at Shahan's Well.

3. Satellite Remote Sensing

3.1 Introduction

Satellite remote sensing involves the use of space borne sensor technologies to gather data about the distribution of land cover, mineralogy, structural features, thermal emissions (e.g. fumaroles and hot springs), and other surficial phenomena over a region of interest. In the case of Pagosa Springs, remote sensing is utilized to gain an alternative perspective of regional faulting and thermal anomalies that may enhance the overall understanding of the area's geothermal system. The digital elevation model (DEM) and thermal data from the Advanced Spaceborne Thermal Emission and Reflection Radiometer (ASTER) constitute the basis of this regional fault and thermal analysis.

Based upon the fault analyses, a fault map was generated by integrating geologic interpretations with remote observations. The geologic maps by Galloway [21] and Warren [22] were used as a reference to interpret faults on the satellite data, although a fair amount of Galloway's proposed faults could not be detected with remote sensing. Proposed faults from the 2012 and 2013 CSM field camps are somewhat distinguishable from the background terrain, but geological and geophysical analysis is needed to verify that these surface expressions are indeed faults.

After processing daytime thermal data from 23 September 2004 to represent surface temperature (in Kelvin), Planck's Law was used to generate a temperature map to show the day scene over Pagosa Springs. This map should especially highlight the hot springs and other surficial geothermal zones, but the poor resolution of the thermal infrared data complicated the ability to distinguish these zones.

3.2 Theory

The following Principal Components Analysis (PCA) theory was acquired from [23] and [24]. All of the following computations were performed using the PCA function built into the ENVI software package.

Principal components analysis is a technique used to represent multiband data in terms of linearly independent basis functions such that a combination of any principal component bands is unique. In essence, a PCA conducts a coordinate transformation in order to make each band independent from the other. The goal of this transformation is to minimize the correlation among the different image components and to maximize the variance of the data across the least amount of bands possible.

The first step in a PCA is to express an image as a vector of length *n*m* where *n* and *m* are the pixel dimensions of the image. This vector is created for each band, so a new matrix, *A*, of dimension *(n*m) x L* is created (*L* is the number of bands).

After matrix *A* is calculated, the covariance matrix, *C*, of *A* is calculated. The covariance matrix is calculated as follows:

$$C_{ij} = \sum_{k=1}^{n*m} \frac{(A_{kj} - \bar{A}_j) * (A_{ki} - \bar{A}_i)}{(n*m-1)}$$

Equation 3.1: Used to calculate the covariance matrix

$\bar{A}_i$ is the mean value of *i*th column of *A*. *C* is the *L x L* covariance matrix, which is symmetric. The diagonal of the covariance matrix is the variance of the *i*th column. The variance, or *S*, of the *i*th column of *C* can be better represented by the following equation:

$$S^2 = \frac{\sum_{k=1}^{n}(x_i - \bar{x})^2}{n-1}$$

Equation 3.2: Used to calculate variance

x represents a diagonal element of the covariance matrix and $\bar{x}$ is the average of the *i*th column of the matrix *C*. *n* is the same quantity described earlier. Accordingly, using the covariance matrix, *C*, two bands, *i* and *j*, would have a high covariance if they are strongly correlated.

Next, eigenvalues and eigenvectors are calculated of the covariance matrix in order to quantify the variability of the scene into linearly independent vectors (i.e. to reduce correlation of components across the image). The eigenvectors are calculated such that $C\vec{v} = \lambda\vec{v}$.

$\vec{v}$ is the eigenvector of length *L*, *C* is the covariance matrix, and λ is the eigenvalue, which is a scalar. The eigenvectors are reordered as the columns of the "feature matrix" such that the matrix is in order of decreasing eigenvalues.

$$[Feature\ Matrix] = [\vec{v}_1\ \vec{v}_2\ \vec{v}_3\ ...\vec{v}_n] \text{ such that } \lambda_1 > \lambda_2 > \lambda_3 > \lambda_n$$

The feature matrix has dimension *L x L*. Using this feature matrix, the image is reconstructed into its original dimensions *(n*m) x L* by taking the dot product between the feature matrix and the original data matrix:

$$[P] = [A] \cdot [V] = ((n*m)\ x\ L) \cdot (L\ x\ L) = ((n*m)\ x\ L)$$

[P] is the new matrix representing the data, [A] is the original $(n*m)\ x\ L$ data matrix, and [V] is the *L x L* feature matrix. Each column of the matrix *P* is a principal component, so the first column is the first principal component; the second column is the second principal component and so forth. The

amount of variability in the scene using this new matrix *P* is quantified by the eigenvalues. Typically, the first three principal components contain about 95% of the scene's variability [23]. Different combinations of these principal components, which are linearly independent from each other, can construct different images.

3.3   Methods

In order to obtain a preliminary understanding of the land cover and spectral variability of Pagosa Springs, a Principal Components Analysis (PCA) was performed using 1999 data from the Landsat 7 ETM+ instrument. In brief, a PCA utilizes mathematical algorithms that create independent bands, or components, that, in combination illustrate the spectral variability of a scene. This spectral variability is indicative of the different types of land cover and mineralogy. A detailed description of the theory behind the PCA is contained in section 3.2   Theory.

ASTER captures high-resolution spatial data in 14 bands that range from the visible to the thermal infrared wavelengths and has a stereo-viewing capability that enables the creation of the global digital elevation model. This study utilizes the thermal infrared (TIR) subsystem, which operates in five thermal bands (bands 10-14) using a fixed nadir-facing sensor (i.e. facing directly below the satellite). The TIR subsystem is a whiskbroom imager, which contains a mirror that scans reflected and emitted light in the across track direction (i.e. across spacecraft motion). This configuration collects data one pixel at a time [25]. As assumed, the TIR subsystem is principally concerned with radiation emitted in the thermal infrared wavelengths from a surface. Unfortunately, the spatial resolution of the TIR instrument is 90m, which exceeds the size of most—if not all—thermal anomalies in this study. The observed hot springs in Pagosa Springs are at most 20m in diameter, so the ability to resolve these small features with the fixed 90m spatial resolution is poor.

The amount of thermal radiation emitted from a surface depends on its temperature. The theory behind thermal emission and remote sensing is expressed by the blackbody concept: a blackbody is a theoretical object that absorbs all electromagnetic radiation regardless of frequency or angle of incidence. A blackbody not only absorbs all radiation, but also emits radiation that depends on its temperature. A blackbody's apparent temperature, or brightness temperature, is related to the emitted spectral radiance over π steradians by Planck's blackbody equation [25]:

$$S(\lambda, T) = 2\pi h \frac{c^2}{\lambda^5} \frac{1}{e^{hc/\lambda kT} - 1}$$

Equation 3.3: Shows Planck's blackbody equation

h is Planck's constant ($6.626*10^{-34}\ Ws^2$). k is Boltzmann's constant ($1.38*10^{-23}\ \frac{Ws}{K}$). c is the speed of light ($3.0*10^8\ \frac{m}{s}$). T is temperature in kelvin. λ is the wavelength (μm) of the thermal emission wave. $S(\lambda, T)$ is the blackbody radiance in $\frac{W}{m^2 \cdot \mu m}$.

However, since the Earth's surface is not considered a perfect blackbody, we must employ a scaling factor called the emissivity, which is characteristic of different surface types. The emissivity of a material is the ratio of energy radiated by this material to energy radiated by a blackbody at some temperature. Accordingly, the radiance at sensor (i.e. the emitted radiation from the ground surface) and surface temperatures (in Kelvin) are related by Planck's Law [23]:

$$S(\lambda, T) = \frac{L_\lambda}{\varepsilon} = \left[\frac{W}{m^2 \cdot \mu m \cdot sr} \right]$$

Equation 3.4: Planck's Law 1

$$\frac{L_\lambda}{\varepsilon} = 2\pi h \frac{c^2}{\lambda^5} \frac{1}{e^{hc/\lambda kT} - 1}$$

Equation 3.5: Planck's Law 2

Solved for temperature (Kelvin), T, Planck's Law is as follows:

$$T = \frac{hc}{\lambda k} \frac{1}{\ln \left(\frac{L_\lambda}{\varepsilon} \frac{2\pi hc^2}{\lambda^5} + 1 \right)}$$

Equation 3.6: Planck's Law 3

The thermal analysis over Pagosa Springs utilized band 10, L_λ, which has a wavelength of 8.291 μm, ε is from ASTER, and the emissivity is assumed to be at a constant of 0.9 throughout the entire scene. All other values are the same as those listed above.

Equation 3.6 [23] was utilized to convert the spectral radiance at sensor values into surface temperature values in order to create the temperature map over Pagosa Springs. However, numerous factors affect the remotely sensed surface temperatures. These factors include diurnal heating effects, ground albedo, thermal inertia, slope aspect, emissivity, atmospheric absorption, atmospheric moisture content, emitted radiation from the atmosphere, and reflected radiation from the atmosphere back to the ground surface (i.e. the greenhouse effect) [26]. Thermal inertia, which may have a significant effect on the data, represents how quickly the temperature of a body or surface adjusts to that of the surroundings [26]. Corrections can be made for most of these factors, including thermal inertia, but these corrections were not made throughout this study because of a lack of data and time.

Despite the lack of corrections, a daytime temperature map was created over Pagosa Springs. Thermal infrared data (i.e. from ASTER) was collected from 23 September 2004 during the day and then analyzed for the presence of hot springs.

Slope and shaded relief maps were created from the ASTER DEM over Pagosa Springs. Slope and shaded relief maps complement each other such that slope maps illustrate slope angles over a region and shaded relief maps illuminate the regional topography from a specified sun elevation and azimuth. Surficial expressions of faults such as fault scarps and land displacement are associated with changes in slope and topography, which is clearly visible in the slope and shaded relief maps. Furthermore, these changes in topography are assumed to occur across linear boundaries that are representative of faults. With these assumptions in mind, the slope and shaded relief maps were interpreted for local and regional faulting that may serve as conduits to geothermal activity.

3.4   Error

The temperature map is not accurate because external corrections such as those for thermal inertia, ground albedo, slope aspect, emissivity, atmospheric moisture content, and others were not completed. Another study by [26] attempted to detect geothermal anomalies after completing corrections such as those mentioned, but the study still struggled to isolate potential anomalies. Although [26] successfully reduced background temperature noise, temperature fallacies still existed due to variations in sensible heat (heat transfer between the ground and atmosphere), latent heat (heat lost through water evaporation), and geothermal heat flux. Additionally, another source of error is the assumption that the whole scene contains a constant emissivity, which actually changes with each material (i.e. rocks, minerals, trees, etc.). Accordingly, the temperature map of Pagosa Springs should not be taken as the absolute truth since corrections were not made.

The poor resolution of the TIR bands inhibits our ability to resolve targets less than that resolution. More specifically, the 90m resolution of the TIR bands cannot accurately resolve hot springs that are at most 20m in diameter. Images will illustrate the average thermal value over each pixel, so all of the thermal activity within the resolution of that pixel will be averaged as one output value as shown in Figure 3.1. For example, the radiated energy from a 20m wide hot spring will be averaged with that of nearby elements such as cold rivers, forest, buildings, and geology, so the hot spring itself will not be very distinguishable relative to its surroundings.
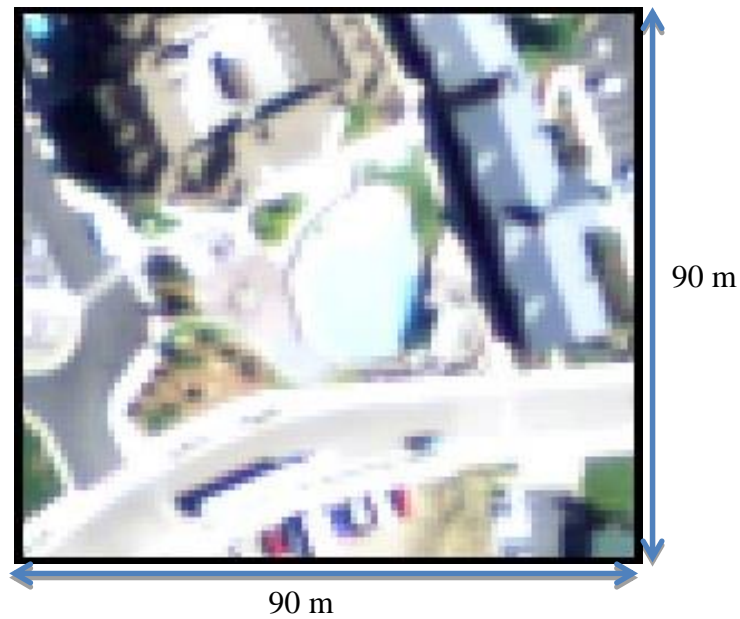
Figure 3. 1: One 90 m x 90 m pixel over the mother spring, which is the resolution of the ASTER TIR bands.

In regard to the fault maps, other linear features such as riverbanks, river deposits, dikes, and other linear features can be misinterpreted as faults.

3.5   Results and Interpretations

A principal components analysis was performed in order to image the distribution of different types of land cover and geology within Pagosa Springs. As seen in Figure 3.2b, Pagosa Springs has a reasonably high spectral variability because of the numerous colored classifications.

2a   2b
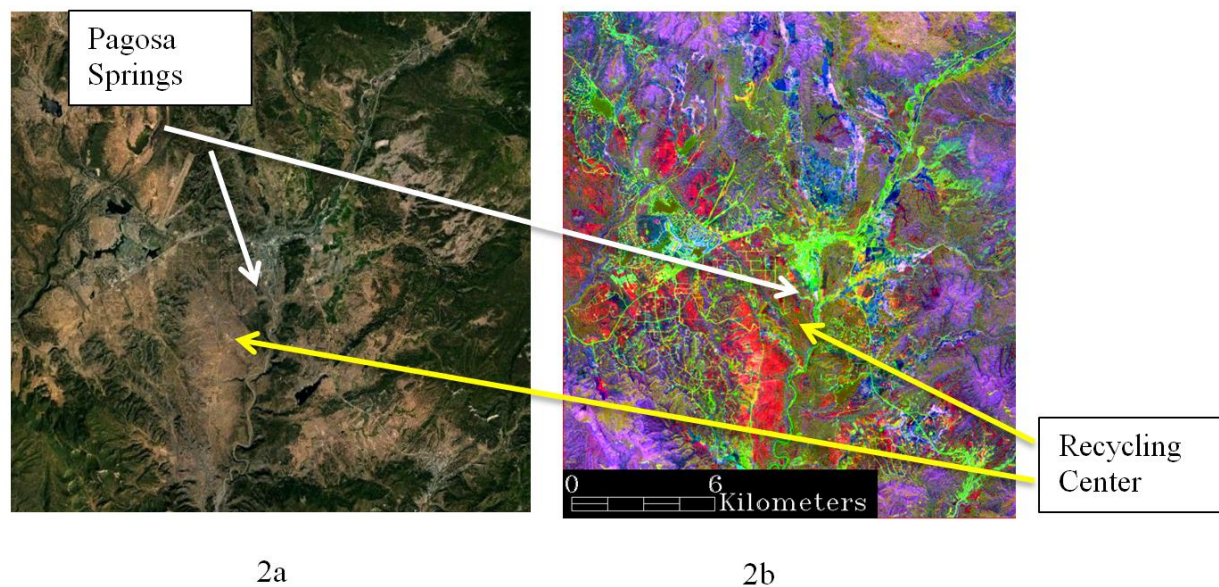
Figure 3. 2: Satellite image (2a) and PCA (2b) of Pagosa Springs, CO

The PCA in Figure 3.2b illustrates urban developments as lime green, bare land as red, forest as purple, grasslands as blue, and areas of high moisture content (i.e. including lakes) as dark green. No direct geologic interpretations of the Mancos Shale or Dakota Sandstone can be made from Figure 3.2b because most geology is covered by vegetation, topsoil, or urban developments. Meanwhile, the Mesa Fault is somewhat distinguishable in Figure 3.2 because of the abrupt change in surface cover along the linear boundary. Near the recycling center in Figure 3.2b, the land cover abruptly changes from moist vegetation (dark green) and forest (purple) to bare land (red) on the southwestern side of the fault.

In terms of the landscape, shaded relief and slope maps were generated in order to investigate the scene for faults that may have geothermal implications. These fault interpretations are solely based on visual inspection of the data with Galloway's geologic map [21] as a guide as shown in Figure 3.3e. The vertical strip in Figure 3.3d is a missing line of data after two ASTER images were stitched together in order to image all of Pagosa Springs.
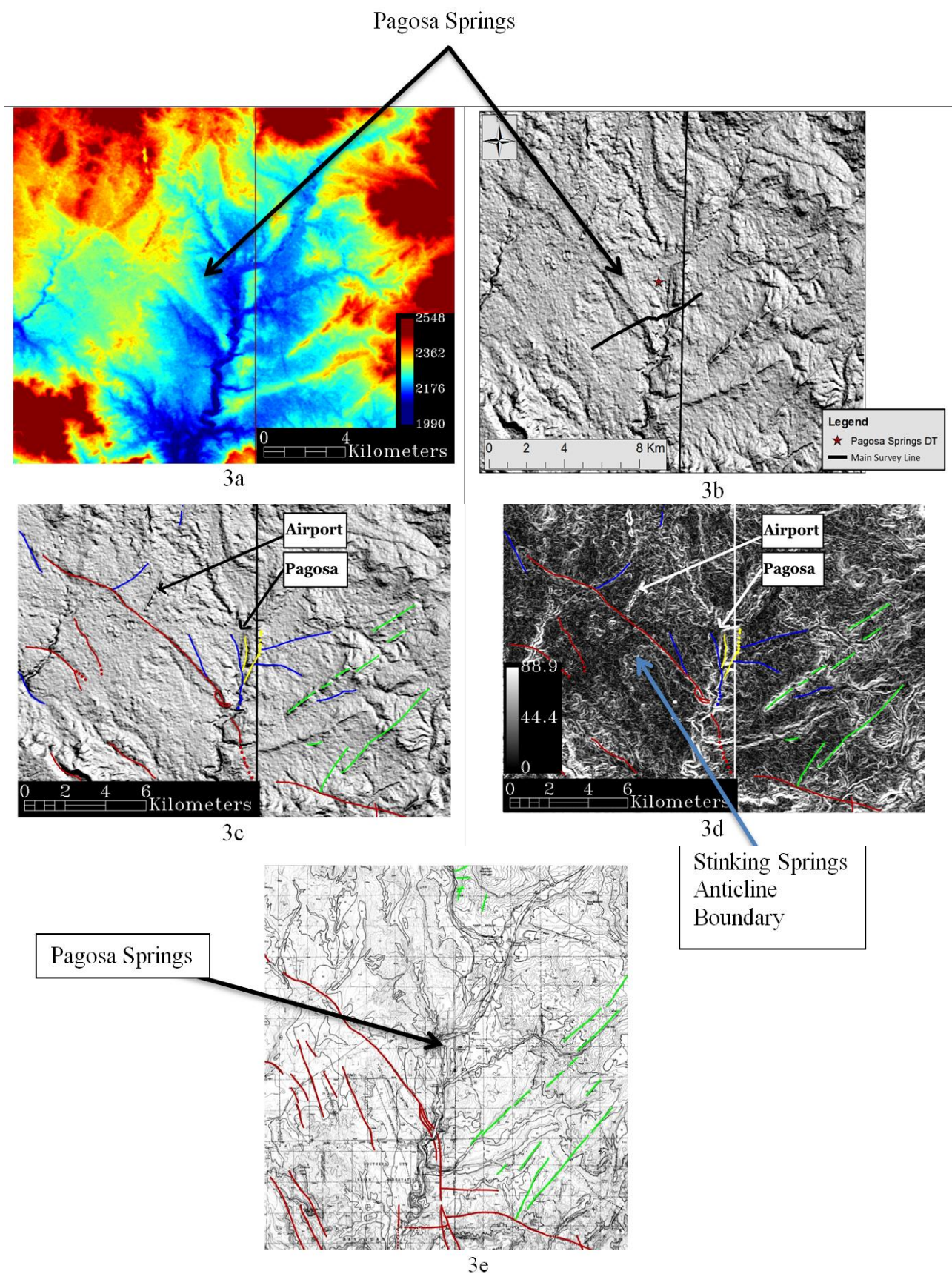
Figure 3. 3: The ASTER DEM (in meters) is shown in (3a), from which the shaded relief map in (3b) was developed. The hypothesized fault map overlays the shaded relief and slope maps in (3c) and (3d), respectively. Galloway's fault map is shown in (3e).

44

In brief, all of the red faults in Figure 3.3c match those proposed by Galloway [21] in Figure 3.3e; blue faults are those proposed only by satellite remote sensing (i.e. not Galloway [21] or Warner [22]); yellow faults are those proposed by the 2012 and 2013 Field Camps; and the green lines indicate dikes. Dotted fault lines indicate inferred faults. Also, the two blue faults that intersect the yellow faults match those proposed by Warner [22].

Many of Galloway's proposed faults [21] were not discovered in Figure 3.3c because they did not show linear surface expressions that are indicative of faulting (e.g. fault scarps or sharp changes in topography). More specifically, nearly all of Galloway's [21] proposed faults west of the Mesa fault ware not apparent in the shaded relief and slope maps. Only faint signatures of a couple of Galloway's faults [21] are present in this region (Figure 3.3c and Figure 3.3d).

The proposed faults from the 2012 and 2013 CSM Field Camps are associated with a change in topography; hence, these faults can be imaged using satellite data (Figure 3.3b and Figure 3.3c). Nevertheless, additional geophysical and geological analysis is needed to verify the existence of these faults. As seen in Figure 3.3c and Figure 3.3d, most faults in Pagosa Springs are NW-SE trending. The only noticeable exceptions are the N-S trending faults proposed by the 2012 and 2013 CSM Field Camps. From a satellite point of view, these N-S trending faults are not completely out of the ordinary because they follow the flow direction of the San Juan River, which likely resides in the geomorphology created by these faults. Intersections, or contacts, of two or more faults may be indicative of geothermal zones since this architecture provides more than one conduit for geothermal water flow.

Figure 3.3d illustrates that most interpreted faults from Figure 3.3c are associated with a change in slope. Additionally, the outline of the stinking springs anticline is visible in Figure 3.3d due to subtle slope changes along the anticline's boundary.

As mentioned earlier, the inaccuracy of the temperature map is due to the poor spatial resolution and the lack of topographic, thermal, and albedo corrections that may have been better able to isolate geothermal zones. Since these corrections could not be made due to lack of data, temperature variations could not be minimized in order to highlight subsurface contributions of geothermal heat. Accordingly, the validity of remote sensing to isolate thermal anomalies is largely limited to anomalies that are exposed at the surface (e.g. hot springs and fumaroles) and large enough to overcome background noise.

4a   4b
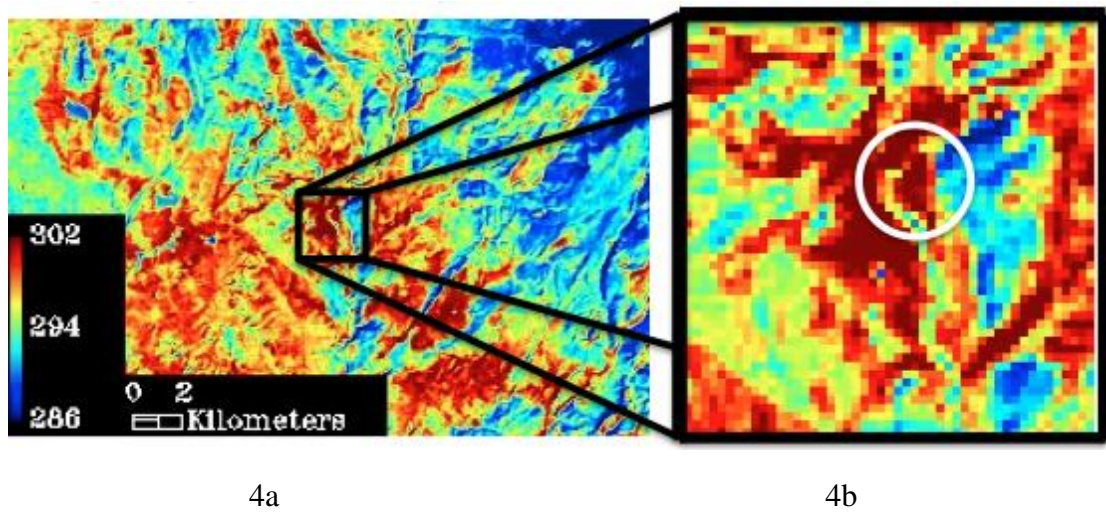
Figure 3. 4: Thermal infrared image of Pagosa Springs (4a) and a zoomed in portion that circles the location of Pagosa's hot springs (4b).

In order to obtain a rough estimation of the hot spring's contribution to the average pixel temperature, we calculated that the area of the pixel is $8100 m^2$; the area of the mother spring (Figure 3.1) is about $380\ m^2$ (4.7% the pixel area); the temperature of the mother spring is about 334 K (142°F); and the average temperature of the remainder of the pixel area is about 294 K (70°F). Using these parameters, the mother spring should increase the average pixel value by about 2 K (3.6 °F).

In this case, the mother spring pixel value in Figure 3.1should be about 296 K (73°F); the average pixel value of the temperature data in Figure 3.4a is about 299 K (79°F). Accordingly, at the current resolution of 90m, the hot springs have a minimal effect on the thermal data. Instead, the thermal data surrounding the hot spring have equal or higher values since the encompassing region contains bare land, parking lots, and rooftops that heat up throughout the day. The Pagosa hot springs are resultantly not readily visible in the TIR bands because they do not increase the average pixel values to the point where they become distinguishable from background elements. Consequently, TIR remote sensing is not a suitable method for identifying hot springs because of the poor data resolution and the dominance of background contributions (e.g. parking lots, bare land, and rooftops) to average temperature values for each pixel.

4. Surveying

4.1 Introduction

Most geophysical methods rely on a positioning system for reproducibility of the survey, localization of geophysical phenomena observed, or the calibration of instruments (e.g. gravity). As satellite Global Positioning Systems (GPS) have become more advanced, the positioning system has been greatly simplified, and the acquisition of data has been streamlined. For this field exercise, surveying information was acquired using one of three methods: handheld GPS for a lower resolution portable solution, differential GPS for more precise measurements, and TDM for additional measurements on the main survey line.

4.2 Handheld GPS

GPS uses satellites to triangulate the position of a receiver on the ground. In effect, the more satellites there are to be referenced, the more accurate the positioning. By measuring the time taken for a signal to reach the receiver from the satellite, it is possible to interpret the distance to the receiver. Time difference correction is applied by analyzing the phasing of a known outbound signal. However, the spatial accuracy of a GPS unit is only in the tens of meters. The following effects can account for this uncertainty [27]:

- Ionospheric/Tropospheric effects (± 5 m): the atmosphere is not a uniform layer, which leads to fluctuations in the signal travel time. These fluctuations can be calibrated for when using a base station but they are difficult to correct for in direct GPS observations.

- Ephemeris errors (± 2.5 m): errors resulting from uncertainties in satellite position.

- Satellite Clock errors (± 2 m): as GPS positioning relies on a timed signal, time calibration between a GPS receiver and satellites lead to clock-related uncertainties.

- Multi-Path Distortion (± 1 m): this error occurs when the signal observed is that of a reflected satellite signal instead of the original direct signal.

- Numerical errors (± 1.5 m): this error is due to bad triangulation. This occurs when signals from satellites are blocked by trees or buildings; there are too few satellites in a direct line of sight.

- Human error (N/A): the available handheld GPS data was not always numerical and often relied on surveyors writing down measurements by hand.

4.3   Differential GPS (DGPS)

While basic GPS is accurate within tens of meters, DGPS allows for precision within one meter. This is accomplished by using radio transmissions and localization between a mobile receiver (rover) and a base station antenna (see Figure 4.1). Transmission from the rover to the base station allows for more precise positioning (relative to the base station). In turn, the base station's position is easier to pinpoint as it is a stable, more reliable antenna than handheld GPS. It should be noted that DGPS methods rely on a minimum of 4 satellites for reliable measurements. In short, the use of DGPS allows for reduction of the atmospheric effects on the signal, thus drastically reducing the major error sources of a GPS system.
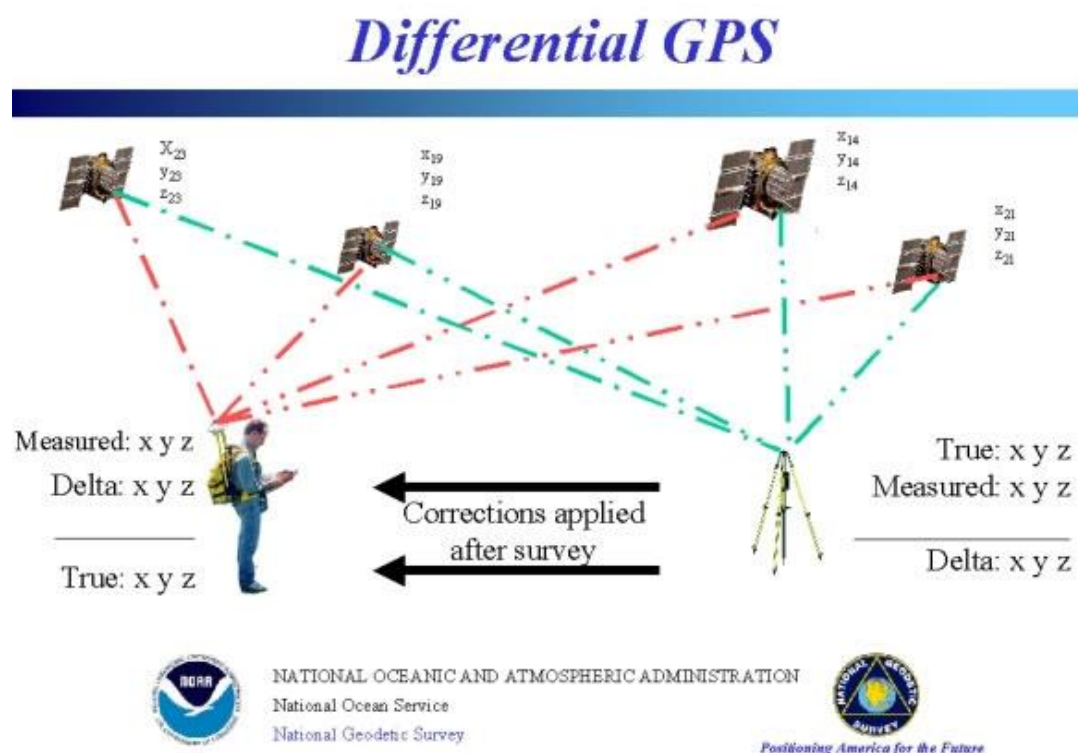
Figure 4. 1: DGPS system illustration

4.4   Total Distance Measurement (TDM)

Figure 4. 2: The TDM setup.

For Total Distance Measurement (TDM), a tripod is mounted with a geodimeter (system 400, associated with a prism rested on a stick). By reflecting a beam of laser light off of the prism, the geodimeter can measure the slope disk (SD), as well as the vertical and horizontal angle (VA and HA). Assuming the location of the tripod is known, the location of the prism may be calculated with relative accuracy. This system is shown in Figure 4.2.

This method was applied solely on the main survey line in areas where the DGPS was insufficient; such inaccuracies came about as a result of a particular method's resolution limitations (gravity measurement), or difficult terrain (presence of trees) which interferes with satellite systems. Although it is a lengthier process, TDM can be used to improve the accuracy of bad sections in the DGPS observations. However, one issue that may arise with TDM is localizing the TDM geodimeter tripod, as all measurements are made relative to it. Additionally, some of the equipment did not contain inbuilt recording systems, and as a result, the possibility exists that a recorder could have written down an incorrect observation.

4.5   Survey design

In the course of the Pagosa Springs geophysics field camp, thorough surveying relied on DGPS and TDM, while handheld GPS was used for general observations. DGPS boasts an accurate horizontal resolution, although elevation measurements are less reliable than those based on TDM.

Table 4.1 displays the various locations surveyed and their associated survey processes. TDM focused on the Main Survey Line, which was the location for most geophysical surveys including the deep seismic survey.

Table 4.1. Survey methods used at each survey locations.

Survey Location	DGPS	Handheld GPS	TDM
Main Survey Line	■		■
Mill Creek	■	■	
Hairpin Turn Dike	■		
South of Hairpin Turn Dike	■		
Shahan's Ranch	■	■	
North Line	■		
South Line	■		

Surveying required little design besides choosing the locations of DGPS base station for the most affective coverage of the surveyed areas.

4.6   Surveying Processing

The main goal of survey processing is to provide information on the location of each survey, as well as the survey components, like the location of electrodes in a direct current resistivity survey. This type of localization is integral in processing many geophysical datasets. The precision of each survey method, its ease of use, and its availability ultimately dictated survey data acquisition.

The main survey line was the bulk of the work and therefore took advantage of the most advanced methods available (DGPS and TDM). Because two survey methods were used, the respective surveys were correlated to create a more accurate location dataset. This type of correlation is particularly useful for gravity surveys, which require precise location data at every station for calibration. For secondary surveys, DGPS was the predominant method, while handheld GPS was also used for a few surveys (in particular, some SP lines near Mill Creek).

Several software packages were utilized in processing data. The program Surfer was used to convert coordinate data, specifically NAT27 UTM Zone 13N (easting and northing) to WGS 1984 (latitude and longitude), although some handheld GPS data initially used NAT83 UTM Zone 13N. Google Earth was used for quick visualization of the survey lines. More detailed location data were available in the form of spread sheets. Finally, ArcMap served to display the survey lines throughout the region.

Nonetheless, the final observations retain uncertainties, particularly handheld GPS. This is illustrated in the representation of the latitude and longitude for the second SP survey at Mill Creek (Figure 4.3). Once outliers are removed, it is possible to extrapolate the position of missing data points with a smooth fitting curve (here, a polynomial of the 7th order). Similarly, the topography can be edited where elevation data is poor, which is an acceptable process when high-accuracy is not required, and the data can be confirmed/correlated with other surveying methods such as TDM or altimeter.
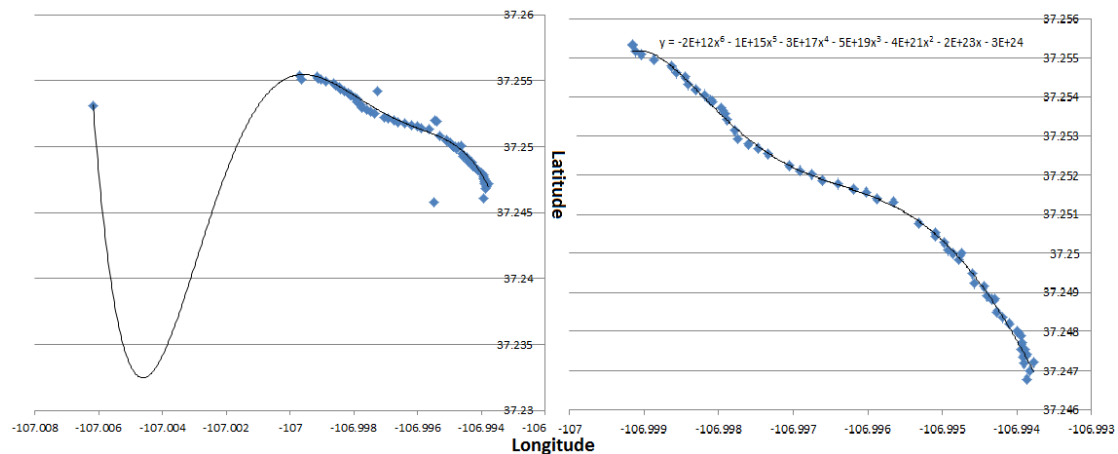
Figure 4. 3: Handheld GPS correction (outliers' removal) for the second SP survey at Mill Creek.

4.7   GPS Recommendations

While DGPS remains a more accurate surveying system than handheld GPS, particularly with the use of post-processed position data, other more advanced techniques provide accurate measurements without the same installation requirements.

Such a system is the Wide-Area Augmentation System (WAAS). Developed by the Federal Aviation Administration, WAAS consists of a network of wide-area ground reference stations. Each station can relay the data to one of two wide-area master stations. These compute correction information for specific geographical areas [29, 30].

 WAAS covers mostly North-America. The Colorado region and Archuleta county receives a good coverage for WAAS (see Table 4.2).

Table 4.2: Uncertainty in the WAAS data.

Property	WAAS (for Denver, CO)
Horizontal error (m)	2.109
Vertical Error (m)	5.983
Availability (due to outages) as a fraction of time.	0.99608
Quarterly availability (due to weather) as a fraction of the time.	0.999314218

While DGPS, particuarly with additional processing capabilities, remains more precise, it is mostly useful for gravity surveys. Indeed, the precision attributed to WAAS should be sufficient for most geophysical methods in use, where errors due to survey layout is comparable to that due to positioning (e.g. laying geophones).

Therefore, we recommend the use of WAAS system, akin in simplicity to using handheld GPS when reliability of positioning observations is not vital. For cases where precise positioning is crucial, such as gravity, TDM and DGPS are sufficient.

4.8   Conclusions

We recommend setting up the Post Processing Kinematics (PPK) ahead of time, so that processing can be streamlined and accelerated. As for reliability, GPS, and particularly DGPS, works well in open, unobstructed areas; TDM and ground-based measurements may be used in areas of high terrain and difficult foliage.

Depending on the type of surveying used, the uncertainty in localization can vary dramatically. To remedy this problem, WAAS systems may be used instead of handheld GPS.

5. Deep Seismic

5.1   Introduction

Seismic is the most effective of all geophysical methods used to identify subsurface geological structures. However, it is not the most efficient due to the need for large crews, expensive equipment, and extensive data processing. The goal of seismic is to create an image of the earth using reflections from the subsurface. This includes geological structures, faults, folds, uplifts, subsidence, and the location of different rock formations. In the Pagosa Springs area, seismic can be used to identify the boundaries of the Mancos Shale, the Dakota Sandstone, the Morrison formation, the Entrada formation, the Precambrian crystalline basement, and large faults.

5.2   Theory

In exploration seismology, an energy source on the surface of the Earth generates a sound wave that propagates through the subsurface. In the solid medium it is called the primary wave, or P-wave, and it propagates as a series of compressions and dilatations in the direction of energy transport. The P-wave travels with the fastest velocity in the medium. This velocity is known as the "seismic velocity" of the rock.
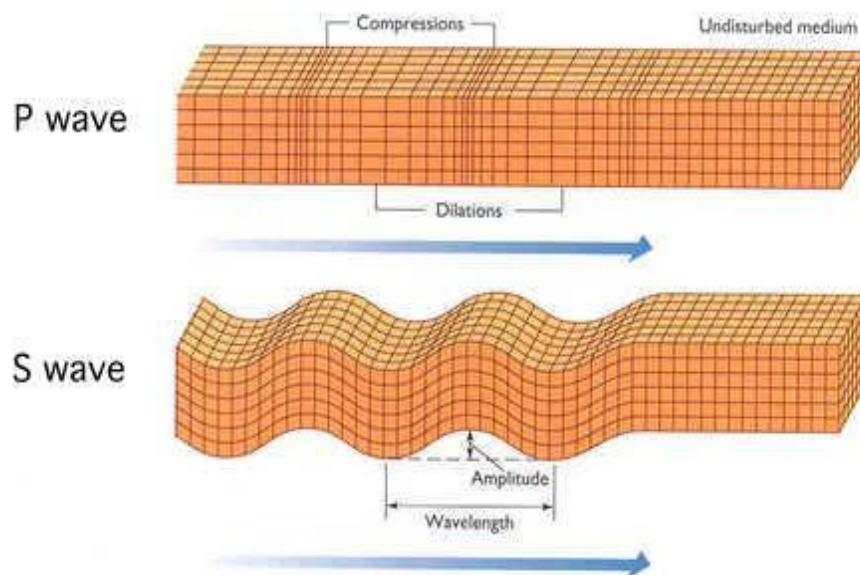
Figure 5.1: P- and S-waves illustration.

When a P-wave encounters an interface it may be converted into a shear wave, or S-wave. The S-waves travel slower than the P-waves and propagate normal to the direction of energy transport. Figure 5.1 shows a cartoon depiction of the P- and S-waves.

Both P- and S-waves are examples of body waves that propagate through the medium. This is in contrast to surface waves that exist only at interfaces. Examples of surface waves are Rayleigh waves, Love waves, and Stoneley waves which have elliptical particle motion and rapidly decay with depth. These waves travel slower than body waves but can be more energetic than reflection events. These can obscure the signal. Together the surface waves are termed "ground roll" and they are filtered during the processing stage as noise.

In the subsurface, portions of the seismic waves are reflected upwards towards the surface when it encounters an area of rapid change in earth material properties. These areas of rapid change are called reflectors. In land exploration, the reflected P-waves are recorded at numerous receivers (geophones) that are planted in the ground and are coupled to the earth to record ground movement. Different geological formations have different material properties such as porosity, lithification, pressure, and fluid saturation that result in different P-wave velocities and densities of the rock layers [31]. The product of the rock density and its P-wave velocity is known as the acoustic impedance of the rock:

$$\mathbf{I} = \mathbf{c}\rho,$$

Equation 5. 1: Acoustic impedance.

Where **c** is the acoustic P-wave velocity vector and ρ is the density of the rock. Figure 5.2 shows a plane interface between two media, incidence, a reflected ray, and refracted rays.
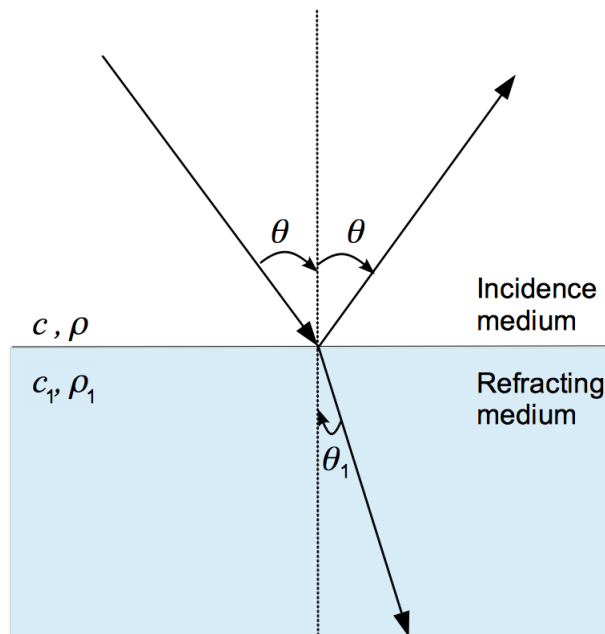
Figure 5.2: Incident reflected and refracted rays.

At normal incidence, the reflection coefficient is the fractional difference between the acoustic impedances of the two media:

$$V = \frac{c_1 \rho_1 - c\rho}{c_1 \rho_1 + c\rho},$$

Where V is the reflection coefficient, and c and ρ are as defined previously. The variables c_1 and ρ_1 are the velocity and density in the refracting medium. A reflection coefficient of 1 is a perfect reflection with no energy being transmitted across the boundary.

In general, the reflection coefficient V and transmission coefficient W depend on the angle of incidence:

$$V = \frac{c_1 \rho_1 \cos\theta - c\rho \cos\theta_1}{c_1 \rho_1 \cos\theta + c\rho \cos\theta_1},$$
$$W = \frac{\rho}{\rho_1}(1+V),$$

Where θ is the incidence angle and θ_1 is the refraction angle.

From Snell's law:

$$\sin\theta_1 = \sin\theta \frac{c_1}{c},$$

The incident angle is equal to reflected angle. The critical angle is the incident angle that corresponds to a transmission angle of 90 degrees:

$$\theta_{cr} = \sin^{-1}\left(\frac{c}{c_1}\right).$$

A critical angle is only possible when the refracting medium is faster than the incident medium.

One of the main assumptions is a single scattering assumption, so that multiples are disregarded. Only the primary reflections are processed. Energy from interbed and free surface multiples may result in artifacts and spurious events and need to be suppressed during processing.

Another assumption is that the incident angle is real which corresponds to homogeneous waves. There are also inhomogeneous waves that correspond to complex incident and refracted angles that are not accounted for in this analysis. For further reference see [32].

5.3 Main seismic line site

Deep Seismic Line Location
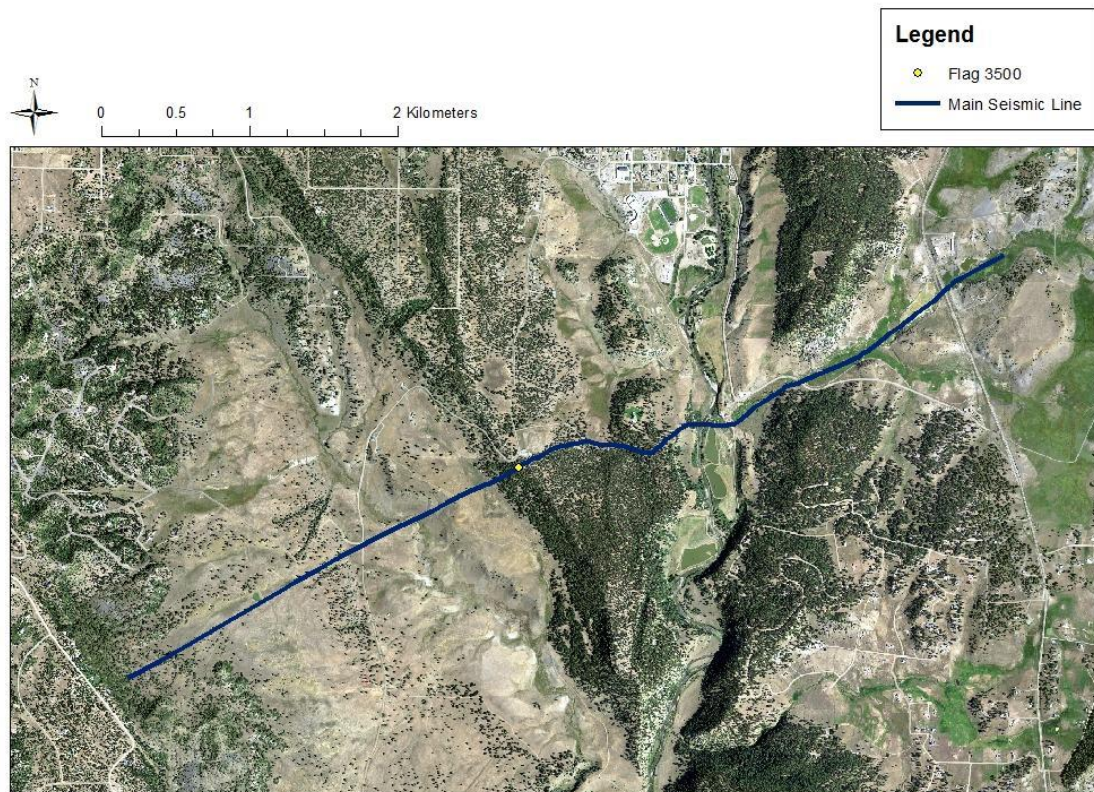
Figure 5.3: Survey line along topography map of Pagosa Springs. The length of the line was 6.965 km.

The survey was conducted through Long Horn Ranch at Pagosa Springs. It ran about 500 meters east of the Stinking Springs to about 10 meters west of Highway 84 (Figure 5.3). Two major bends in the line occurred due to difficult terrain. The first bend was due to the San Juan River. The river was approximately 40 meters across and was not possible for the Vibroseis trucks to cross. The second bend was due to a small marshland slightly to the east of the river.

The far west side of the line was covered by a pasture. These areas were mostly flat and grassy which simplified data acquisition in these areas. Further east, there were steep sloped ridges with thick tree cover that were not suitable for the Vibroseis truck operation. The truck stayed as close to the line as possible in these areas, but was forced to follow the road in other areas. On the east side of the line, the area became a pasture again. A few shot points were skipped due to the danger of the Vibroseis truck getting stuck in the soft ground.

5.4   Survey Design

In Pagosa Springs, the deep seismic survey was designed to be a 2D land survey to build on last year's field camp findings [33]. A 2D survey is more time and cost efficient compared to a 3D survey, but it assumes that the waves propagate in a 2D plane and thus it does not account for 3D effects. The recorded signals not from the 2D plane are regarded as noise. The recorded seismic data contains travel times from each source to receiver along this line. Processed seismic data displays a vertical cross-section of the Earth beneath the seismic line. Another important assumption is that we have an isotropic medium. An isotropic medium simplifies the processing because only P-wave velocities need to be estimated. The anisotropic linear-elastic medium more adequately describes the subsurface but requires complex processing and computing.

The 2013 survey line was placed as straight as possible in the East-West direction with the intent of crossing the major fault slightly to the west of Pagosa and totaled 6.965 km. The energy source was generated by 12 foot Vibroseis trucks. The line ran from the west most flag, 3201, to the east most flag, 3872, with a flag spacing of 10 meters. The receivers were spaced between each flag 1.5 meters from the next geophone. At each flag, the sweep was shot 5 times from 5 to 300 Hz using an upsweep. The total number of shots was 516. The first shot was at flag 3201 and the last shot was at flag 3816. The sweep time was 16 seconds. The geophones listened for a total of 3 seconds. The coordinates and elevations of each receiver and source were recorded for geometry processing.

Both upsweep and downsweep seismic signals were tested in the field. An upsweep is created by Vibroseis truck starting to vibrate the ground at a low frequency and ending at a high frequency as was done during the survey, see Figure 5.4.

Figure 5.4: A. Upsweep - the frequency increases with time; B. Downsweep - the frequency decreases with time.

When the Vibroseis truck shook the ground at each station, the time it took the wave front to hit a reflector and return to the surface was recorded by the geophones on the surface and is called the two-way travel time (TWTT) (Figure 5.5). Each shot was taken and processed to create a full 2D image of the subsurface. The targets were shallow with the approximate time of the basement reflection at 250 ms. The target reflections from the overlying formations occurred even earlier.
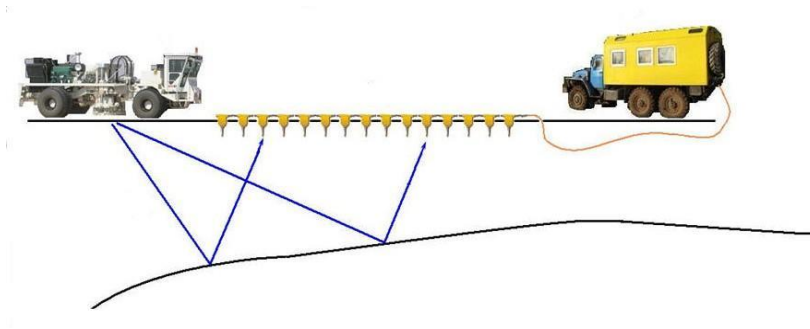
Figure 5.5: Land seismic acquisition setup.

The topography along the survey line was highly variable. The survey elevation of receivers along the line is shown below in Figure 5.6.
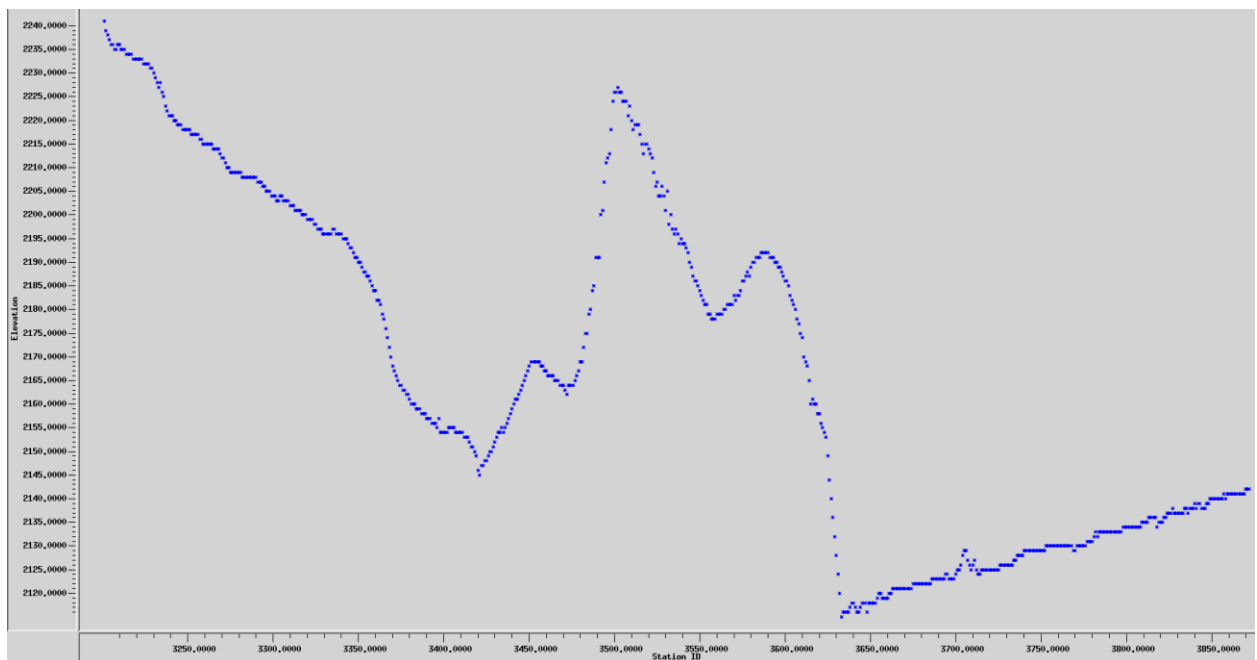
Figure 5.6: Elevation profile of the stations along the deep seismic line.

5.5   Processing

To produce an image of the Earth's geologic structures, recorded seismic data needs to be processed. The recorded data contains a combination of the source pulse, the earth response to that pulse, and background noise. The noise and the source signature need to be removed in order to uncover only the Earth response.

The data was processed using ProMAX® software. The processing flow is shown in the chart below, Figure 5.7. Details of each procedure will be discussed in Appendex A.**2 Processing**.
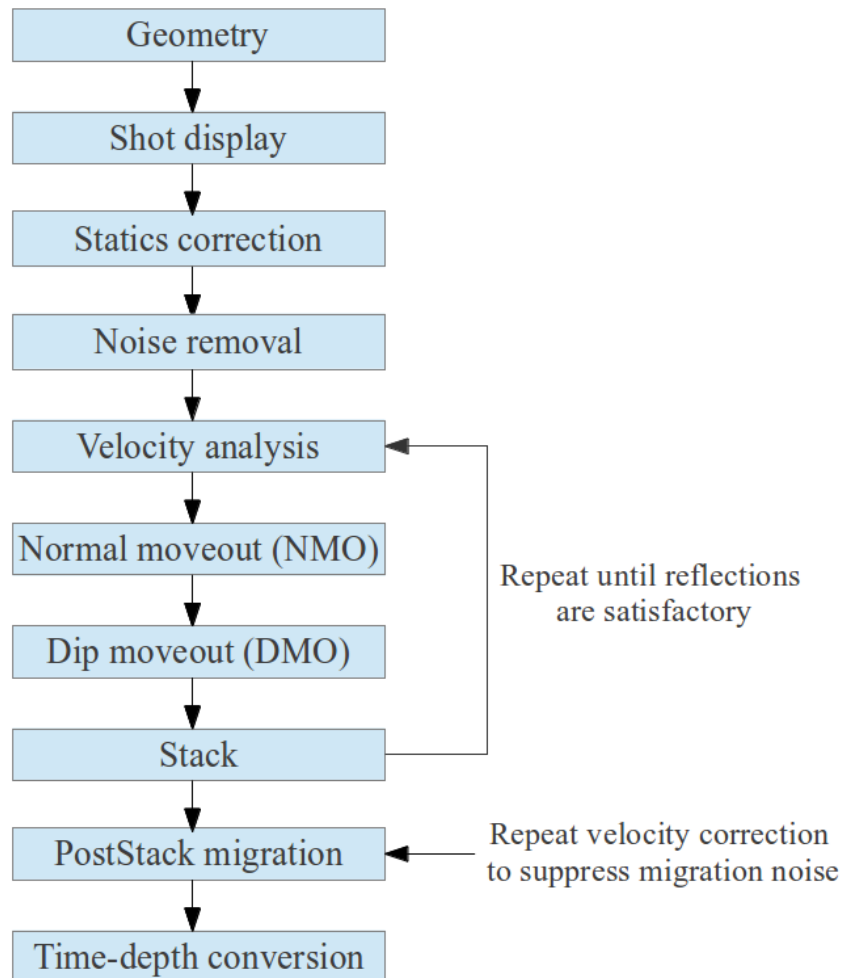
Figure 5.7: The seismic data processing flow.

5.6   Uncertainties/Errors

The image of the subsurface will be poor if the reflectors are not illuminated well. Illumination issues are caused by insufficient data coverage, poor data quality, gaps in the data due to terrain, and complex overburdens that distort the seismic wave fields.

Due to terrain difficulties, there were missing data across the river and Highway 84. Terrain also affected the Vibroseis truck's ability to position its truck plate exactly at the flag location during acquisition. In the field the truck was often offset from the flag, and the offset was reported by the Vibroseis truck driver to the recording station. During processing, the truck's offset from the flags needed to be taken into account, and the offset usually was not precise.

During the geometry configuration processing stage, there may have been round-off errors because the ProMAX processing system can only handle 8 digits or less.

Determining the seismic velocity field is crucial for processing and interpretation. Velocity is iteratively updated using semblance analysis and CDP gather flattening. However, the process is user dependent and is very subjective and never perfect.

5.7 Interpretation

The final stack was interpreted to understand the geology of the Pagosa Springs region. Three large-scale faults were interpreted based on the seismic stack section: the 8-mile Mesa Fault, the Warren Fault, and a new 2013 Field Camp Fault. The dike outcrop located at the hairpin turn was also imaged, and the associated unit on the seismic line could potentially be a volcanic intrusion that formed a volcanic sill. This volcanic intrusion could be the source of heat for the geothermal system in Pagosa Springs. There are other igneous rocks in the area north of Pagosa Springs that could be connected to the dike on the seismic line.

The dike penetrates through the Mancos Shale and the Dakota Sandstone. The volcanic sill was interpreted to intrude below the top of the Dakota, however the geology team did not interpret a sill to be in the area. The interpretation was based on the P-1 well, which is slightly offset from the main seismic line. The well penetrated Dakota Sandstone down to the basement, as shown in Table 5.3. The thickness of all the layers are assumed to correspond to the stratigraphy beneath the seismic line.

Table 5.3: Stratigraphic column from the well P-1

Formation	Thickness (meters)
Mancos Shale	67
Dakota Sandstone	60
Morrison Fm	208
Wanakah	29
Entrada	48

Due to the lack of well control on the seismic line, the average constant velocity of 3000 m/s was used to convert the depths of each formation into TWTT in order to interpret the seismic section. The depth to the top of the Dakota and the top of the Basement is 67 meters and 413 meters respectively. The average TWTT to the top of the Dakota Sandstone and the top of the Basement reflector is 44 ms and 275 ms, respectively. This information was then used to try to locate the top of the Dakota and the top of the Basement reflectors.

The VSP data was acquired in a well by the Hammer seismic crew. Their main conclusion was that the seismic velocity through the Mancos shale is around 2500 m/s and seismic velocity through the Dakota is from 2500 m/s to 3000 m/s, which does not contradict with the assumed average velocities. One of the main uncertainties in the seismic interpretation was the fault throw across the Mesa fault. However, according to Galloway, the Mesa fault has 100 m of vertical displacement, and this was considered an interpretation [41]. Figure 5.8 and Figure 5.9 below shows the depth converted section with a Kirchhoff time stack and no interpretation. Three reflectors were interpreted: the top of the Dakota, the top of the Basement, and intra-Morrison reflectors.
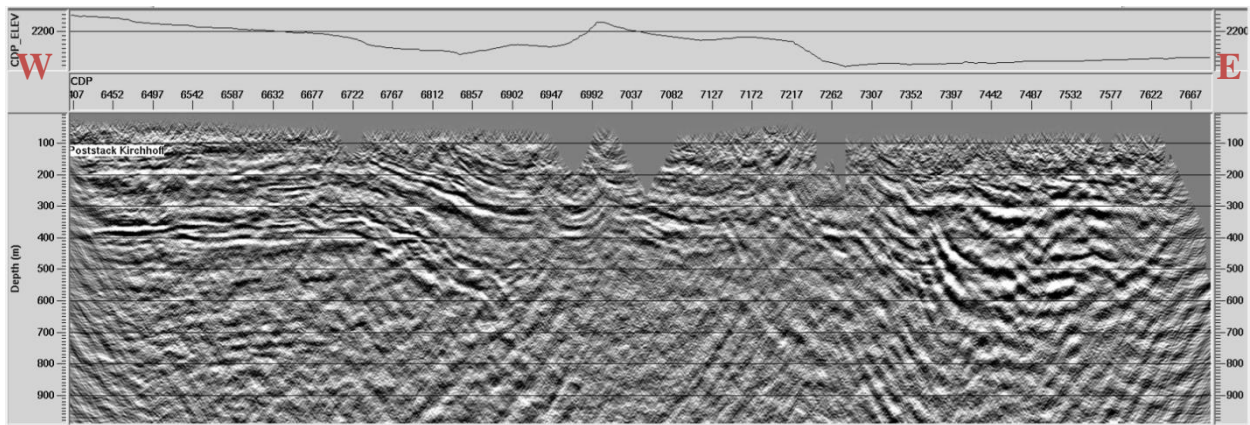
Figure 5.8: It shows the depth converted section of Kirchhoff time migration stack without interpretation.

The top of the Basement reflector is not clearly shown in the upthrown side of the Mesa fault due to a low fold in the middle of the seismic line, as shown in Figure A. .
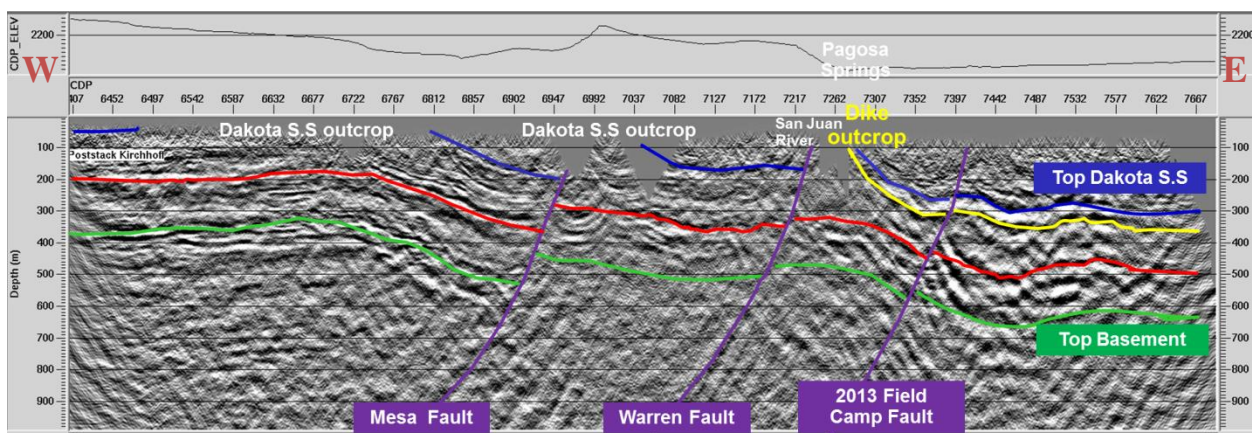
Figure 5.9: It shows the depth converted section of Kirchhoff time migration stack with interpretation.

5.8   Integrated interpretation

The final stack was interpreted to contain the geology of the Pagosa Springs region. Three large-scale faults were interpreted based on the seismic stack section: the 8-mile Mesa Fault, the Warren Fault, and the 2013 Field Camp Fault.

The deep seismic result was combined with other geophysical and geological information to yield integrated interpretation results for the main seismic line. As is the case with seismic interpretation, there are always many different views that can be interpreted from one seismic stack section. For example, the geology team interpreted four main faults on the section and did not put in a sill. However, the quality of the seismic section was poor in the east part of the line so interpretations were less certain.

The DC team confirmed the presence of the 8-mile Mesa Fault. The magnetic line coincided with the seismic line and only saw the dike anomaly and a generally increasing trend above the potential sill where the basement is even deeper. The gravity team confirmed the 8-mile Mesa Fault and another fault to the east. Gravity response also showed an increasing trend east of the dike, which could confirm the presence of a dense body above the deep basement. A dense body above the basement would explain the observed gravity and magnetics trends.

5.9   Conclusions and discussion

A complete processing flow was applied to the main seismic line to try to image the top of the Dakota, the top of the Basement, the main faults, and the geologic structures in the area. This could help explain the geologic evolution which led to the existence of hot springs in the Pagosa Springs area. The top of the Dakota and the top of the Basement reflectors were successfully imaged with new discoveries in the eastern part of the seismic line. The dike was imaged on the surface and a potential sill layer was interpreted as an intrusion through the Dakota Sandstone. The sill may act as a heat source for the hot springs system; however, the sill is imaged to be very shallow.

6. Shallow Seismic

6.1 Introduction

Shallow seismic involves recording and interpreting the subsurface by using an impulse source, such as a sledgehammer, rather than a controlled source (Vibroseis). When the sledgehammer hits the metal plate resting on the surface of the ground, a direct, acoustic wave travels through the subsurface and reflects off of a boundary that separates rocks with different densities (Figure 6.1). Refractions occur when the lower rock layer has a higher seismic velocity than the upper layer; either a direct wave hits the boundary at its critical angle, or a non-continuous body diffracts the wave. In this case, the acoustic waves propagate along the boundary until they return to the surface where they are recorded by geophones (Figure 6.2).
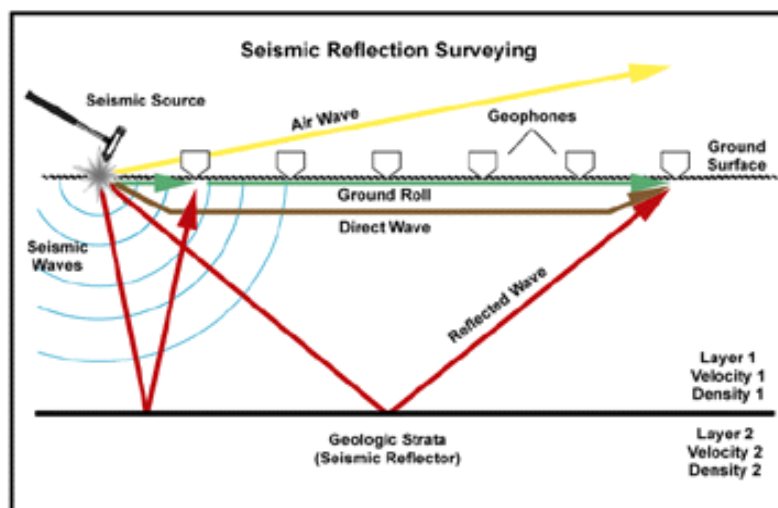
Figure 6.1: Shallow seismic reflection survey using a sledgehammer [42].
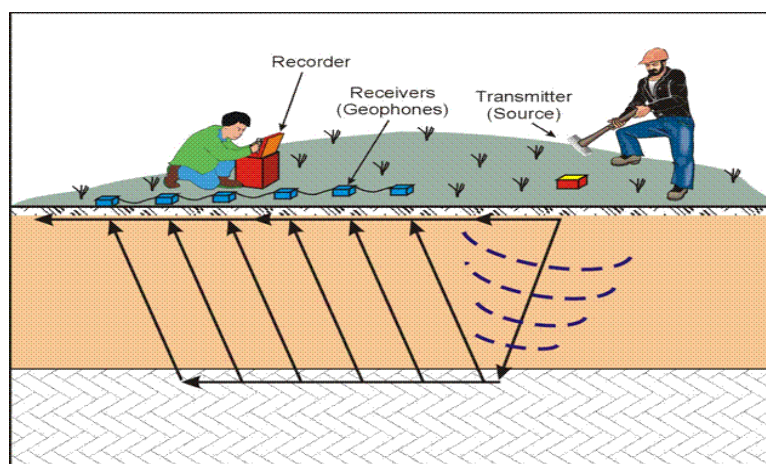
Figure 6.2: . Shallow seismic refraction survey using a sledgehammer [43].

This year, the primary source of interpretation for shallow seismic is the reflected waves. Reflections are interpreted in a common midpoint gather plot by identifying a change in slope after the first arrivals. The first arrival is the direct wave; however, refractions or "head waves" appear before the

63

direct wave because they travel at a faster velocity on the boundary and return to the surface earlier. A velocity model is created when the geological information, the various known velocities of the different rock layers, and the wave properties identified in the seismic data are correlated.
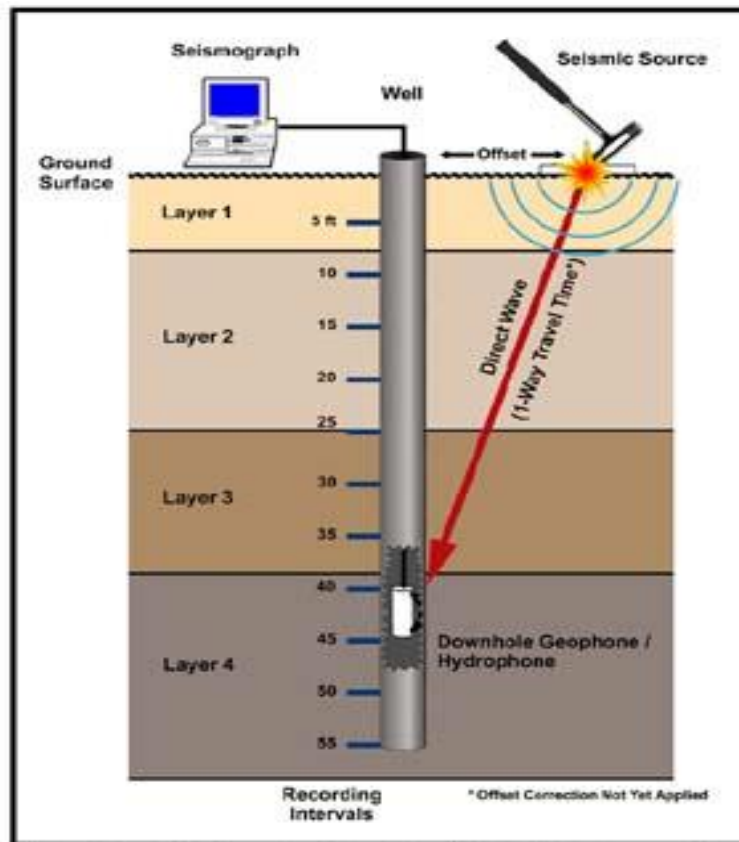
Figure 6.3: Vertical seismic profile using a sledgehammer [44].

Vertical seismic profiling (Figure 6.3) is used in order to more accurately identify rock layers when a well log is available to compare. This method involves sending hydrophones down a well and continuing the line outside of the well using geophones. Shot locations are based on the surface, and the hydrophones pick up the acoustic waves that reflect off of the nearby rock layers. This is particularly useful when the surface data is being processed, in order to correlate the two interpretations.

6.2 Survey Locations

Three locations were chosen to conduct a hammer seismic survey. Figure 6.4 shows the locations of the two Pagosa Springs survey areas in relation to the main seismic line. The third location is at Shahan's Ranch.
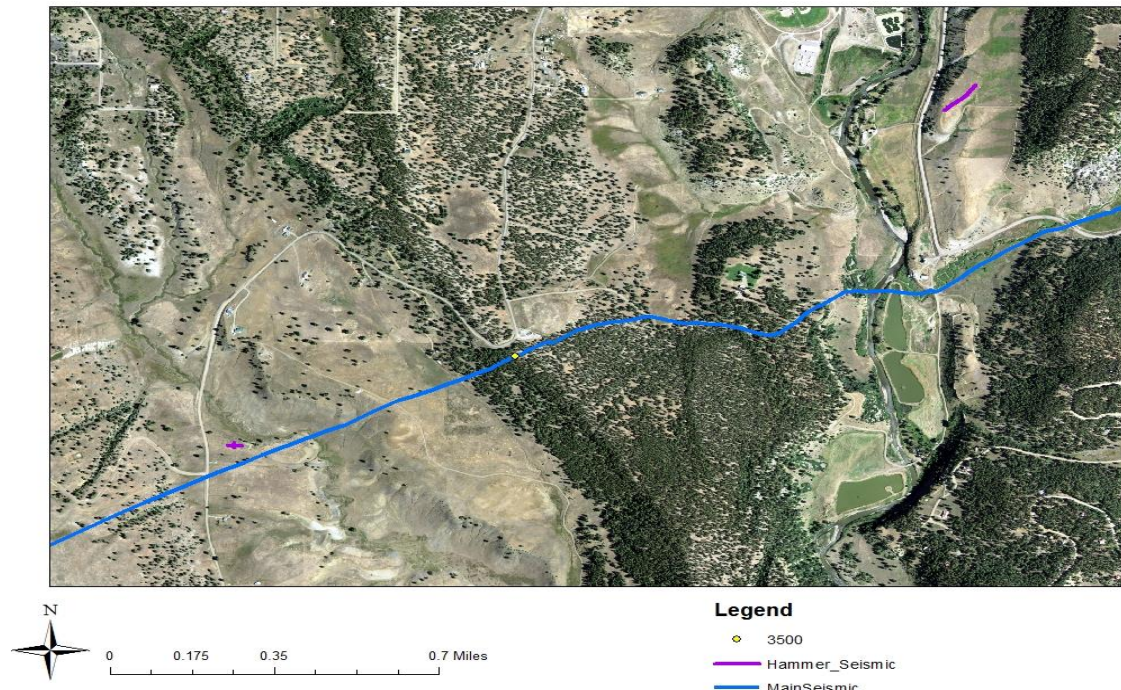
Figure 6.4: Map of the main seismic line with the locations of the hammer seismic lines north of the dike and at well 1.

(1) North of the dike (Figure 6.5): Three survey lines were laid out in this area. The goal of the surveys in this area was to map a limestone layer located in the Mancos Shale. The lines had a South-West to North-East orientation which was parallel to the dip direction. Flat topography was chosen for these lines, to eliminate the need for topographic corrections.

Figure 6.5: Location of the hammer seismic line north of the dike.

(2) Shahan's Ranch (Figure 6.6): This survey line was along the main EM survey line. The goal of this survey was to image the boundary between the Mancos Shale and the Dakota Sandstone and support the DC survey conducted in the area.
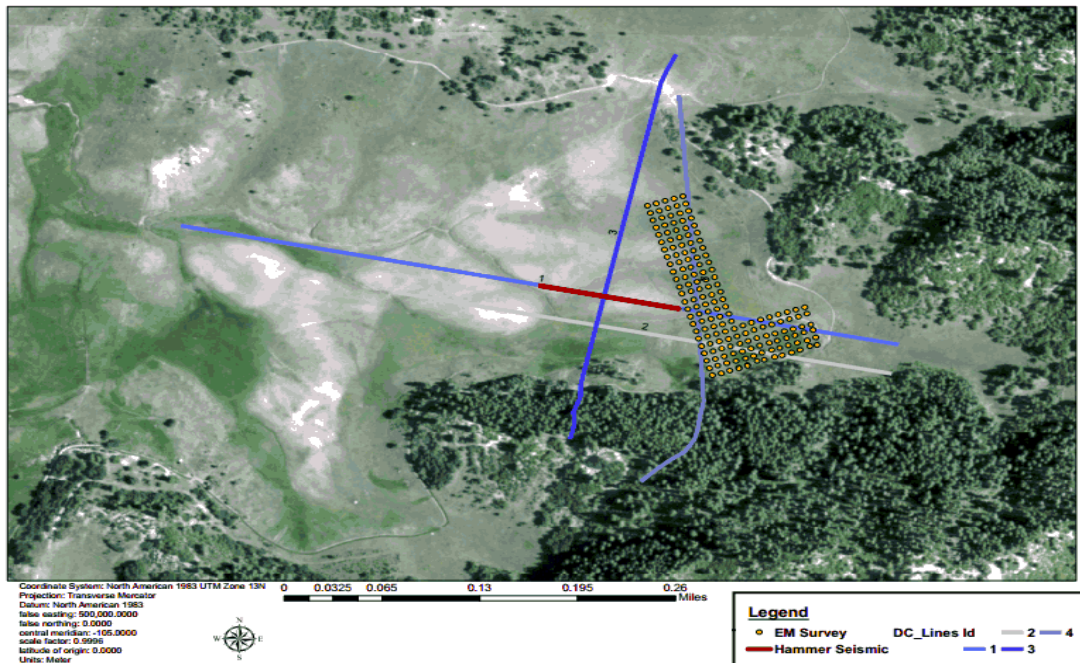
Figure 6.6: Shahan Ranch location with all of the surveys mapped (hammer seismic is in red, follows the DC line).

(3) Well 1 near the main seismic line (Figure 6.7): Two perpendicular lines were used. One with an East-West orientation, and the other with a North-South orientation. The well was at the center of both survey lines. The goal of the lines in this location was to determine the velocity and the anisotropy of the Dakota Sandstone layer, which was approximated to be 2 meters below the surface.

66

6.3   Survey design

North of the dike, at the location that was also commonly referred to as the bench, a sampling interval of 0.25 milliseconds and trace duration of 1 second were applied throughout the whole survey. The first part of the survey consisted of 48 geophone channels at 2 meters spacing. The shots had a 2-meter spacing starting 9 meters outside the first channel and ending 15 meters outside the last channel, channel 48. Three stacks were used per shot. The second part of the survey moved the first 24 geophones from the first layout to the end of the line. Shots were at 2 meter spacing; starting 15 meters from the first channel, channel 25, and ending 15 meters away from the last channel, channel 72. Three stacks were used per shot, and 5 stacks were used during windy shots. The second day moved channels 25 to 48 to the end of the line towards the northeast. Since the wind was resulting in noisy data, three shot points with 6 stacks per shot were used: one shot at the center of the line and two shots offset by 14 meters outside of the first and last geophones. Horizontal geophones were used for this part of the survey that measured only the vertical direction (as opposed to VSP).

The second location, Shahan's Ranch, had 48 geophone channels with 3 meters spacing. Shots were located at a distance of 30, 60 and 90 meters away from the beginning and end of the line, and at 36 meters spacing along the line. Each shot had 5 stacks. A sampling interval of 0.5 milliseconds and trace duration of 1 second was used.

For the third location, at Well 1 (Figure 6.8), both lines had 24 geophone channels at 2 meter spacing and 12 hydrophone channels down borehole of the well at 1 meter spacing. The shots had 8 meter spacing, with the first shot starting one meter away from the beginning of the line. Each shot had three stacks. A sampling interval of 0.5 milliseconds and trace duration of 1 second was used. For both

lines, data was collected for three hydrophone depths, such that the first hydrophone was at 4.5, 11.5 then 17.5 meters from the surface of the ground.
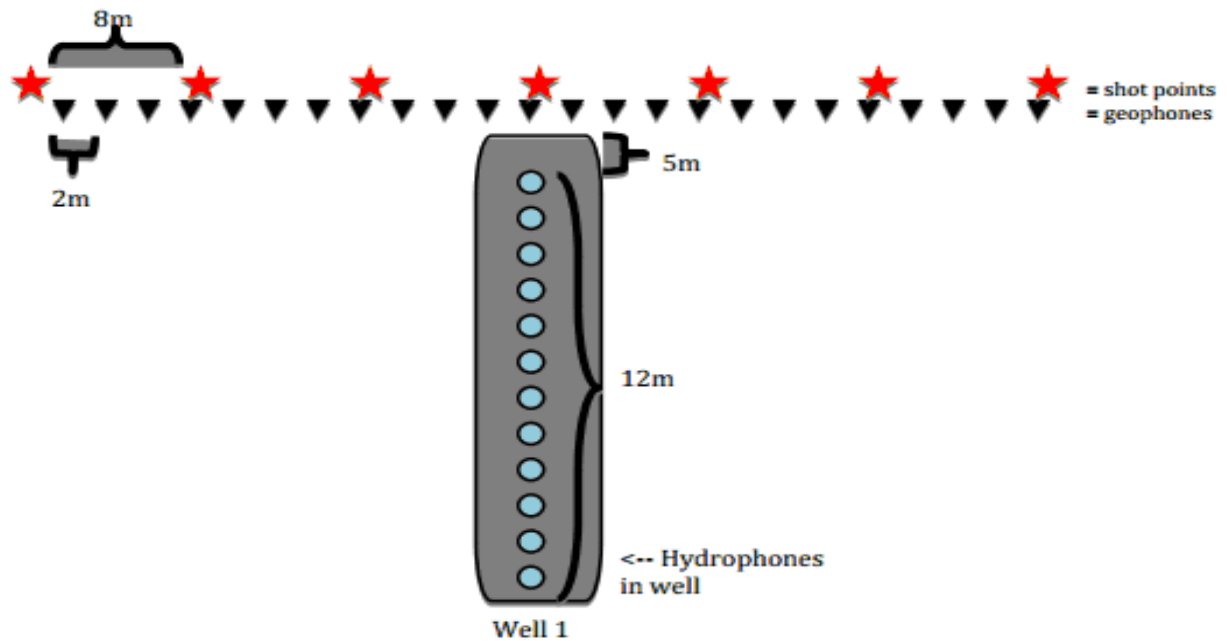
Figure 6.8: Layout of the VSP survey.

6.4   Processing

6.4.1   Shallow Seismic Processing: General Overview

The first step in data processing workflow is to download the data into the appropriate software. A total of three data sets needed to be processed: two at Pagosa Springs and one at Shahan's Ranch. The Shahan Ranch data as well as one of the data sets from Pagosa Springs, called the VSP or Well 1 data set, were processed using ProMAX. The other data set from Pagosa Springs, called the bench data set, was processed using Seismic Unix. All of the files were first saved as .sgy files and were then downloaded onto a computer. Note that for processing on Seismic Unix, .sgy files were converted into .su files.

Quality Control

After the raw data files were properly downloaded, they were displayed onto the computer. Shot gathers were viewed to get a rough idea of the data quality: noise, missing traces, acquisition artifact, etc. The goal of this step is to get a general overview of the data to be processed and to identify the main features that it contains.

After the data was displayed, acquisition geometry/parameters were reviewed in order to make sure correct information was inputted into the data headers. The header information included trace numbers, source position, receiver position, common mid-point (CMP) number, offset, sampling rate, number of samples per trace, time and date of acquisition. Stacking charts were plotted of receiver

locations versus source locations to identify possible missing traces during acquisition. At this point, any anomalous or poor quality traces were deleted from the datasets.

CMP Sort

In most cases, data are sorted into CMP gathers and then processed, which includes velocity analysis, NMO corrections, DMO or pre-stack migrations, etc. Before sorting the data into CMP gathers, it is also useful to sort the data into shot gathers in order to mute the direct arrivals and head waves. Note that for the Shahan Ranch data, the fold was particularly low (around 3 traces per CMP gather). Therefore, muting and velocity analysis were conducted on the shot gathers.

Muting

In each seismic acquisition, there are many types of waves that are not of interest for reflection analysis: direct waves, head waves, Rayleigh waves (for land acquisition), etc. In order to obtain a good stack of when we sum the traces in each CMP gather, it will be necessary to mute (or suppress) the noisier signals as mentioned above. The muting is done by manually picking and suppressing the unwanted events.

Velocity Analysis

This step allows for a rough estimate of the RMS velocities within the subsurface. Using a semblance map, RMS velocities can manually be picked for each reflection and therefore create a RMS velocity profile of the subsurface. This step is usually conducted on the CMP gathers.

NMO Correction

Once the velocity analysis is completed, normal move-out (NMO) is corrected for. If the velocity analysis was done correctly, each reflection event on the CMP gathers should be flat. The data are then stacked in order to increase the signal to noise ratio.

6.4.2 Shallow Seismic Processing: By Location
Bench Location

First, two days' worth of data was inputted into one file so corrections can be made from there. Figure 6.9 shows five shot gathers before the processing began. These shot gathers were all combined into one line to make the data easier to work with. The geometry for the line was then created to show the locations of sources and receivers relative to one another. This also shows the correct geometry for when the common depth plots were created. Next, several traces were killed which were noisy throughout the survey. These channels were ones that did not really pick up any waves and were a consistent noise from the beginning of the survey to the end. A bandpass filter was also added to minimize frequencies such as wind and refractions, but also to maximize the reflections.

Next, traces were muted, which involved hiding all of the unnecessary data such as refractions, noise, and anything else that doesn't make sense. NMO correction was applied where the reflection plane was corrected to be level as opposed to following the trend of the ground roll. This is so that there is a more accurate representation of the subsurface so the reflection depth can be accurate. After NMO, the group stacked the data which amplifies the areas where the reflections are consistent and minimizes areas where there are inconsistent data. Once the data was stacked, a second top and bottom mute was added so as to get a clearer focus area on the reflection. Also, a second bandpass filter was added to eliminate some of the noise that may have been present and get a clearer plot. A trace mixer was also added to make the data clearer by mainly averaging a group of five traces together. This yielded the time plot which is in Figure 6.10. A time to depth conversion was made with a conversion of 2000 m/s as a general velocity which is shown in Figure 6.11. The explanation for this can be seen in the interpretation section for the bench location.
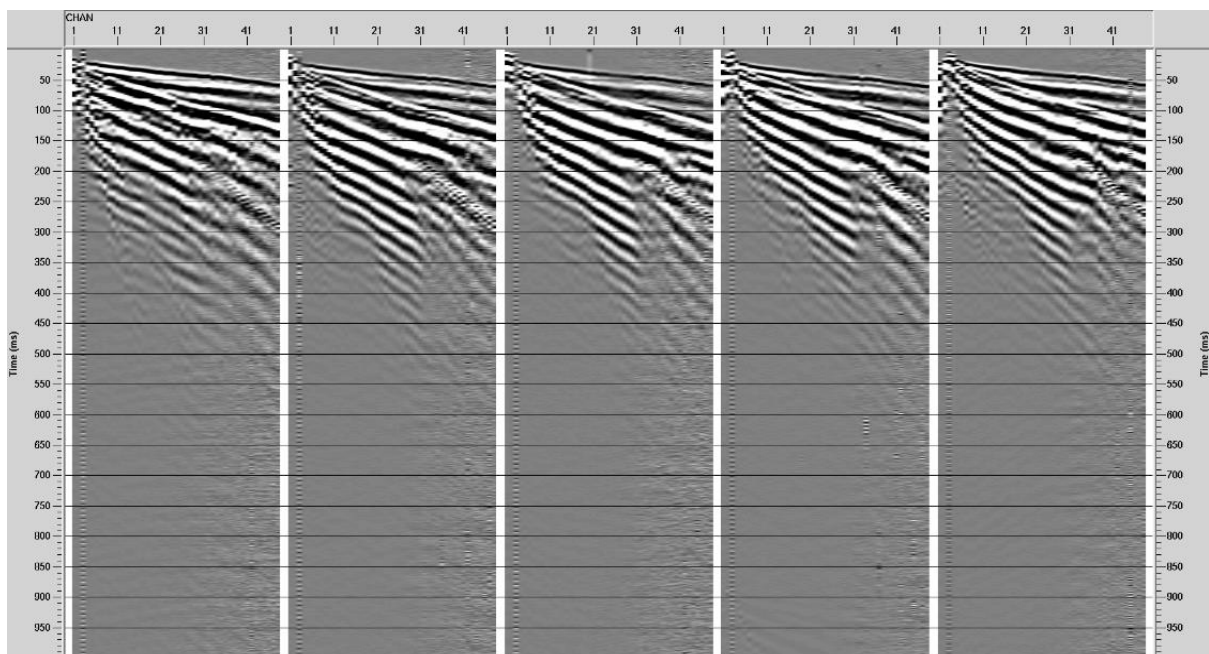
Figure 6.9: The pre-processed shot gathers.

Well 1 Location

The first step was inputting the raw data (.sgy files) onto a ProMAX disk so that the files that were manipulated did not affect the original data. The next step was to select a certain number of traces in order to separate the VSP data from the surface data. After that, the geometry was inputted into ProMAX in order to use the sloping tool to find velocities. A bandpass filter was used in order to increase the signal-to-noise ratio so that the higher-frequency data could be interpreted. When the data was stacked next to each other from the same locations, the waves did not connect to form a straight line; therefore, useful reflections could not be found, the VSP data was just used to find the velocity of the first arrivals in order to compare with the surface data. The surface data was the better option to

interpret out of the two data sets. Two lines were surveyed, one was oriented East-West, and the other was oriented North-South. The velocities for both of the lines were interpreted using a slope tool on ProMAX, shown in Figure 6.12, and the depths of each of the layers were found using those velocities and the intercept time.

Shahan's Ranch

The processing of the data for the Shahan's Ranch site proved to be quite difficult due to the lack of data that was acquired during acquisition. The software used in order to process this data is known as Seismic Unix maintained by John Stockwell at the Colorado School of Mines. As was done with the other sites, the data in SEG-Y (.sgy) format needed to be downloaded and then converted into the Seismic Unix format (.su). Once this was done, each file was windowed into individual shot gathers and then the geometry was set according to the source and receiver layout for each shot. After having set the geometry, the noisy signals such as ground roll and the direct arrivals were muted in order to better visualize the reflections. After muting, the bad traces were killed and then a NMO correction was applied to each shot gather. Velocities were chosen in order to correct for the move-out in each shot gather, making all of the reflections flat. Once a flat reflection was obtained, each section was concatenated, sorted into the CMP domain and then stacked to produce a very crude reflection section. In order to create data that is easier to interpret, trace mixing and normalization were applied along with random noise suppression, resulting in the final Shahan reflection section.

6.5   Uncertainties/Errors

Sources of error in hammer seismic surveys include:

(1) Ground Roll: near surface seismic sources produce surface waves called Rayleigh waves which have strong amplitudes that can interfere with reflections. Ground roll can affect the data especially when reflections are weak. These Rayleigh waves can be eliminated through frequency filtering since their frequency is usually lower than that of the reflected P-waves [45].

(2) Wind: to compensate for the wind, the number of shots at each shot location was increased from 3 shots to 5 shots. The increase in shots improved the signal to noise ratio significantly.

(3) Power lines: the errors caused by power lines can have an unpredictable amount of interference picked up by the geophones. The amount of interference of power lines depends on three main factors. First, the magnitude of the current leaking from the power line system can be picked up by the geophones. Second, the variable current flow in power lines induces an electromotive force in the geophones that interference with the primary EMF induced by seismic signals. Third, the strength of the electric field in the cables and geophones used in the survey determines the amount of noise power lines would create in the data [46]. The stronger the electric field in the geophones, the less noise the power lines would create in the data.

(4) Noisy channels: a couple of channels were noisy throughout the survey. This is most likely because of a short in the cable that created the noisy channels.

(5) Strength of impulse: several different people were used to create the shots, so the strength of the impulse, and therefore quality of the data varied. Also, the hammerers most likely got tired during the end of the survey so the strength of the shots was not as strong as the beginning.

6.6   Interpretations

Bench Interpretation
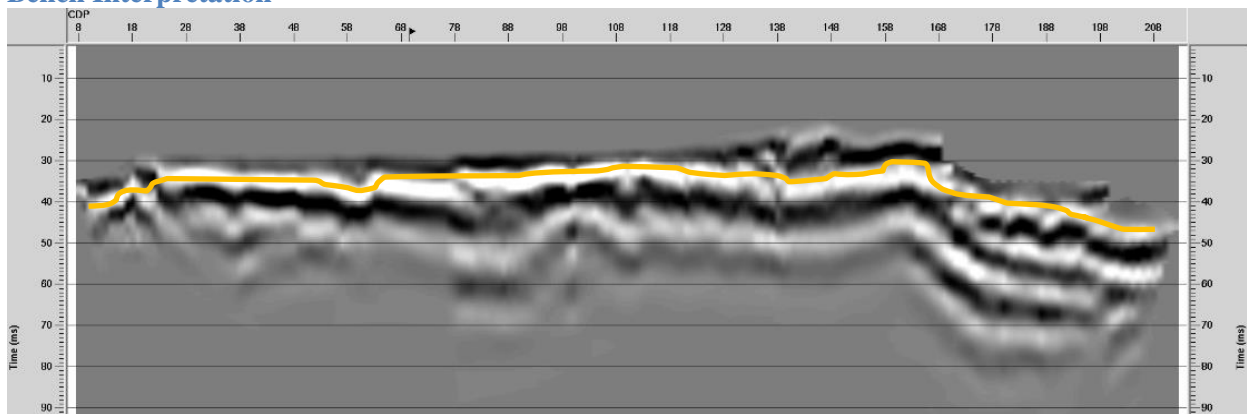
Figure 6.10: Stacked time bench data starting at the SW and moving to the NE.
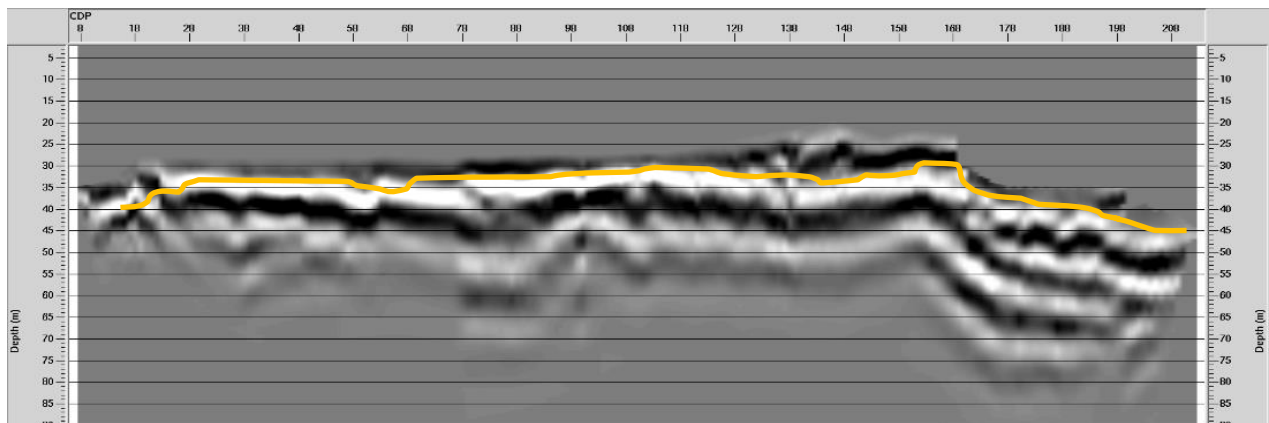
Figure 6.11: Time to Depth Conversion on Bench data (Southwest to Northeast).

On the bench data, there is a clear reflector that follows most of the line at about 35 meters (Figure 6.11). This is consistent with the depth of the Dakota Sandstone. At about 168m offset (NE end of the line), there appears to be a fault in the subsurface. This is consistent because the strong reflector seems to drop a significant amount from the SW side to the NE side. The approximate range of velocity for the Dakota Sandstone is from about 2500m/s to 3100m/s. Illustrations' two and three both show that strong reflector on the top. The depth conversion is to quantify the results in terms of the geological subsurface. The Dakota Sandstone reflector is at 35 meters. This makes sense because the Niobrara layer occurred approximately 5 meters beneath the surface of the survey. This is known because the start of the survey was above an outcrop of the Niobrara that could be seen from road cut

north of the Hairpin dike. With this knowledge and the geological knowledge that the Dakota should occur about 30 meters beneath the Niobrara, then the strong reflector at 35 meters must be the Dakota Sandstone.

2013 Field Camp Support

When double checking with the deep seismic line on their results, the hammer seismic group found that the fault hypothesis is plausible since the deep seismic line found a fault in the same location. Along with that fault, a lot of the data from the deep seismic line appears to have the same geometry as the hammer seismic lines.

Outside Support

When looking back at the 2012 field camp report, the group found that the DC line had discovered a fault that runs along this bench area. They named it Victoire Fault. This also supports the hammer seismic claim of a fault in the NE of the line.

Well 1 Interpretation

The velocities were chosen from the VSP surface data using the technique outlined in Figure 8, and then the heights of the two rock layers were found using these equations:

$$h_1 = \frac{t_i}{2} \frac{V_2 V_1}{(V_2^2 - V_1^2)^{1/2}}$$

Equation 6.1: Finding the depth of the first layer (rock with a common seismic velocity).

$$h_2 = \left(t_{i_2} - \frac{2 h_1 (V_3^2 - V_1^2)^{1/2}}{V_3 V_1} \right) \frac{V_3 V_2}{2(V_3^2 - V_2^2)^{1/2}}$$

Equation 6.2: Finding the depth of the second layer (rock with a common seismic velocity).

The velocities collected using the slope tool on the shot gathers indicate that the velocity of the first layer falls in the range of 200-300 m/s, which is indicative of a soil layer (the acoustic waves do not travel through soil as fast as rock due to the high permeability). The second layer has a velocity in the range of 700-1200 m/s, which may indicate a transition zone between the top soil layer and the rock layer below. This velocity is consistent with that of loose sediment; however, the velocity is higher than that of soil. The third layer has a velocity in the range of 1800-2600 m/s. This velocity is usually associated with that of the Mancos shale, and the geology indicates that the shale was the primary layer that was surveyed. The sandstone is predicted to have a velocity of approximately 3000 m/s, but the sandstone layer that is seen in this location may be weathered (contains many fractures that slows down the velocity), or the sandstone may be mixed with the Mancos shale that precedes this layer in other areas of Pagosa Springs. All three layers and velocities were found using the slope tool on ProMAX, and are shown in Figure 6.12 and Figure 6.13 below.
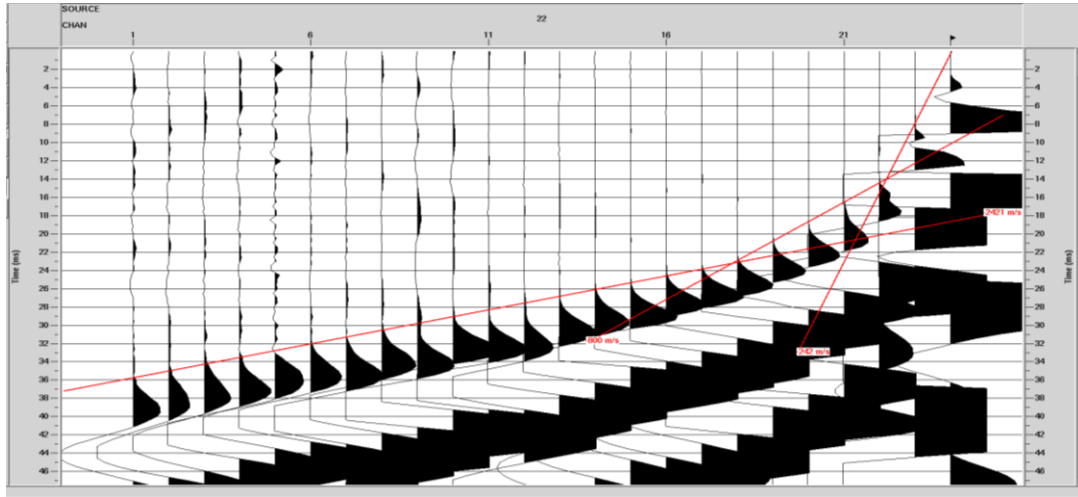
Figure 6.12: Selection of three velocities on the FFID 2025 by following the tops of the reversed polarization wiggle plot.
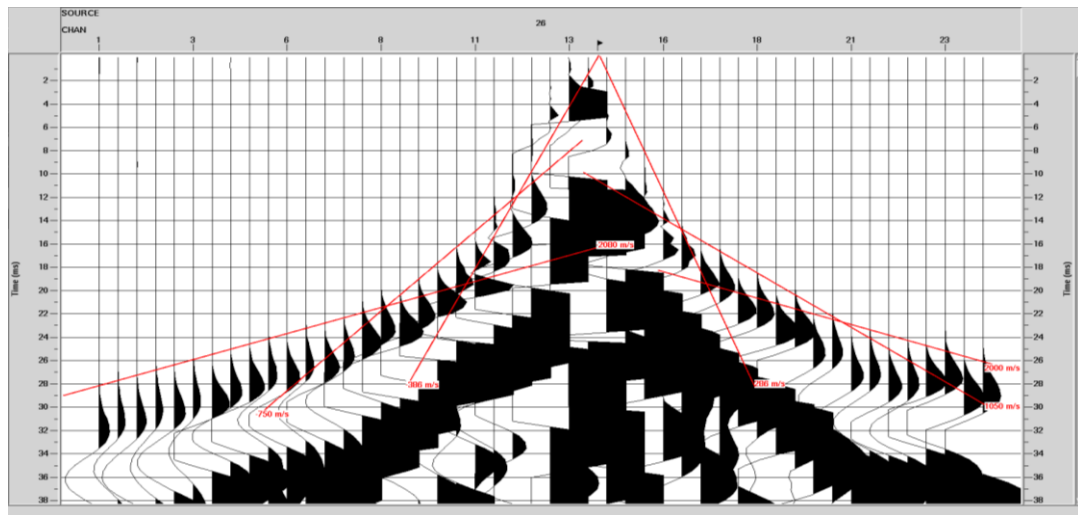
Figure 6.13: Selection of three velocities on the FFID 2028, 2029 by following the tops of the reversed polarization wiggle plot.
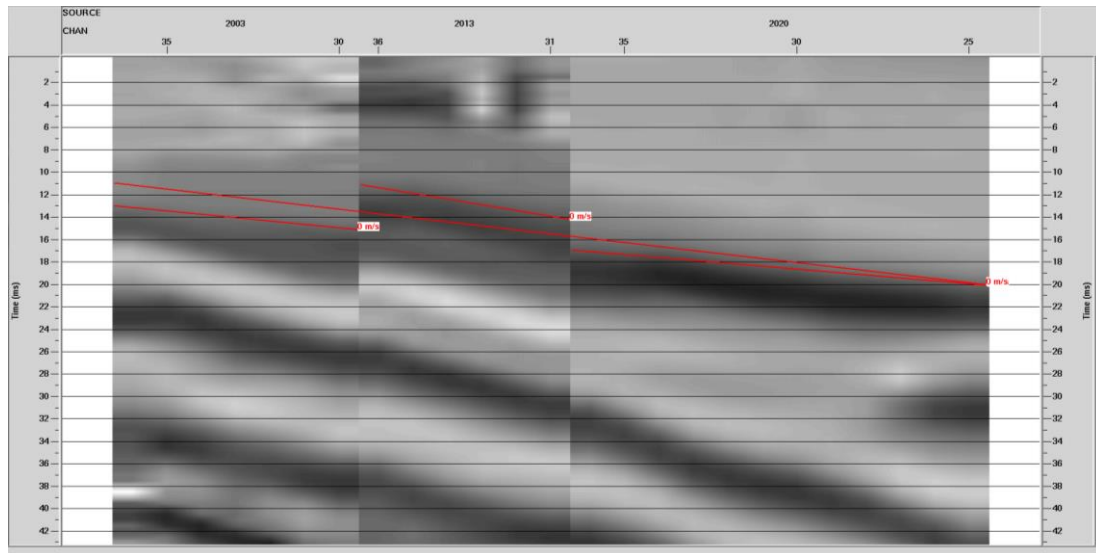
Figure 6.14: Finding velocities using the VSP data at the shot location of 17m.

Figure 6.14 shows the average velocity picked over three stacked sections from the same location (17m). Individual velocities from each of the three FFIDs were also collected in order to determine how far off each of them was from the overall picked velocity. The average velocity for this figure is 2777 m/s. That correlates nicely with the velocity collected from the 33m location, as that velocity was measured at 2941 m/s. Those two locations are the closest shot locations on either side of the well. Since those shots came in at an angle toward the hydrophones, they are an overestimate of the actual rock velocities. That matches the velocities found using the surface VSP data. The 25m location (right on the well) gave a velocity of approximately 1500 m/s (lines shown in Figure 6.15). That is the velocity of water, and the rock velocities were not found.
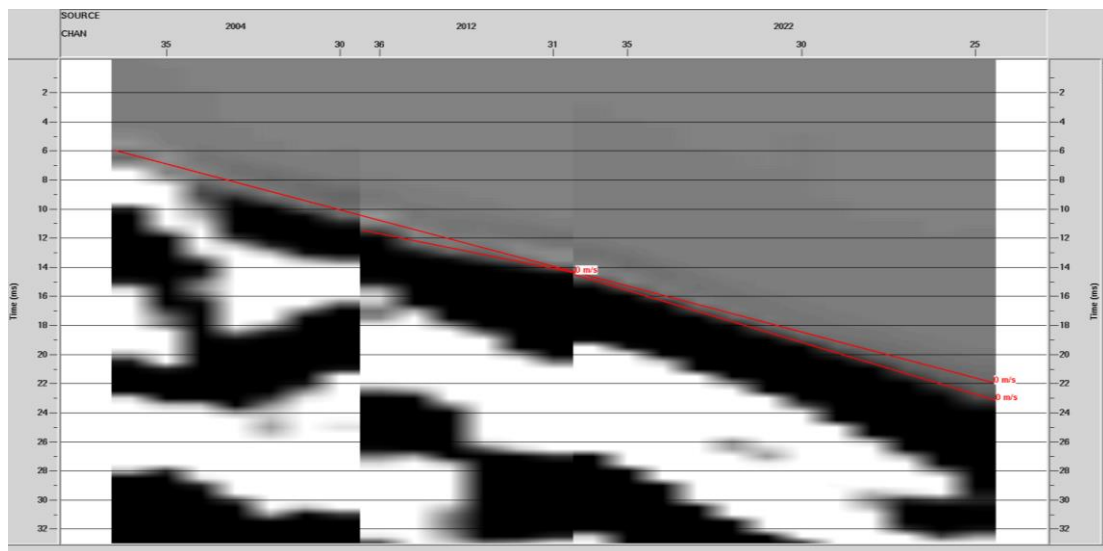
Figure 6.15: Finding velocities using the VSP data at 25m (closest to the well).

Figure 6.16 shows the velocities that were found in the shot gathers as well as the calculated depths of the two layers. These were found using Equation 6.1 and Equation 6.2. Layer 1 has an average

velocity of 287.5 m/s, which corresponds to a top soil layer, as the velocity is much slower than average rock velocity. Layer 2 has an average velocity of 873 m/s, which is still slow for a rock layer, but the range of velocities for that layer may correspond to a slow Mancos shale velocity or a sedimentary layer. Finally, the average velocity for layer 3 is 2440.5 m/s, which is high enough for a solid rock layer.

Formation Heights (North/South)

h1

Time ti (s)	0.007	0.011	0.013	0.01
Velocity v2 (m/s)	590	923	1238	800
Velocity v1 (m/s)	286	290	254	379
Total Height h1 (m)	1.144451109	1.68008	1.68689	2.1518

h2

Time ti2 (s)	0.0215	0.011	0.013	0.019
Velocity V3 (m/s)	4000			2706
Velocity V2 (m/s)	590	923	1238	800
Velocity V1 (m/s)	286	290	254	379
Height h1 (m/s)	1.144451109	1.68008	1.68689	2.1518
h2 (m)	4.031710583			3.2479

Formation Heights (East/West)

h1

Time ti (s)	0.0056	0.0095	0.0045	0.009	0.006	0.0095
Velocity v2 (m/s)	750	1086	723	1171	649	800
Velocity v1 (m/s)	386	175	348	178	337	242
Total Height h1 (m)	1.260569346	0.84226	0.89328	0.81042	1.18299	1.206

h2

Time ti2 (s)	0.016	0.016	0.017	0.012	0.021	0.0185
Velocity V3 (m/s)	2080	1778	2100	1600	2839	2421
Velocity V2 (m/s)	750	1086	723	1171	649	800
Velocity V1 (m/s)	358	175	348	178	337	242
Height h1 (m/s)	1.260569346	0.84226	0.89328	0.81042	1.18299	1.206
h2 (m)	3.643663636	4.40343	4.59628	2.53528	4.67622	3.63752
h_total:East/West (m)	4.904232981	5.24568	5.48956	3.3457	5.8592	4.84352
h_total_average: East/West (m)	**4.947984032**					
h_total:North/South (m)	5.176161692	1.68008	1.68689	5.3997		
h_total_average: North/South (m)	**5.287929987**					

Average velocity for layer 1 (m/s):	**287.5**
Average velocity for layer 2 (m/s):	**873**
Average velocity for layer 3 (m/s):	**2440.5**

Figure 6.16: Calculation of depths using the velocities that were traced on ProMAX.
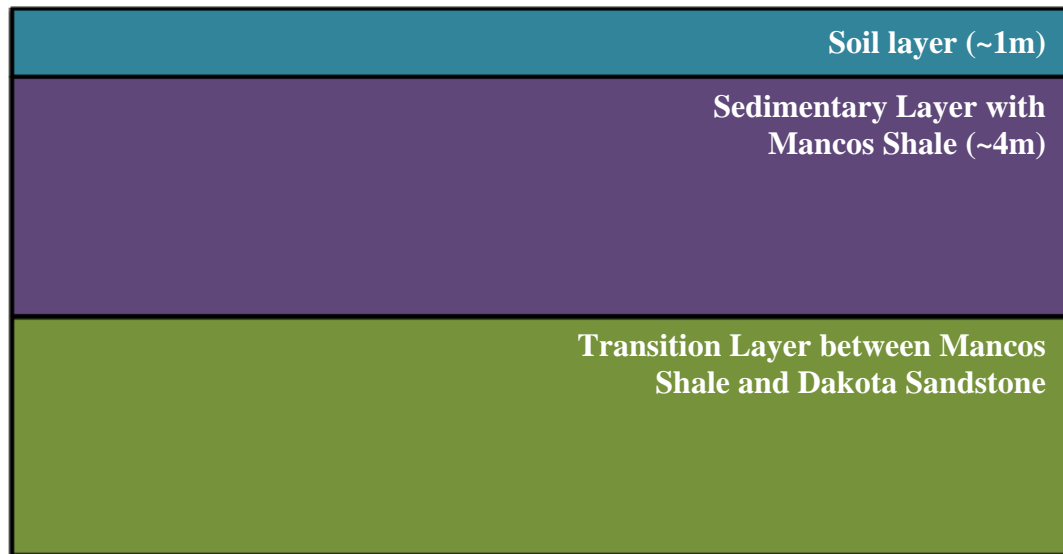
A basic velocity model is shown in Figure 6.17, where the type of rock and their corresponding depths are given. Initially, while conducting the survey at Well 1, the survey crew believed that the Dakota sandstone was located just a few meters below the survey because they saw crumbles of Dakota sandstone off the edge of the hill near the survey location. That rock has a velocity of approximately 2500 m/s, which is indicative of a slow sandstone velocity. The Dakota sandstone that is observed in the velocity data may be significantly weathered (as observed by the survey crew), and it may be intermingled with the Mancos shale that precedes it. The geology from Figure 6.17 was compared with the geologic map of the area (Figure 6.21), and they both agree that the first layer that is encountered is the Mancos shale.
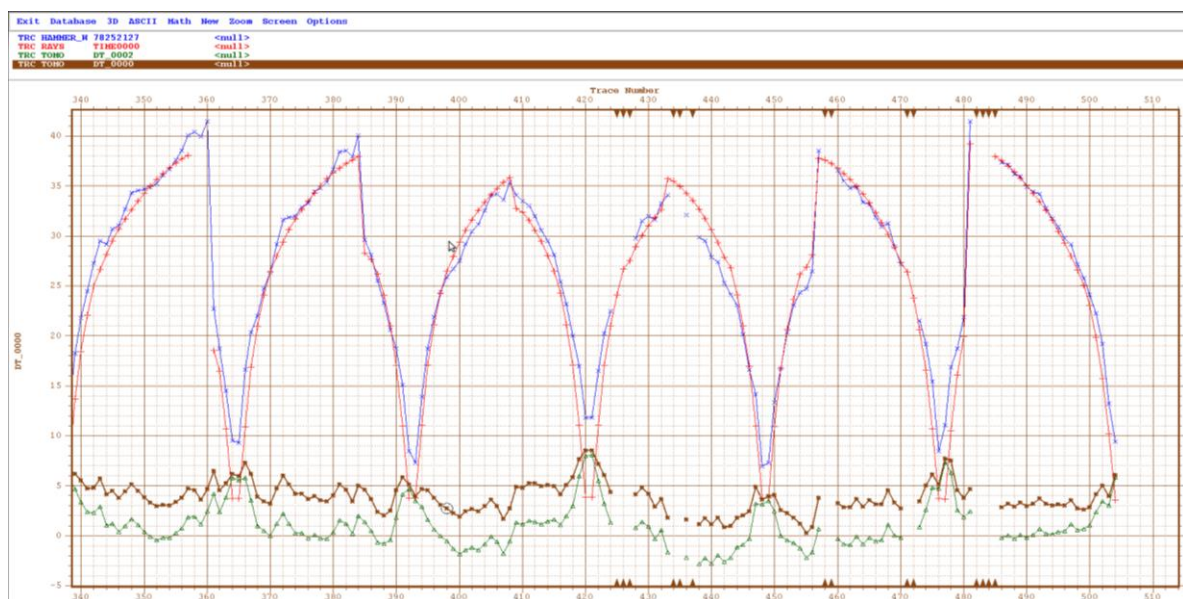
Figure 6.18: First break picks in relation to the velocity model predicted arrival times.

77
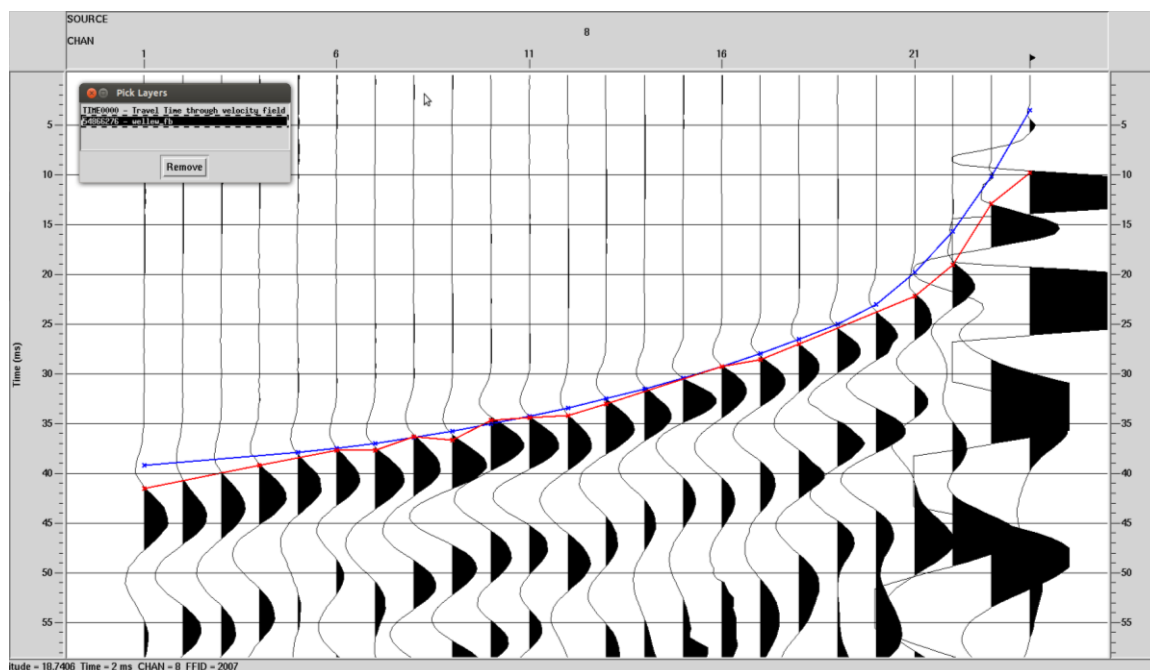
Figure 6.19: Shot gather showing first break picks and the velocity model predicted arrival times.

The first break picks were matched up with the predicted arrival times (Figure 6.18 and Figure 6.19) using forward modeling, and a velocity model was created via the inversion software on ProMAX. Figure 6.20 represents the velocity model that was created, and shows the gradient of the velocities that were predicted using the shot gathers.
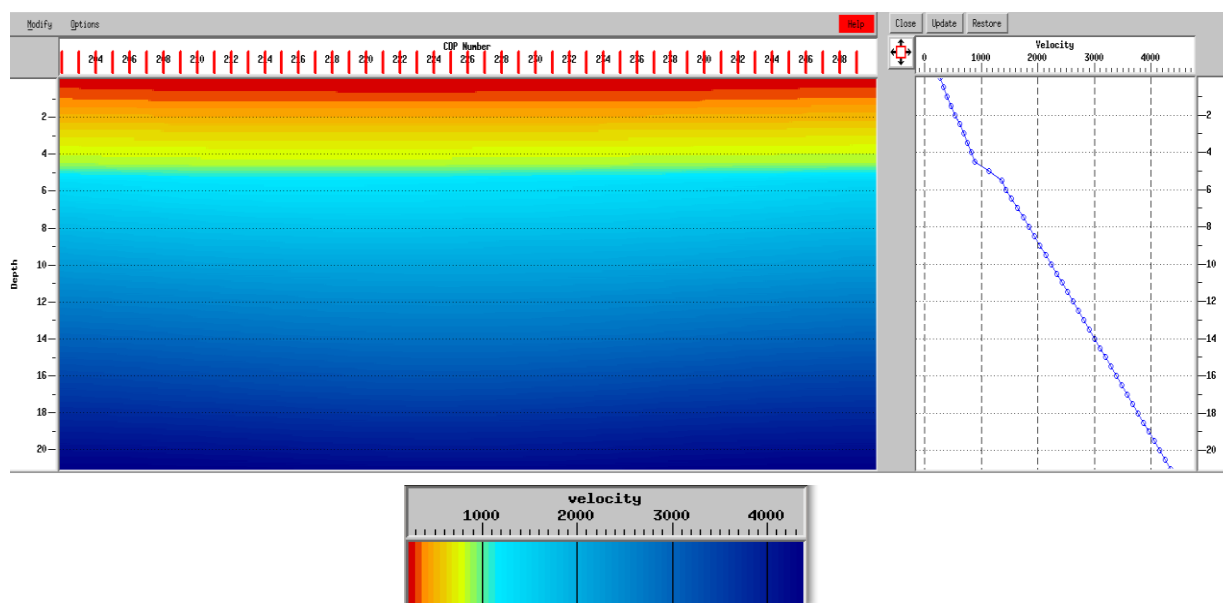
Figure 6.20: Velocity model of well 1 data.

Figure 6.21: Geologic map of the Well 1 survey area.

Ultimately, the interpretations that were made for the Well 1 location were a result of the correlation between the VSP data, the surface hammer seismic data, and the geologic information. It was perceived that the Dakota sandstone should have been identified because of the surveyors' observations; however, based on the measured velocities, a solid transition to the Dakota sandstone was not detected.

2013 Field Camp Support

The geology group helped verify that the Well 1 survey observed the Mancos shale velocity at a depth of approximately 4m. The Bench hammer seismic location also verified the velocities of the Mancos and the transition to the Dakota sandstone.

Outside Support

Last year's report concluded that the Dakota sandstone had variable velocities depending on the location. That was due to the amount of weathering that occurred. Our results verify that the velocities change depending on the composition of the sandstone as well as the amount of weathering.

Shahan's Ranch Interpretation

The goal of the hammer seismic survey at Shahan's Ranch was to identify the depth from the surface to the top of the Dakota sandstone and get the compressional wave velocity of the Mancos shale in the same process.

Assumptions

Due to the topographic structure at Shahan's Ranch as well as the lack of data, the assumption was made that the subsurface was only one dimensional (laterally invariant). Hence, dipping beds, potential faults or other more complex geological features were not accounted for.

Interpretation

The first interpretation of the data was to identify what was thought to correspond to an important reflection (bright spot on shot gather located at 0.12s on shot gather 1007.su). This reflection is believed to correspond to the acoustic impedance increase from the Mancos shale layer to the Dakota sandstone layer.

Unfortunately, due to weather conditions, the acquisition crew was not able to complete the entire survey. Therefore, there was not enough coverage of the survey line. Moreover, in some of the obtained shot gathers, the data were not of a high enough quality. Due to these conditions, this reflection was not able to be identified on several shot gathers. The idea was to base the interpretation on the shot gather that seemed the most reliable to us (1007.su).
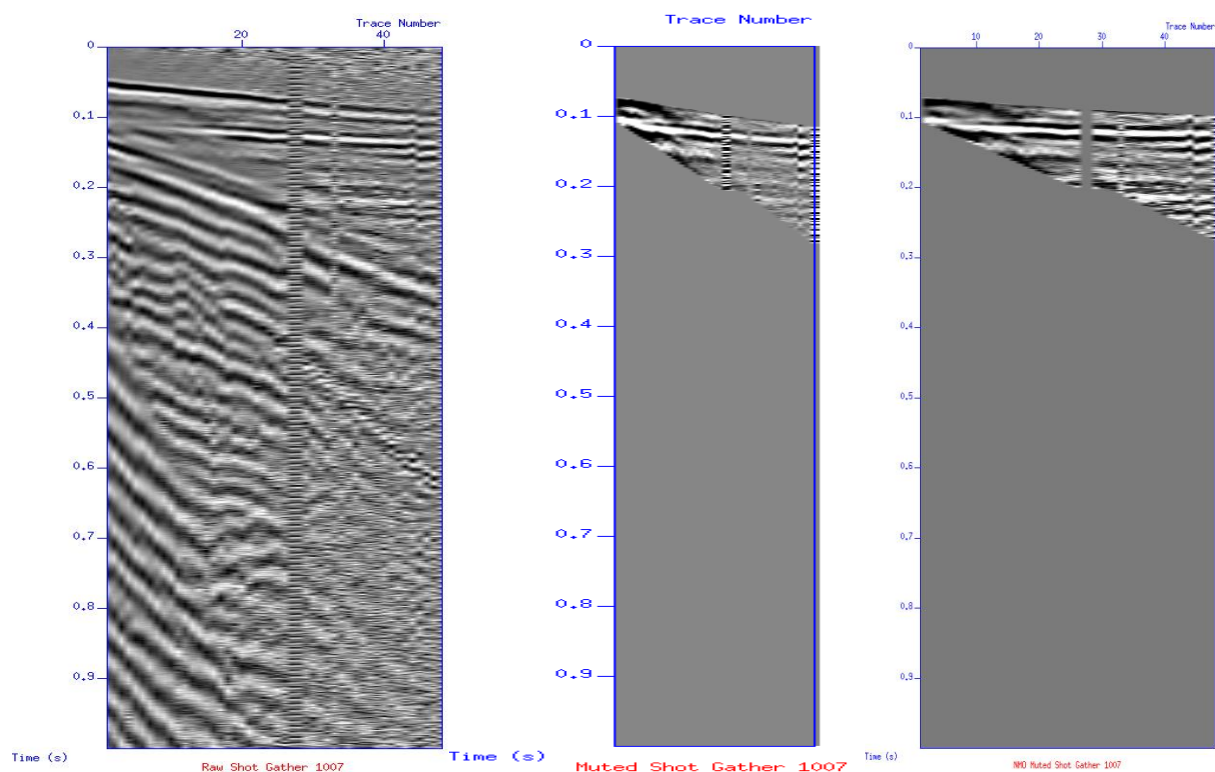
Muting, NMO Correction and Stacking

This interpretation, as the case with many interpretations, required an iterative method to obtain the optimal result. For this NMO correction, due to low fold (2-3 traces per CMP gather), the correction was done directly on the shot gathers. One to two NMO velocities were picked for each shot gather in order to correct for the hyperbolic move-out. The average NMO velocity used over the 14 shot gathers was 2100m/s, which was identified to be the Mancos shale's compressional wave velocity. The traces were sorted in CMP gathers and stacked (Figure 6.23 and Figure 6.24)
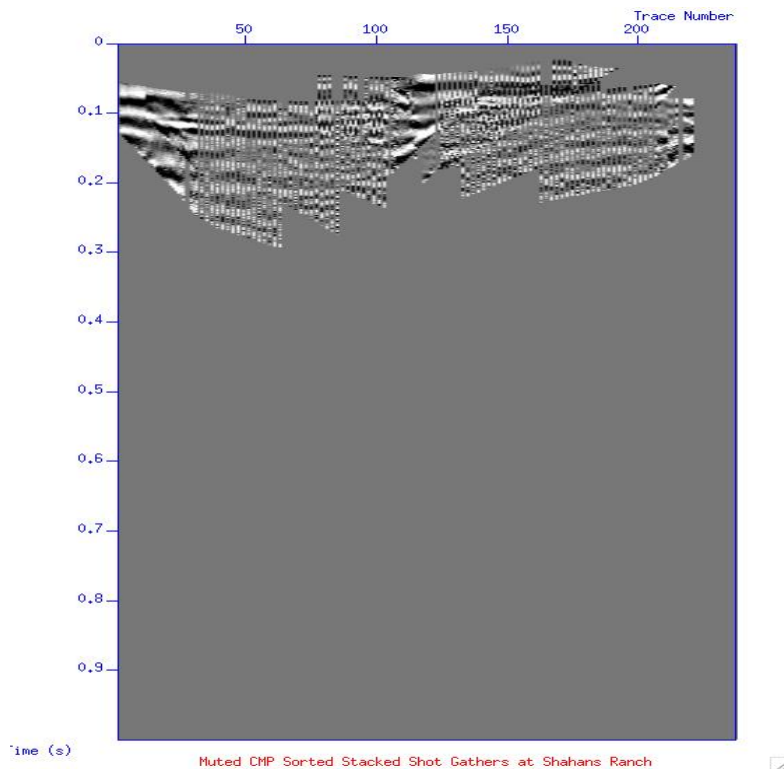
Figure 6.23: The Figure shown above displays the raw stack of the muted CMP gathers.

Normalizing functions, trace mixing, as well as random noise suppression (FX de-convolution) were all employed in order to make up for missing traces for certain CMPs.
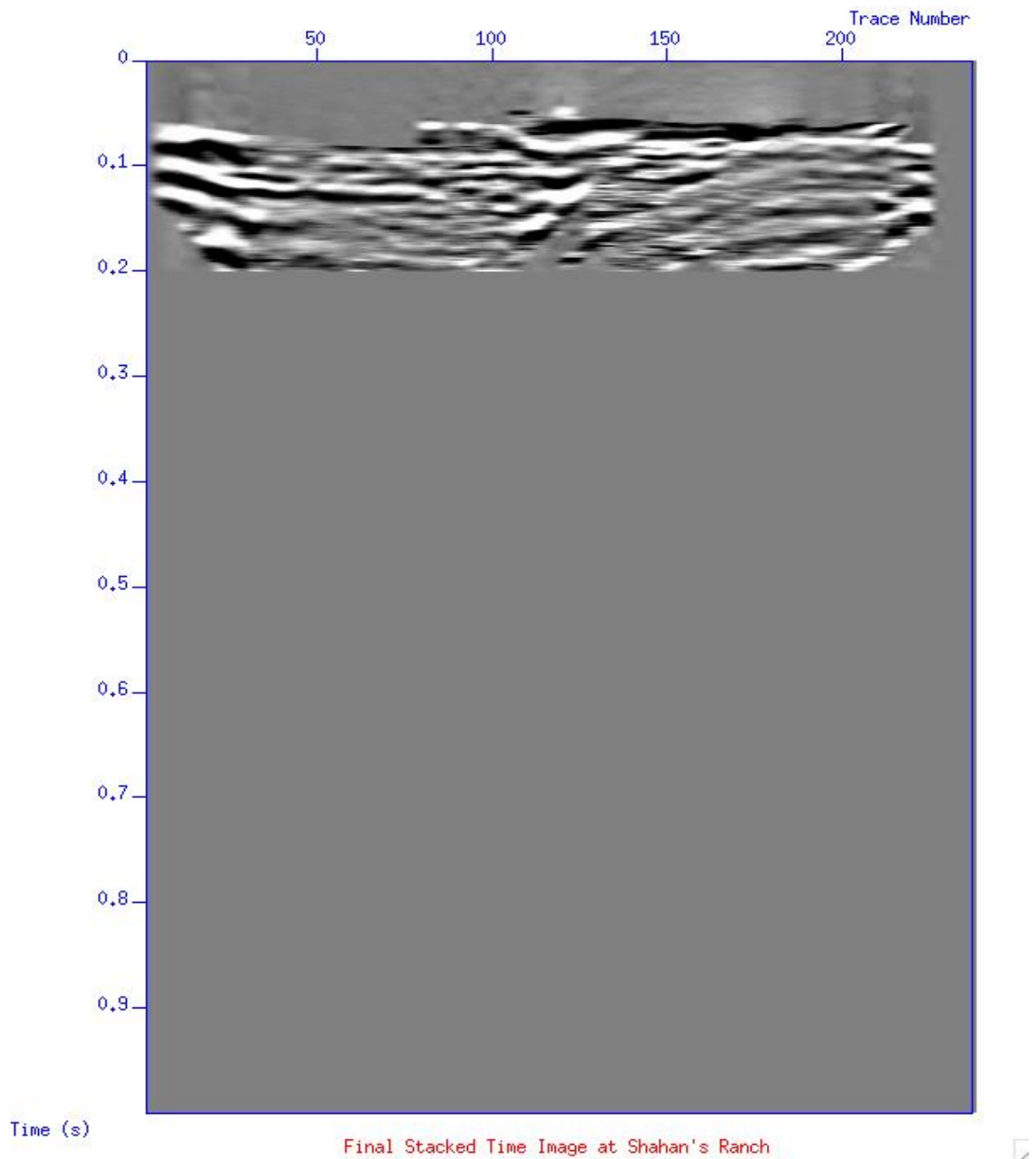
Figure 6.24: The above figure shows the final stacked time image with trace mixing and random noise suppression.

In order to obtain the seismic section in depth (Figure 6.25), the time section was converted using a Seismic Unix function (suttoz), with a chosen Mancos shale velocity of 2100m/s.
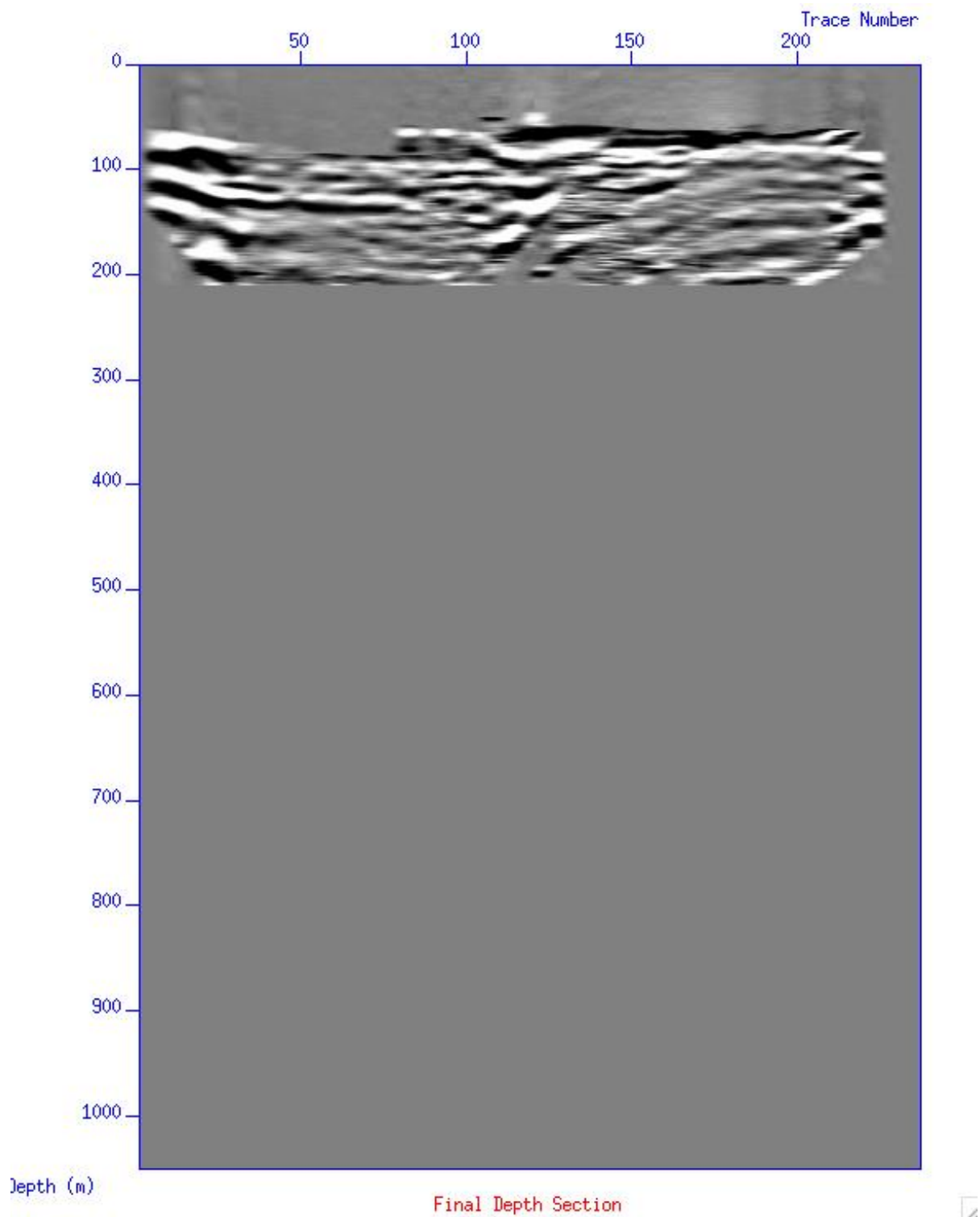
Figure 6.25: The above figure shows the final depth reflection section.

Final Interpretation

Using the assumption of the known time of the reflection on top of the Dakota sandstone on the shot gather 1007, its location was able to be identified on the both the final stacked time and depth sections (Figure 6.26).

Final Depth Section at Shahan's Ranch
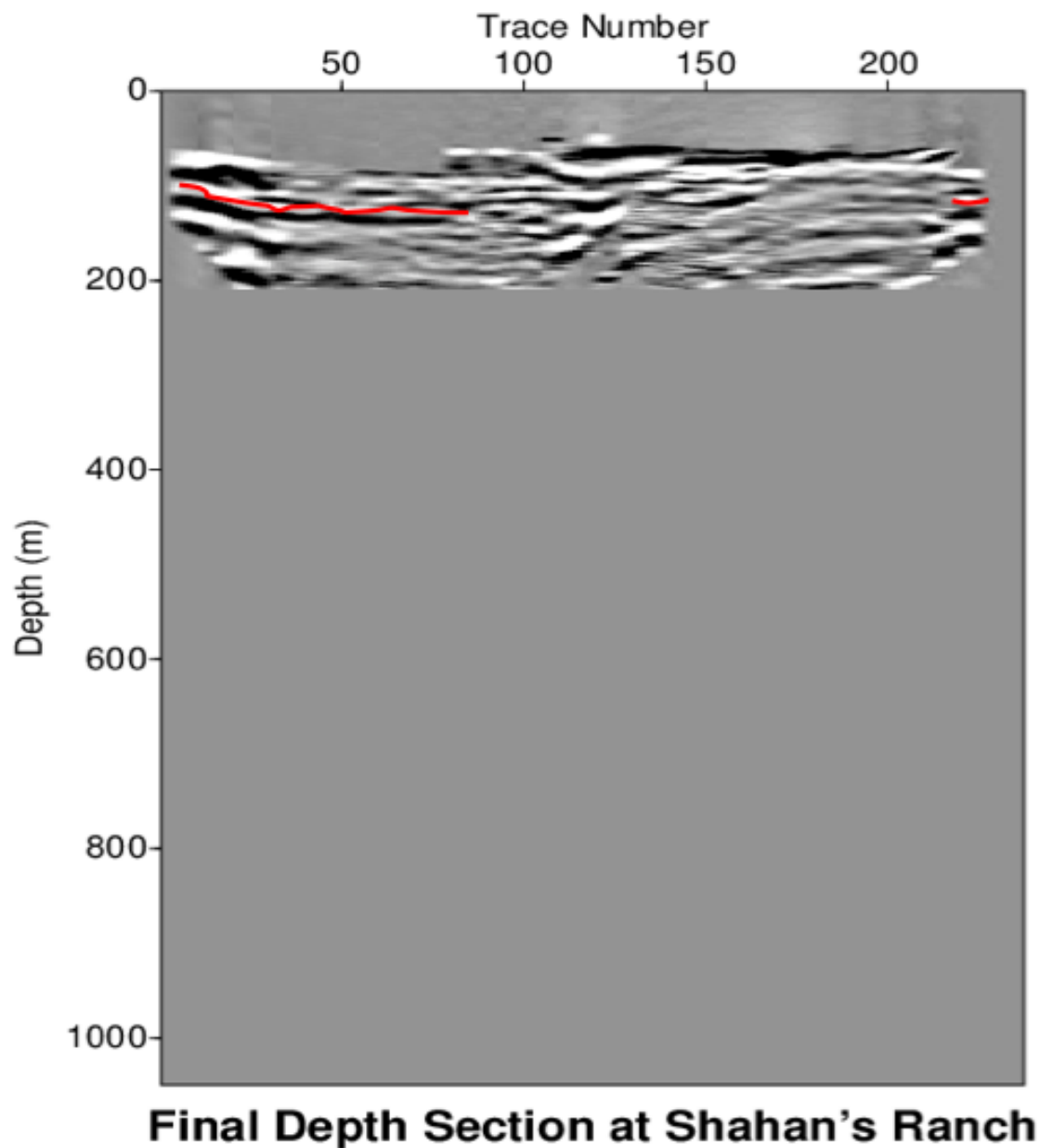
Figure 6.26: The above figure shows the interpreted Dakota Sandstone horizon on the final depth section.

The reflection of interest is clearly identified on the North-West part of the section (Figure 6.26). From there, a depth of about 100m for the top of the Dakota sandstone was estimated.

Around trace 85, it seems like we have an abrupt discontinuity in the Dakota sandstone reflection. This is likely due to an artifact in the chosen NMO velocities. Please note that this is not a geological feature.

Around trace 125, the main reflector disappears. It is believed that this is due to the poor quality of data and low fold. It is very difficult to interpret from this point towards the end the section where it reappears in the last ten traces.

6.7   Conclusions and Discussions

There are some final generalizations that can be made when comparing the bench seismic line with the well 1 line. First, the Dakota Sandstone velocity was consistently around 2750m/s when comparing the two data sets. In the bench data, the Dakota Sandstone was interpreted to be 35 meters below the surface, along with a fault near the north-eastern part of the line. This can be verified by last year's DC line and with this year's deep seismic line.

In the Well 1 data, the group found three layers: the first layer had velocities in the range of 200-300 m/s, consistent with a soil layer, the second layer has velocities in the range of 700-1200 m/s (sedimentary layer mixed with Mancos shale), and the third layer has velocities in the range of 1800-2600 m/s (transition between Mancos shale and weathered Dakota sandstone). The geology of the area as well as the VSP data verifies the findings.

The biggest concern encountered at the student site was the lack of data (dangerous weather conditions during the acquisition led the team to stop prematurely). However, the top of the Dakota sandstone is believed to have been identified as well as its depth. The North-West part of the seismic line was used for this interpretation and is the clearest part of the seismic line. The rest of the section is of relatively poor quality and is difficult to interpret, especially towards the mid part of the section. The geological structure of the subsurface at Shahan's Ranch seems to confirm the assumptions made at the beginning of the processing flow: relatively low lateral variations. Future work could include another acquisition at the same location with denser shots. The priority is to obtain better fold and improve the mid part of the section towards the South East.

7. Gravity

7.1 Introduction

Gravity method, a non-invasive, passive geophysical technique, utilizes the Earth's naturally occurring gravitational field to locate and characterize structures in the subsurface. The Earth's gravitational field is derived from Newton's Universal Gravitational Law, which is seen in Equation 7.1. In Equation 7.1, m_1 and m_2 are two masses measured in kilograms, and r is the separation between the two masses in meters [47]. The measurement of the Earth's gravity field can provide valuable knowledge about the densities of subsurface structures.

$$F = G \; \frac{m_1 m_2}{r^2}$$

$$G = 6.67 \times 10^{11} \; \frac{N \; m^2}{kg^2}$$

Equation 7.1: Universal Gravitational Law.

The gravitational acceleration produced by a body is determined by its physical properties such as size and density. Since rocks form by various processes (heating, cooling, depositional environment, etc.), they end up having significantly different properties. One of the most important properties of rocks measured with the gravity method is density [47]. A rock's density is influenced by the porosity of the rock as well its mineral content, crystal lattice structure, and fluid content.
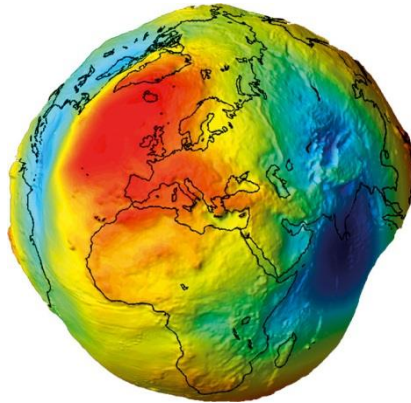
Figure 7.1: The geoidal representation of the Earth [48].

The gravity field of the Earth is measured using a device called a gravity meter (Figure 7.2). The gravity meter measures the total gravity field due to several factors that affect the Earth's geoid, a representation of mean sea level only influenced by gravity [49] (Figure 7.1). The factors that need to be corrected for a land-based acquisition are tidal/instrument drift, free-air

effect, Bouguer slab, latitude, and terrain. The corrections that must be applied to the observed gravity readings will depend on how they affect Earth's gravitational field.
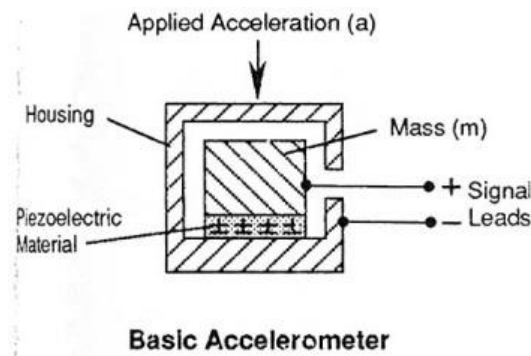
Figure 7.2: How an accelerometer works [50].

In this year's field camp, two gravity meters were used: the LaCoste & Romberg Model-G Geodetic Gravity Meter (L&R) and the Scintrex CG-5 Autograv Gravity Meter (CG-5), seen in Figure 7.3 and Figure 7.4, respectively. These two instruments work by measuring the changes in the acceleration due to gravity of the Earth caused by mass variations in the subsurface. Gravity meters either measure relative or absolute gravity [47]. The L&R and CG-5 gravity meters both measure relative gravity. Using a gravitational benchmark provided by the USGS, the gravity meters can be calibrated to reflect true gravity values.

Figure 7.3: L&R [51].

Figure 7.4: CG-5 [52].

7.2 Survey Sites

The gravity surveys completed in this year's field camp were carefully performed in several different areas of interest to provide spatially correlated gravity data, allowing for a better interpretation of the subsurface in these areas.

7.2.1 Main Seismic Line

The primary location for gravity measurements was the main seismic line. The main seismic line runs in an approximately SW to NE direction in the southern portion of Pagosa Springs. Gravity data was collected along the main seismic line, seen in Figure 7.5, in order to enhance the interpretations of other methods conducted along the same line. Since gravity provides an understanding of density contrasts present in the subsurface, these density contrasts can provide a deeper understanding of subsurface geometry and assist in interpretation of other methods' processed data.
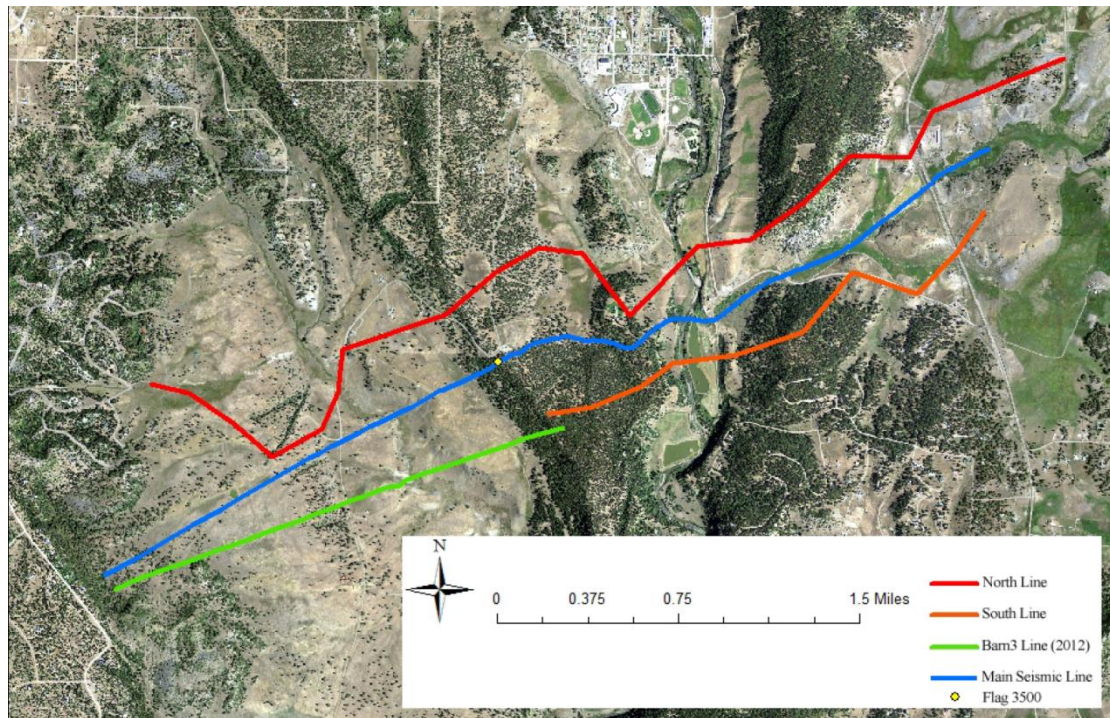
Figure 7.5: Gravity survey lines in Pagosa Springs.

7.2.2 North and South Lines

Gravity data was collected to both the north and south of the main seismic line in order to better understand the main seismic line geologic profile. The North Survey line was run roughly parallel to the main survey line with geographic deviations. The South Survey line was planned in an effort to tie-in this year's data with the data collected in last year's Barn3 survey line.

7.2.3 Shahan's Ranch

Another gravity survey location was Shahan's Ranch, located south of Pagosa Springs near the Colorado - New Mexico border. Shahan's Ranch was chosen as the primary student site for the 2013 Field Camp due to the presence of a flowing hot-water well and an active geothermal system. The gravity surveys at this location were designed to image the geology of the area near the flowing well and to find potential leaks in the drainage and irrigation system. The gravity survey was completed along the main DC resistivity line.

7.3 Survey Design

The main portion of the gravity survey was conducted on the main seismic line. Since the main seismic line runs over areas of interesting geology and several probable faults, it is

advantageous to use as many different geophysical methods over this line as possible in order to get an accurate picture of the subsurface. A linear survey was used because it is not very time-consuming and provides good spatial coverage of the area. The density of measurements along the survey line were decided based on geological features of interest in the area and how much time there was available for the survey. Generally, gravity measurements were taken with a spacing of 20 or 40 meters with 3 readings at each survey location. Station spacing increased during the final days of the survey in order to finish the line in a reasonable amount of time.

The North and South lines were designed by the students to run parallel with the main seismic line.. These lines were intended to provide an enhanced data set in interesting areas and to provide opportunities for identifying 3D trends in the data. The South Line was also designed to tie-in with the Barn3 Line, which was conducted during the 2012 Mines Geophysics Field Camp.

The gravity survey line at Shahan's Ranch followed the main DC resistivity line. Gravity measurements were taken at every 10 meters for the first several stations, then at every 20 meters for the rest of the line. Station spacing for this line was shifted to 20 meters in order to finish the line during the course of one day. As with gravity measurements conducted on the main seismic line, the gravity survey at Shahan's was designed with hopes of imaging any interesting geological structures in this area and correlating data between various methods.

7.4 Processing

7.4.1 Pre-processing

Before any corrections or processing measures were made on the data, the measurements at each station were examined for accuracy and precision by comparing the measurements with each other; for example, if one of the measurements taken at a station was not consistent with other readings, the non-plausible reading was marked as an outlier and removed from the data set. After the measurements at each station were checked, the measurements, as well as the standard deviation and time of the readings, were averaged and exported to a new file for processing. After this, several corrections were applied in an effort to correct for naturally-occurring variations in the Earth's gravitational field and reduce the data to corresponding geologic information. The process of removing the effects of the Earth's gravitational field from the data is known as data reduction.

7.4.2 Tidal/instrument drift correction

In order to reduce the data, the first correction applied was the tidal/instrument drift correction. The tidal/instrument drift correction removes the effects of the sun and moon's own gravity fields from the data and account for the presence of instrument drift. In order to correct for instrument drift, readings are taken at a designated base station at the beginning of each day of surveying, every 2-3 hours during the course of the survey day, and at the end of the day [53]. For the survey on the main seismic line, the gravity base station for the entire multi-day survey was located at Seismic flag 3500. Because drift occurs in a semi-linear fashion over a several hours, it is assumed that the drift occurring between different base station readings can be plotted, linearized, and subsequently removed from the data. The equation used to correct the data for tidal/instrument drift is presented in Equation 7.2. In this equation, g_b is the observed reading at the first base station of the loop, g_e is the observed reading at the last base station of the loop, and g_1 is the observed reading at the very first gravity base station. All observed gravity readings area in mGal. In addition, t is the time of a measurement between base stations, t_b is time of the reading at beginning of the loop, and t_e is the time of the reading at the end of the loop, with all times in decimal time.

$$\Delta g_d = g_b + (t - t_b) \frac{g_e - g_b}{t_e - t_b} - g_1$$

Equation 7.2: Tidal/instrument drift equation [53].

7.4.3 Latitude correction

After the tidal/instrument drift correction is completed, the data is corrected for latitude. Gravity varies with latitude due to the influence of the reference spheroid. If the Earth was a perfect sphere, no gravity corrections for latitude would be necessary [53]. However, the Earth has an elliptical shape and rotation orbit with complexities arising from topography and underlying geology [54]. The latitude correction is calculated using Equation 7.3, where φ is the latitude of the station in degrees.

$$\Delta g_L = 0.812 \sin(2\varphi)$$

Equation 7.3: Latitude equation [53].

7.4.4 Free-air correction

The free-air correction is then applied. The free-air correction is needed because the measured gravity value is a function of the distance from the measurement point to the center

of the Earth [55]. Because of this, variations in elevation can result in the creation of a false anomaly in the data. The free-air correction helps remove the effect of the vertical gravity gradient associated with a change in elevation. If gravity readings are taken on a hill or incline, the movement of the gravity meter up and down the hill or along the incline will result in a variable elevation along the survey line. The free-air correction is calculated using Equation 7.4, where h is the elevation of the station in meters.

$$\Delta g_{FA} = 0.3086 \, h$$

Equation 7.4: Free-air equation [53].

7.4.5 Simple Bouguer correction

After both tidal/instrument drift and free-air corrections were applied to the raw data, a simple Bouguer correction was applied. The simple Bouguer correction accounts for the mass that exists between an observational point and a reference level below it. The mass in between can increase the gravitational field on the observation point relative to a point on the reference level. Likewise, a lack of mass between observation and reference can decrease the observed gravity measurement. Thus, the excess gravitational acceleration due to the excess mass must be subtracted. The Bouguer correction requires the knowledge of the density of the excess mass between the observational point and the reference level. One way to improve the Bouguer correction is to know the topography, thereby accounting for the gravity due to the mass at each point [47]. The Simple Bouguer correction is performed using Equation 7.5 where h is the elevation of the station in meters.

$$\Delta g_S = 0.1119 \, h$$

Equation 7.5: Simple Bouguer equation [53].

7.4.6 Terrain correction

The last correction that needed to be applied to the data was the terrain correction. Unlike the simple Bouguer correction, the terrain correction follows the irregular shape of the topography, and is always positive. This is because if the measurement of the gravity field is being done on a hill, the excess mass of the hill will pull on the small mass attached to the spring inside the gravity meter, thus reducing the actual gravity reading. On the other hand, if the measurement of the gravity field is being done in a valley, then the absence of mass in the

valley will not affect the small mass attached to the spring inside the gravity meter. The terrain equation is too complex to carry out with an equation, so this reduction must be calculated with a code accounting for the survey terrain [47].

7.5 Uncertainties/Errors

7.5.1 Instrument errors

Gravity meters have some inherent instrument errors. Due to its design, the L&R has a precision of 0.1 μGal, a resolution of 1 μGal, a present minimum error budget of less than +/- 1 μGal, a random error of +/- 1 μGal, and a systematic error of less than 0.1 μGal [56]. The CG-5 has a resolution of 1 μGal, a standard deviation of less than 5 μGal, and a residual long-term drift of less than 0.02 mGal per day [57]. Both the CG-5 and L&R are very sensitive to spatial orientation, making it necessary to accurately level the instruments in order to ensure a correct reading of the gravity field. Because of this, it is sometimes necessary to use creative leveling techniques while taking gravity measurements on slopes or on soft ground. If the instrument is improperly leveled, it may produce anomalous measurements that must be removed later.

7.5.2 Operating errors

Another common error that happens in the field is failure of the operator or recorder to take good notes about the survey parameters and/or record the measurements taken at each survey location. The recorder should write down the measurements taken at each station, the standard deviations of each measurement, and the time at which each measurement was taken. Neglecting to do so may cause issues in processing. A written copy of the data can also be useful in the event of instrument malfunction or failure.

7.5.3 Other sources of error

Some errors are introduced into the gravity data without the influence of the instrument operator. One of these errors is incorrect GPS and elevation measurements. Since several of the corrections used in the data reduction process require very accurate latitudes and elevation data, any errors in this data are amplified in the reduced gravity data. Another thing to consider that can cause major noise and uncertainty in the gravity readings is taking measurements near large objects such as large boulders and trees. Since these objects have a large mass, a pseudo-anomaly may remain in the reduced gravity data set [53]. Also, if

surveys such as deep seismic are being conducted at the same time in the same location, some interference may occur due to the presence of large Vibroseis trucks moving along the line.

7.5.4 Assumptions

During the process of data reduction and processing, several assumptions are made. Many of the assumptions used are implicit, meaning that they include underlying arguments made in the development of the argument. These assumptions include the presence of a constant linear drift occurring between the base station loops, a constant free-air gradient, very accurate position and elevation data for all stations, and a constant Bouguer slab. Also, it is assumed that the gravity survey is conducted assuming that atmospheric mass does not have an effect on the observed gravity value and that the density value used in the inversion process is a plausible value. During the inversion process, it is also assumed that the Earth can be described across the profile in 2D with homogenous layers. Explicitly, each Earth layer was assumed to have a constant density.

7.6 Interpretations

The geological analysis of the area shows that there are several rock layers that may be detected through geophysical methods. The Mancos shale and the Dakota sandstone layers are interesting because hot water may travel across the Mancos shale/Dakota sandstone interface and up through the Dakota via faults. Thus, the analysis of the gravity data should reinforce the previously predicted geologic model, in description of where different structures and faults are located in the Dakota sandstone.

The type of rocks in the subsurface affects the gravity field of the Earth. Rocks tend to have different properties due to the process that formed them. As a result, different rocks will either be porous (less dense) in the case of most sandstones, or non-porous (very dense) in the case of most igneous rocks. A table of the expected density values from the rock layers in this area is seen in Table 7.1. By measuring the differences in the Earth's gravity field, it becomes possible to determine the type of rocks that are beneath the subsurface.

Table 7.1: Density values (g/cc).

	Density	Porosity	Shaliness
Mancos Shale	2.55	0%	100%
Dakota Sandstone	2.61	2%	40%
Morrison	2.52	3%	60%
Wanakah	2.63	1%	51%
Entrada	2.5	2%	55%
Basement	2.8	0%	0%

No geophysical method is perfect on its own. This is why results obtained from the several different surveying methods are used in conjunction to complement each other's shortcomings. For example, gravity can be used to detect different structures in the subsurface to confirm what a seismic cross-section shows.

The main seismic line inversion created model depended on the results of several other methods, such as seismic profiles, magnetic data, and geological cross-sections. This is because the gravity results are supposed to support the interpretations of the other methods. Contradiction in results between the different methods can be attributed to several factors, such as having bad data to begin with or having the wrong interpretation of the data.

The corrected gravity data was imported into the Oasis Montaj software to perform the terrain correction, and then was exported into GM SYS software in order to produce the inverted model. This model is used to fit the predicted data to the observed data, thus producing a forward model of the subsurface that corresponds to the observed gravity data.

7.6.1 Main Seismic Line

The observed gravity data are represented as black dots in Figure 7.6 below. Local maxima in the data indicate that there is an area of higher density at that specific location compared to locations around it. Conversely, local minima show the opposite effect. Therefore, the gravity response above the locations where the faults are expected to be should show a min/max response. This can be seen in Figure 7.6 around the middle section, where there are several local maxima, which indicates that the density is changing at that location relative to nearby locations. Thus, it is safe to assume that there are two faults seen in the data. Another fault is possible to the right of the two main faults, but this cannot be confirmed by the gravity data. This is based on the gravity response shape starting at the middle of the figure and continuing to the right side.
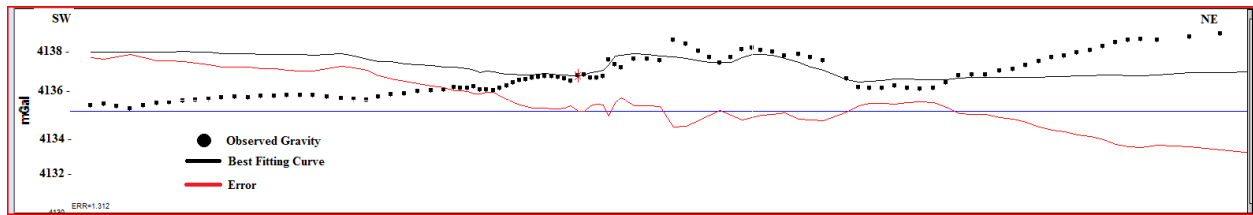
Figure 7.6: Main seismic line observed gravity profile.
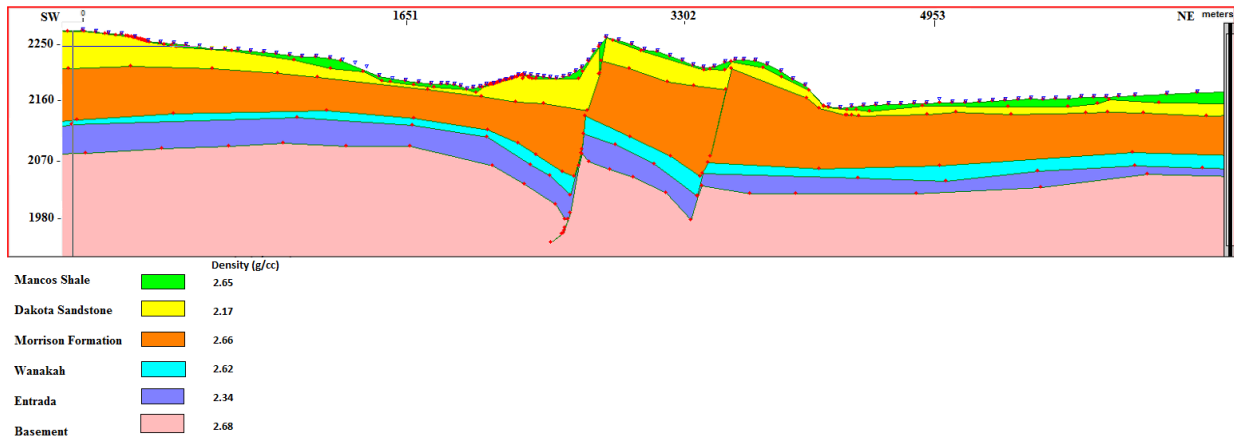
Figure 7.7: Main seismic line fitted cross section.

When making the proposed geologic cross section, the seismic depth section and the magnetics data were used to drive the geologic data fitting. Figure 7.7 shows the result of fitting the gravity data to the observed data. The black line in Figure 7.6 shows the gravitational response of Figure 7.7 with the red line being the error and the black dots being the observed points. Given the poor quality of the mid-section of the GPS data (causing corrections to be inaccurate in that area), the geologic model produces a clean and precise representation of the underlying geology. This geologic model, seen in Figure 7.7, shows two of the main faults proposed by the geologic cross section. The third fault proposed in the geologic cross section was not adequately supported in the data.

In the Eastern most part of Mill Creek, the proposed model creates a much lower response than the observed data. This could be due to unknown a high-density body in the subsurface such as a dike or a sill. Based on the electromagnetics data and the seismic depth section in the Mill Creek region, this interpretation is plausible but still highly suspect. In the West, thicker less dense layers could explain the lack of a gravity response. Based on the gravity response, the West and East sides of the section are unknown.

7.6.2 North Main Seismic Line

The observed gravity values are represented as black dots in Figure 7.8. Generally, these values indicate an increasing nonlinear trend stretching from the west side of the line to the east side. Within this general trend, there are several slight highs and lows in the observed data trend. When the gravity response values change from low to high, this change may indicate the presence of a structure or a fault in the subsurface. This is because a fault may move denser material closer to the surface. In Figure 7.8, there are three proposed faults, all in the middle section of the profile. The slight increasing trend may indicate that a denser layer is dipping closer to the surface, but this is unlikely to happen geologically. Since the data is sparse and has low resolution, it is hard to make a conclusive interpretation. Thus, it is necessary to see what the results of the other methods are saying about the subsurface on the North main seismic line.
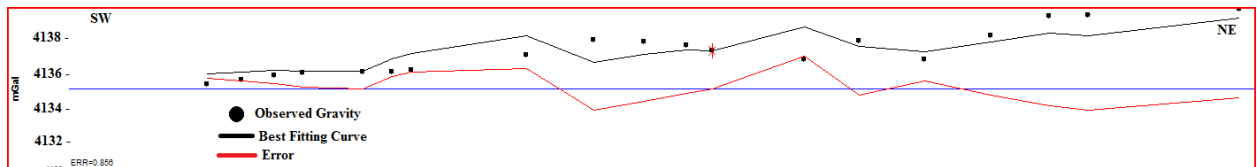
Figure 7.8: North main seismic line observed gravity profile.
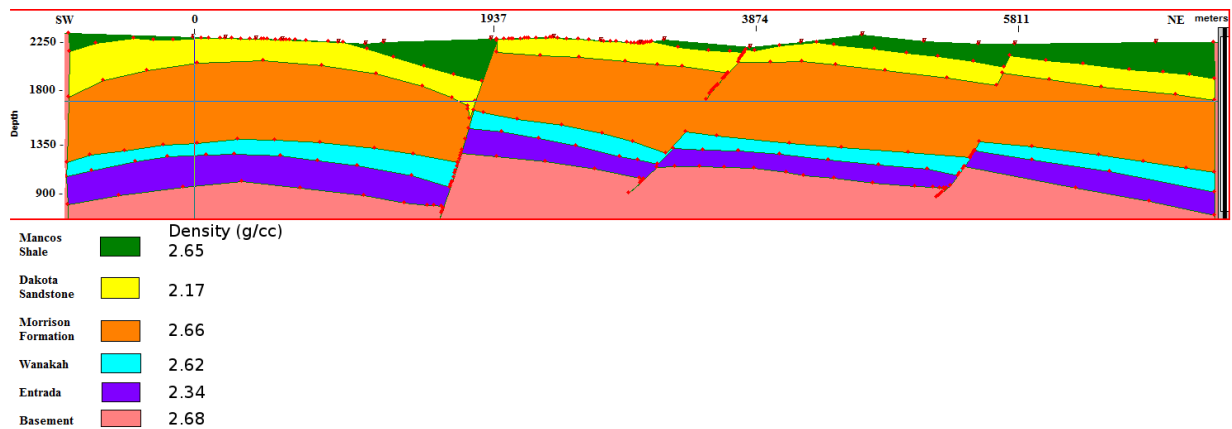
Figure 7.9: North main seismic line fitted cross section.

The North main seismic line runs roughly parallel with the normal main seismic line so using the main line's fitted cross section as a starting point is reasonable. From this starting point, the fitted cross section in Figure 7.9 was composed. This cross-section suggests that the same faults seen on the main seismic line are also present at the same locations on the North main seismic line; however, the data suggests the presence of a third fault in the east. This observation is somewhat predictable, seeing that the North main seismic line runs parallel and relatively close to the main seismic line, further suggesting that there is a continuous geologic

system between the two seismic lines. The eastern-most fault is not detectable in any but the north main seismic line section.

7.6.3 South Main seismic line

Along the South main seismic line, the observed gravity values are represented by the black dots in Figure 7.10. The general trend of this data is linearly increasing to the east. Due to the linear nature of the data, it is difficult to interpret this section. About halfway through the data there is a jump in the gravity values. This is most likely due to a fault in the area up throwing a more dense body closer to the surface. The linear trend suggests that there is dense material near (or at) the surface in the east of the line while in the west the denser material is deeper in the subsurface. The linear upward trend could suggest a dense layer such as the Dakota dipping to the west, but based on geology this is not possible. The model for the South main seismic line, seen in Figure 7.11, shows the faults seen on the main seismic line at the same locations. This interpretation supports what the gravity data on the main seismic line shows. As mentioned before, the fact that the faults are found at approximately the same locations on both the South main seismic line and the main seismic line can be a strong indicator to a continuous geological system.
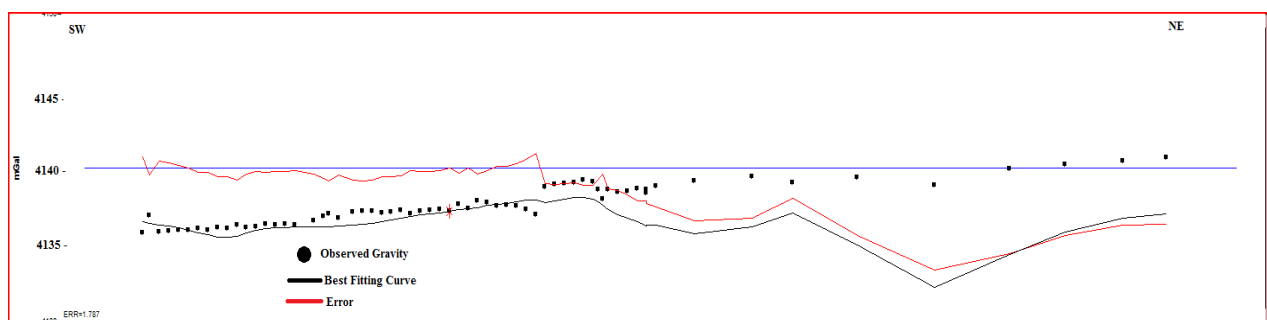
Figure 7.10: South main seismic line observed gravity profile.

	Density (g/cc)
Mancos Shale	2.65
Dakota Sandstone	2.17
Morrison Formation	2.66
Wanakah	2.62
Entrada	2.34
Basement	2.68
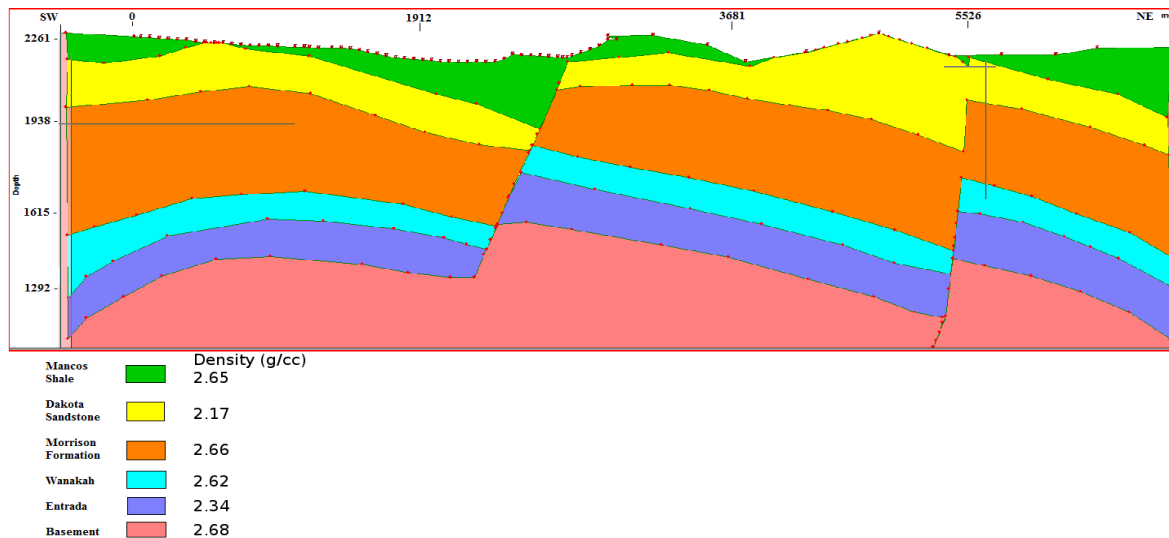
Figure 7.11: South main seismic line fitted cross section.

7.6.4 Inter-method Seismic line

By comparing the observed gravity values with both the magnetics data and the seismic cross-section of the Main Seismic Line, a better, much more detailed fitted cross-section can be created. This is because the manual fitted section can use the depth generated from the seismic section and the magnetics data as a check to the model and confirm its accuracy, thus allowing a simple visual approximation of the thickness of the layers. The collected magnetic data over the survey line will usually show a spike in the regions where structures such as dikes and faults are expected to be. This is due to the sudden changes in magnetic susceptibility. Therefore, it can be a good way to check the feasibility of the observed gravity model. If another parameter such as density can be determined from other methods, this parameter can be used to guide the fitting process.

The observed gravity data does indicate the presence of several faults that are consistent with the Main Seismic Line profile. In the previous three fittings, the seismic depth section was used to gauge the thickness of the layers. As mentioned above, the magnetics data was used as an extra check to the quality of the model.

Electromagnetic surveys were conducted in Mill Creek, a small area along the east-central portion of the Main Seismic Line. In this area, the EM surveys indicated the presence of a thin layer of Mancos shale overlaying about 60 meters of Dakota sandstone. These two layers overlay a very thick layer of Morrison formation. In this area, the layers had virtually no dip, meaning that they were relatively flat lying. These results in this small section of the line

concur with the gravity response in this area, as the observed gravity data does not indicate the presence of any faults in this immediate area.

According to the DC resistivity survey conducted along the Main Seismic Line, the south-west portion of the line overlays an anticlinal structure that intersects a fault. Both the presence of an anticlinal surface and a fault along the west side of the Main Seismic Line are supported by the observed gravity values. DC resistivity also suggested the presence of two other faults along the Main Seismic Line. This interpretation of the DC resistivity data is consistent with the geological cross-section and is supported by what the observed gravity data shows.

The observed gravity data from the North and South Seismic Lines are consistent with what the observed gravity data from the Main Seismic Line show. Assuming that the North and South Seismic Lines are reasonably close to the Main Seismic Line and span roughly the same area, it is very possible that the faults seen in the Main Seismic Line observed gravity data are the same faults in the same area. This would indicate a continuous geological system.

7.6.5 Shahan's Ranch

In a heuristic model, the Shahan's data (Figure 7.12) is useless. This is because there should not be large jumps in the data and it should have general trends that are discernible from the rest of the model. There may be an overarching increasing linear trend suggesting a slight dip to the West of the layers. However, based on the geology of the region, this is not possible because the beds are dipping to the East.
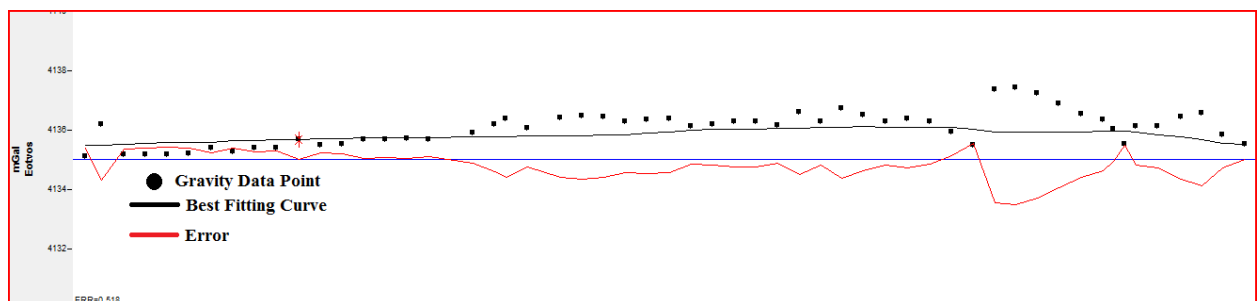
Figure 7.12: Shahan's Ranch observed gravity profile.

Combining the gravity data with the other methods, we can gain a better understanding of the underlying geology of the region. Based on the interpretation generated by Hammer Seismic the layers at Shahan's Ranch are relatively flat and are dipping less than 10 degrees to the

east. The DC Resistivity interpretation for the area suggests that a thick layer (at least 100 ft) of Mancos Shale underlies the Shahan's Ranch area. To the east of the DC resistivity line, flowing water is present, which may cause a gravity low in this area. The geologic cross section of the area shows that the survey line is near the fold axis of anticline on the east dipping side.
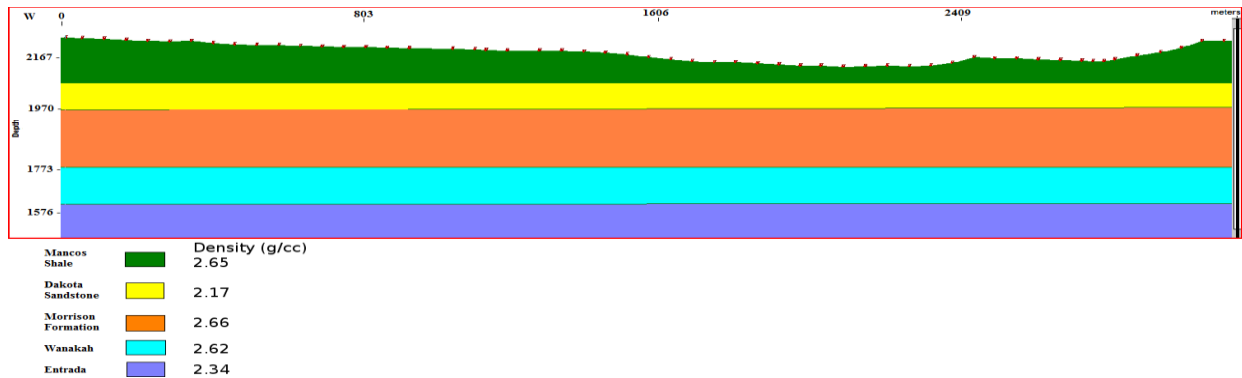
Figure 7.13: Shahan's Ranch fitted cross section.

Tying Hammer Seismic, DC Resistivity and local geology together, the geologic cross section of Shahan's Ranch, seen in Figure 7.13, is constructed. While the layers in the generated cross section are flat, the subtle dip of the layers would not be readily apparent on the observed gravity data. The gravitational response of this cross section shows that it is far from a perfect fit of the data. However, the data collected along the Shahan's Ranch Line is full of noise and contains survey errors that could not be corrected for accurately and the response from the model is what is expected of the geology of the area.

7.7 Conclusions and discussions

Even though gravity on its own can be an effective method when looking for general structures in the subsurface such as faults, it becomes much more effective when combined with other geophysical methods to form a very detailed interpretation of the subsurface. In this year's field camp, gravity surveys were used on four main locations, the Main Seismic Line, the North Main Seismic Line, the South Main Seismic Line, and finally the Shahan's Ranch, which was this year's student survey site. The main purpose of doing gravity surveys on these locations was to support what other active methods such as seismic show.

The observed gravity data obtained from the gravity survey done over the Main Seismic Line supported what the seismic, DC resistivity, and magnetics data represent. The seismic cross-section of the Main Seismic Line shows that there are at least two faults with relatively equal

spacing between them. These faults extend from the Precambrian basement to the surface. These faults can provide an excellent path along which water can travel.

The gravity survey done across the North Main Seismic Line is very interesting because the line runs parallel to the Main Seismic Line and covers roughly the same area. Therefore, it is safe to assume that the geological features and subsurface structures that were observed at the Main Seismic Line will continue to the North Main Seismic Line. As mentioned before, structures that appear in multiple parallel survey lines indicate continuous subsurface structures.

The South Main Seismic Line also runs parallel to the Main Seismic Line. The gravity data obtained at the South Main Seismic Line shows subsurface continuity with both the Main Seismic Line and the North Main Seismic Line. This is particularly good because it confirms the existence of the same subsurface structures and geological systems proposed in this area.

The interpretation made using the observed gravity data from this year's student site, Shahan's Ranch, was not particularly helpful in understanding the area. Several problems rendered this data unclear. The most important factor was that the survey was inadequately documented, adding unnecessary noise to the data. The relatively flat layers at Shahan's Ranch proposed in the geologic cross section were confirmed by the gravity data.

Given the results for all of the above-mentioned surveys, it was discovered that the digital elevation model used for the terrain correction was offset by an unknown amount from the true coordinates. This means that the terrain correction added anomalous data instead of taking away the terrain values. This accounts for some of the error in the model. However, all the points are offset from the correct terrain by a similar amount so it should not create a drastic difference.

8. Magnetics

8.1 Introduction

Magnetic surveys are capable of detecting differences in magnetic susceptibility within targets through changes in the Earth's primary magnetic field. General levels of magnetic susceptibility are known for certain rock types and this knowledge was used in conjunction with a magnetic survey to determine the depth of different rock types, the thickness of layers with different susceptibilities, and sharp contrasts between different rock types. Magnetic data is shallow because the strength of the magnetic response from an anomalous source falls off with an exponential (r^3) relation to distance. The goal of the Magnetics survey was to qualify the igneous intrusion in the form of the hairpin dike and to try to find any obvious intrusions under the seismic line. Knowledge of igneous intrusions in the area could help with qualifying the geothermal source of the hot springs as well as the local geology. Additionally other studies have found magnetic surveys to be somewhat useful in characterizing geothermal systems [60].

8.2 Magnetic Surveying Sites

The magnetics method was used at two sites. The first and smaller of these sites was near an exposure of an igneous dike within the Mancos shale located at a hairpin turn south of Pagosa Springs. The survey was completed around the dike in areas where the dike was not exposed. The surveys were all on top of the Mancos Shale. The reason the magnetic survey focused on the dike was that it was one of the few geologic features in the area that would have a high magnetic susceptibility. While there are igneous cobbles in the area the Pagosa Springs basin is a depositional sedimentary basin which means that there are few igneous/mineral feature. See Appendix D and Figure D.1for a full description on the theory behind magnetic surveying and why it works best with igneous rocks.

The second survey was completed along the main seismic line running from west to east. This was to aid in interpretation when the magnetic data would be combined with several other surveys taken on the same line. In this survey, magnetics would be used to help interpret the layers of rock within the subsurface as well as faults that may affect the water flow within the geothermal system under Pagosa Springs.

8.3 Survey Design

8.3.1 Hairpin Dike Survey

These surveys were conducted across two days. On the first day both a proton precession magnetometer G-856 AX and a cesium magnetometer G-858 MagMapper (Figure D 3 & Figure D 4)

were used on the same line. This line was perpendicular to the dike and approximately twenty meters north of the dike's exposure. The survey was 200 meters long with one meter spacing (Line 1 in Figure 8.1). By placing the exploratory survey line perpendicular to the known direction of the dike, the survey was more likely to determine the existence and location of the dike. This would allow for confirmation that the dike did exist beyond its exposure which would then focus the surveys conducted the next day on the probable extent of the dike.

Figure 8.1: Map of surveys performed around Hairpin Dike.

The second day of magnetic surveying near the dike at the hairpin turn included four survey lines. All four lines roughly paralleled the survey completed on the previous day. The first of these surveys was located approximately twenty meters to the north of the line from the previous day; along a DC survey line acquired on the first day of data acquisition. This survey line was 200 meters in length (Line A in Figure 8.1). The second survey was located 75 meters to the south and was 70 meters in length. This survey was on the down slope side of the exposure of the dike (Line 2). After this a third survey was located further to the south and was 200 meters in length (Line 3). A fourth and final survey was completed even further south of the third line (Line 4). This survey was approximately 100 meters in length and crossed over the Dakota Sandstone Quarry.

8.3.2 Main Seismic Line Survey
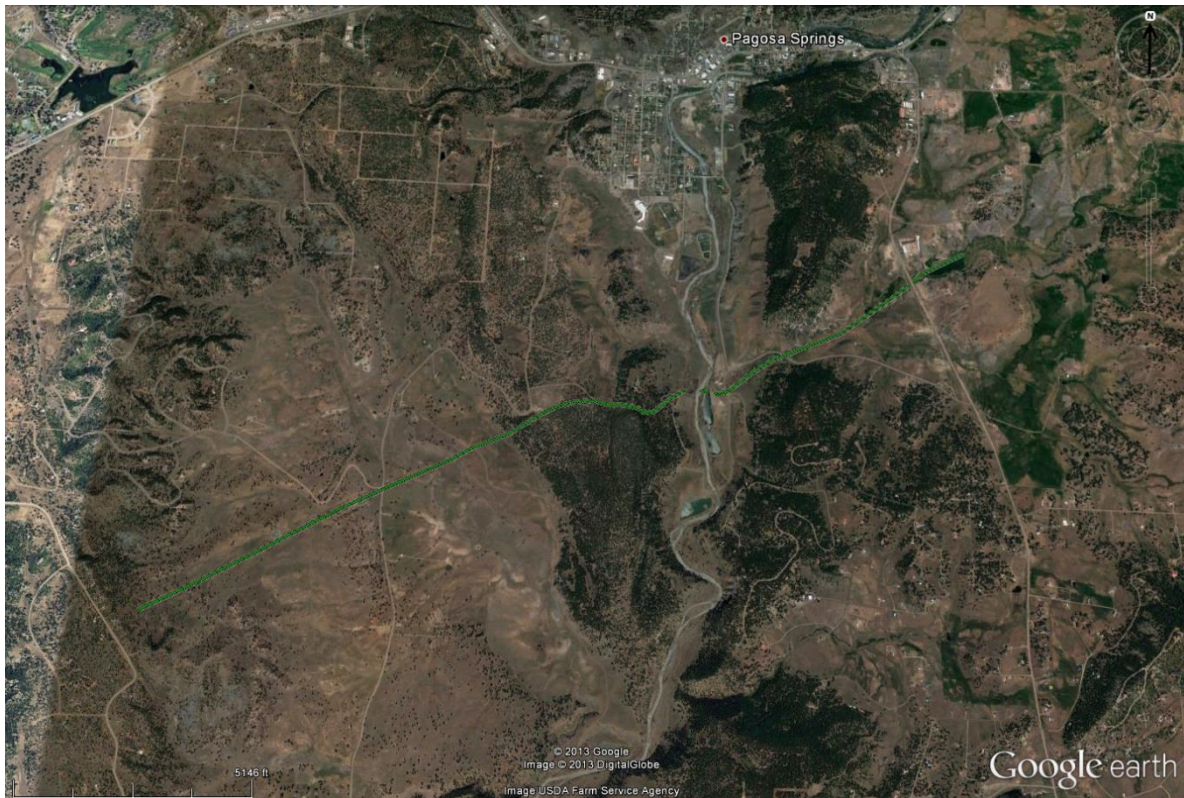
Figure 8.2: Map of Seismic Line over Pagosa Springs.

The survey along the main seismic line (Figure 8.2) had measurements taken at every seismic geophone takeout flag. These geophone take out flags were spaced 10 meters apart. The line was almost seven kilometers long. The line traveled west to east with a kink occurring at a point one third the total distance of the line. The main seismic line's purpose was to locate a pair of faults within the area and magnetics served as a complimentary method to the seismic exploration. As the seismic line was spread over a long distance the magnetic surveys were performed in segments over a period of three days.

8.4   Processing

The initial step of processing the data was processing the base station data. The data contained several large spikes unrelated to geologic anomalies. These spikes had to be removed using a range despike filter. Additionally the data was smoothed to provide a better recording of the change in the local magnetic field throughout the day without the shorter period variations. This despiking and smoothing was done within the MagMap2000 software by Geometrics.

After the base station data had been processed, it was then used in order to correct the magnetic surveys for diurnal variations within the local magnetic field. MagMap2000 was again used to correlate the data from the base stations to the survey data from both magnetometers. This drift corrected data was then exported for further processing.

Once this data was exported from MapMap2000, it was opened in Excel where each of the measurements was correlated to a flag location and GPS location. At this time any field notes on possible outside sources such as power lines or large metal objects were input into the excel file for use during interpretation. Overlapping survey data was also combined such that it could later be aggregated as a single survey. Additionally these GPS locations from the surveys were plotted out in geospatial software so the locations of the surveys could be easily referenced.

The surveys conducted over the hairpin dike (Lines A, 1, 2, 3, 4 in Figure 8.1) were not able to be corrected for magnetic drift. This was due to human errors done in the course of the two days in which these lines were surveyed. However, as the surveys occurred over a relatively short time (approximately one hour per survey) magnetic drift is a minor concern. These datasets had the average field recorded by the base stations subtracted from them. This cancelled the magnetic field due to the Earth and brought the datasets to a common axis.

After the data was processed into excel files, two different filters were applied to decrease noise. The first filter applied was a truncated despike filter created in excel. The truncated despike filter was applied to the top sensor's magnetic measurements removing all points that varied more than one standard deviation from the previous measurement. It was also used to remove variations greater than two standard deviations in the bottom sensor's data set and removed variations greater than one half standard deviation in the vertical gradient. This truncated despike filter provided a significant reduction in noise.

The final filter applied was a Butterworth low pass filter. This filter was of order 5 and at a frequency of 0.5 Hertz. The Butterworth filter was applied using a function within Matlab. The Butterworth filter smoothed the data out to lower frequency, removing the high frequency variations that were estimated to be either general noise or small surface anomalies. The final result of the filter was determined to be a good balance between reducing noise and removing data that could possibly an indication of subsurface anomalies.

8.5 Uncertainties/Errors

A possible source of error was the misallocation of magnetic data to flag numbers along the main seismic line. While the majority of the magnetic data matched correctly to its corresponding flag, in some areas a high level of uncertainty exists on the location of some measurements. This may have caused an offset in the geographic correlation of measurements to the line. This offset may have shifted the readings resulting in an interpretation that is slightly off due to shifted locations. This was a significant issue when working with other methods that are spatially located to the same line as the final product should retain consistency across the methods' data.

Additionally several large spikes had to be removed from base station data. We are uncertain of the effects of solar storms, as there were reports of sun spot activity, but there were no known effects on the data [61]. It is possible that an animal or person could have walked up to the base station and disrupted the readings. As there was nobody standing at or monitoring the base station during the day it is uncertain if anything with a significant effect on the base station's readings came in close proximity to it during the day.

Another source of error in this study is the assumptions we've made in planning our survey. We are assuming that there should be distinctive magnetic signals between geologic layers. Furthermore, we are assuming that for coherent data solar storm activity and influence on the base station from unseen animals is negligible. When the hairpin dike data was corrected we assumed that subtracting the average magnetic field would be an accurate correction for the data since the surveying time was so short. We also assume that the acquisition crew knows how to perform correct data acquisition procedures. When we despiked the data we were assuming that the spikes were not caused by geologic magnetics.

8.6 Interpretations

8.6.1 Hairpin Dike Survey

The graphs for the hairpin dike surveys were as follows:
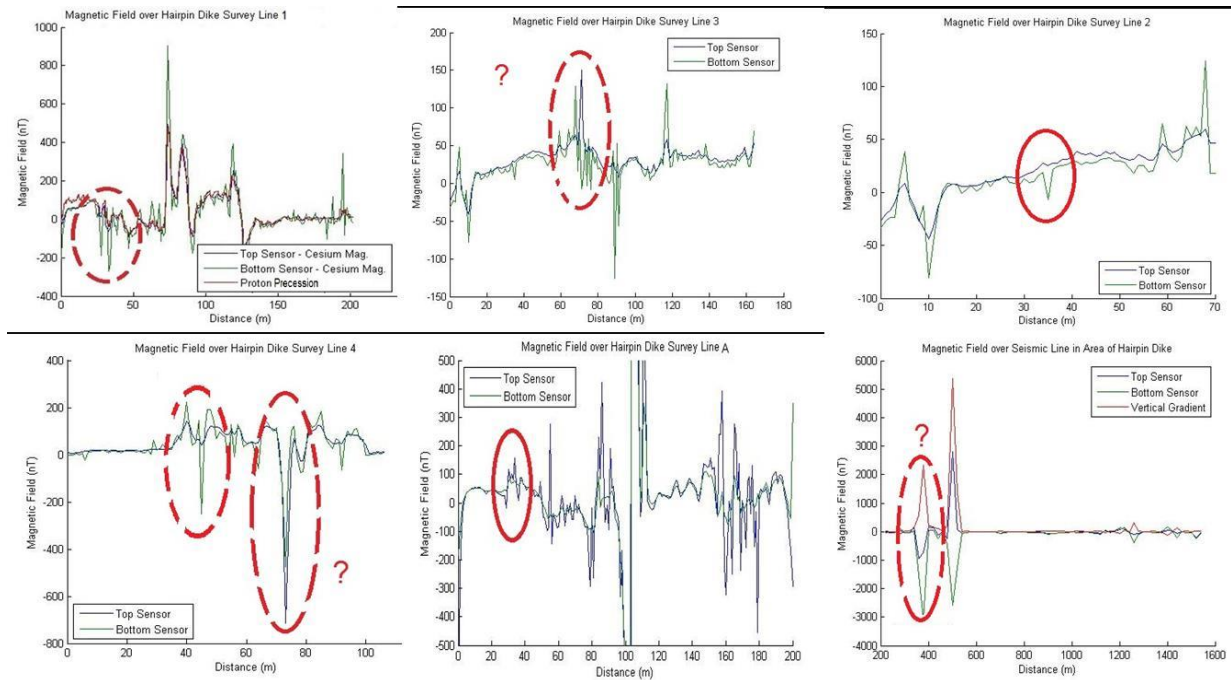
Figure 8.3: Graphs of Magnetic Field recorded over surveys in area of Hairpin Dike.

As seen in Figure 8.3 above, only two of the survey lines reliably show an anomaly that can be associated with a dike. The first survey line and the local seismic section show a negative dipolar anomaly that is typical of areas in the northern hemisphere. However, these anomalies are so large that is most likely due to the power line in the area rather than the dike. While there are data points in the other graphs that look anomalous, they are not definitive enough to be completely sure that they represent the dike. There is however enough anomalies that loosely fit the response expected from the dike to extract an interpretation of the anomaly. Using the surficial exposure of the dike and the possible anomalies we came up with the following map (Figure 8.4).

Figure 8.4: Map of Possible Dike Shape (red).

8.6.2 Main Survey Line

After filtering the data we recorded over the main seismic line we generated the following graphs:
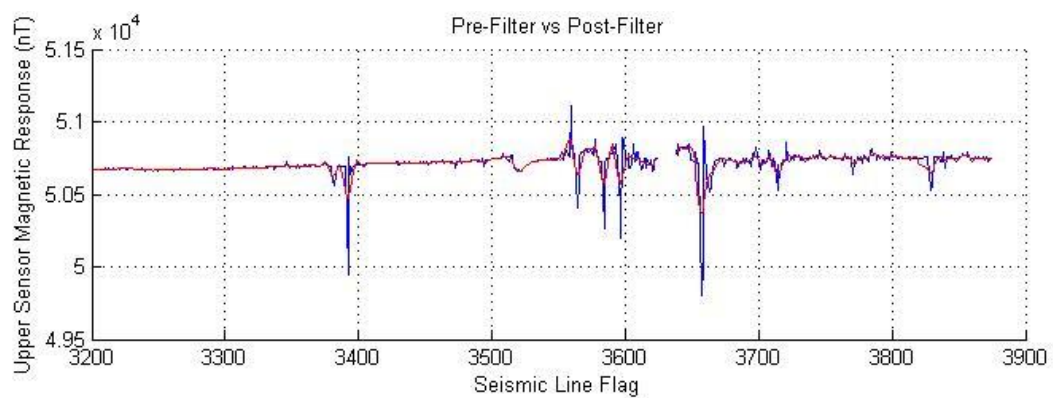
Figure 8.5: Pre vs. Post filtered (Butterworth and Despike) Data for the Top Sensor.
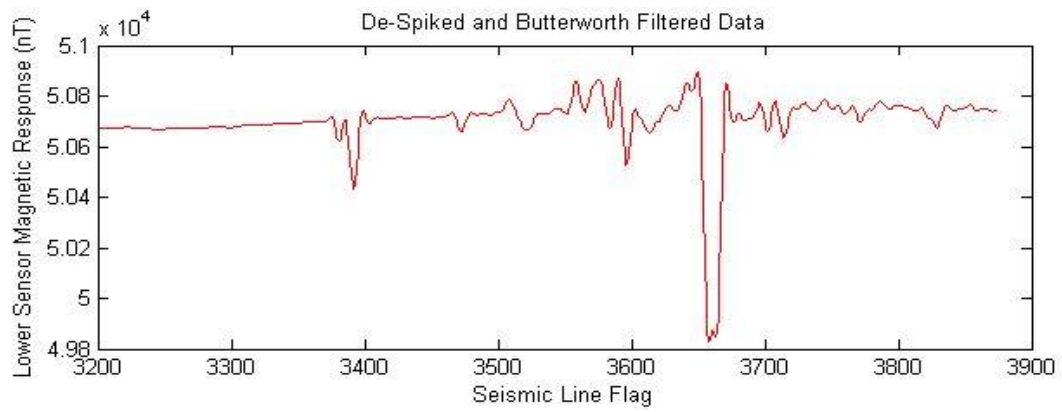
Figure 8.6: Filtered Data for the Bottom Sensor.
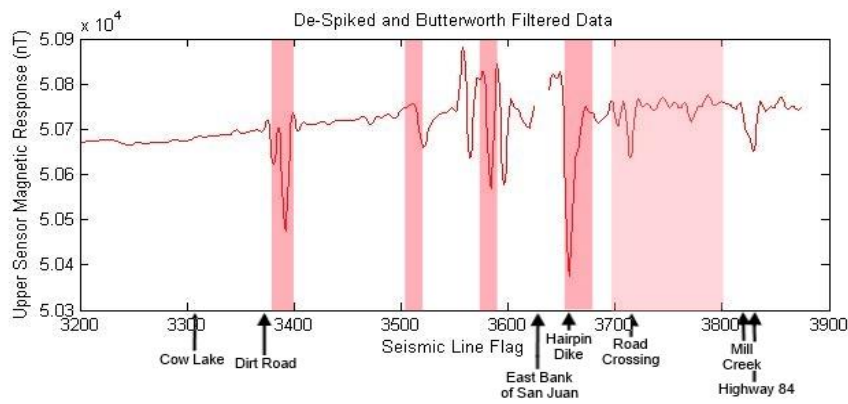
Figure 8.7: Filtered Data for the Top Sensor, areas with external noise noted in red. The light pink portion denotes minor noise characteristics.
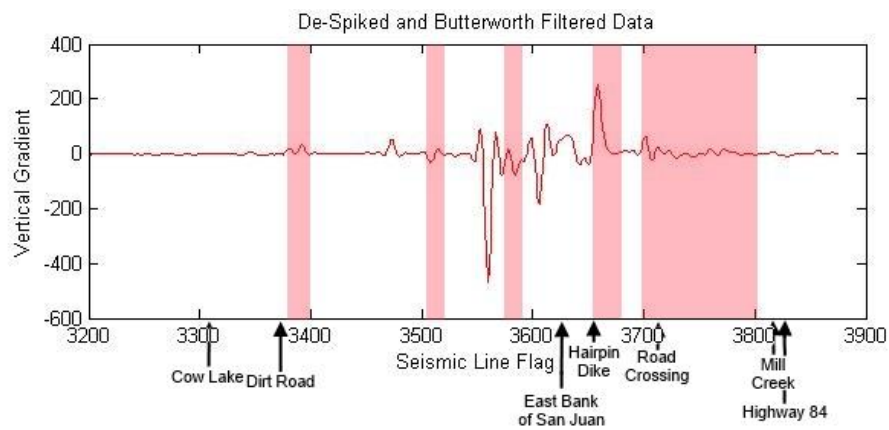
Figure 8.8: Filtered Data for the Vertical gradient, areas with external noise noted in red.

The red sections in Figure 8.7 and Figure 8.8 indicate areas that could possibly be the result of noise from magnetic objects near the survey lines. Of note is the large anomaly that is seen on all the graphs around the 3650-3670 flag marks. This is in the area of the hairpin dike. We originally theorized that

110

this was due to the hairpin dike, but it could just as easily be attributed to a power line in the area that was not recorded by the ground crews.

When comparing this to the brute stack for the seismic data we found the following:
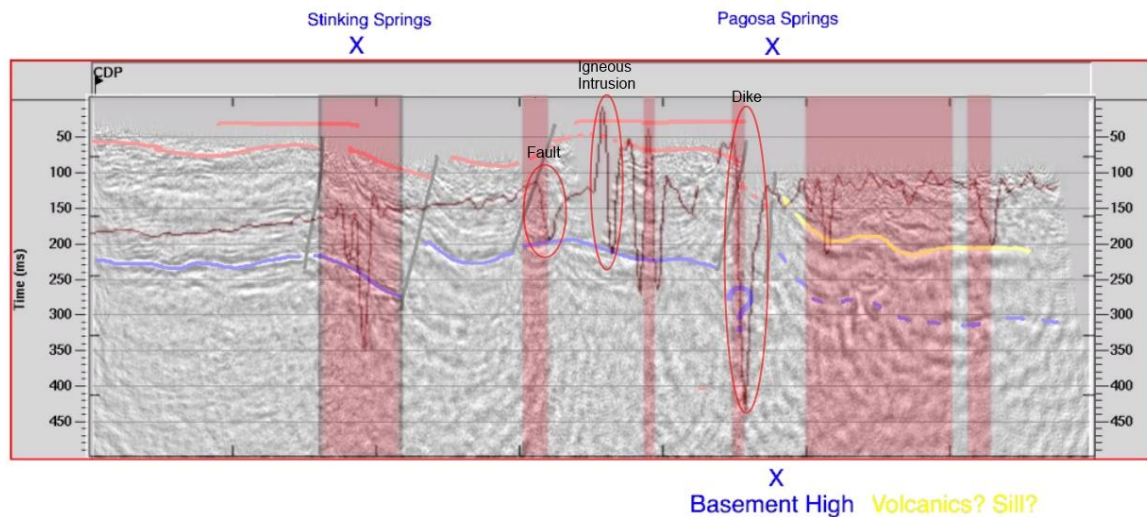
Figure 8.9: Top Sensor overlain Seismic Brute Stack.
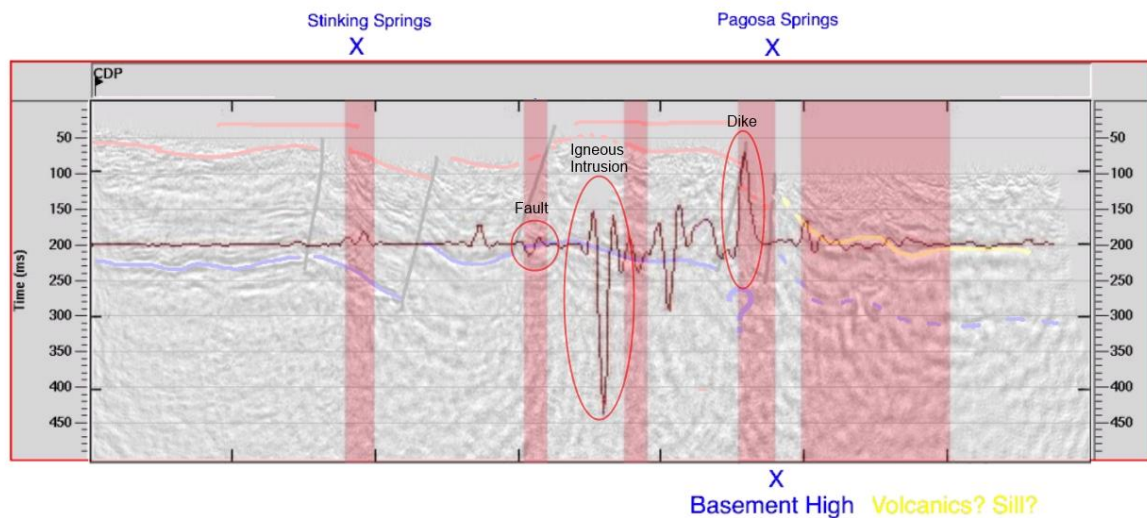
Figure 8.10: Gradient overlain Seismic Brute Stack.

For all the faults picked by the seismic team, we were unable to find a serious correlation between magnetics and any faulting in the area. Near flag 3,500 we were able to pick a dipolar anomaly over the area of one fault. This can be seen both in the gradient and the top sensor analysis. The problem is that this area is right over a segment of the seismic section that was noted for being around metal objects.

There is a strong anomaly located near flag 3,550. This anomaly is very high in magnitude and does not correspond to any sort of ground noise. When comparing this to the anomaly of the possible dike

picked up at around the 3,650 flag mark, we can conclude that this is similar to the anomaly of our theorized dike. However both anomalies are very high in magnitude, so it could be likely that they are magnetic noise from objects not picked up by the ground crew.
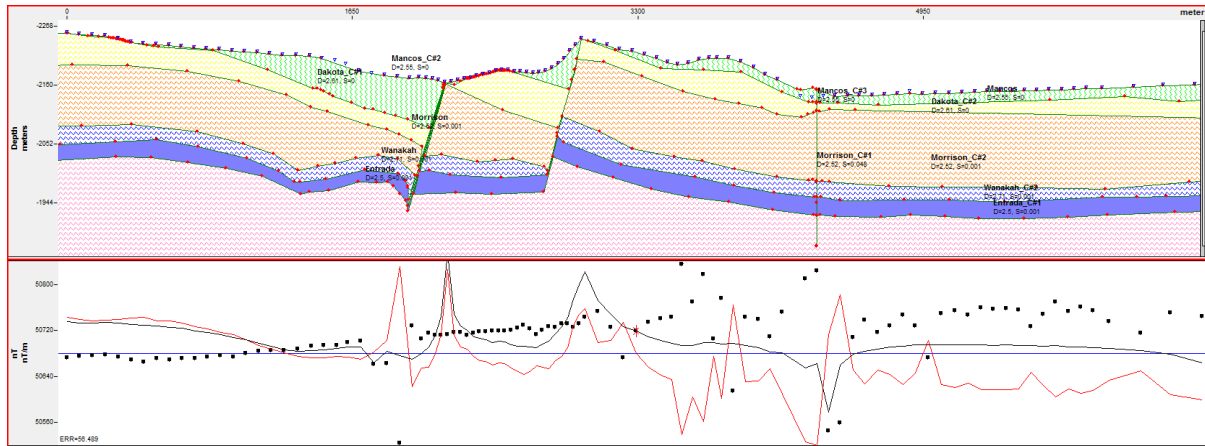
Figure 8.11: Model Fitted to Magnetic Mainline Data.

The model in Figure 8.11 showed that the magnetic anomalies expected from faulted bedrock did not show up in our survey. Furthermore most faults should have shown some sort of anomaly over them which was not what we saw in the data. While we were able to generate a dipole over the dike, it seems that none of the layers we saw had significant magnetic susceptibility including the bedrock.

8.7   Conclusions and discussions

We can conclude from the comparison of the seismic section and the magnetic line that there is no serious correlation between regional faulting and magnetic anomalies. This makes sense as both layers in the immediate subsurface are a shale and sandstone. As such their magnetic susceptibilities are very low.

The hairpin dike was not clearly picked up by the main line survey. The smaller surveys done in the immediate area were far less successful in picking out the igneous dike. The second survey line, despite being directly over the dike, did not pick up on it. However, the first survey line picked up on a large magnetic anomaly but it was theorized that this was because of a nearby power line. The data from the other sections shows only a few anomalies, none of them strong.

From the data it appears that dike does propagate under the surface, however it would be difficult to determine to what the extent and in what direction propagation follows. Figure 8.4 shows our best attempt at correlating these anomalies together to find the shape of the dike.

Furthermore, from the analysis of the brute stack we can state that there is a possible subsurface dike located somewhere around the 3,550 flag mark. This anomaly has the same magnitude as the

theorized dike and dipolar properties that are typical of magnetic anomalies. It remains to be seen if this is an anomaly from a dike as we are unable to conclude that the hairpin dike was picked up on in the first place.

The model we made based on the geologic cross section was not very illuminating. It seems to confirm that our environment did not have a measurable magnetic susceptibility contrast as we were unable to see many fault style anomalies in our data. It would be rash to describe the dipoles we saw as the result of faults but it is a definite possibility. We have concluded that the majority of measured magnetic spikes in the data are the result of noise.

9. Electromagnetics

9.1 Introduction

Electromagnetic (EM) geophysical methods measure subsurface deviations in electromagnetic conductivity by detecting subsurface currents. These currents may be induced with time-varying magnetic fields generated by coils on the Earth's surface.

Faraday discovered that a conductor, when positioned within a varying magnetic field, exhibits an induced voltage perpendicular to the direction of field charge. With this potential difference, a current will flow in any closed circuit contained within the flux. The equations governing this relationship are relatively simple, but geological conductors are invariably complex, and analyses of the currents generated within these, known as eddy currents, are greatly simplified within most geophysical models [65].

The magnitude of eddy currents are controlled by the conductivity and permittivity of the medium and governed by the relationships described as Maxwell's constitutive equations:

Table 9. 1: Maxwell's Equations of Electromagnetism in Differential Form

Name	Differential equations
Gauss's law	$\nabla \cdot \mathbf{E} = \dfrac{\rho}{\varepsilon_0}$
Gauss's law for magnetism	$\nabla \cdot \mathbf{B} = 0$
Maxwell–Faraday law of induction	$\nabla \times \mathbf{E} = -\dfrac{\partial \mathbf{B}}{\partial t}$
Ampère's circuital law (with Maxwell's correction)	$\nabla \times \mathbf{B} = \mu_0 \left(\mathbf{J} + \varepsilon_0 \dfrac{\partial \mathbf{E}}{\partial t} \right)$

Note that electric current density, J, the magnetic field, B, and electric field, E, are vector fields, where each generally have time-dependence and J = σe, where σ is conductivity. The permittivity of free space ε_0 and the permeability of free space μ_0 are universal constants.

Information on the electrical conductivity of the subsurface combined with knowledge of the physical properties of common minerals allow us to infer lithology and fluid properties by means of geophysical modeling without the need of invasive techniques. Electromagnetic geophysical methods are often used to identify ore bodies and aid the mapping of their size and structure in order to

determine economic viability. These techniques are also utilized in the mapping of lithology or fluid variations in the subsurface with contrasting conductivities [66].

EM systems monitor the effects on a known transmitted field caused by conductivity variations within the field, as shown in Figure 9.1. Broadly there exist two methods: time-domain electromagnetic (TDEM) whereby induction is caused by the abrupt termination of the transmitted field, and continuous wave electromagnetic (CWEM), also known as frequency-domain EM, which uses an alternating current to induce an eddy current in the earth. In some areas, high water content in the subsurface can produce conductivities too high for CWEM to be effective [65]. The conductive regions within the generated field will accommodate eddy currents and consequently alter the effective field by the generation of its own secondary field; this effect is monitored by a receiver system.
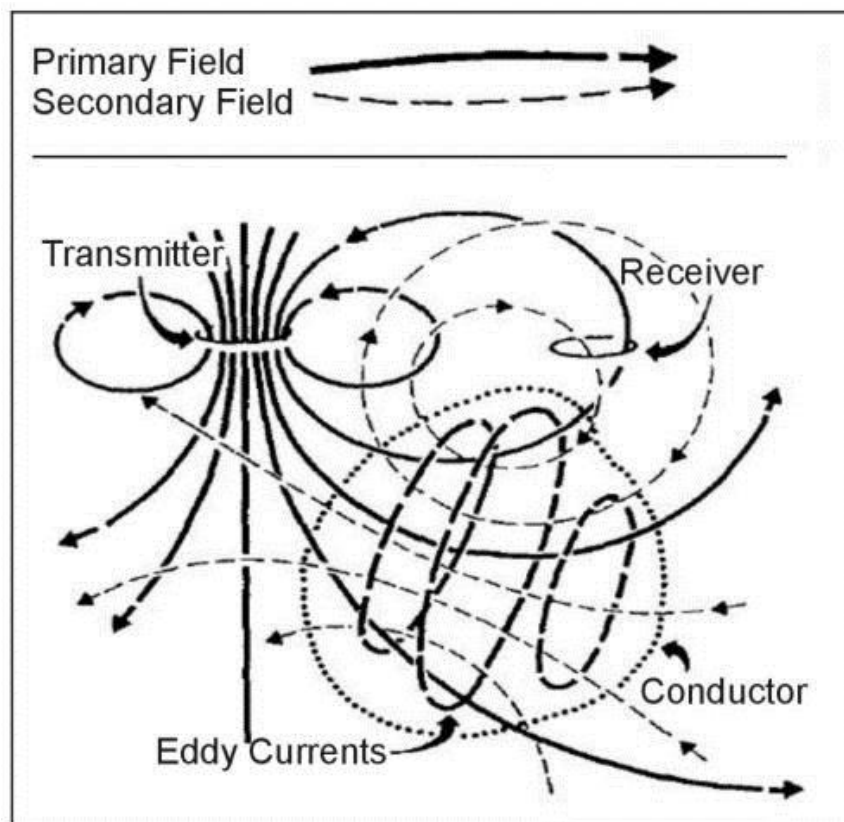
Figure 9.1: Electromagnetic induction schematic diagram. A transmitted electromagnetic field induces eddy currents in conductive material, which in turn disturbs the effective field detected at the receiver system [67].

Both the continuous wave and time-domain electromagnetic survey methods were utilized in the area surrounding Pagosa Springs, CO. Geonics Ltd. manufactured the equipment used during this field session; the models EM31and EM34 were used to acquire CWEM data, while EM47 and EM57 were used to acquire TDEM data.

9.2 EM Acquisition Sites:

Five primary sites were chosen for EM acquisition, each with their own targets, instrumentation, and depths of investigation:

Table 9. 2: Locations and description of the EM acquisition sites.

Location:	UTM Coordinates:	Description:	Technique:
Main Seismic Line	320138E 4123145N	Grassy open pasture with longhorn cattle grazing.	Deep sounding attempted with EM 57 (250m loop) in order to attempt calibration with seismic profile.
Hairpin Dike:	323121E 4124612N	Tight hairpin turn with a vertical igneous dike exposed on a steep slope of Mancos Shale, baked zone visible.	EM31 used in an attempt to image the subsurface geometry of the dike.
Shahan Ranch:	321404E 4124011N	Open flat valley with water channels, surrounded by steep slopes.	EM 31 used to attempt to image shallow subsurface flow pattern around well.
Mill Creek:	342194E 4096209N	Flat pasture (with Herefordshire cattle grazing) situated in the east of the main seismic line.	All instruments available were employed here as a means to establish a comparison between the techniques.
Pagosa Springs Geothermal Pipe network	321509E 4126274N	Downtown urban setting in the back alleys of Pagosa Springs.	EM 31 was employed here in an attempt to detect the location of the leak in the town's geothermal heating system.

9.3 Survey design

When choosing appropriate sites for EM acquisition, a number of factors must be considered. Primarily, a target must be identified, which may just be an exploratory sounding around a certain depth. Secondly, an appropriate instrument must be decided upon before choosing the geometry of the system, source-receiver separation, and time or frequency domain. Many of these parameters are

complimentary and interrelated, although they may be restricted by field logistics, available instrumentation, and signal to noise ratio.

One of the more vital steps is to estimate, from knowledge of the basic geology of the area, the range of depths to a target and a range of possible conductivities; this determines a choice of source-receiver separation. The skin depth sensitivity of an instrument is defined as the depth at which the current density falls to 1/e:

$$\delta = 503\sqrt{1/\sigma f}$$

Where skin depth, δ, is inversely proportional to conductivity, σ, and frequency, f.

TEM or CWEM data collection methods may also be combined in order to gather the most information possible on the various depths at which they specialize (detailed in Appendix E2.)

Table 9. 3: Locations of EM surveys and the instrumentation used.

Location	EM 31	EM 34	EM 47	EM57
Main Seismic Line				X
Hairpin Dike	X			
Shahan Ranch	X			
Mill Creek	X	X	X	X
Pagosa Geothermal Pipes	X			

The EM 31 instrument utilizes CWEM technology and is useful in detecting shallow targets. With this in mind, the EM 31 was applied for the leak detection survey of the geothermal pipes in downtown Pagosa Springs. Practically speaking, the instrument is easy to set up, repeatable and the most viable for difficult terrain. As a frequency domain method the results are generally superior in high coherent noise environments (such as an urban setting) and for shallow soundings.

The EM 34 instrument also operates in the frequency domain, sharing similar properties and advantages as the EM31, with the added advantage of source-receiver separation customization with the disadvantage of being less portable.

The EM 47 and EM 57 instruments utilize time-domain methods and must be static when measuring. These methods utilize a wire loop source and varying receiver position. The EM 57 offers deep sounding potential, with data sensitivity up to 500m depth.

The choice of instrument was determined mainly by the required investigation depth, which may or may not have been known prior to the survey. In such a case a combination of techniques were used to obtain and resolve data at a variety of depths.

9.4   Processing

Four electromagnetic datasets were collected in total from the EM31, EM34, PROTEM 47 and PROTEM 57. They can be categorized into two main types, which are Frequency-domain Electromagnetics (FEM) and Time-domain Electromagnetics (TEM). Time-domain and frequency-domain electromagnetic datasets require two different processing methods.

Frequency-domain Electromagnetic (FEM)

EM 31 and EM34 require less processing than PROTEM 47 and PROTEM 57 because these two systems instantly convert the measurement to conductivity. Thus, all of the data is plotted along the traverse line. However, these two systems have minor differences between them. EM31 measures the voltage of the earth induced by the constant current at constant frequency (9.8 kHz) from the transmitter loop. Although the receiver loop records the same frequency as the transmitter loop, it does not necessarily record the same phase as transmitter loop. EM31 records induced voltage of the earth and it readily decomposes the voltage into two components which are in-phase component and quadrature component. After that, the amplitude of quadrature component is internally converted into apparent conductivity (μS/m) with a simple transformation. On the other hand, EM34 measures only the quadrature component of the vertical and horizontal components of the induced magnetic field which result in apparent conductivity measurements (μS/m) of these two configurations.

Time-domain Electromagnetic (TEM)

Three main processing steps are applied to the raw datasets from PROTEM 47 and PROTEM 57. They are (1) pre-processing (2) conductivity depth imaging and (3) inversion. The processing sequence of time-domain electromagnetic is summarized in Figure 9.2.

Measurement data

Voltage by area (unit)

$$\frac{\partial B}{\partial t} = \frac{19.2 \times V_0}{A_{eff} \times 2^N}$$

Decay of Induced magnetic Field

$$\frac{\partial B}{\partial t}$$

Pre-processing Quality Control

Plot of change in induced magnetic field by time

$$\rho_a = \left[\frac{I \times A_{eff}}{\frac{\partial B}{\partial t} \times 20}\right]^{\frac{2}{3}} \left[\frac{\mu}{t}\right]^{\frac{5}{3}} \pi^{-\frac{1}{3}}$$

Conductivity Depth Imaging

Inversion

Initial model

The initial model of the subsurface comes from the first guess interpretation of the geology and physical parameters associated with the lithology and fluids

Misfit Evaluation

Evaluate misfit of model and data

Model Update

Update model until criteria are satisfied.

Interpretation ← **Final Inversion Results**

Figure 9.2: Processing sequence of PROTEM 47 and PROTEM 57.

9.4.1 Pre-processing

The objective of pre-processing is to organize and check datasets at each station. To achieve the goal, the log-log plots of $\log\left(\frac{\partial B}{\partial t}\right)$ versus time are used. Theoretically, an electromagnetic field decays exponentially with time; thus, the expected shape of the plot in Figure 9.3 should be decreasing $\log\left(\frac{\partial B}{\partial t}\right)$ with increasing time. Another advantage of Figure 9.3 is to have a quick-look at the signal to noise ratio in datasets, especially at the later time event where electromagnetic signal is weaker than noise level. Typically, an electromagnetic survey measures decay of voltage per area of transmitter in the subsurface through time. Different earth materials have different decay rates proportional to the conductivity of the material in which they propagate. Thus, a transformation from voltage decay to material conductivities is needed. Equation 9.1 is applied to obtain the decay of an induced magnetic field through time. The example in Figure 9.3 shows a plot of $\log\left(\frac{\partial B}{\partial t}\right)$ decreasing with time at each station.

119

$$\frac{\partial B}{\partial t} = \frac{19.2 \times V_0}{A_{eff} \times 2^N}$$

Equation 9.1: Decay of the induced magnetic field.

Where $\dfrac{\partial B}{\partial t}$ = Changes of induced magnetic field over time (V/m^2)

V_0 = Instrument Voltage measurement (V)

A_{eff} = Effective area of transmitter (m^2)

N = Number of gain
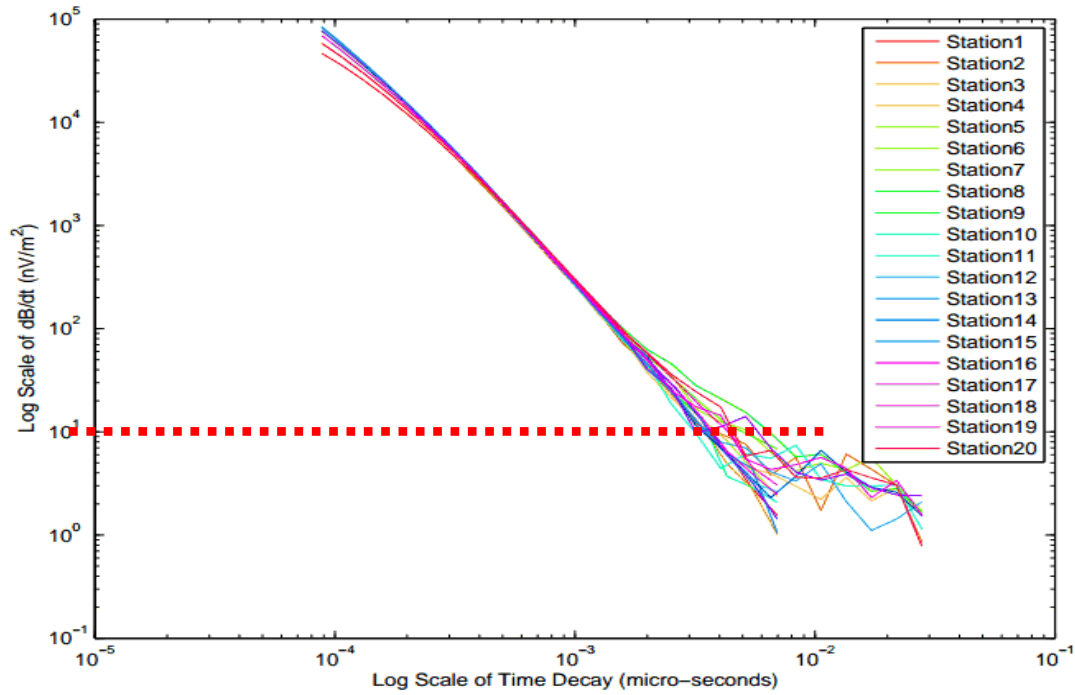
Figure 9.3: Log-log plot of time decay and rate of change of magnetic flux at all stations in Line 1899 from PROTEM57 at Mill Creek location. Red dashed line corresponds to the noise floor at 30 Hz.

9.4.2 Conductivity depth Imaging

The main goal of conductivity depth imaging is to have an overview and check the quality of the dataset before inversion. The plot of apparent conductivity versus apparent depth from conductivity depth imaging is used to define the relationship between apparent resistivity, voltage and time of measurement. In this analysis, only one station at the center of the transmitter loop is selected, as a representative of each dataset because the equation used is applicable only when the receiver is at the center of the transmitter loop. Transformation from change of induced magnetic field to apparent conductivity is required and it is displayed in Equation 9.2. Figure 9.4 depicts the logarithmic relationship of apparent resistivity and apparent depth.

$$\rho_a = \left[\frac{I \times A_{eff}}{\frac{\partial B}{\partial t} \times 20} \right]^{\frac{2}{3}} \left[\frac{\mu}{t} \right]^{\frac{5}{3}} \pi^{-\frac{1}{3}}$$

Equation 9.2: Apparent conductivity with relation to magnetic field, current, and area of transmitter.

Where
ρ_a = Apparent resistivity (Ωm)

I = Current (A)

A_{eff} = Effective area of transmitter (m^2)

$\frac{\partial B}{\partial t}$ = Changes of induced magnetic field by time (nV/m^2)

μ = Permeability of free space = $4\pi \times 10^{-7}$ V•s/(A•m)

t = Recording time (s)
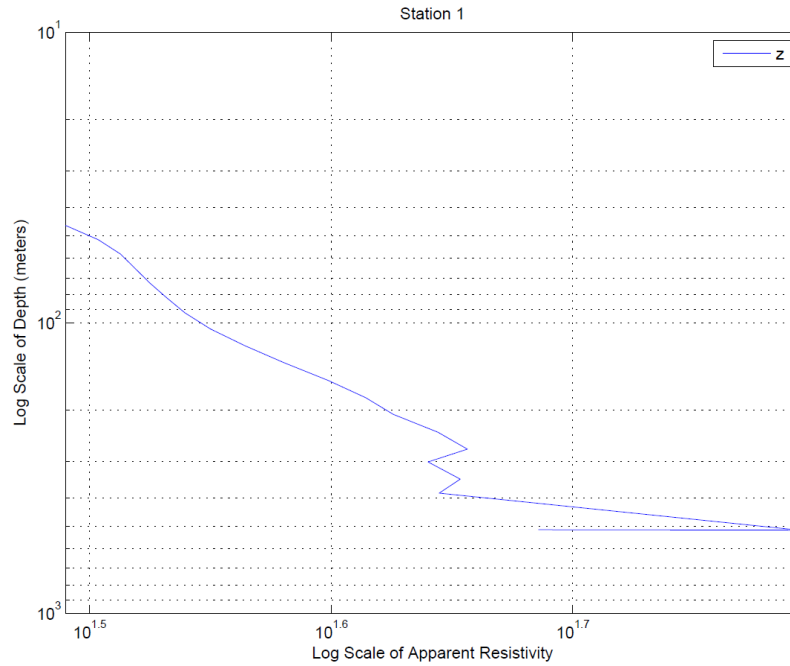
Figure 9.4: Log-log plot of apparent resistivity versus apparent depth of the central station (Line 1901) from PROTEM57 survey at Mill Creek.

9.4.3 Inversion

The ultimate goal of the electromagnetic survey is to characterize the hot spring system. Inversion provides the pseudo-2D cross-section of conductivity with depth for further interpretation from conductivity properties of subsurface. Inversion is conducted by using Interprex 1D software package. In general, there are many inversion algorithms to be used. In this study, the smooth inversion (Occam's Inversion) is used. This algorithm works by assuming a layered earth with a certain thicknesses and unknown resistivity. The inversion algorithm evaluates the misfit between the initial model and measured data points from an associated acquisition geometry at each receiver location.

Then, the model is updated to minimize the misfit between model and measured data points until it satisfies the criteria of inversion with the smoothest model. Additionally, inversions of PROTEM47 and PROTEM 57 are conducted as 1D models beneath the actual receiver points. All 1D models are then aligned together to display a 2D cross section along survey. Figure 9.5describes parameterization of the inversion algorithm used for this analysis. Table 9.7and Table 9.8 show the parameters related to EM47 and EM57 inversions respectively.
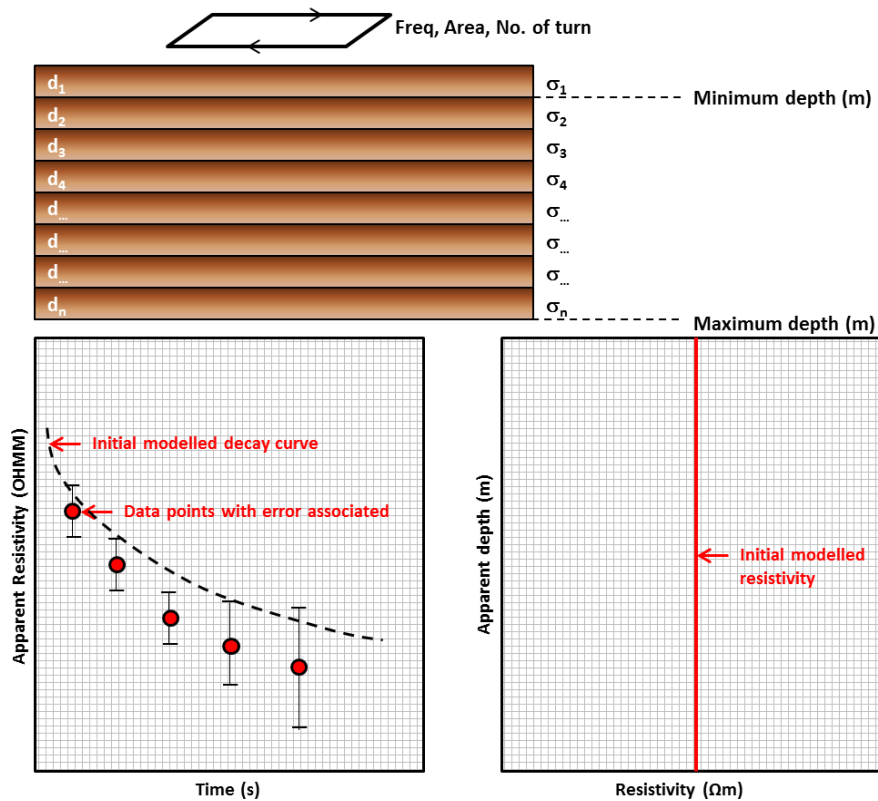
Figure 9.5: Parameterization of PROTEM 47 and PROTEM 57.

Table 9. 4: Parameters used in PROTEM 47 inversion at Mill Creek location.

Parameters		Values
Acquisition Parameters	Transmitter Frequency (Hz)	75
	Ramp up Time (μs)	10
	Receiver Coil Area (m^2)	31.40
	Current (A)	2.0
	Number of Transmitter Turn	1
Inversion Parameters	Number of Layers	15
	Minimum Depth (m)	1
	Maximum Depth (m)	300

Parameters		Values
	Initial Resistivity (Ωm)	1

Table 9. 5: Parameters used in PROTEM 57 inversion at Mill Creek Location.

Parameters		Values
Acquisition Parameters	Transmitter Frequency (Hz)	30
	Ramp up Time (µs)	9
	Receiver Coil Area (m^2)	100
	Current (A)	20
	Number of Transmitter Turn	1
Inversion Parameters	Number of Layers	100
	Minimum Depth (m)	10
	Maximum Depth (m)	500
	Initial Resistivity (Ωm)	10

9.5 Uncertainties/Errors

9.5.1 External noise

EM data can be affected by any metallic material that is not a part of survey targets. These include power lines and transformers (causing induced noise), metal fences, roads, wind and, occasionally, passing-by vehicles, mobile phones and radios.

It is worth noting that power line interference has been reduced by filtering given frequencies on the EM instrument, i.e. 60 Hz filter for standard American power lines. Lightning is also a common source of noise for EM, however, there is no observation of any lightning during data acquisition.

9.5.2 Instrumental noise

Instrumental noise can be caused by error or lack of calibration, instrument drift (clock drift), and spatial misalignment of instrument when acquiring data. EM 31 and EM 34 are calibrated prior to the start of measurement (daily). EM 47 and EM 57 calibration data is unknown.

9.5.3 Uncertainty due to geology

Uncertainty in data processing and interpretation could be caused by incorrect or imprecise geological information in the area. Important information includes anisotropy, dipping layer, change of topography and frequency-dependent conductivity (IP effects).

Other than the above geology related source of uncertainties, one known geological environment is the presence of Mancos shale. This shale introduces induced polarization due to its chargeability.

Subsequently, this capacitor-like shale produces current flow but with opposite direction from the transmitter loop. Hence, the amplitude of transient response is reduced (thus increasing the apparent resistivity). In summary, Mancos shale potentially reduces the signal amplitude due to induced polarization effects.

9.5.4 Data processing assumptions

- Acceptable data uncertainty is set to 5-15%

- Noisy data is QC and edited out point by point (mask).

- Flat surface (no topographic correction required)

- Constant electromagnetic permeability (μ)

- The transmitter loop is deployed in square pattern.

- The constant current is fed into the transmitter loop with consistent ramp of time 5 μsec.

- 1D data inversion in the survey area is assumed sufficient for 2D imaging (by merging 1D inversion profiles into 2D sections)

9.6 Interpretations

9.6.1 Mill Creek

EM57 Inversion Results

An EM57 survey grid was executed at Mill Creek using both a 30Hz and 7.5Hz repetition rate. The location of this survey at Mill Creek is near Highway 84 shown in Figure 9.6. The EM57 grid is shown as the orange circles closest to the highway. The western most line was called 1899 and increasing to the east the lines were 1900, 1901, 19022, and 1903. Only the 30Hz data from the 1899, 1901, and 1903 were used for inversions. These lines correspond to the western-most, center, and eastern-most lines of the EM57 survey at Mill Creek.

Coordinate System: North American 1983 UTM Zone 13N
Projection: Transverse Mercator
Datum: North American 1983
false easting: 500,000.0000
false northing: 0.0000
central meridian: -105.0000
scale factor: 0.9996
latitude of origin: 0.0000
Units: Meter

EM Survey (Mill Creek)

0   0.0275   0.055   0.11 Kilometers

Legend
▲ (Mill Creek) EM Corners
○ (Mill Creek) EM Locations

Figure 9.6: Shows the GPS locations of the EM57 grid and the EM47 lines at Mill Creek near the highway (Highway 84 is on the right side of the image).

Based on the geologic observations in the field and using Google Earth, the limestone area outcrops on the hill north of the EM57 survey. Google Earth showed that the elevation of the Niobrara layer was at 7130ft and the approximate elevation of the surface of the EM57 survey was 7080ft. The distance between the small Niobrara layer and the top of the Dakota Sandstone was determined to be about 30m from field observations. Based on these observations, the top of the Dakota Sandstone should be approximately 15m below the surface at Mill Creek. These insights were used to guide the interpretations of the inverted EM57 sections. The inverted sections for lines 1899, 1901, and 1903 are shown in Figure 9.7,Figure 9.8, and Figure 9.9 respectively. The inverted section for 1901 shown in Figure 9.8 had data from two receiver locations removed – RX-0 and RX-6 – because these inversions were obscure. In the inverted sections, Station Number 1 is the northern-most receiver location RX-0 and Station 10 is the southern-most receiver location RX-9.
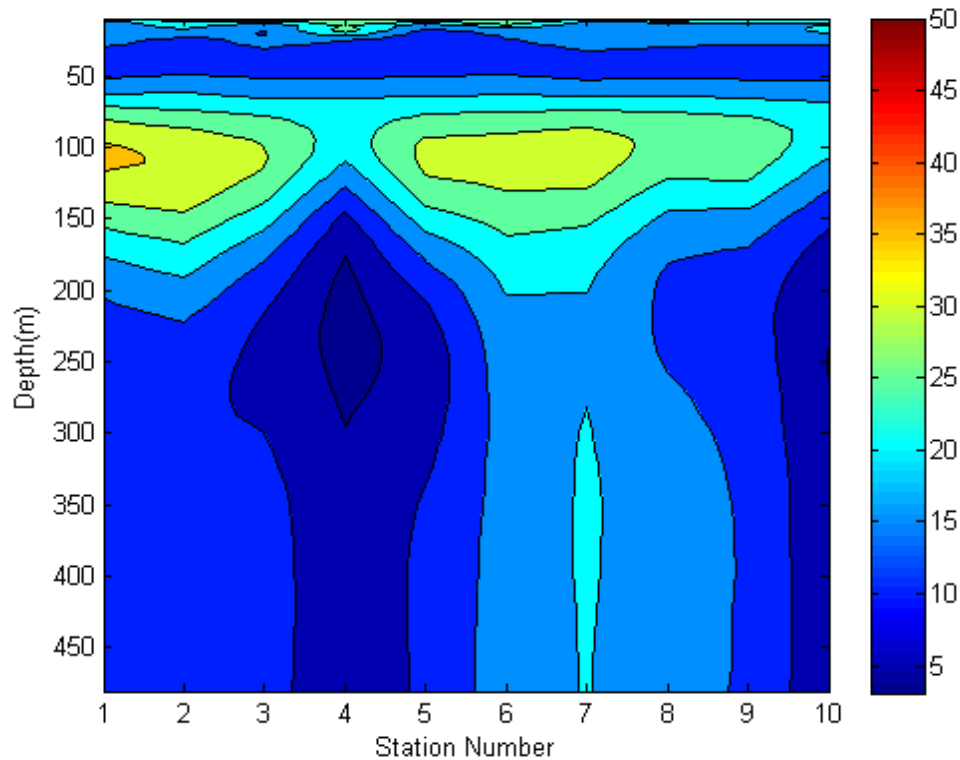
Figure 9.7: Shows the inverted results for the EM57 line 1899. The contour image shows results in resistivity (Ωm).

The results of these inversions are presented with red contours representing highly resistive areas and blue contours representing more conductive areas. Notice at the top of each of these images there is a very shallow resistive layer that is approximately 10-15m deep. This pertains to the shallow portion of the Lower Mancos Shale in this region. A majority of the Mancos Shale has eroded away and only about 10-15m of the shale remains on the surface in the Mill Creek area. Below the shallow layer of Mancos Shale is the Dakota Sandstone. Based off of the data from the P-1 well, the Dakota Sandstone is approximately 60m thick. If the top of the Dakota Sandstone is approximately 10m from the surface, then we would expect to see the bottom of the Dakota Sandstone and the top of the Morrison Formation at about 70m down from the surface. The whole Dakota Sandstone unit is present from about 10m depth to 60m depth in Figure 9.7,Figure 9.8, and Figure 9.9 and is shown as a light-blue to blue area in the figures. In the 10-70m region in Figure 9.8 there is a highly resistive area located at RX-1. After some interpretation, this 'anomaly' seemed to be noise because there is no data in the right-most portion of Figure 9.7 that would suggest that this resistive body continues.
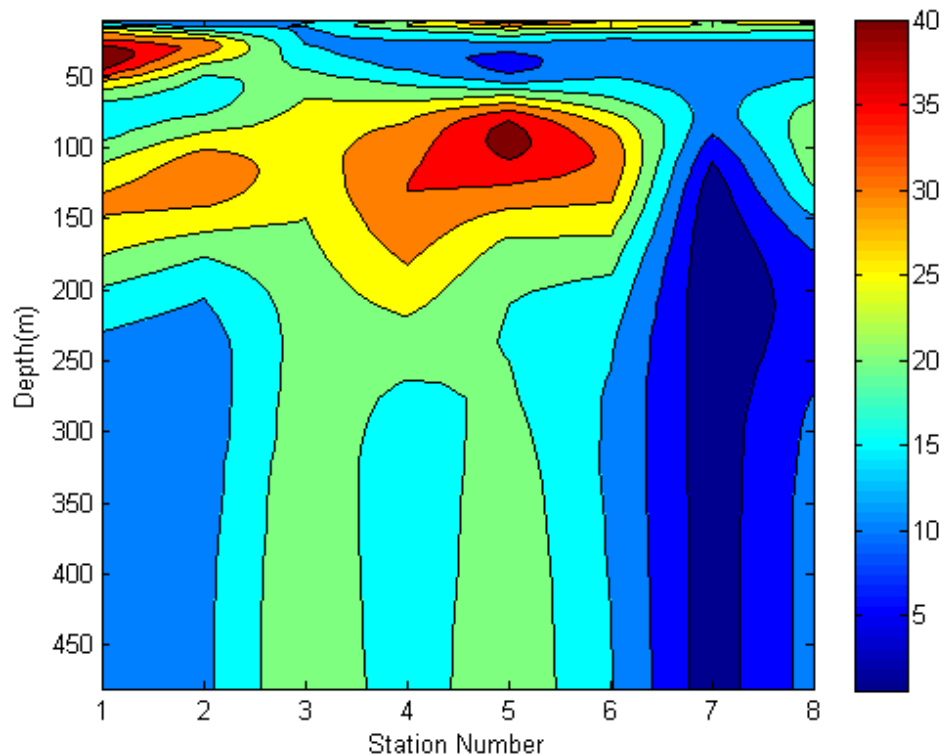
126

The next region of importance in these inverted results is the area below the Dakota Sandstone. Prior geologic knowledge from the P-1 well shows that the next unit after the Dakota Sandstone was the Morrison Formation with a thickness about 200 m. This is fairly consistent with what the results show above in the inverted sections. The inverted sections show a transition from conductive to resistive at about 60-70m and this resistive layer continues to a depth of about 200m. This layer corresponds to the Morrison Formation. The results show that the Morrison Formation is about 150m thick, not 200m thick, indicating the EM57 results loosely correlate to the stratification of the P-1 well. The areas below the Morrison Formation are fairly inconclusive. Based on the geologic cross sections the basement should be approximately 300 m depth. This is not present in the inversion results, because it would be expected for the basement to be resistive and there is no obvious resistive boundary at this depth. The Entrada Sandstone, located above the basement and below the Morrison Formation, might be conductive causing the EM signal at these later time gates being unable to penetrate through this potential conductive layer and provide a visible signal. This could explain the highly conductive areas below the Morrison Formation in the EM57 inverted sections, but the sensitivity of the instrument may be low at this point causing the deeper data to be mostly noise. More accurate data at depth is needed to make interpretations beyond the Morrison Formation.
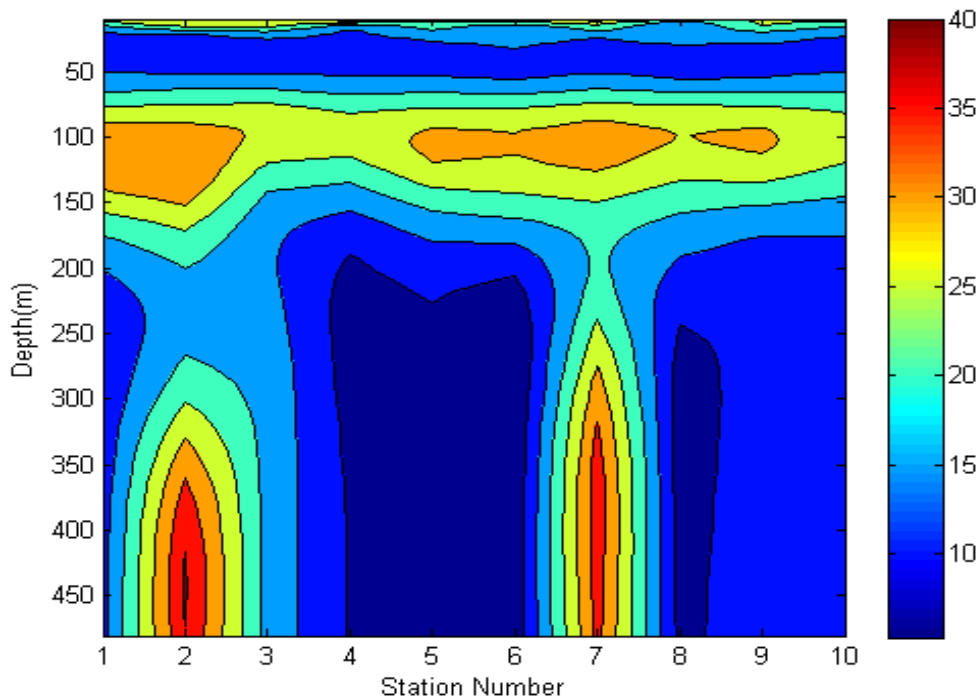
Figure 9.9: Shows the inverted results for the EM57 line 1903. The contour image shows results in resistivity (Ωm).

EM47 Inversion Results

EM47 data was also collected at Mill Creek in the same area as the EM57. There were three EM47 surveys done at Mill Creek and their geometry is shown below in Figure 9.10. The three EM47 surveys consisted of three 50m x 50m grids right next to each other as shown. Line 17 was done in the EM57 grid described above and the other two EM47 lines correspond to the two lines to the west of the EM57 grid in Figure 9.6. The EM47 line to the far west was conducted using two different frequencies. The 285 Hz frequency was discarded because the inversion was inaccurate—only the 75 Hz frequency was kept. Line 17 was also discarded because the inversion was inaccurate and had little correlation to the other lines. Line 18 and Line 20 were kept and the inversion results from these lines are shown in Figure 9.11: Shows the inverted results for the 75 Hz EM47 line 18. The contour image shows results in resistivity (Ωm).and Figure 9.12: Shows the inverted results for the 75 Hz EM47 line 20. The contour image shows results in resistivity (Ωm). respectively. Line 18 has only 6 stations whereas Line 20 has 9 Stations. The stations outside of the transmitter loop were removed from Line 18 because the inverted results were inaccurate. The center loop was removed as well because it was 5m away from both stations on either side of it and in order to keep the geometry consistent of having 10m between stations it was removed. This resulted in 6 stations.

EM47 Mill Creek
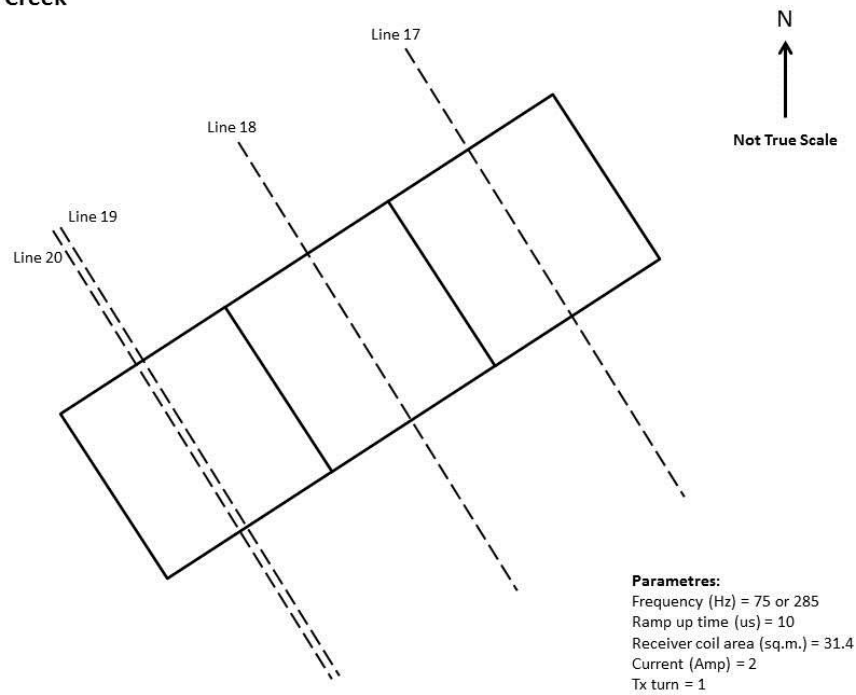
Figure 9.10: Shows the orientation of the EM47 surveys are Mill Creek.
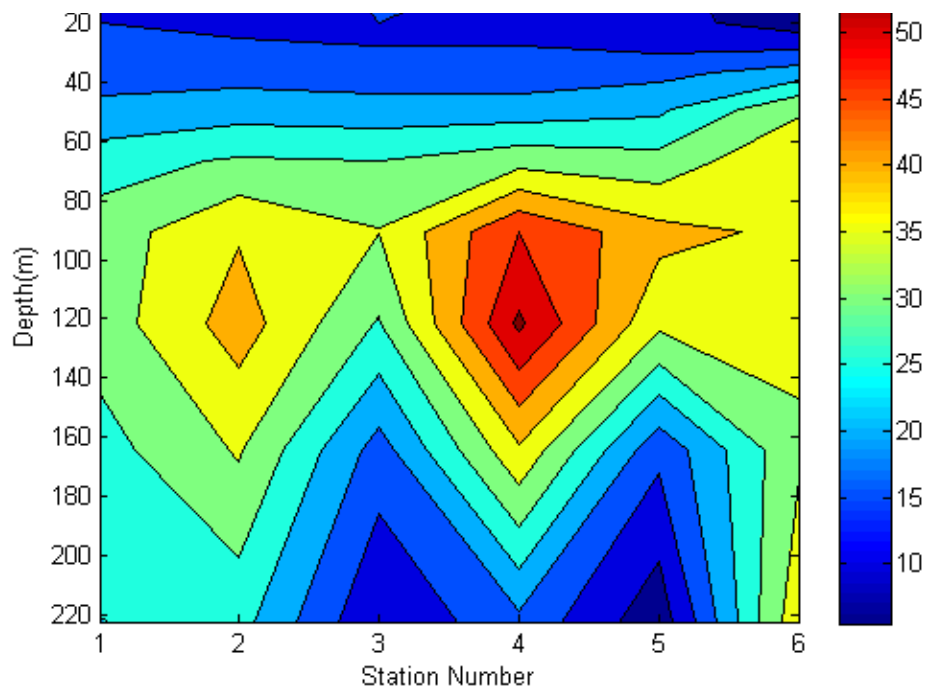
Figure 9.11: Shows the inverted results for the 75 Hz EM47 line 18. The contour image shows results in resistivity (Ωm).

129
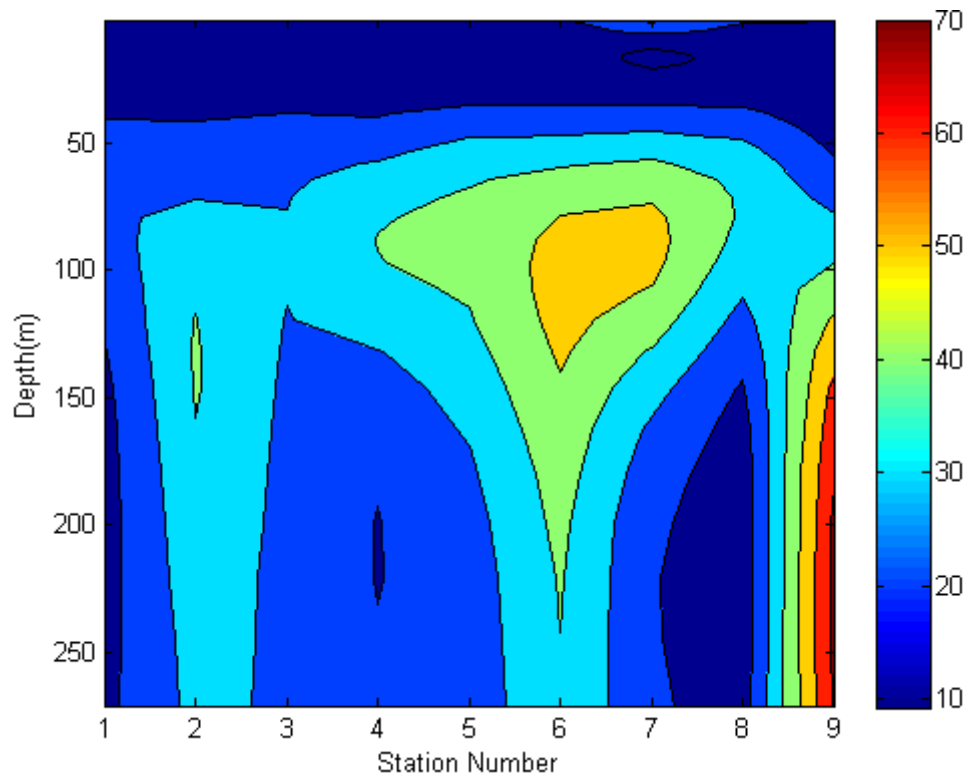
Figure 9.12: Shows the inverted results for the 75 Hz EM47 line 20. The contour image shows results in resistivity (Ωm).

Notice how there is no 'resistive' top layer in the EM47 inversion results compared to EM57 results which showed a shallow resistive layer on top, the Mancos Shale. The EM group concluded that this was due to surface variations from weather. There was a moderate amount of rain throughout the days that these EM47 surveys were conducted so the resistive top layer is most likely not present in these inversion results because the rain saturated the Mancos Shale. If this holds true, then the data from the EM47 and EM57 inversion results are consistent. Figure 9.11shows that there is a conductive layer that is about 50m thick representing a saturated and fractured Dakota Sandstone. The large resistive body below this is once again the Morrison Formation. The accurate of these inversions decays after about 150-200m. The inversion results in Figure 9.12are not as clear as those in Figure 9.11, but they loosely support the same interpretation.

EM34 Results

The remaining EM data of importance gathered at Mill Creek is the EM34 data. The EM34 lines had no GPS, but according to those who did the surveys, the survey locations were close to those of the EM47 shown in Figure 9.6. There were 2-4 days of acquisition with the EM34 in the same area to see if the data was repeatable. The data from the vertical coplanar mode (horizontal dipole) seemed to be more consistent throughout the days, so this data was preferred to correlate what the EM57 and EM47 showed. The data sets from the EM34 for 10m, 20m, and 40m spacing are shown in Figure 9.13, Figure 9.14, and Figure 9.15 respectively.
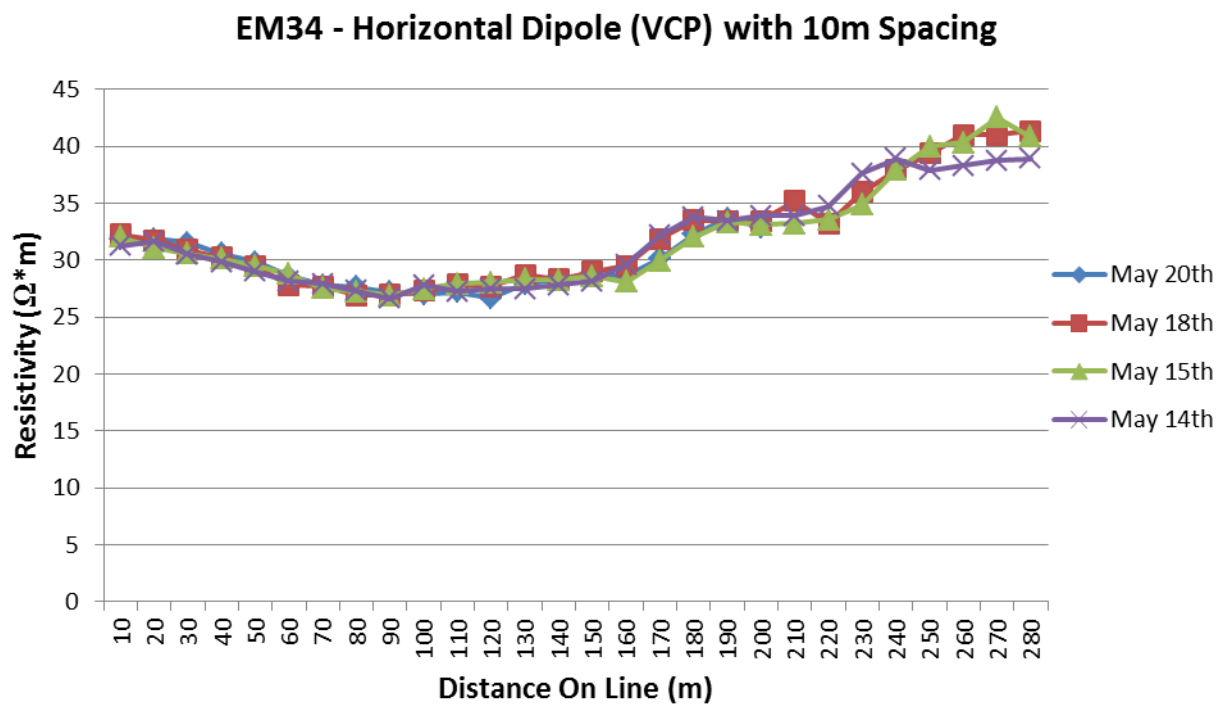
Figure 9.13: Shows the 10m spacing vertical coplanar EM34 data at Mill Creek across 4 days.
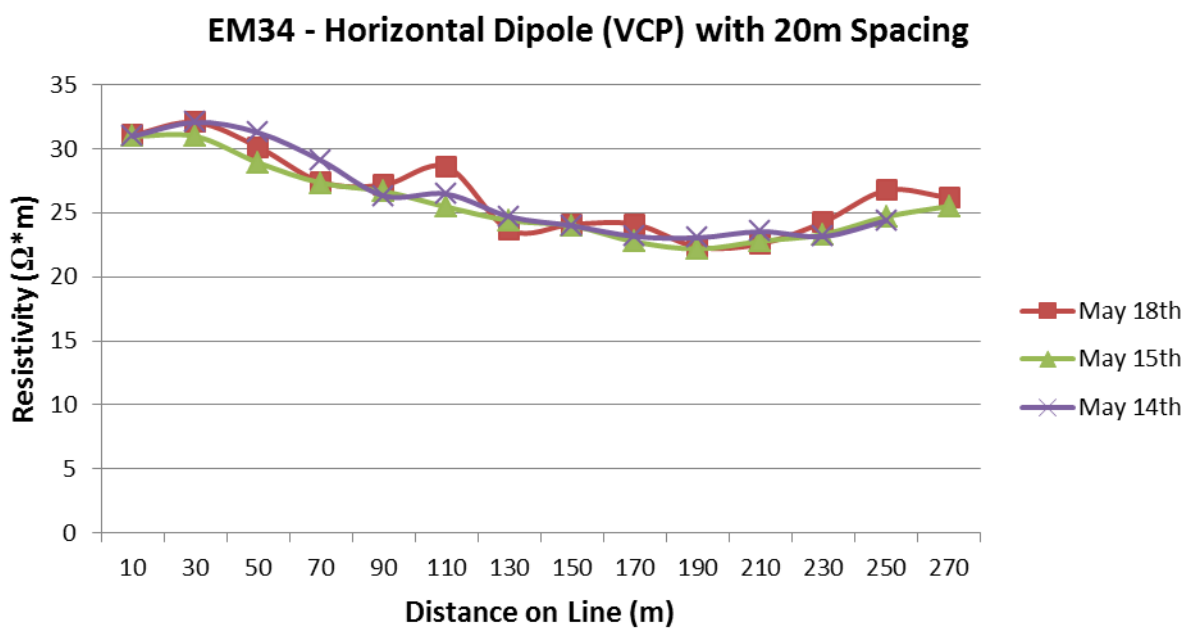
Figure 9.14: Shows the 20m spacing vertical coplanar EM34 data at Mill Creek across 3 days.

131

EM34 - Horizontal Dipole (VCP) with 40m Spacing
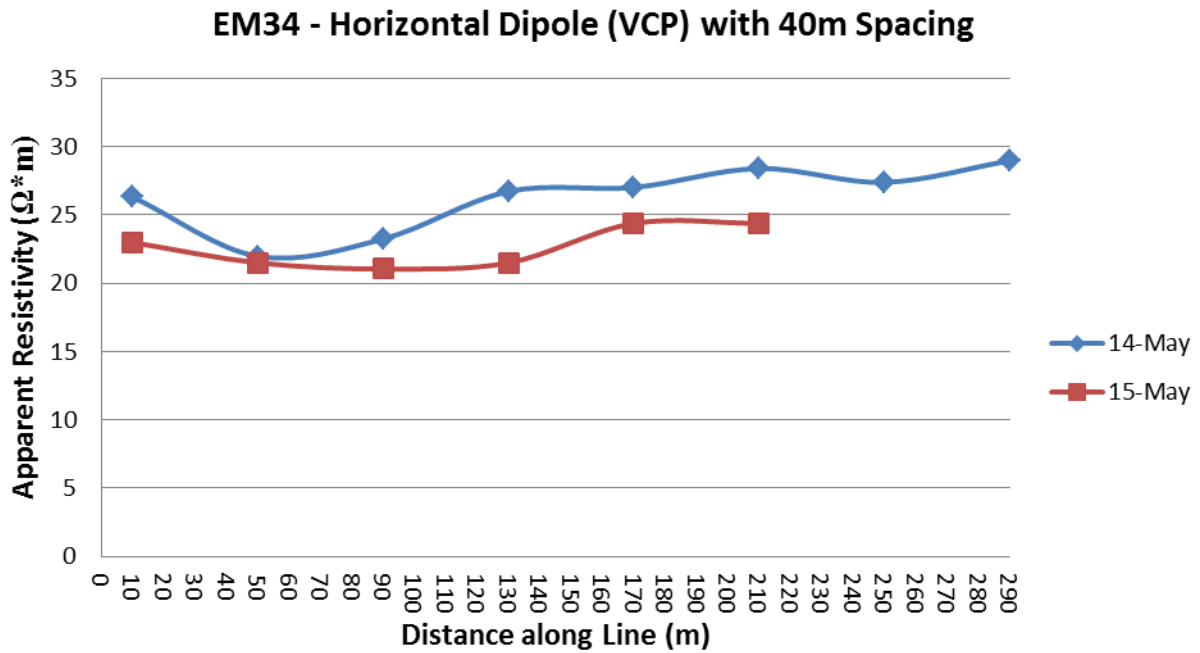
Figure 9.15: Shows the 40m spacing vertical coplanar EM34 data at Mill Creek across 2 days.

The actual data from the EM34 comes in apparent conductivity, but it was converted to apparent resistivity for each EM34 data set used so it could be roughly compared to the inversion results from the EM57 and EM47 since those results are in terms of resistivities. Note that the values for the EM34 are in apparent resistivity not actual resistivity, so the values themselves were not directly compared to the EM47 and EM57. Even though the values for the EM34 in Figure 9.13,Figure 9.14, and Figure 9.15 are in apparent resistivity, there are some general trends that support the EM47 and EM57 inversion results based on the depths of investigation of using more than one spacing for the EM34. Table 9. 6 shows the important data to take away from the Figure 9.13,Figure 9.14, and Figure 9.15. As the spacing increases, the depth of investigation increases as well. So, at shallow depths of investigation it would be expected that the apparent resistivities would be high because these readings would be taken in the Mancos Shale.

Table 9. 6: Shows the corresponding spacing, depth of investigation, and range of apparent resistivities for Figure 9.13, 9.14, and 9.15.

Figure	Spacing	Depth of Investigation	Range of Apparent Resistivities
9.13	10m	15m	30-40 Ωm
9.14	20m	30m	23-30 Ωm
9.15	40m	60m	21-29 Ωm

Table 9. 6 shows that when the depth of investigation was 15m the apparent resistivities ranged from 30-40 Ωm. With a depth of investigation of 30m, the EM47 and EM57 results showed that the Dakota Sandstone is at this depth and is comparatively conductive to the overlying Mancos Shale. This is

verified with the EM34 data with a depth of investigation of 30m. At this depth the apparent resistivities are 23-30Ωm which is lower than what the apparent resistivities were closer at the surface. When the depth of investigation is 60m, the EM57 and EM47 show that this is approximately the bottom of the Dakota Sandstone. The EM34 data at this depth shows that the apparent resistivities are 21-29 Ωm. These values are also lower than the top 'resistive' layer and are in the range of the values with the depth of investigation of 30m. This is consistent because the EM57 and EM47 data showed that the Dakota Sandstone was in this range of 30-60m and the EM34 data is relatively conductive in this region. Overall, the EM34 supports the hypothesis that there is a resistive layer towards the surface – the Mancos Shale – and a conductive layer beneath that – the Dakota Sandstone.

Correlation to DC

DC Resistivity was also gathered in this area by Mill Creek, and a survey line called the Mill Creek East Line ran near the EM57 grid. A location of this DC line at Mill Creek is shown in Figure 10.1.
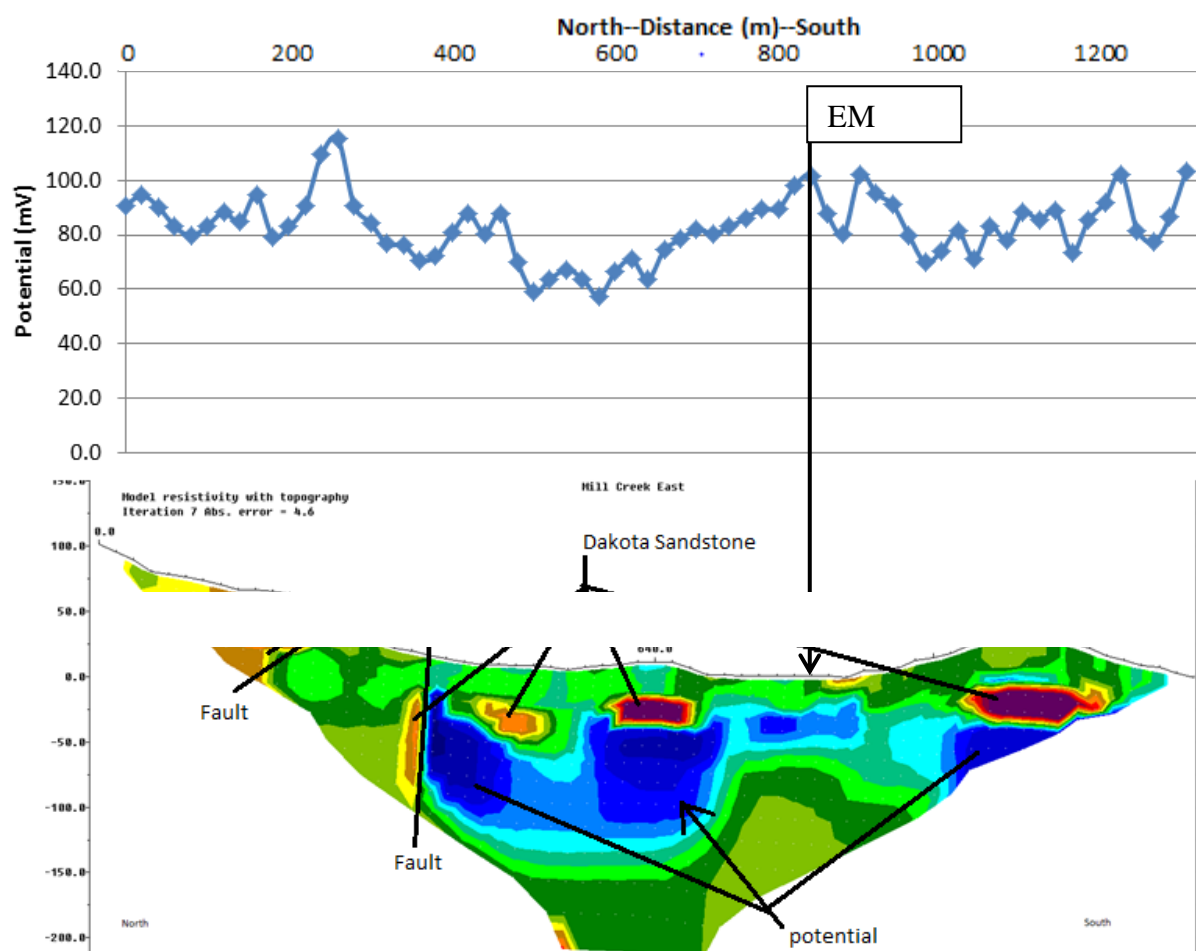
Figure 9.16: Shows the DC/SP results at the Mill Creek East location. The location of the EM 57 & 47 sites are noted for reference.

Figure 9.16 shows the DC/SP results along this survey line at Mill Creek. An arrow is shown in the

133

figure to denote where the EM grids and lines are approximately located. The DC inverted results below the EM sites location loosely verify the previous interpretation from the EM57, EM47, and EM34. The DC results show that there is a resistive top layer of approximately 50-60 Ωm with a thickness of about 20m. Under this layer there is a conductive region of about 20 Ωm and is this layer is about 50m thick. Beneath this layer is another resistive unit that continues to the bottom of the section and this must be the Morrison Formation. This roughly correlates to the results from the EM data. There is a resistive top layer which correlates to the Mancos Shale and a conductive Dakota Sandstone beneath the Mancos Shale. The resistivity values themselves are in the same range of those that are shown in the inverted EM data. The thicknesses of the determined units are slightly different in Figure 9.16 than what was previously determined. The Mancos Shale is slightly thicker than what the EM57 data showed and the Dakota Sandstone is slightly thinner than what both the EM47 and EM57 showed. Even though there are slight differences between what the EM and DC data shows, it is evident that they are both showing the same stratigraphic picture in the Mill Creek area.

9.6.2   Pagosa Springs Geothermal Pipe Network

The Problem

On May 20th, 2013, students met with the Pagosa Springs City Manager to discuss future seismic lines and the potential of doing a survey in downtown Pagosa Springs over the geothermal pipe system, which is currently leaking approximately 30,000 L/day. With help from Streets Superintendent Chris Gallegos and Sanitation Supervisor Gene Tautges, the surveying area of interest was narrowed from the entire pipe line to the Eastern side of the pipe line, Figure 9.17. Students walked this section of the pipeline with Mr. Gallegos to determine where the pipes were and to learn of any other important features in the subsurface that would affect the survey results. While walking the line with Mr. Gallegos, locations of pipes and shut-off valves were marked.

The Survey

The survey line was walked again and survey points were marked roughly 10 meters apart. The survey conducted was a time-lapse EM 31 that was run several times over the pipes, when the pipes were at different temperatures and pressures. The initial goal was to define a background noise of the system that took into account the various vehicles, buildings, power lines, and other conductive objects that were located along the survey line. Once the water was turned on at full pressure, the goal shifted to observing an localized increases in conductivity along the survey line that could be related to potential leaks in the system. The increase in pressure was used as a means of producing a larger rate of leaking that would produce a larger signal in the survey. The increase in temperature was used as another means of increasing the signal strength, as water increases in conductivity by roughly 1-3% per 1°C [67].

The survey began on May 22, 2013. Two baseline surveys were run at 30 psi with a pipe system temperature of 38°C. With these settings, the system was leaking at a rate of about 23 L/min. These surveys were run in the morning, and once finished, the temperature and pressure of the system was turned up as high as safely possible. Due to the severity of the leak, the maximum pressure that the system was able to reach was 61 psi at a temperature of $49°C$, which produced a leak of about 53 L/min. To give the leak time to fully saturate the ground, a third high-pressure survey was run the following day, May 23. However, after running the survey the next morning, it was learned that system had shut down overnight due to an alarm and had only been operating at 6 psi.

The Interpretation

Of the five datasets that were recorded over May 22nd and 23rd, three were chosen due to their relatively high levels of correlation: the first low-pressure and high-pressure surveys on May 22nd as well as the survey from May 23rd. To reduce the amount of noise in the data, the change in conductivity relative to the low-pressure survey was used for interpretation. The resulting plot in Figure 9.18 shows changes from the baseline for both of the later surveys.

Before determining areas of interest along the survey line, field notes and observations were used to evaluate the collected data. Due to abnormally high and inconsistent conductivity measurements near the middle school, data from 600-850 m along the survey line was not considered in the interpretation. Additionally, while the survey line from 300-350 m does not correspond to conductivity spikes for both plotted lines, two wet sections of pavement were noted at about 320 m on both days of surveying, despite a lack of precipitation and persistent sunshine that should have evaporated any surface water. It was unclear in the field as to what the source of the water was, but it is a significant and anomalous feature that warrants future attention.

The three remaining areas of interest seen in both Figure 9.17 and Figure 9.18 correspond to increases in conductivity seen for each day of surveying. These areas occur on the survey line from 140-200m, 940-1000m, and 1170-1300m. However, without further geophysical investigation in these areas, it is not possible to make any definitive conclusions about the source of the conductivity changes.
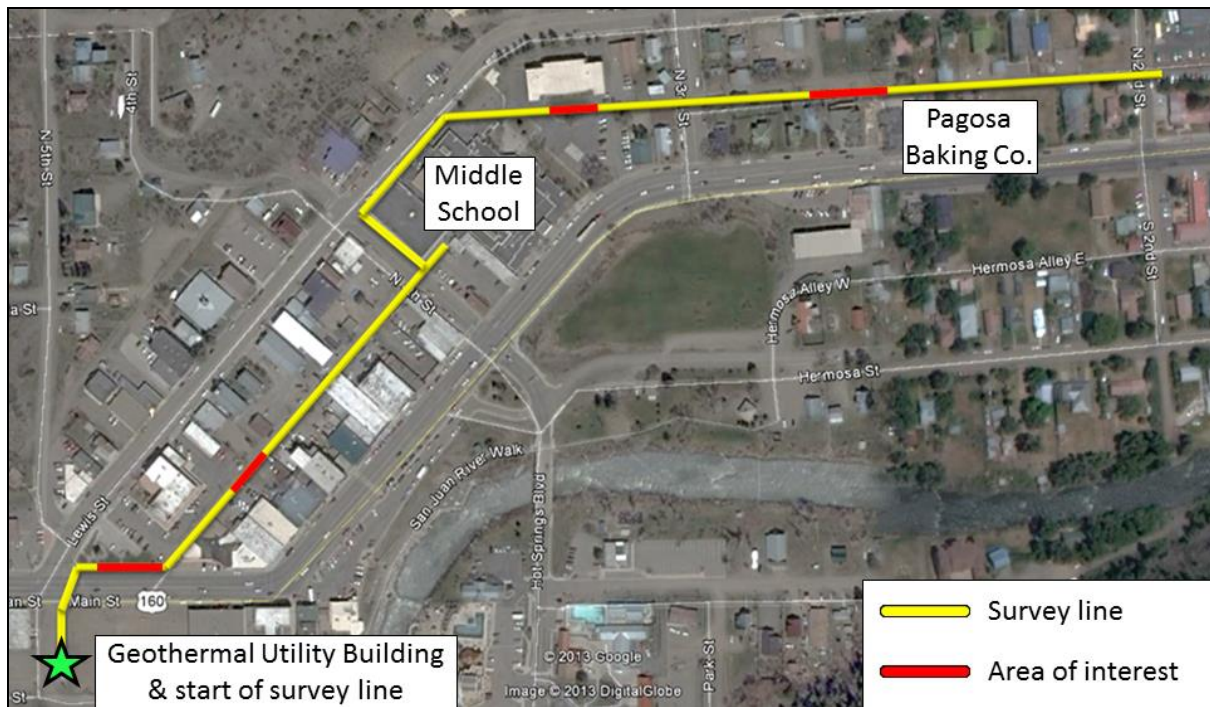
Figure 9.17: Map view of downtown Pagosa Springs geothermal system survey line and highlighted areas of interest.
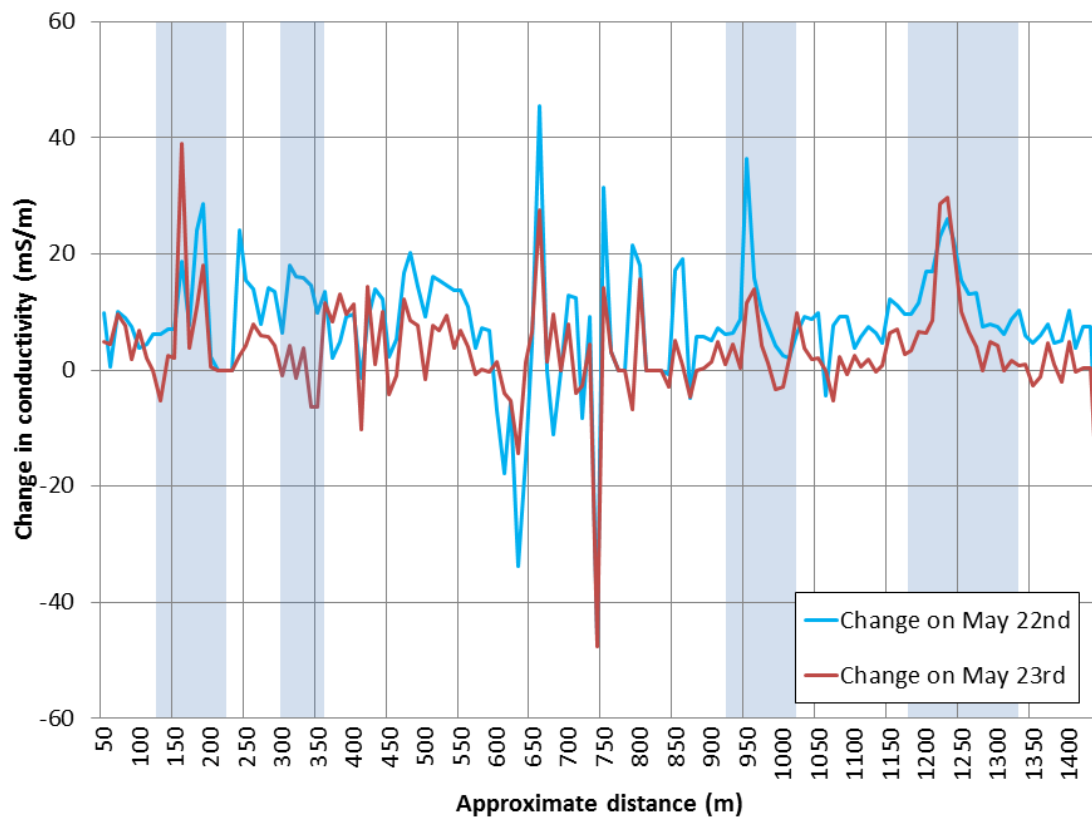
Figure 9.18: Changes in conductivity between high-pressure surveys taken on May 22nd (blue) and May 23rd (red) from baseline low-pressure survey. Shaded regions on plot indicate areas of interest, which are indicated in red on the map above.

9.6.3 Shahan's Ranch

An EM31 grid was set up near the hot springs of Shahan's Ranch to map the drainage patterns. The grid data was acquired on May 18th and May 20th, but the data on the 20th was not used due to errors in acquisition. The data from the 18th was collected in 23 lines each a length of 40m. Each line was spaced 10m apart and the survey started on the southern side of the ridge, see Figure 9.19 for position relative to the map. The scale on Figure 9.19 is based on conductivity in mS/m where purple is a highly conductive region. These highly conductive regions are indicators of water. The EM group believes that the region between 160 m and 180m is indicative of a drainage system. When at Shahan's Ranch, the vegetation in this area was a different color, most likely attributed to the minerals from the hot spring. The high conductivity region at 80 m is anomalous, most likely due to the operator getting too close to a vehicle. The EM group believes this to be the case, because of the low conductivity regions surrounding this one point.

Figure 9.19: The location of the EM grid in Shahan's map is shown above. The processed data does not include the portion that extends west. The processed data only extends 40m west and then extends north from there.
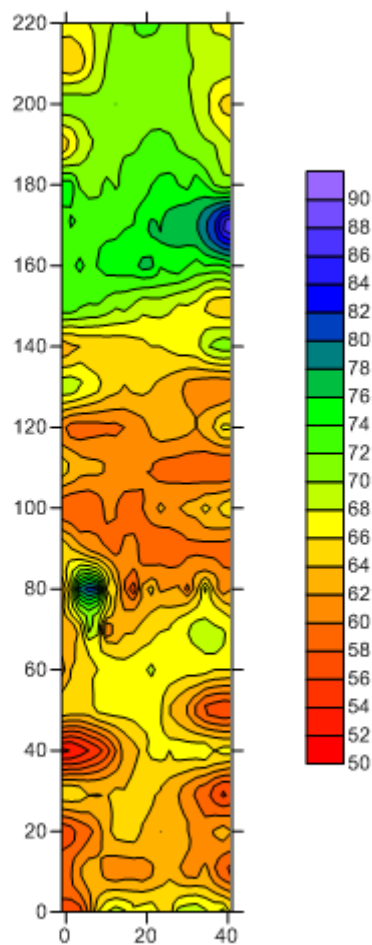
9.7 Conclusions and Discussions

Mill Creek

Based on the EM57, EM47, EM34, and the DC results it can be concluded that the bottom of the Mancos Shale is what is present at the Mill Creek area from the surface down to approximately 10-20m. The Mancos Shale was determined to be resistive from all four of these data sets. The Dakota Sandstone lies beneath the Mancos Shale and based on what all the results showed this unit is conductive. The Dakota Sandstone in this area is relatively conductive because it most likely fractured and saturated. The last unit that could be interpreted at depth with the EM47, EM57, and the DC results is the Morrison Formation. The Morrison Formation was determined to be comparatively resistive on all three of these data sets. Overall, the results from the EM and DC data sets in the Mill Creek area support this hypothesis. There is also support external to the data that supports this analysis. The external support for this conclusion is based off of the Niobrara datum and well log data.

As previously noted, the geology crew in Pagosa Springs determined that the top of the Dakota Sandstone is about 100 ft below this limestone layer called the Niobrara Formation. Outcrops of the Niobrara formation were found around Mill Creek and the location of this unit was used as a proxy to estimate where the top of the Dakota Sandstone should be in the data. Based on the surface expressions of the Niobrara, it was determined that the Dakota Sandstone should be 10-20m below the surface at the Mill Creek survey locations. Another source of supporting evidence for this claim is well log data from the P-1 well. A resistivity log was done on this well and a stratigraphic column was created as a result. The resistivity log showed that the Dakota Sandstone was more conductive than the overlying Mancos Shale which supports the claim. The stratigraphic column made from this P-1 well data also gave thickness of units that were used throughout these interpretations at Mill Creek and the data from Mill Creek supported the thickness primarily of the Dakota Sandstone. To better understand the geology of this area a few more surveys should be done. In order to understand what is happening geologically beyond the Morrison Formation another EM57 survey should be done with 7.5 Hz. The EM57 7.5Hz data had to be thrown out because the later time gate data was inaccurate. In order to improve the later time gate data a larger transmitter loop should be used to increase the signal which will improve the signal at later time gates. It would also be recommended that more EM47 surveys should be done at 285 Hz in order to better understand the thickness of the Mancos Shale.

Pagosa Springs Geothermal Pipe Network

To improve the quality of the data for the pipe system, it is recommended that a three-day EM31 survey be conducted along the same survey line. The first day of surveying should consist of numerous baseline readings taken with the pipe system at a low pressure. The two baseline readings taken in this initial survey were not adequate to determine a consistent baseline for the survey line. Thus, it is recommended that as many baseline readings as possible be recorded on the first day. On the second day, the pipe system should be pressurized as much as possible. This will increase the rate of the leak and increase the response from the subsurface water. Once this has been done, additional surveys should be conducted throughout the day to monitor any subsurface changes. On the third day, with the water given time to leak and seep into the ground overnight, more surveys should be run along the line to detect the seepage plume.

Shahan's Ranch

The data acquired from the EM31 only had a depth of about 6 m. This means that the interpretation of the region is mainly a surface expression of the geology and water flows. To improve the quality of this data, it would be preferred that a large survey is acquired with other methods run along the grid to correlate and support the findings. This would allow us to map the surface flows more accurately and provide a better picture of the region.

10. DC Resistivity

10.1 Introduction

Direct current (DC) resistivity is an active geophysical method in which current is injected into the subsurface using a man-made source, creating an observable electric potential. The Earth's potential response is governed by the Poisson-Boltzmann equation:

$$\nabla \cdot \sigma \nabla V = I\delta(x - x_s)$$

<p align="center">Equation 10.1: Poisson-Boltzmann equation.</p>

Where x_s is the position in meters of the current carrying electrode, V is the electrical potential in volts, I is the current in amps, and σ is the conductivity in Siemens per meter. The conductivity, σ, and resistivity, ρ, are related by:

$$\rho = \frac{1}{\sigma}$$

<p align="center">Equation 10.2: Resistivity-Conductivity relation.</p>

Where ρ is the resistivity in Ohm-meters.

The equipment required to conduct a DC survey includes a current source, electrodes, and cables. DC resistivity is based on the principle that the electric potential measured around a current carrying electrode is affected by the electrical resistivity distribution in the subsurface (DC 1). Using the measured apparent resistivity data, the data can then be inverted for the subsurface resistivity profile. The relation between resistivity and other subsurface material properties is approximated by Archie's Law [73]:

$$R = a\phi^{-m}S_w{}^{-n}R_w$$

<p align="center">Equation 10.3: Archie's Law.</p>

Where a is a dimensionless tortuosity factor, ϕ is the dimensionless porosity, S_w is the dimensionless brine saturation, m is the dimensionless cementation exponent of the rock, n is the dimensionless saturation exponent, and R_w is the brine resistivity in Ohms. From a resistivity profile, it can be inferred the locations of fractured areas and subsurface aquifers. Also, because heat transfer and groundwater flow are coupled, the DC resistivity method can be used to characterize certain aspects of geothermal systems.

10.2 Survey Sites and Design

DC resistivity surveys were conducted at four survey sites (Figure 10.1): the first survey followed the deep seismic line, the second survey was at Mill Creek, the third survey was at the Hairpin Dike, and

the fourth survey was at the student site at Shahan Ranch. The surveys along the deep seismic line, at Mill Creek, and at Hairpin Dike were conducted using the ABEM Terrameter 4000 System, while the survey at Shahan's Ranch (Figure 10.1) and an additional survey at Mill Creek were conducted using the AGI SuperSting 3D Resistivity Imaging System (Figure 10.1). Refer to section 2 of Appendix F for descriptions of the equipment and how they operate.

Table 10.1: DC resistivity survey sites

Area	Number of lines	Names of lines
Deep Seismic Line	1	Main Survey Line
Mill Creek	2	Mill Creek Central Line, Mill Creek East Line
Hairpin Dike	2	Hairpin Dike Line 1, Hairpin Dike Line 2
Shahan Ranch	4	Shahan Line 1, Shahan Line 2, Shahan Line 3, Shahan Line 4
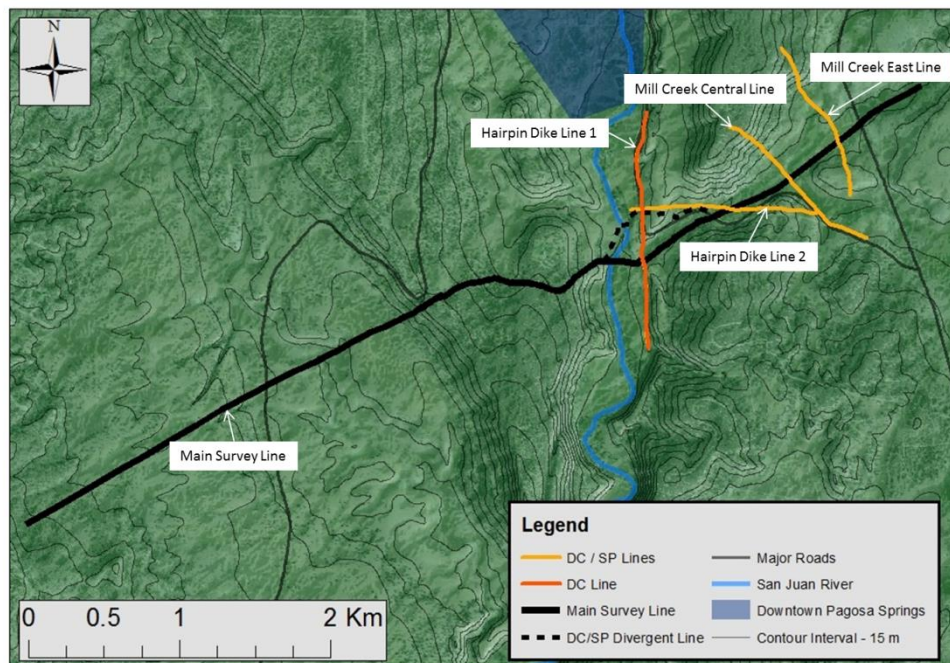
Figure 10.1: Map view of DC resistivity survey lines.

10.2.1 Main Survey

The main DC resistivity survey line closely followed the deep seismic line. This main survey line (Figure 10.1) was a rollover survey conducted using the ABEM Terrameter 4000 System and used 320 electrodes with 20 meter spacing (Table 10.1). A rollover survey is a survey where the total number of electrodes does not reach the full distance needed, so it "rolls along" by taking electrodes from the back and placing them at the front. A Wenner electrode configuration was used to provide the greatest signal to noise ratio in the data. The reason for conducting this survey following the seismic line was to obtain additional resistivity data to complement the seismic data. Resistivity is governed by Archie's Law, so it depends on water saturation and porosity among other factors. With these different types of data, the different properties of the subsurface can be potentially estimated, and the imaged geologic structures can be compared with each method.

10.2.2 Mill Creek

A geologic study of the main seismic survey line east of the San Juan River showed evidence for faulting. Faults and fractures are believed to be responsible for much of the hydrothermal system of Pagosa Springs, so characterizing these would prove useful for analysis of heat and water flow in the region. Mill Creek provided an easily accessible, relatively flat site for DC resistivity surveys. One line was located in the central Mill Creek area, and the other was on the eastern end of the creek (Figure 10.1). Both lines consisted of 64 electrodes spaced 20 meters apart (Table 10.2). The lines were oriented northwest to southeast and were roughly perpendicular to the deep seismic line. With this geometry, the combination of these survey lines with the main survey line following the deep seismic line can give a 3D sense of the geology in the area.

An additional five survey lines (Mill Creek Lines 1-5) were conducted using the AGI SuperSting 3D Resistivity Imaging System at Mill Creek. These five lines were oriented northwest to southeast and were spaced 25 meters apart. Each line consisted of 28 electrodes spaced 5 meters apart (Table 10.2). Our goal with this smaller electrode spacing was to image and characterize with a potential fault under Mill Creek with higher resolution. Unfortunately, the resulting resistivity sections from this SuperSting data showed little to no useful information and did not image any faulting. As the Mill Creek Central Line and Mill Creek East Line imaged this area well, the SuperSting data (Mill Creek Lines 1-5) was not included in the results and interpretation sections. This allowed us to avoid confusion while still imaging the faulting in this area.

Table 10.2: Mill Creek survey lines

Line	Number of Electrodes	Electrode Spacing (m)	System	Acquisition Type
Mill Creek Central Line	64	20	ABEM	Wenner, IP
Mill Creek East Line	64	20	ABEM	Wenner, Dipole-Dipole
Mill Creek Line 1	28	5	SuperSting	Dipole-Dipole
Mill Creek Line 2	28	5	SuperSting	Dipole-Dipole
Mill Creek Line 3	28	5	SuperSting	Dipole-Dipole
Mill Creek Line 4	28	5	SuperSting	Wenner, Dipole-Dipole
Mill Creek Line 5	28	5	SuperSting	Wenner, Dipole-Dipole

Figure 10.2: Mill Creek (WSW camera view).

Figure 10.3: Mill Creek (WSW camera view).

10.2.3 Hairpin Dike

The ABEM Terrameter 4000 System was used to survey two DC resistivity lines around the Hairpin Dike. The goal of the first survey (Hairpin Dike Line 1 in Figure 10.1) was to simply image the underlying dike. The goal of the second survey line (Hairpin Dike Line 2 in Figure 10.1) was to image a potential fault that is suspected to cut through Mill Creek. The first survey line was a rollover survey conducted using 80 electrodes with 20 meter electrode spacing, while the second survey was conducted using 64 electrodes with 20 meter electrode spacing (Table 10.3).

Table 10.3: Hairpin Dike survey lines

Line	Number of Electrodes	Electrode Spacing (m)	System	Acquisition Type
Hairpin Dike Line 1	80	20	ABEM	Wenner
Hairpin Dike Line 2	64	20	ABEM	Wenner

10.2.4 Shahan Ranch

The student site at Shahan Ranch was surveyed using the AGI SupserSting 3D Resistivity Imaging System. Four lines were surveyed: Shahan Line 1 and Shahan Line 2 ran east to west, while Shahan Line 3 and Shahan 4 ran north to south and were roughly perpendicular to Shahan Line 1 and Shahan

Line 2. All four lines were surveyed using 28 electrodes with 20 meter electrode spacing, and resistivity data were acquired along each line for both Wenner and dipole-dipole array configurations.

Table 10.4: Shahan Ranch survey lines

Line	Number of Electrodes	Electrode Spacing (m)	System	Acquisition Type
Shahan Line 1	28	20	SuperSting	Wenner, Dipole-Dipole
Shahan Line 2	28	20	SuperSting	Wenner, Dipole-Dipole
Shahan Line 3	28	20	SuperSting	Wenner, Dipole-Dipole
Shahan Line 4	28	20	SuperSting	Wenner, Dipole-Dipole
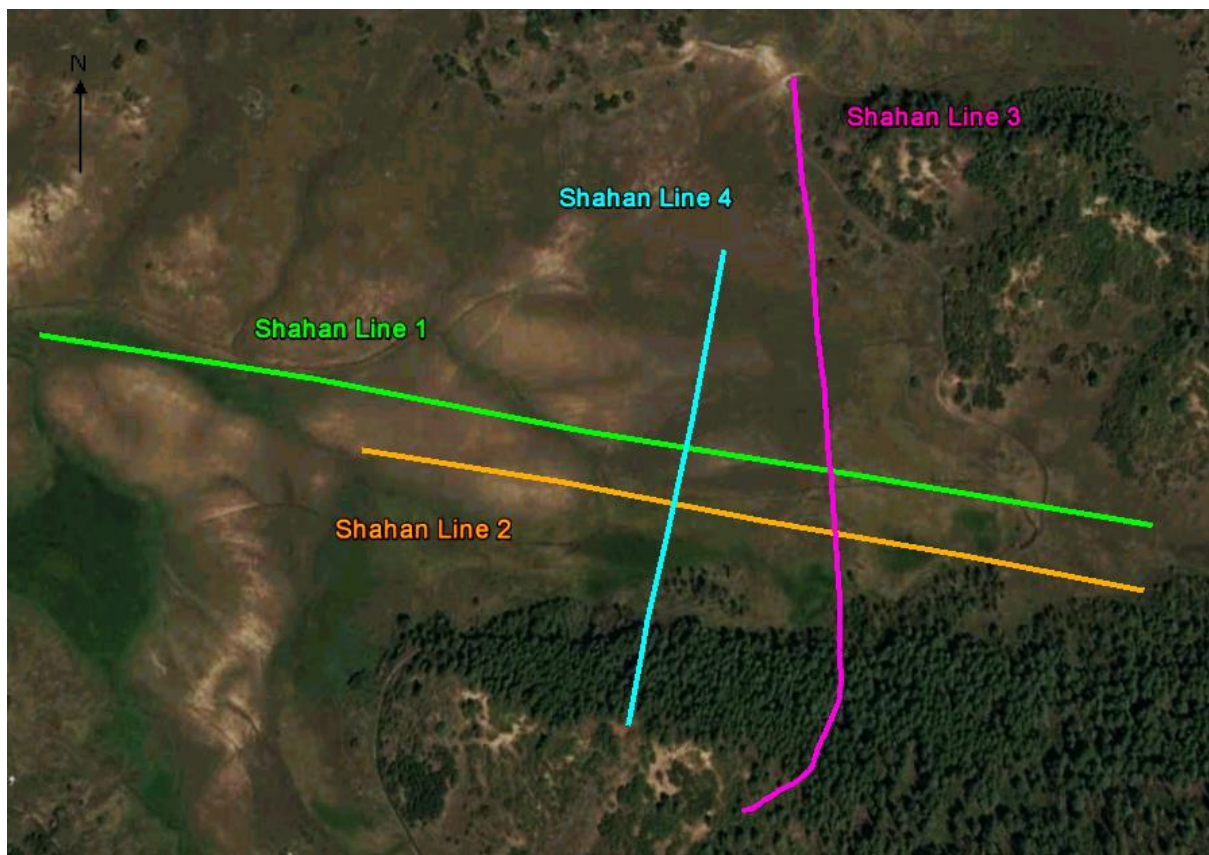
Figure 10.4: Map view of DC resistivity survey lines at Shahan Ranch

10.3 Processing

10.3.1 Data Software and Hardware

ABEM

The ABEM is a small computer brought out to the field and hooked up to the DC survey line. It first tests each electrode to see if it is able to collect data. It automates the array configurations along a survey line that has electrodes planted at fixed separation distances. It allows the user to quickly acquire data for various array set-ups. The files are stored within the ABEM computer as an .S4K file and are downloaded and converted by SAS4000 software into a .DAT, which are then processed by the inversion software.

SuperSting

Very similar to the ABEM, the SuperSting is a small, field-ready computer hooked up to a DC survey. The main difference is that the SuperSting is slightly less powerful and tends to be used on smaller arrays, while the ABEM handles big arrays. It outputs the data as a .STG file, which is then converted into a .DAT file, ready to invert.

Inversion Software

The inversion software used was RES2DINV. Inversion, here, is the process of taking the data collected and using mathematics to obtain a subsurface interpretation of the geology. The inversion software also has the ability to account for topography, and many of the geologic structures become more evident when this is included. At the end of the inversion, the software displays the subsurface image with the calculated resistivity values of the rocks.

10.3.2 Data Reduction

The first process applied before inputting the data into the RES2DINV software is to add the topographical data to the .DAT file. This is done using a combination of altimeter and GPS data.
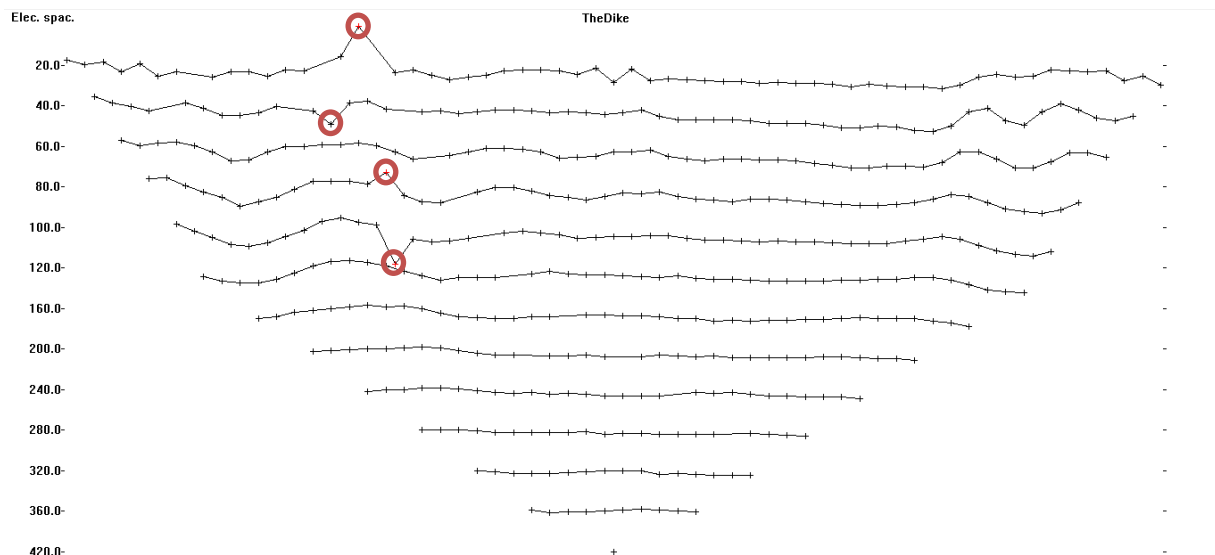
Figure 10.5: Selecting poor data points in RES2DINV

Once the data is uploaded into the RES2DINV software, data are reduced in an attempt to make them more accurate and easier to process. The first step is to remove the outliers within the data. These are the points that are several standard deviations away from the previous point and the next point (essentially a large spike). The points to be removed are shown in red in Figure 10.5, some of the data from the Hairpin Dike area. This type of data reduction is a quick and easy way to increase the signal to noise ratio. After this process has been applied, the data will be saved in a new .DAT file and will be inverted.

Once the inversion has been completed, more data reduction may be applied if necessary. The RES2DINV program is able to provide the user statistics about the error from each point. Figure 10.6 shows a histogram of the error contributed from each point.
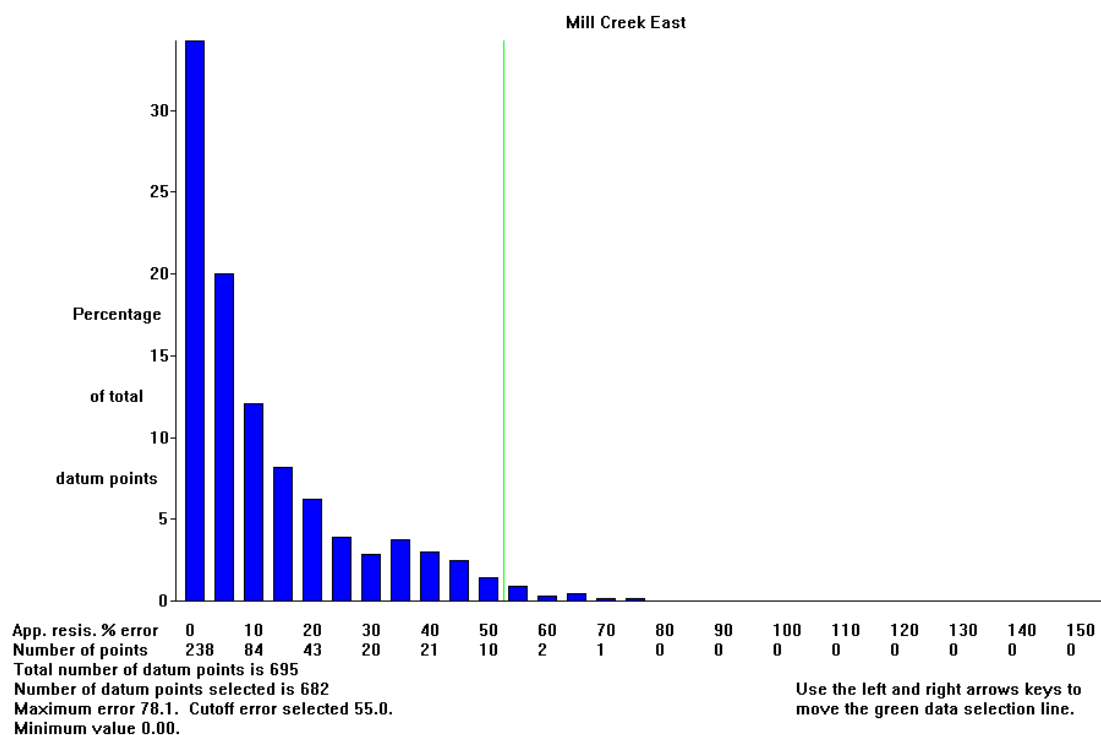
Figure 10.6: Contributions from each point to the error

The program allows the user to select a threshold of error above which the points get cut off. Figure 10.6 shows an error threshold of 55%, shown by the vertical green bar. This means that points containing a higher error than 55% will be excluded. This threshold was chosen based off of the fact that the user does not want to remove too many data points, but also wants to remove some of the errors. This data set is then saved as a new .DAT file and a new inversion is done with this reduced data set with an increased signal to noise ratio.

On the SuperSting data sets, extra processing was done even before inputting the data into the program. Unrealistic datum points were eliminated because they exceeded the bounds of a realistic scenario.

148
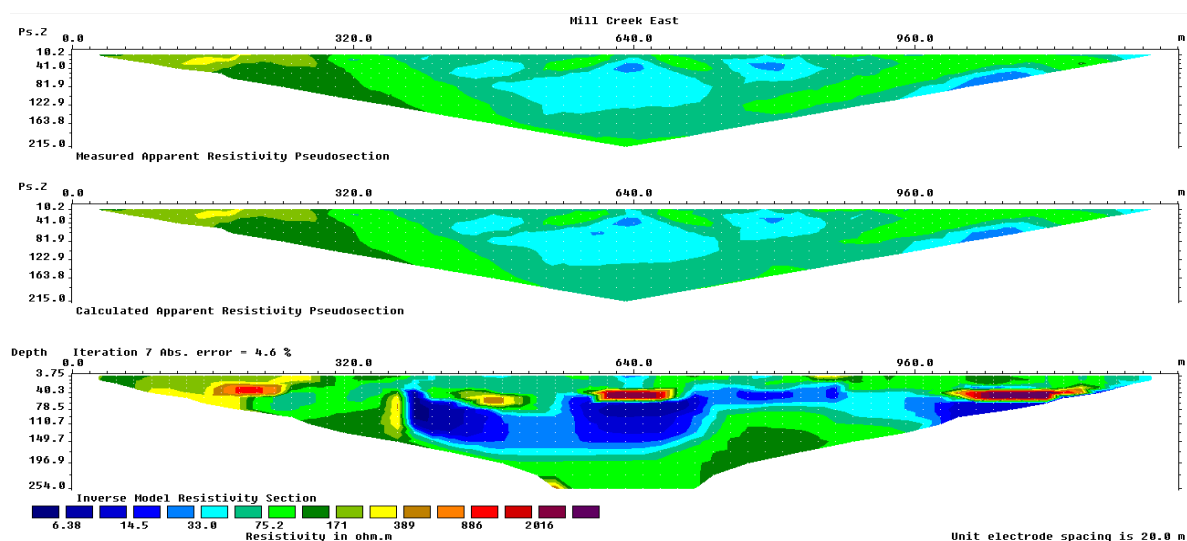
10.3.3 Inversion

Figure 10.7: Output of inversion from RES2DINV software

For the DC, IP, and SuperSting datasets, the RES2DINV software was used to invert each line. There were many lines inverted and the results of the important lines will be discussed in the interpretation section. A least-squares inversion was used in each scenario. The recommended parameters of the RES2DINV software were used for each inversion due to time constraints. An example of the output from the inversion software is shown in Figure 10.7.

The first two images are pseudosections, essentially visual organizations of the data controlled by electrode position; these do not pertain to structures in the subsurface. The third image is the actual inversion result. The number of iterations shown is seven, meaning that the error-reduction process of the inversion was completed seven times. The reason that this is done is to decrease the error from the inversion. The value of the error in Figure 10.7 is shown to the right of the number of iterations and has a value of 4.6%. Each iteration reduces our total error percentage, increasing the correlation between the actual subsurface structure and our image.

10.4 Uncertainties/Errors

A large source of uncertainty in DC resistivity methods is the accuracy of station elevations and GPS locations. A differential GPS (DGPS), TDM, and handheld barometric altimeter were used to record spatial coordinates and altitude data at each electrode location of the survey lines (except PGSA07, which had only altimeter data). In areas where DGPS could not collect data due to rough terrain or excessive tree cover, handheld GPS units were used. The DGPS is accurate to within 10 centimeters in good conditions, but near buildings and in thick trees the accuracy drops significantly due to loss of connection with satellites. To supplement the DGPS data, TDM units were used to provide accurate spatial information along many survey lines. Unfortunately, the TDM process is very time intensive,

149

so not all locations could be recorded with this method. The combination of all these data resulted in an accurate spatial model of the DC survey lines, so this should not be an issue during interpretation.

Uncertainty can also come from assumptions of investigation depth. This value is affected by many factors, such as electrode coupling with the ground, near surface conductivity/moisture, and subsurface anisotropy. The large survey lines used, as well as qualitative assessment of each survey area, serves to counteract these effects, and thus get a more easily estimated depth of investigation.

Error can be sourced from bad equipment, poor survey setup, oxidized contact between electrodes and connectors, and outliers in the data. For example, if a cable is damaged, it may read electrodes as being connected when there is no electrode present, and vice-versa. If this is the case, erroneous measurements may be recorded. Additionally, if any cable connectors are attached backwards, incorrect values will be measured. This can be checked via the ABEM control console. Oxidized contact between electrodes and connectors can prevent current from flowing, or interfere with voltage measurements. Therefore, it is important to slide the connector up and down after connecting it to an electrode to ensure oxidation does not prevent a solid connection. Even when equipment is not malfunctioning and all connections are solid and accurate, outliers can still be present in data. These are removed manually in processing with the RES2DINV software. Points can be individually removed before inversion, and then points with high RMS error post-inversion can be trimmed from the data (see Data Reduction section above for more information regarding this process).

10.5 Interpretations

Along each of the lines that were completed in the Pagosa Springs area, some rough geologic features can be interpreted when combining the DC Resistivity and SP data. With DC Resistivity it can be seen that anomalies exist in the electrical conductivity of the subsurface. Areas of interest are places with high conductivity, places with low conductivity, and places with a sharp contrast between conductivities. In the SP data, areas that are of interest are peaks and troughs of the potential (excepting outliers). When analyzing groundwater, peaks typically correspond to upwelling of water and troughs typically correspond to descending water.

10.5.1 Main Survey Line
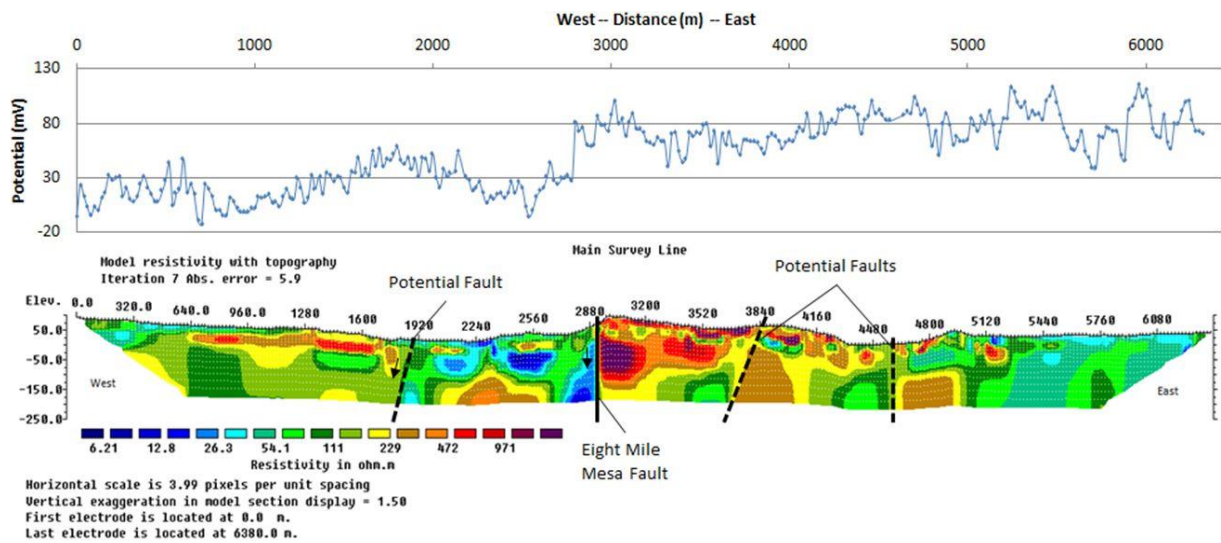
Figure 10.8: DC Resistivity and SP data compared along the main survey line
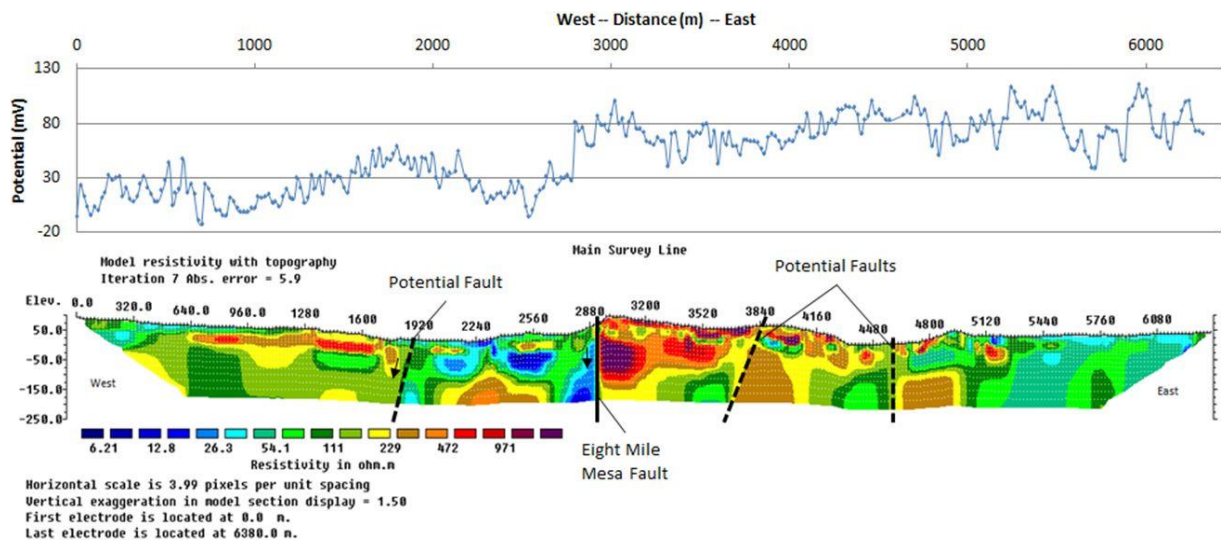
Figure 10.8 shows the final inverted resistivity cross-section of the main seismic survey line, as well the corresponding self-potential measurements along this line. There appears to be an anticlinal structure ranging from 320m to 1920m on the section. From past geologic reports it is known that the Eight Mile Mesa Fault falls around 2900m along our survey line. This location corresponds to a large resistivity contrast in the subsurface—potentially indicative of a fault. These are the two largest

features   seen   in
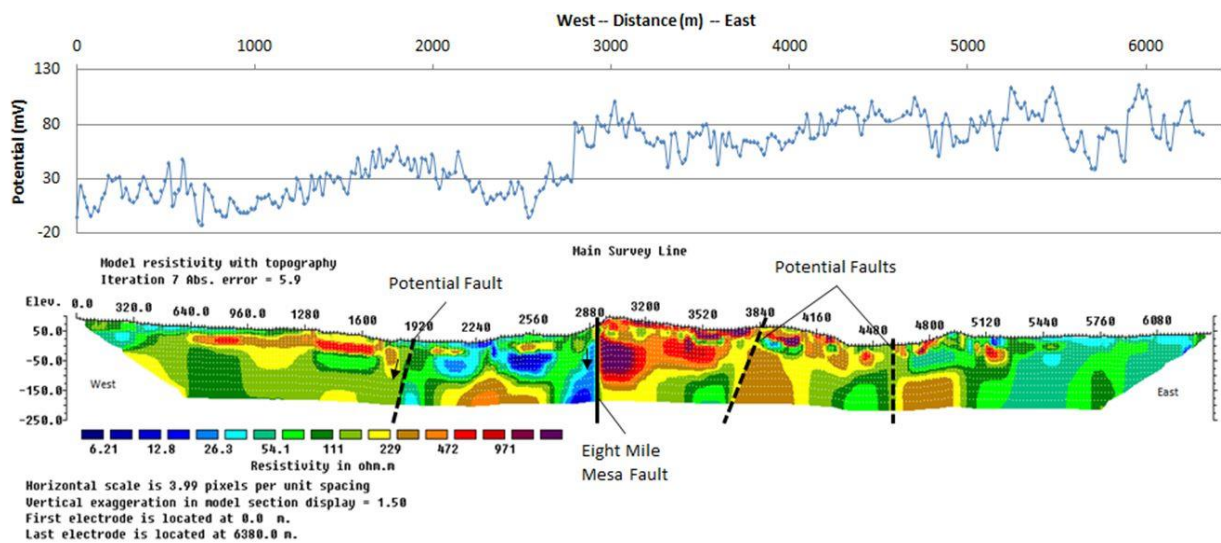
Figure 10.8. Otherwise there are several smaller faults that are not quite as clear. Using the Eight Mile Mesa Fault anomaly as a model, these smaller faults were located at 3840m and 4600m. Additionally, the contrast seen at the east end of the anticlinal structure at 1920m is interpreted as another potential fault location. These locations also display a resistivity contrast of the same form as the Eight Mile Mesa Fault. These, however, have quite a bit of uncertainty associated with them because they are not as high-contrast and could be due to terrain, processing artifacts, etc. For example, the fault located at 4600m is very close to the San Juan River, which is an area associated with high uncertainty, as electrodes were not able to be planted in the river, so resistivity data was not collected over part of the survey line. Additionally, there are no surficial geologic indications of the faults located at 3840m and 4600m.

Structurally speaking, it is reasonable to assume that near-surface warm-colored areas correspond to Dakota sandstone, as this group is highly resistive. Two of these areas occur in the 1200m to 1600m range, as well as the 2900m to 3800m range. From geology exercises in the field, it is known that these areas have Dakota sandstone outcropping at the surface.

In the raw SP data, a large anomalous spike at about 2050m was seen, but as it was only one point, it was less trustworthy and was removed from the data. When this was removed, the rest of the SP data was simpler to interpret. There exists a general upward trend along the line and a jump in the data at 2700m. This small jump may mean that there is an upwelling of water in this area, corresponding to the fault, meaning that there is water coming up from the subsurface along the fault.

10.5.2 Mill Creek
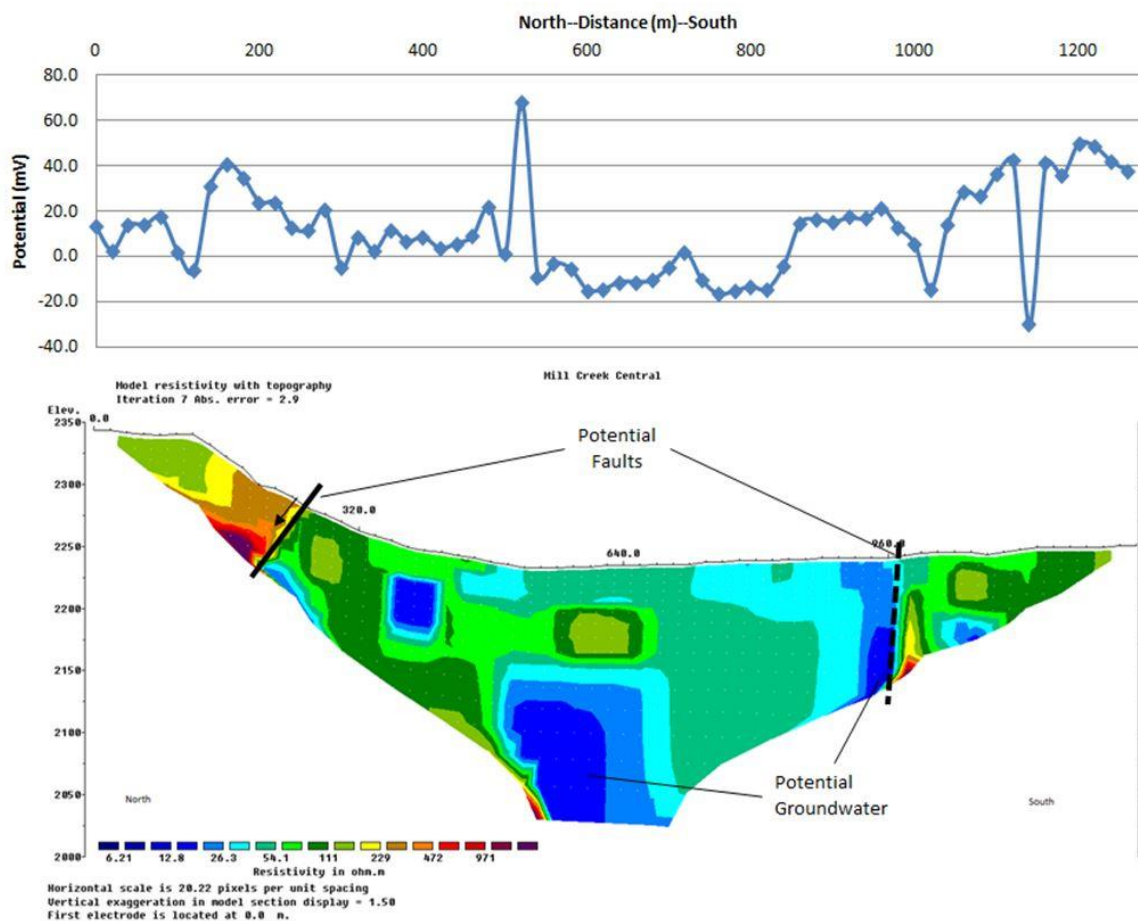
Figure 10.9: DC Resistivity and SP data compared in the Central Mill Creek area

In Figure 10.9 and Figure 10.10, DC resistivity and SP profiles of the central and eastern portions of the Mill Creek area are seen, respectively. Along the central Mill Creek line, there are two main faults. These faults exist at about 250m and 980m. The SP data shows a peak at the northern fault and a trough at the southern fault. This may point to water flowing up from the north and down through the south. There exists a large conductive body in the middle of the section. This is likely due to ground water. The eastern Mill Creek line also shows two main faults. There exists one again at about 250m, and another fault at 380m. There exist three highly resistive blocks at 230m, 640m, and 1000m. These do not correspond to any trend in the SP data, so they most likely do not have anything to do with water flow and instead are more resistive blocks in the subsurface. It is most likely that these resistive areas correspond to a layer of Dakota Sandstone in the subsurface. When viewing the SP data, there exists one peak that sticks out above the others, roughly corresponding to the area of the fault at 250m. From this it seems as water is upwelling through the fault, and that the smaller peaks in the SP data in the central Mill Creek line do correspond to anomalous regions. Once again, there is a high conductivity region in the middle of the section below what was interpreted as Dakota Sandstone. This also likely is due to ground water. In the Mill Creek area, a geochemistry report also claims that there is likely ground water in the subsurface. The best course of action would be to

compare these results with other geophysical methods and with the geology to reach a reasonable conclusion.
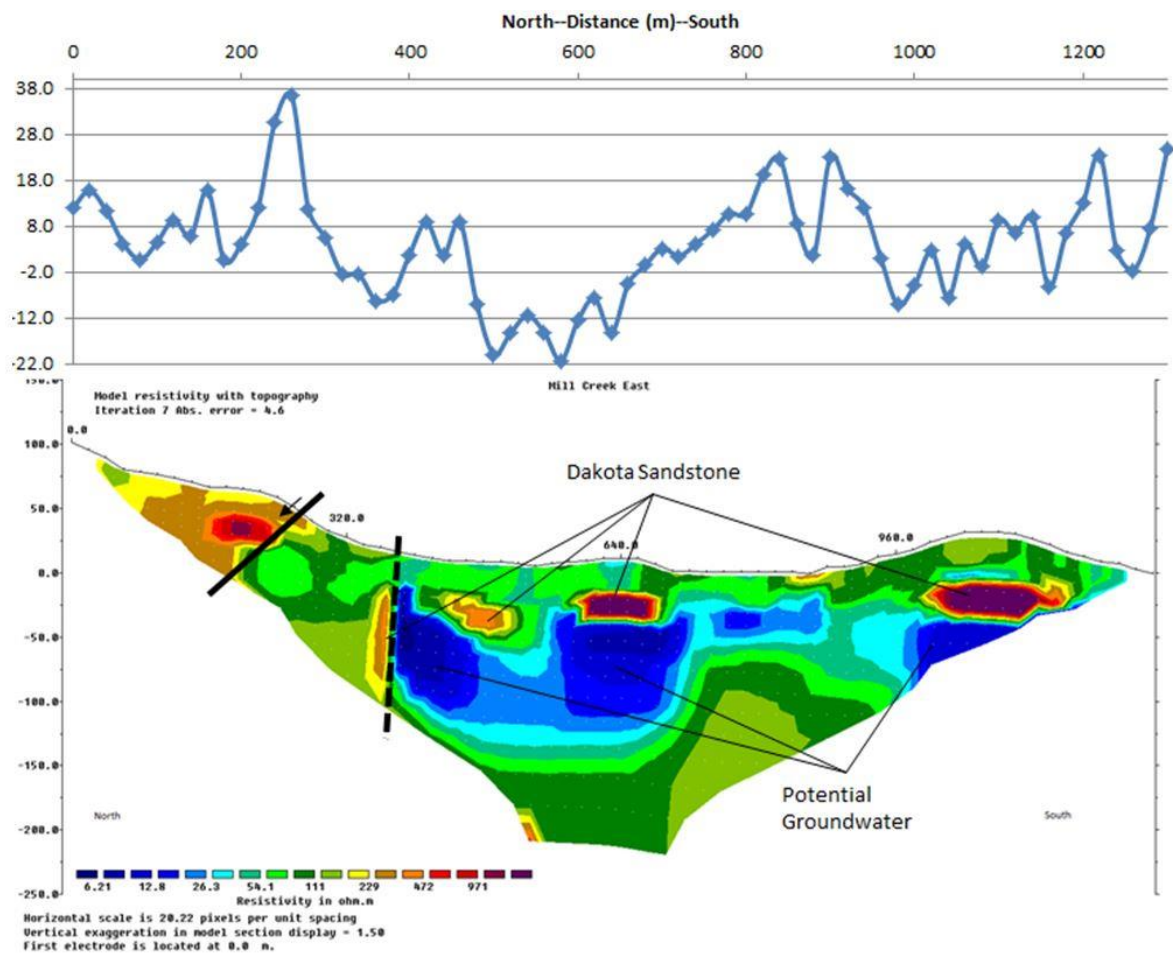
Figure 10.10: DC Resistivity and SP data compared in the Eastern Mill Creek area.

154

10.5.3 Hairpin
Dike
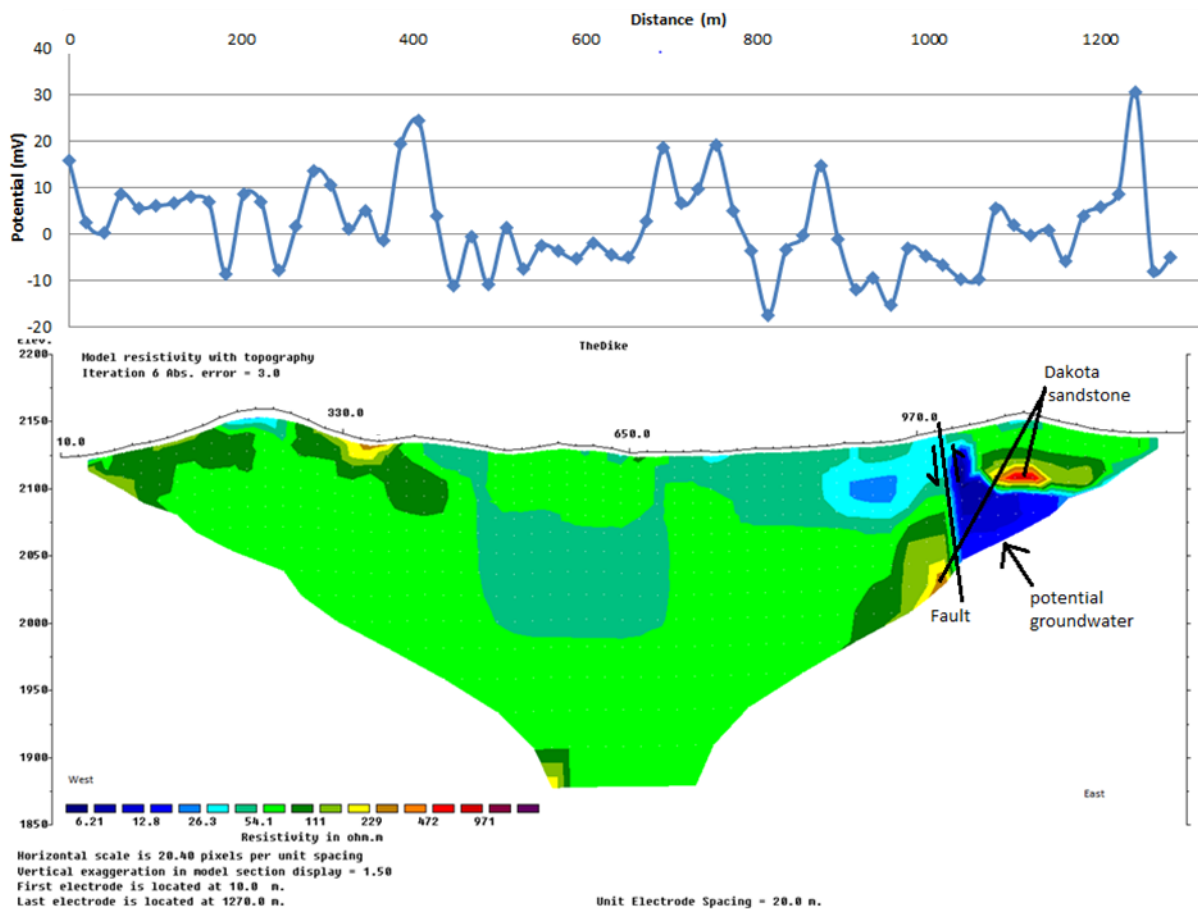
Figure 10.11: Hairpin Dike

Looking at Figure 10.11, there are two notable features. At approximately 330m to 390m, there appears to be evidence of a more resistive body. This resistive body is surrounded by Mancos Shale which has the characteristics of being more conductive than Dakota Sandstone. This is not believed to be the dike, because although an igneous dike would be more resistive, it shouldn't be located on the side of the hill.

Another noticeable feature occurs at 990m. The rapid change in resistivity values could indicate a potential fault. The supporting evidence for this claim is that the Dakota Sandstone appears on both sides of the fault at different depths. Another important feature seen is the potential groundwater reservoir.

The groundwater potentially running along the faults may be geothermally heated. In the future, if there are any wells near the area, it would be beneficial to investigate the temperature of the water at different depths.

155

10.5.4 Possible Location of Groundwater
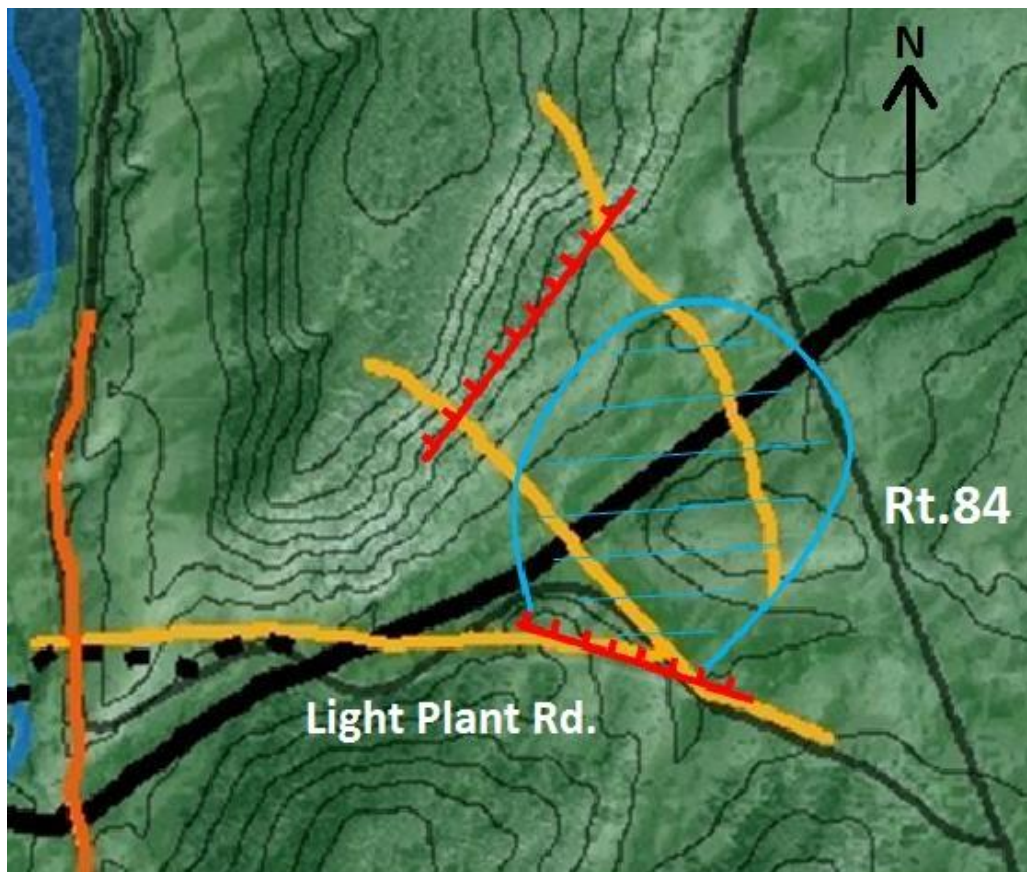
Figure 10.11: Hairpin Dike Line 2 (purple), Mill Creek Central (green), Mill Creek East (yellow), reverse faults (red), and potential subsurface groundwater supply (blue striped).

Analysis of the Hairpin Dike Line 2, Central Mill Creek line, and the Eastern Mill Creek line shows evidence of a possible aquifer located near these lines (Figure 10.11). The resistivity sections of central and eastern Mill Creek both display a very low resistivity structure capped by a more resistive layer (Figure 10.9 and Figure 10.10, respectively). As this resistive layer is most likely Dakota sandstone, and the Dakota group is roughly 60 m thick, it is reasonable to say that the Dakota group extends down from the thin resistive layers shown. This would extend the Dakota into the conductive areas, which would make sense if there is an aquifer located there. The Dakota sandstone is highly fractured, and these fractures would allow water to be stored within the formation. This potential aquifer increases in depth to the southwest, and may truncate at the reverse fault intersecting the Hairpin Dike Line 2 and the Central Mill Creek line (Figure 10.9 and Figure 10.11). Another reverse fault can be inferred from the northern ends of the Central and Eastern Mill Creek lines, which may be causing the uplift in this area (Figure 10.9 and Figure 10.10). The fault on the southwestern end of the inferred aquifer may or may not extend far enough into the subsurface to provide heat to the water. More geophysical data would be required to interpret the depth extent of this fault.

10.5.5 Shahan's Ranch
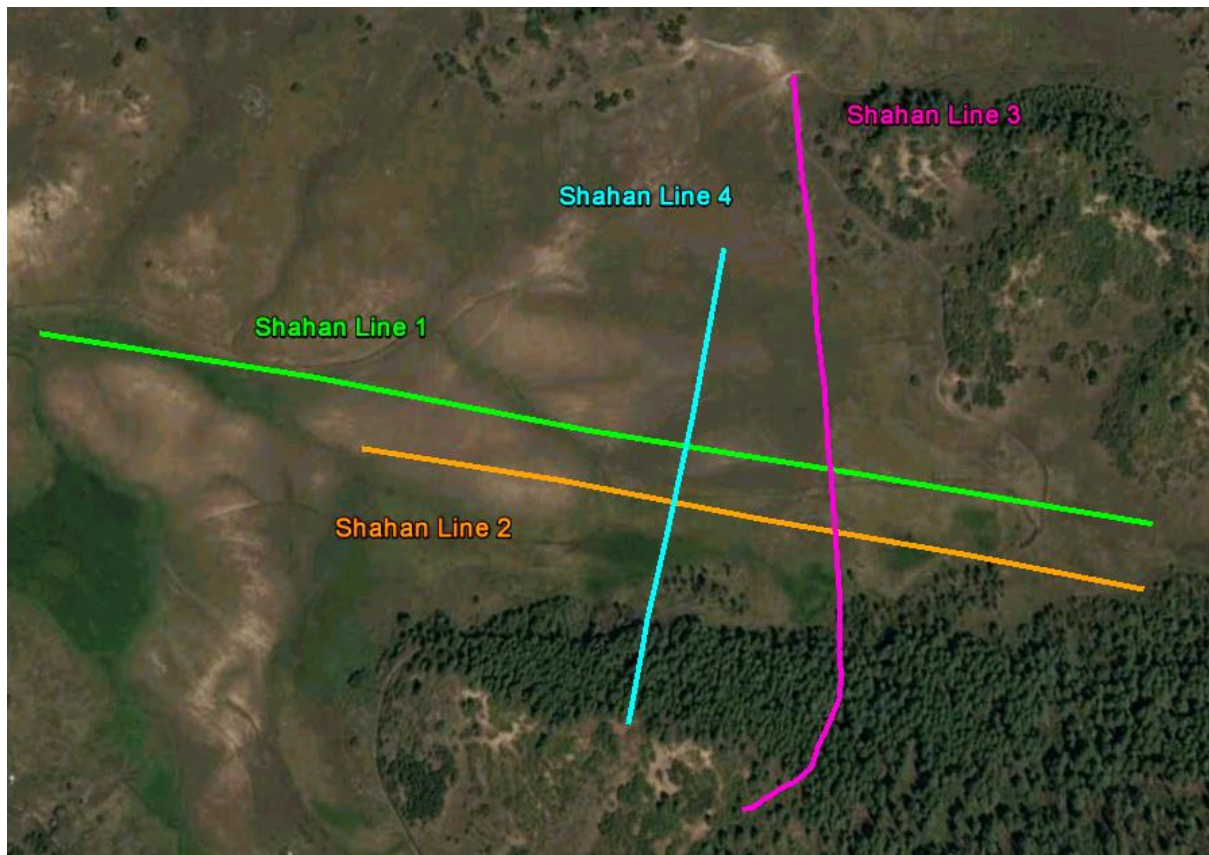
Figure 10.12: Shahan's Ranch Survey Lines
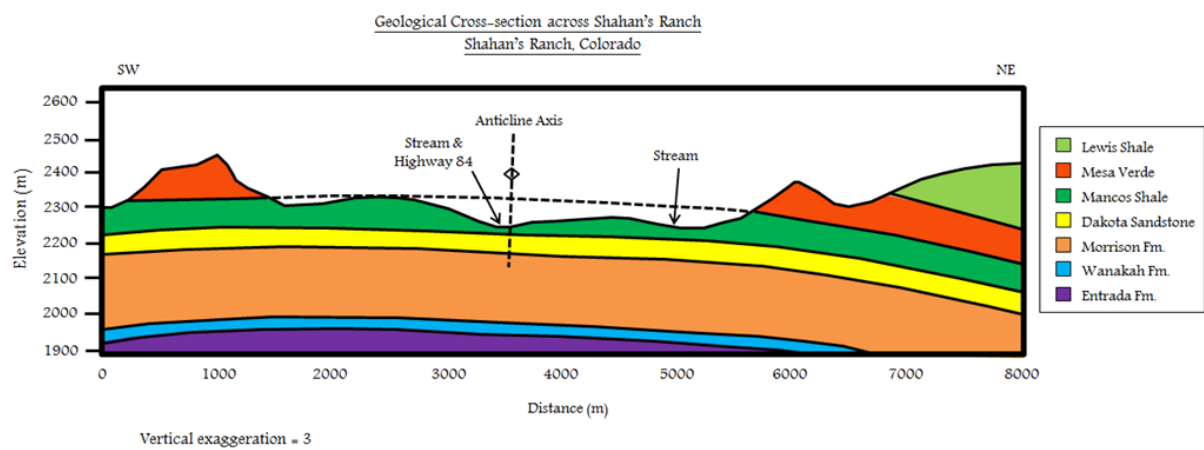
Figure 10.13: Shahan's Ranch Geology
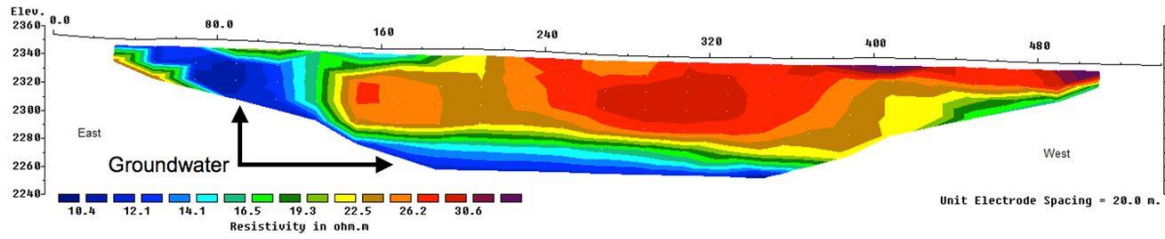
Figure 10.14: Shahan's Ranch Line Wenner Array.
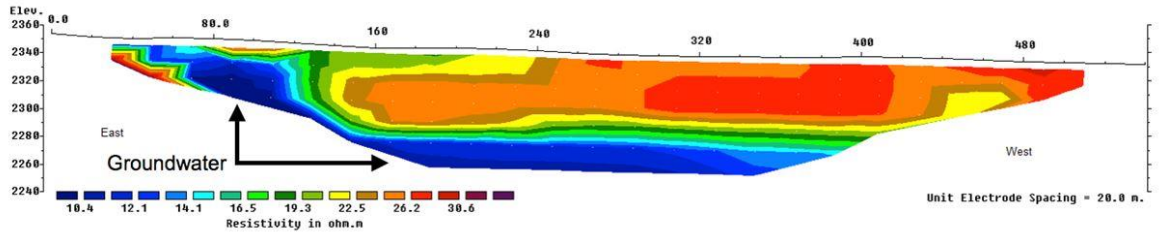
Figure 10.15: Shahan's Ranch Line 2 (Top Wenner Array bottom Dipole-Dipole)
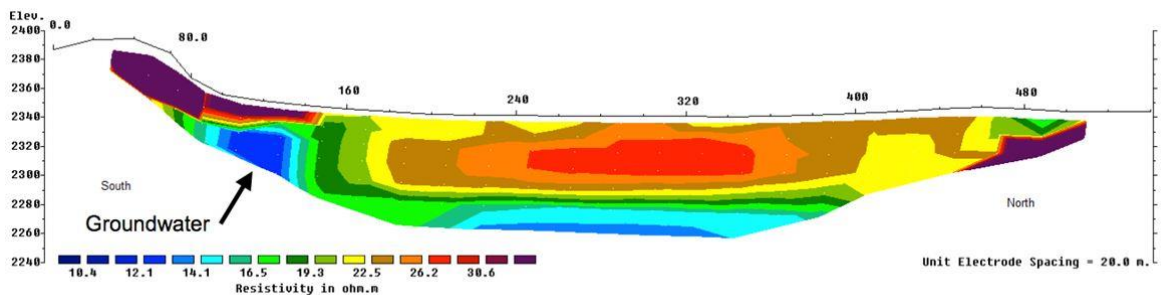
Figure 10.16: Shahan's Ranch Line 3 (Top Wenner Array bottom Dipole-Dipole)
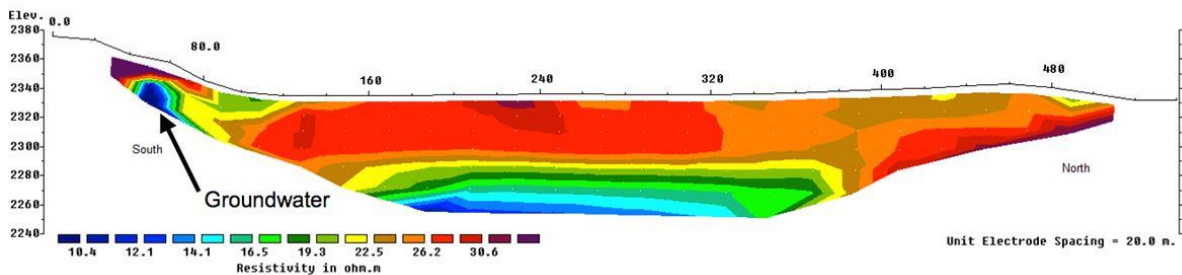
Figure 10.17: Shahan's Ranch Line 4 (Top Wenner Array bottom Dipole-Dipole)

Shahan Lines 1-4 were acquired at Shahan's Ranch using the SuperSting. Both the Weiner Array and Dipole-Dipole configuration were used. Shahan Lines 1-2 are oriented east-west. Shahan Lines 3-4 are oriented south-north. The well is on the east side. In order to make logical sense of the interpretation it is important to understand the geology of the area

As can be seen in Figure 10.13 the first layer of geology consists of shale. In general, shale has the properties of being less resistive than other types of lithology. At Shahan's Ranch there is a visible hot

158

springs and stream. This means by using DC methods, it should be possible to see the difference in conductivity between the water and shale. In fact, this is visible in Figure 10.14, Figure 10.15, Figure 10.16, and Figure 10.17. The blue shading in these figures probably indicates ground water. The SP data shows a sharp decrease in self potential around 60 meters which could correspond to fractures that are a way for the water to travel through the subsurface.

Shahan Line 3 and Shahan Line 4 were oriented roughly north to south, perpendicular to Shahan Line 1 and Shahan Line 2 (Figure 10.12). The low resistivity areas seen in Figure 10.14, Figure 10.15, Figure 10.16, and Figure 10.17 can be interpreted as areas of groundwater. There exist areas of (relatively) high resistivity near the ground surface, which were interpreted as the Mancos Shale. This interpretation is corroborated by geological cross-sections of Shahan Ranch Figure 10.13.

Another feature noticed is a potential fault (Figure 10.16). This assertion is supported by the geological cross section.

10.6 Conclusions and discussions

In the two week process of collecting DC Resistivity data at Pagosa Springs, and the two weeks of processing at the Colorado School of Mines, many interpretations were able to be made. There were at total of 5 DC resistivity lines at Pagosa Springs and 4 lines at Shahan's Ranch.

The locations in the Pagosa Springs area consisted of Mill Creek Central, Mill Creek East, Hairpin Dike 1, Hairpin Dike 2, and the Main Survey Line. All of these DC survey setups used the ABEM and Wenner Array. The Wenner Array was used because it has a higher signal to noise ratio, which is related to a greater depth of investigation. The length of the lines ranged from 1.28km-6.4km.

10.6.1 Shahan's Ranch Discussion

At Shahan's Ranch the interpretation consisted of approximating where the potential water leaking from the well is located. In order to confirm this more thoroughly, it is advised that a DC Resistivity survey is conducted using the ABEM. This will give a greater depth of investigation and a higher signal to noise ratio.

10.6.2 Mill Creek Discussion

After analyzing both Mill Creek Central and Mill Creek East, there is evidence of three potential faults. This can be seen in Figure 10.10 and Figure 10.9. The potential faults are evident because of the contrast in resistivity. A geochemical study of the area reported that there is the existence of warm water underneath the subsurface in the Mill Creek Area. This agrees with the results found by DC

inversion. There is a more conductive portion of the Dakota Sandstone thought to contain water. In the future it is recommended that another DC survey is performed in the area. The survey should have another DC line east of current Mill Creek East Line, in order to confirm the existence and extent of the potential aquifer.

10.6.3   Main Survey Line

The DC survey on the main line produced 4 clear faults. Other faults may exist, but are not as clear in the DC data collected. It is highly likely that water in this area is flowing up through the faulted areas, using the Dakota Sandstone as a reservoir. It is also likely that this reservoir is being replenished by meteoric water, as interpreted by the geology section.

10.6.4   Hairpin Dike

The hairpin dike produced one noticeable fault. This fault is also seen at the Central Mill Creek Line. In the future it is recommended that the dike should be directly crossed and not offset so that the response of this feature can be more accurately identified.

10.6.5 Comparison to Field Camp 2012

To help validate the results, it is useful to compare the computed resistivity profiles with resistivity profiles from last year's field camp, which was also held at Pagosa Springs. Only one resistivity line from 2012 overlapped with the 2013 resistivity lines. As shown in Figure 10.18, the southern end of the PAGO 04 line surveyed in 2012 overlaps with the northern end of Hairpin Dike Line 1 that was surveyed.

Comparing the resistivity profiles for these two lines (Figure 10.18), some similar features were seen. For example, both profiles show a high resistivity zone (the black circles in Figure 10.19) that was interpreted in 2012 to be the Dakota sandstone. The south end of the 2013 line shows three areas of higher resistivity, which may also be the Dakota group. Unfortunately, because only the end of both lines overlap, it is difficult to compare other features seen in the resistivity profiles.
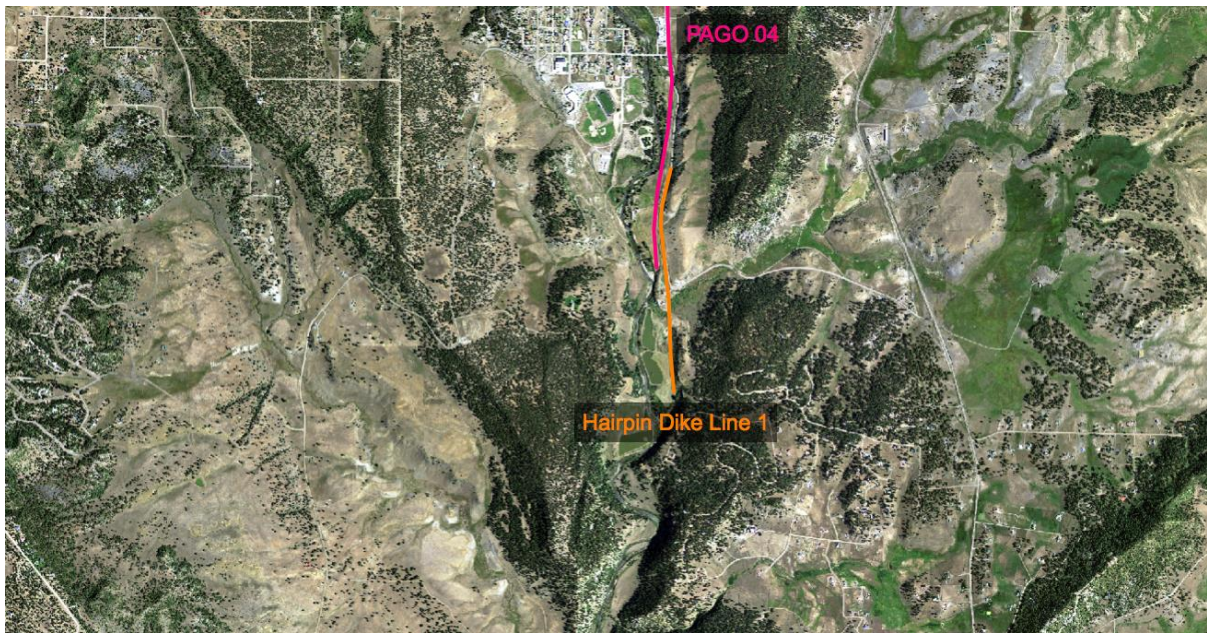
Figure 10.18: The northern end of Hairpin Dike Line 1 surveyed in 2013 overlaps the southern end of PAGO 04 surveyed in 2012
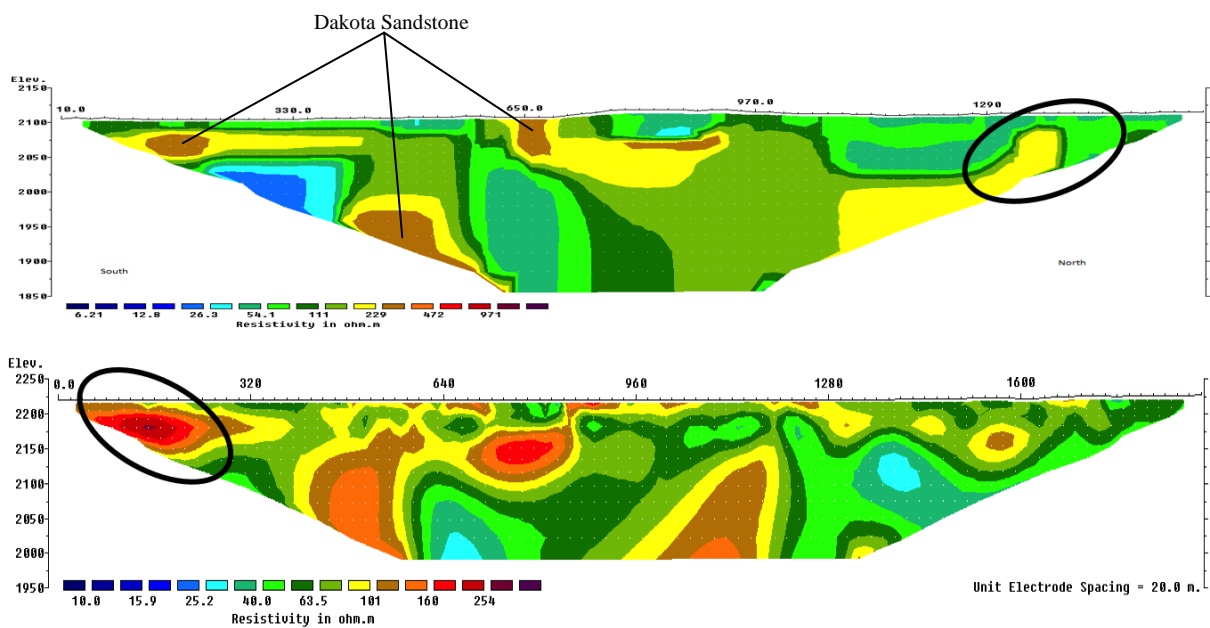
Figure 10.19: Resistivity profiles for Hairpin Dike Line 1 (top) and PAGO 04 (bottom). Notice the area of high resistivity in both profiles indicated by the black circles

10.6.6 Comparison: Deep Seismic and DC Resistivity

Since most of the DC line followed the main deep seismic line, the two surveys can be compared to confirm or disprove potential findings. Figure 10.20 shows the faults that seismic combined with DC Resistivity confirm, disprove, and supplement. Seismic data disproves every fault that DC Resistivity

interpreted besides Eight Mile Mesa Fault (see X's Figure 10.20) as there is no visible offset in the seismic section at our proposed fault locations. Also using the deep seismic data, two potential new faults become apparent (see red lines Figure 10.20). DC Resistivity interpretation for faults is non-trivial when the fault is small, as the faults seismic picked up are not clear anomalies in the resistivity data. Additionally, the faults that are believed to be apparent in the resistivity data are not visible in the seismic section. It is possible that following the model of the Eight Mile Mesa Fault is not the correct approach. More knowledge of DC resistivity interpretation would have been beneficial in the preliminary interpretation stages.
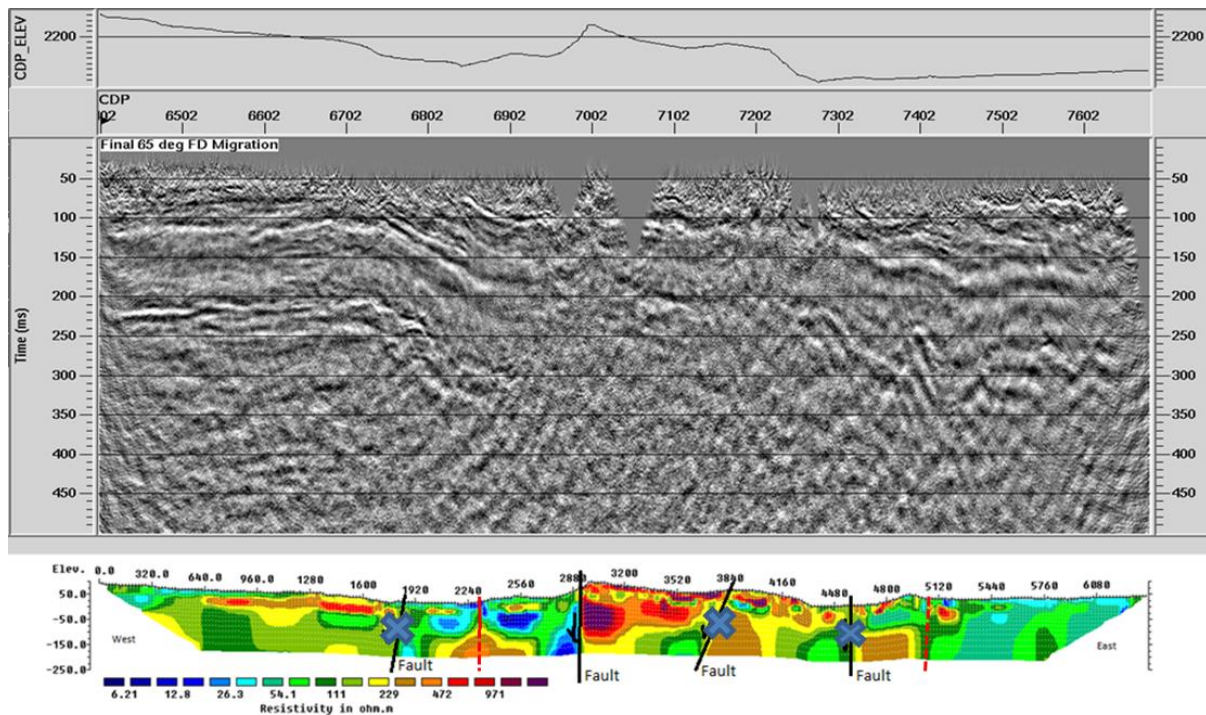
Figure 10.20: Deep Seismic and DC Resistivity Overlay

162

11. Self-Potential

11.1 Introduction

Naturally flowing electrical current in the subsurface can be created by a variety of processes generating a potential difference in the surrounding medium [75]. The produced voltage can be used to help us understand and characterize the subsurface. For example, the flow of fluid generates electrical current producing a voltage, according to Ohm's Law. Therefore, when the voltage is examined carefully, fluid direction can be determined.

Self-potential (SP) is a passive geophysical method that may be used in characterizing underground water flow. This method primarily measures the difference between potentials in two different locations. Measured anomalies are usually very small and of the order of a few hundred millivolts.

SP is widely used not only in groundwater studies, but also in mineral exploration because it can detect the mineralization potential. Moreover, this method is very cheap and easily executed, which gives it an advantage over other geophysical methods.

Figure 11.1 below shows how different underground water flow patterns affect the general shape of the SP graph. With the results of the surveys and the help of Figure 11.1, underground water flow direction can be interpreted. Therefore, this assists in understanding the geothermal system of Pagosa Springs.
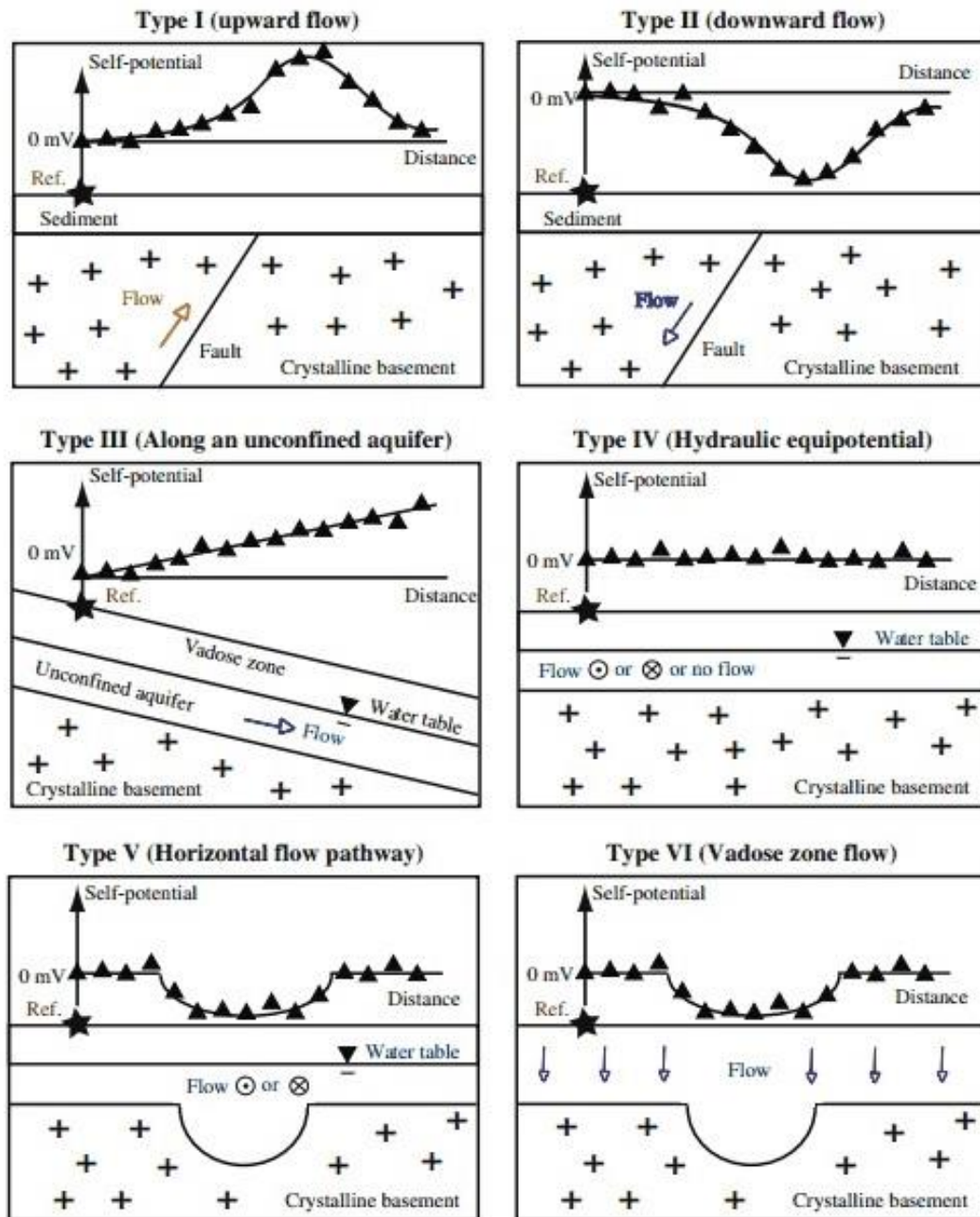
Figure 11.1: Typical self-potential anomalies [76].

11.2 Survey Locations and Design

In order to better understand the geothermal system of Pagosa Springs, a number of SP surveys were conducted along the main seismic/DC line and the secondary DC lines. By having different surveys done on the same line, correlating data becomes very helpful in achieving the ultimate goal of understanding the geothermal system, Figure 11.2.

Figure 11.2: An aerial photo of where the SP secondary surveys were executed.

Both Mill Creek lines were designed in such a way so that they cross two locations where faults were suspected to be present from preliminary processing of DC resistivity data. If confirmed, it is highly likely that water could be traveling through these fractures.

All three lines were intentionally designed so they touch at some point. This allows the data to be tied together. In this way, some of the processing stages become easier. For instance, the correction of reference electrodes. Table 11.1 below shows the specifications of each line:

Table 11.1: Specifications of Survey Lines

Line	Total Length (m)	Electrodes Spacing(m)	Number of Electrodes
Hairpin Dike	1260	20	64
Mill Creek Central	1260	20	64
Mill Creek East	1260	20	64

11.3 Processing

Like any other geophysical survey, self-potential data must be processed before they are ready for interpretation. Processing SP data is not as complicated as processing other data as it only consists of two corrections. The first correction accounts for drift in the electrodes. The second correction ties datasets together so they might share the same reference electrode despite the real location of reference electrode varying between surveys. These two corrections have to be performed in this order. If the reference correction were to be performed first, the ΔV that is applied to the second data set would be incorrectly greater due to the drift effect. After the corrections have been performed, a program called "Surfer" plotted the data.

11.3.1 Drift Correction

There should be no difference between potential measurements at the same location. However, as the survey progresses, that is not the case. There often is a difference and the magnitude of the difference depends on the type of electrodes used. The drift correction aims primarily to zero out this difference in potential measurements.

The electrodes used in the field were first generation which means they are worn and less accurate. Soaking the electrodes in water before use helps minimize the effect of drift. However, this does not eliminate all drift.

In order to be able to perform the drift correction, the potential at the reference location was measured at the beginning, the middle, and the end of the survey. It is also assumed that a linear drift effect exists. Equation 11.1 was used to calculate the equation of the line, and this when then applied to the data.

$$D = m * n + b$$

Equation 11.1: Correction for Drift

Here, *m* is the slope of the line which is equivalent to $\frac{\Delta V_1 - \Delta V_2}{-(N-1)}$, *N* is the total number of indices, *n* is

the current index, and *b* is ΔV_1.

Drift Correction
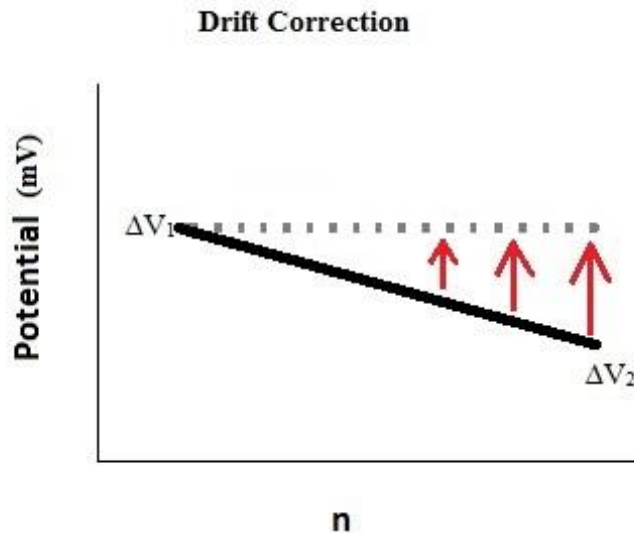
Figure 11. 3: Plot shows how drift is corrected

As illustrated in Figure 11. 3, the way drift is corrected is to try and match the value of the second measurement of the potential at the reference location with the first. Below in Figure 11.4, raw data is plotted in blue and drift corrected data is plotted in red. The difference in potential at the beginning is approximately 0 mV. However, due to the drift effect, the raw data started around 150 mV. Therefore, when doing drift correction, the data had to be shifted down.
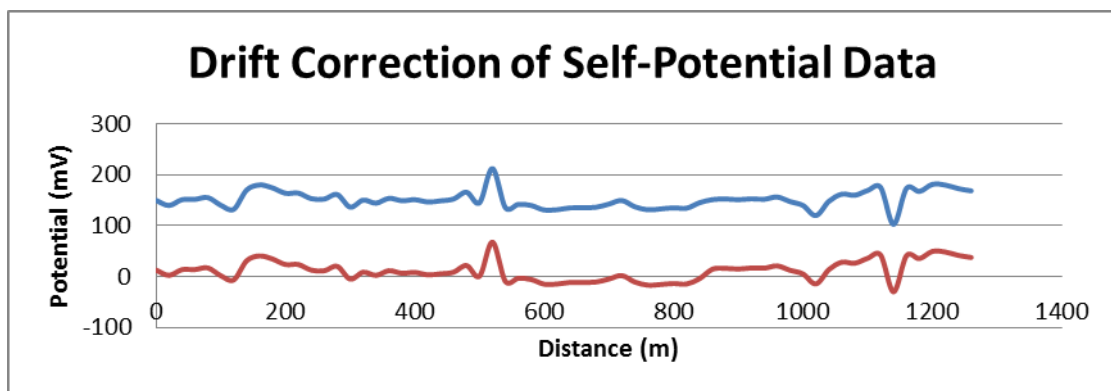
Figure 11.4: Effect of Drift on Data

11.3.2 Reference Correction

The reference electrode is an essential element in every self-potential survey. This is due to the measured values in the survey being relative to the electrode's value rather than being absolute.

The length of the reels creates a limiting factor to the size of the survey. Therefore, in large surveys, the reference electrode location must be moved. As the location of the reference electrode changes, the measurements will start from approximately 0 mV again.

In order to be able to correct for changing in reference location, there must be overlapping data from both sections. So, when starting a new section with a new reference electrode location, two to four

167

measurements have to be taken from the previous section. The average of these is equivalent to the amount the second section must be shifted. Figure 11.5 shows the error caused by changing the reference location and how it is corrected. Essentially, all sections are shifted by the average of the difference between the overlapping points except for the first section.
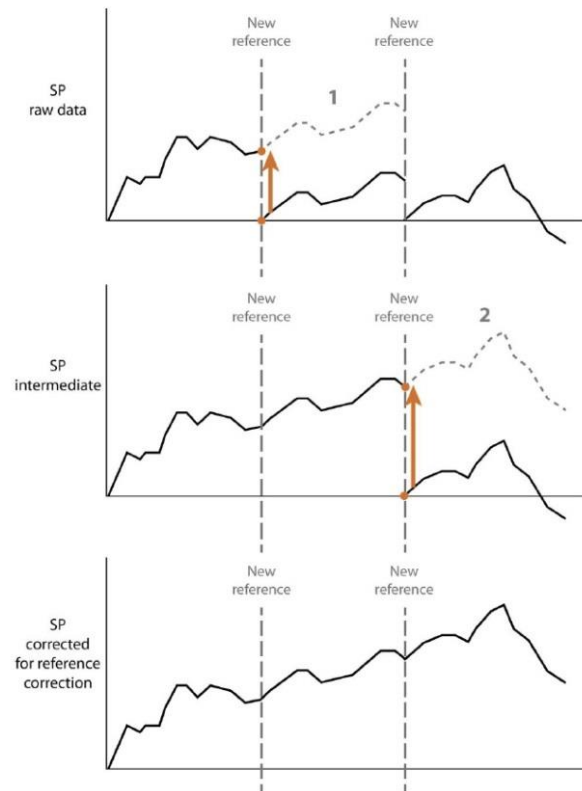
Figure 11.5: Reference Correction [77].
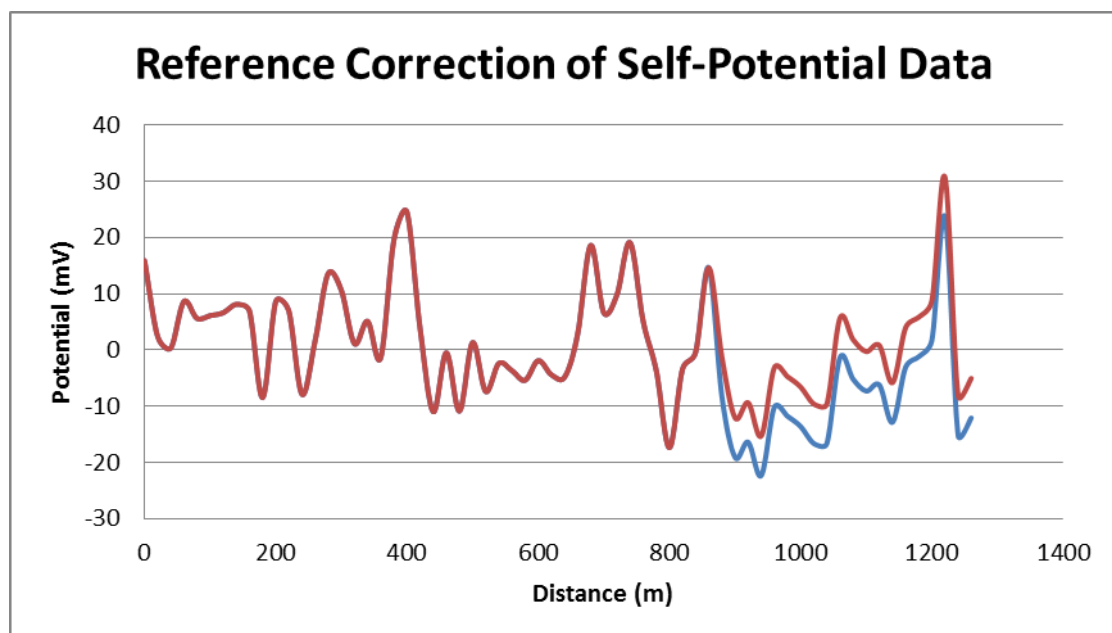
Figure 11.6: Reference Effect on Data.

168

As illustrated in Figure 11.6, a new reference location is placed at 880 m. Blue corresponds to reference uncorrected data whereas red corresponds to the corrected data. All data points after 880 m in the uncorrected plot were shifted up by 7 mV which is the average of the difference between the overlapping data points.

Finally, after correcting the three lines, the data was all referenced to the main line running along the deep seismic line. This is done so that all datasets are referenced to the same electrode and to ultimately enable the creation of a 2D map.

11.3.3 2D SP Map Using Surfer

After all of the corrections were applied to all SP data from the Hairpin Line, the Mill Creek Central Line, Mill Creek East Line, and the main seismic line East of the San Juan River were compiled. Next, the compiled data was used as an input file in Surfer to create a variogram (Figure 11.7). This variogram was then used as a model guiding the optimal interpolation between data points using the kriging method. Lastly, the interpolated and acquired data were used to create the desired 2D SP map of the region [77]. The parameters used for the variogram are Nugget Effect and the Quadratic Effect.

Table 11.2 shows the parameters for the Nugget and Quadratic Effect used to create this variogram. Note that an interest exists in the regional SP trend. Thus, any variogram that fits the data better than the model in Figure 11.7 results in over-fitting and the 2D map would show only the local contrast of the SP data instead of the regional SP trend. For a detailed description of the kriging method and its variogram, refer to Appendix G.1.

Table 11.2: Variogram parameters for SP 2D map.

Effect Used	Error Variance	Micro Variance	Scale	Length	Anisotropy Ratio	Anisotropy Angle (degrees)
Nugget Effect	108.8	0	None	None	None	None
Quadratic Effect	None	None	176.8	396.2	1.274	167.0
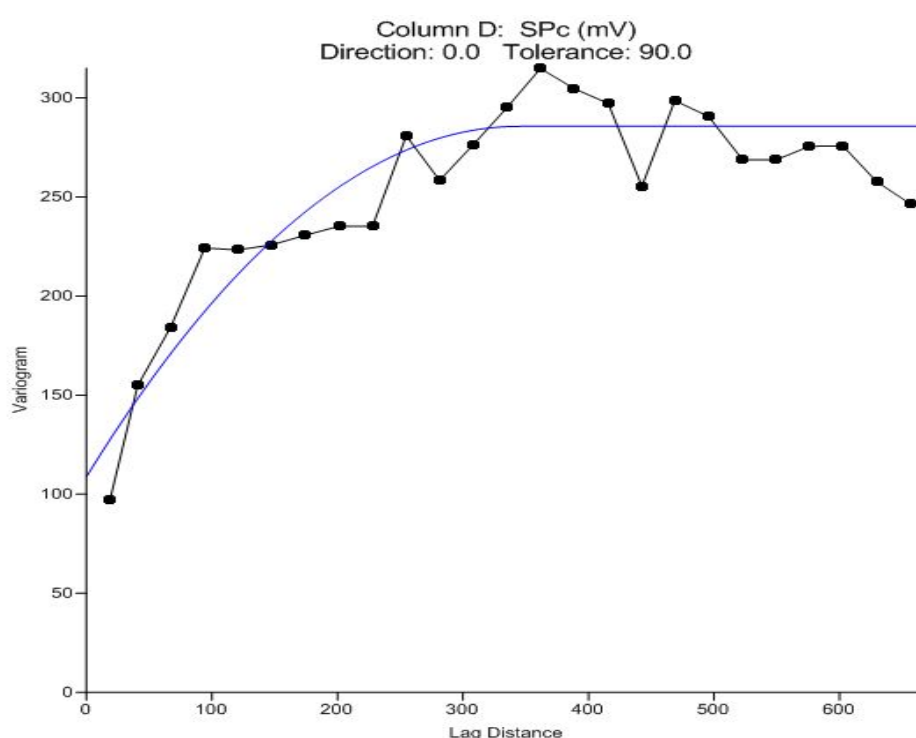
Figure 11.7: Resulted Surfer Variogram.

11.4 Uncertainties/Errors

As with all geophysical methods, assumptions are made in both acquiring and processing the data. The assumptions made during the data acquisition and processing include the SP responses on both sides of the banks of San Juan River being the same, and the instrumental drift being linear. This made it possible to make the assumption that the SP responses on both banks of San Juan River are similar as the soil and rock layers on both sides of the banks were determined to have the same stratigraphy. Thus, the water penetration depths and patterns should be similar on both East and West banks and their effects on the SP response should also similar. With this assumption, difficulties in crossing the river could be avoided. Also, it was assumed that the instrumental drift is linear. This is a

simple model, requiring only having to record the instrumental drift value at the beginning and end of each survey. The uncertainty observed is the fluctuations of the SP response readings. The range of reading variations was recorded for future reference. Lastly, a small error may have occurred during the acquisition process since the electrodes were the first generation equipment and their sensitivity might be lower than that of more recent equipment.

11.5 Interpretations

Interpreting self-potential data without the aid of other datasets from other methods is unlikely to be very reliable. However, with the use of geology and DC resistivity models, this becomes an easy task that could confirm some of the hypothesis built based on the results of other datasets.

In reality, there are a number of sources that could generate SP signals, like subsurface chemical reactions. However, for the sake of simplicity, all the SP signals measured are assumed to be generated by underground water flow.

11.5.1 Mill Creek Central

The DC resistivity data showed that there could be faults on both ends of this profile. In order to confirm the existence of these faults, the SP profile was used. It can be clearly seen in Figure 11. 8 8 that there are self-potential anomalies at their locations of the faults. With the aid of Figure 11.1, the northern anomaly is indicative of underground water traveling up through the fault fracture. On the other hand, using the same figure and some geologic perception, the southern anomaly is more likely to be where the water infiltrates the ground due to the shape of the anomaly and the fact that it is located on the bottom of the valley.

Like any other geophysical surveys, SP surveys usually incorporate data noise. Crossed data points in Figure 11. 8 below are believed to be noise due to inconsistency with adjacent data points. If the noisy spike at 520 m were to be disregarded, the anomaly at the middle would be clearer and follow the topography of the potential aquifer.
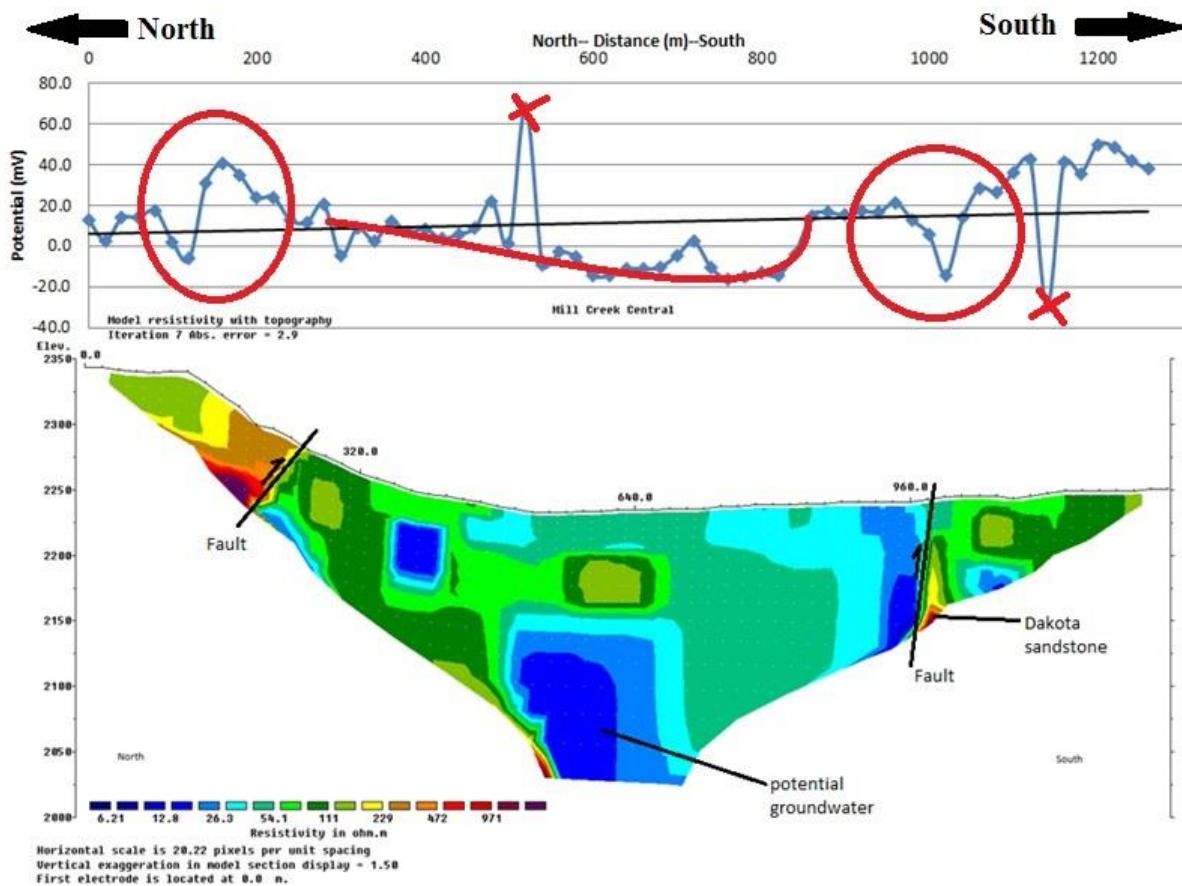
Figure 11. 8: DC Resistivity and SP data in the Mill Creek Central area

11.5.2 Mill Creek East

The self-potential as well as the DC resistivity profiles show a number of anomalies in along this line. The DC shows that there are two potential faults in the subsurface, however only one of them was present in the SP data. This line runs not far from the Mill Creek Central line, so it is possible to correlate the results.

The northern fault that cuts through the Mill Creek Central line appears in the northern part of this line as well. The anomaly in circle A of Figure 11. 9 below corresponds to the fault as underground water travels through it.

The middle section of the SP profile seems smooth and would characterize the same aquifer as in the Mill Creek Central line. High SP measurements (anomalies) identified in Figure 11. 9 such as circle B is an area of interest. The anomalies could be caused by subsurface fluid flow as in Figure 11.1 type III where fluid flows up. This interpretation is also supported by a geochemistry study which was carried out in the area. The geochemistry results show high temperature in this area. Generally, high temperature fluid tends to flow upwards while low temperature fluid tends to flow downward. In conclusion, both SP measurement and geochemistry study results lead to the interpretation that, potentially, there is hot water flowing upward in the area B.

172

The survey log indicates that the measurements taken in circle C (Figure 11. 9) are located over the North and South banks of the creek. Hence, the anomalies in circle C are likely to be caused by fluid flow in the creek.
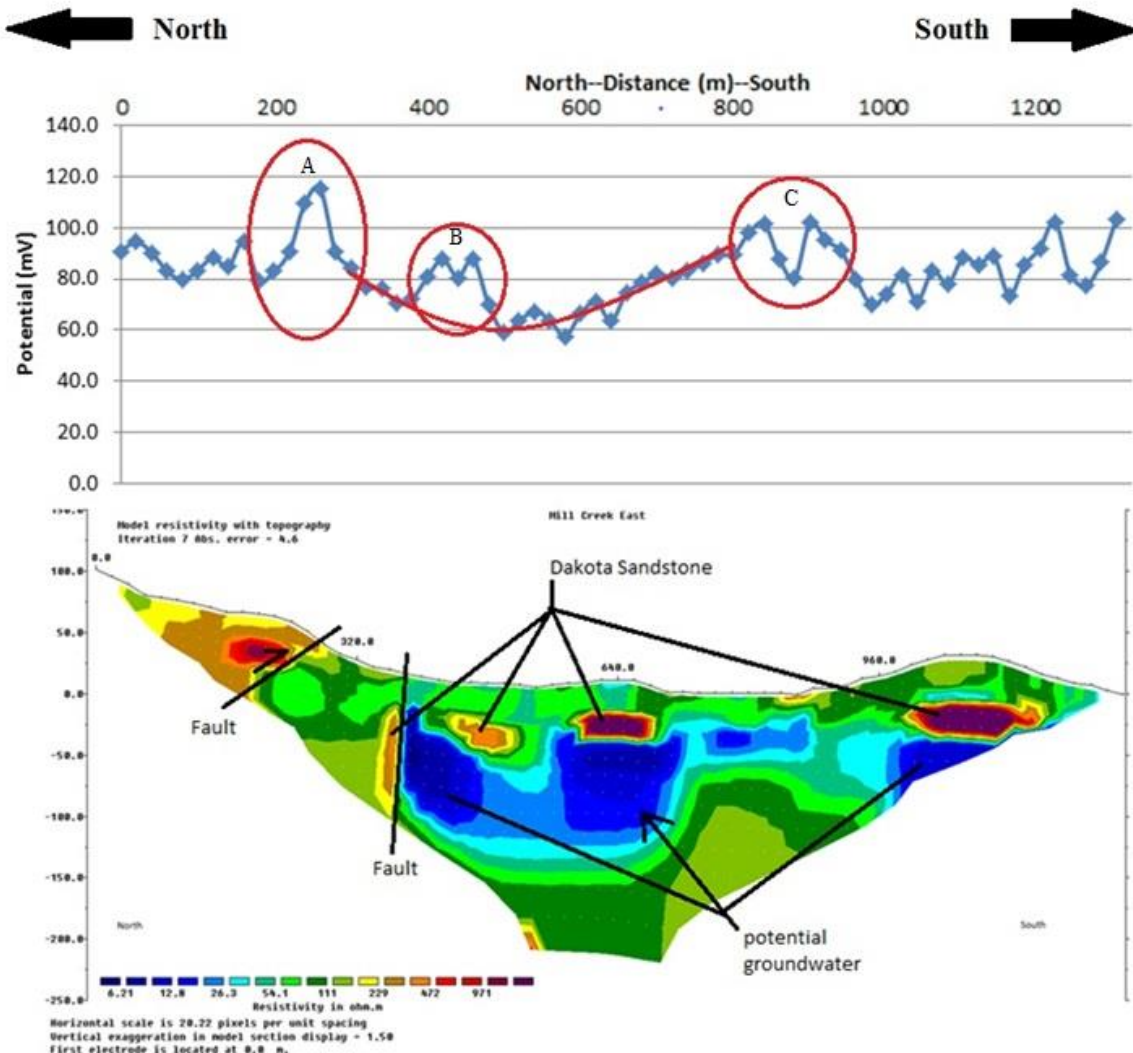
Figure 11. 9: DC Resistivity and SP data in the Mill Creek East area.

11.5.3 Shahan's Ranch

As an important introduction of this line at Shahan's ranch is that the topography was moderately flat. Also, the area is mainly covered by the Mancos shale, which has high conductance unlike the Dakota Sandstone, which is very resistive.

A temperature probe was inserted into the artesian well in order to measure both the temperature gradient and the depth of the well. The depth of the well is a very useful piece of information when interpreting the DC and SP data. As illustrated in Figure 11.10, the DC resistivity profile shows that there is a very conductive layer below the shale. This layer cannot be the underground water upwelling because the temperature/depth measurement

showed that the depth of the well is more than a 330 m, whereas the conductive layer is coming from a depth of 27 m.

There were areas on the ground at the Shahan's Ranch where it was very saturated. This is an indicative of leakage along the channels that runs from the well to the entire ranch. The leaking water is represented by very conductive areas of the DC resistivity profile.

Observing the SP profile, it agrees with the DC resistivity profile in regions of model ambiguity. Line A, towards the East part of the profile, shows that there is little change in the ground potential as it is mostly saturated with water. However at circle B, there exists a sharp trough, this is explained by the transition between the saturated soils to the dry Mancos shale. Finally, line C resembles type III in Figure 11.1 which corresponds to water flowing downward East to West. This is interpreted to be leaking water peculating through fractures in the shale.
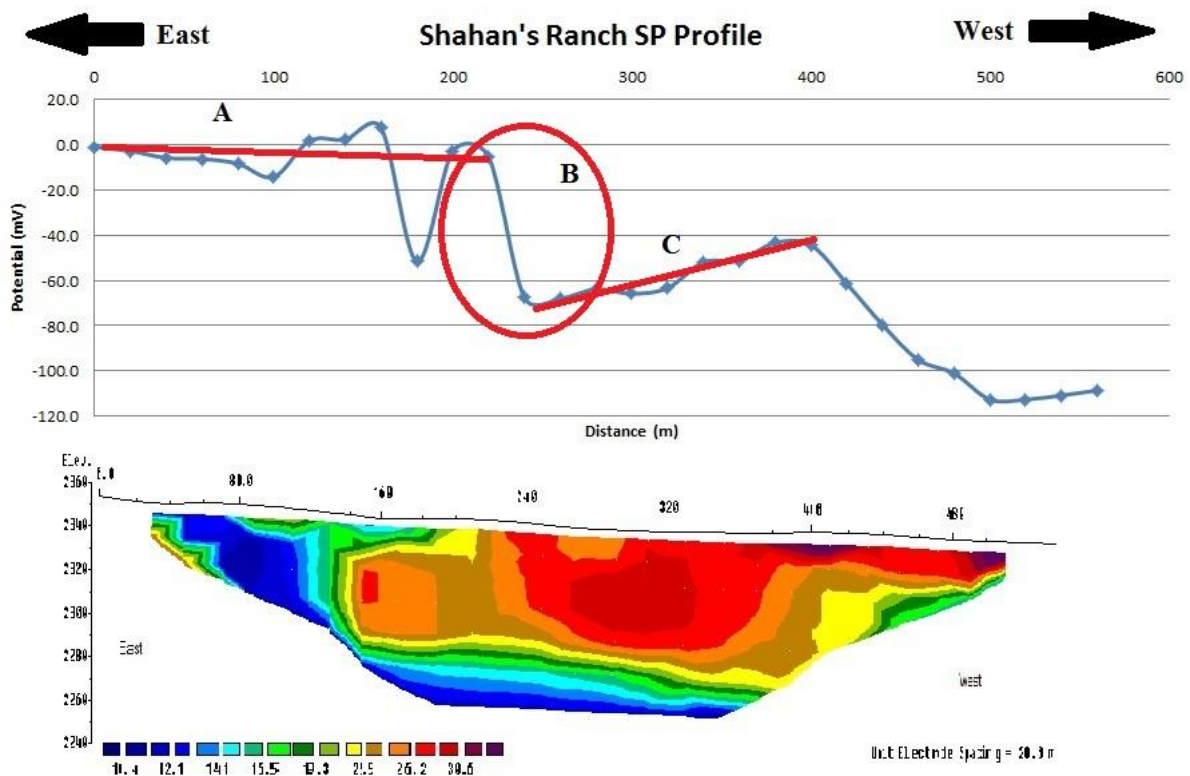
Figure 11.10: DC resistivity and SP profiles.

174

11.5.4 Deep Seismic

The deep seismic survey was the major line where most of the geophysical methods were conducted. Along this line the DC resistivity data showed four locations of potential faults, one of which has been confirmed by field observations.

The smooth curve A in the SP profile, Figure 11.11, is likely to be caused by upwelling water traveling through the fault interpreted by the DC resistivity data. On the other hand, the anomaly at location B in the SP profile confirms the presence of the major fault, which was also observed in the field.

The data appears shifted up at the location of fault B and remains at this level. This might be caused by poor processing or data collection. Consequently, no further interpretation can be made.
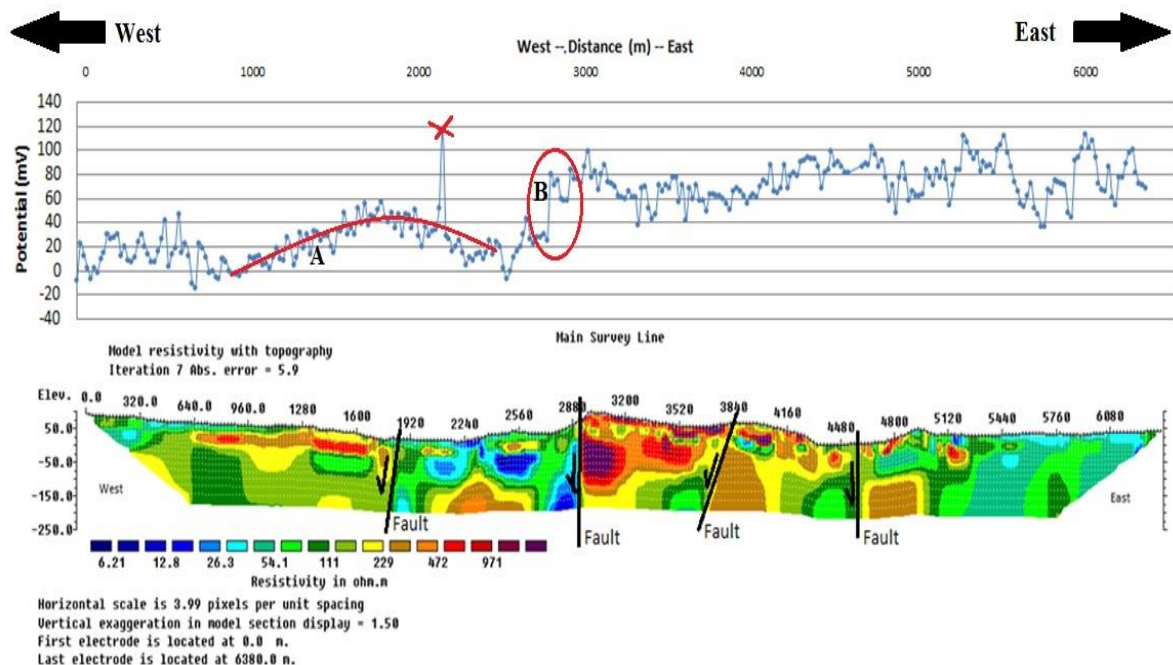
Figure 11.11: Main Seismic/DC_SP line with DC and SP profiles.

11.5.1 Surfer 2D Plot

After the datasets have been fully processed and referenced to a single reference electrode, they were used to plot an interpolated 2D map of the whole surveys area. This map can be used to understand the broad regional pattern of water flow.

As Figure 11.12 illustrates, towards the bottom right corner there is a high anomaly. This can be a location where water is upwelling. There exists some anomalies toward the North in both Mill Creek East and Central lines. This indicates the location of the fault that runs through both   of   the   lines.

As the map shows, the most of the North and the north-western parts of the region are missing. Therefore, this could be an excellent line proposal for the 2014 field session. The reason why the missing region should be surveyed is to better image the fault that runs North-East and to try to understand how it contributes to the overall geothermal system of Pagosa Springs.
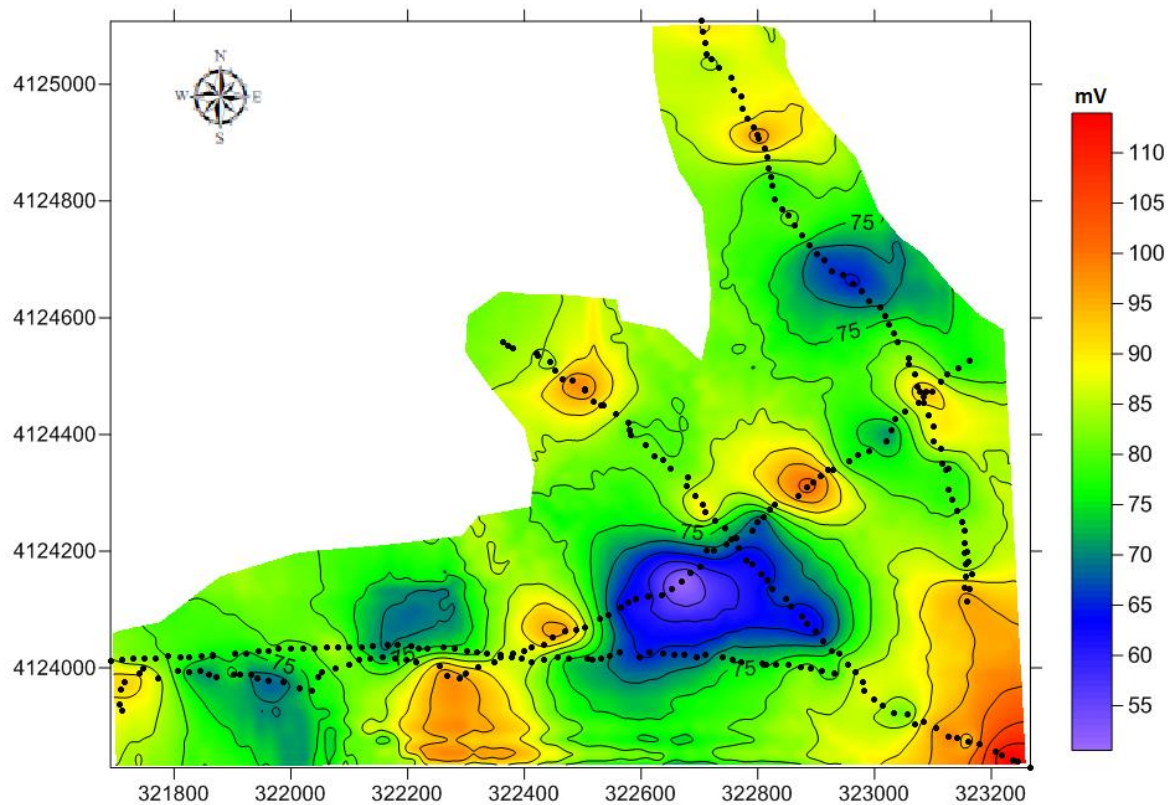
Figure 11.12: An interpolated SP contour map over the Mill Creek area.

11.6 Conclusions

In conclusion, the geothermal system of Pagosa Springs is complicated. In order to understand the system, one has to answer some questions, for instance, where is the water coming from? Where is the heat source coming from? And how does the water travel in the subsurface?

A vital step to understand is how the water travels underground, primarily resolved by studying the geology of the area. In Pagosa Springs, the two main ways of water traveling through rock is either through the Dakota Sandstone, as it is highly fractured, or along fault planes. Self-potential is a geophysical method that is used to characterize underground water flow pattern. Therefore SP anomalies could indicate the existence of faults, or flowing aquifers. Locating faults is crucial in understanding the geothermal system of Pagosa Springs.

SP data are hard to interpret by themselves; this is why they are usually correlated with other geophysical techniques, often DC-resistivity. Further geophysical methods were employed in the area in order to find the geometry of the Pagosa Springs regional geothermal network. Combining this data from various techniques supports the conclusions drawn from any singular method.

12. Ground Penetrating Radar (GPR)

12.1 Introduction

Ground penetrating radar (GPR) is an active geophysical technique that is conceptually similar to seismic exploration, but uses electromagnetic (EM) waves instead of acoustic waves. GPR acquisition involves transmitting EM waves of radio frequency into the ground from a transmitter located on the surface. These waves undergo reflection, refraction, and diffraction at boundaries between subsurface layers that possess different EM properties. Among these properties are the electrical conductivity and the dielectric permittivity, both of which affect the velocity of the EM waves in geologic layers [79]. The responses from the subsurface are recorded in a receiver and stored as a digital signal to be processed later. In general, different rock units have different electrical properties and thus GPR can be applied to understand the structure and orientation of those rocks in relation to each other. Importantly, subsurface groundwater is also a key control on the propagation of EM energy.

Within media with elevated electrical conductivity, such as clay or soil, EM waves experience greater attenuation. Under these conditions the depth of penetration of EM waves will be low and only the layers of rock/soil very close to the surface will be imaged. Under favorable conditions, GPR provides the highest resolution images of any subsurface measurement. This is typically on the centimeter scale, but even then the typical depth of penetration is only around 5 meters. An acquisition parameter trade-off must be made between the depth of investigation and the resolution of the resulting data.

12.2 GPR Survey Locations

GPR data was acquired in 8 different locations of interest (Figure 12.1) around Pagosa Springs, with the focus being on understanding the properties of the various rock types belonging to the geothermal system e.g. the Dakota Sandstone, Mancos Shale and Travertine deposits.

The 8 locations are as follows (with further location details provided in the interpretations section):

1) Dakota Bench
2) Dakota Seismic
3) Hairpin dike
4) Travertine deposit at the mother spring in town
5) Chemical precipitates (here termed 'White Patches') to the West of the San Juan near the hairpin dike
6) Start of seismic line
7) Pagosa pipes

8) Fort Lewis cemetery
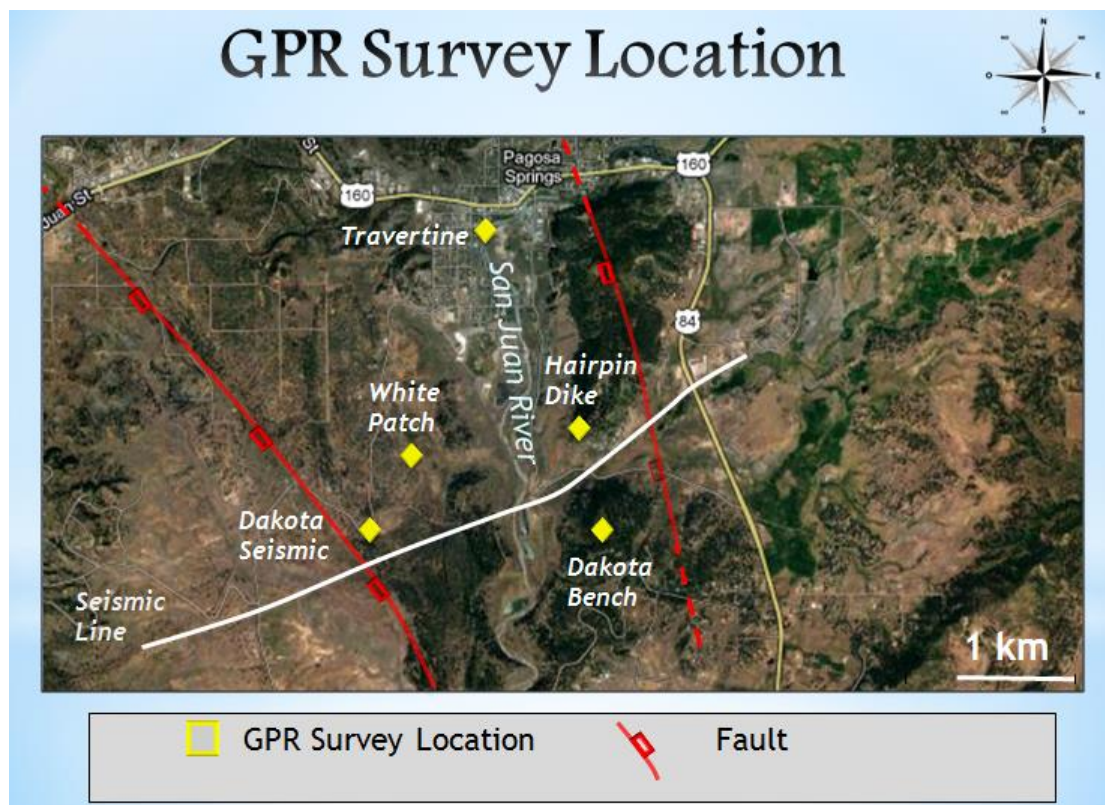
Figure 12.1: Location Map of GPR surveys

Given the relevance to the content of this report, processing and interpretation of locations 1 through 5 were prioritized. The data quality of the remaining surveys limited their applicability to this report. Survey 7 was conducted at the request of the town council in order to attempt to identify leaks in pipes servicing the town. Survey 8 was an attempt to discover the locations of unmarked graves. Issues with both of these surveys were related to the coupling of the odometer to the wheel which reduced the reliability of spatial information within the data. Nevertheless, we recommend processing of the data to be completed at a later date to explore their findings. The general steps taken in processing each of the surveys, along with an overview of processing theory can be found in H.2 Processing. Interpretations of the 5 processed data sets can be found in 12.5 Interpretations.

12.3 Survey design

The piece of equipment used throughout the GPR surveys at Pagosa Springs was the Sensors & Software PulseEKKO PRO. The equipment consisted of control and recorder units that are linked to 500 MHz center-frequency receiver and transmitter units (Figure 12.2). When used in common-offset configuration, the transmitter and receiver units are separated in a skid plate by a fixed distance of 23 cm and transmissions are triggered by a calibrated odometer wheel mounted on the rear of the plate. The units are mounted in the skid plate which ensures a consistent coupling with the ground. The

plate is then simply pulled across the surface behind the operator to conduct a single 'sweep'. In general our GPR surveys were configured as a sweep of parallel lines in a rectangular grid. The typical grid size is on the order of 30x30 meters, with an acquisition line spacing of 50 cm. Throughout each survey the odometer was set to trigger a reading every 4 cm along each line.

All acquisitions were carried out in common-offset mode. This mode of operation makes acquisition and subsequent processing of the data easier, faster, and more robust. However it restricts the range of processing algorithms compared to a typical reflection seismic routine (it is not possible, for example, to perform stacking or pre-stack migration operations). A small amount of common midpoint (CMP) data was acquired for velocity control. A transmission frequency of 500 MHz was used throughout the Pagosa Springs investigation which for a typical GPR velocity of ~0.1 m/ns gives a wavelength of 20 cm. After migration, spatial resolution is improved to one fourth of the wavelength.

Figure 12.2: Sensors & Software pulseEKKO PRO GPR system [80]

12.4   Uncertainties/Errors

The main source of error in the dataset is directly related to the topography. Topography affects the coupling of the skid plate and the ground which allows airborne GPR energy to reverberate in the underlying air gap. Such airborne energy typically has higher amplitude than ground-propagating energy which can mask useful signal energy. Poor coupling also means that the depth of penetration will be less than expected, resulting in lower quality data. Since acquisition grids are established using tape measures, topography also influences the accuracy of grid dimensions. Another important factor that could cause uncertainties is the sensitivity of the odometer; if the wheel does not turn or is caught in any way, it will not trigger the recording device to take a measurement. Such difficulties were encountered during acquisition at the Ft. Lewis Cemetery location.

When the GPR grid data was acquired, the PulseEKKO was dragged alongside the tape measure. It might not have been consistently parallel to the tape measure. Also, the start and end of each line might not be at the exact same distance along the grid; no inter-survey GPS data was available to correct and quantify this error. During processing this is taken care of by application of a simplistic linear interpolation algorithm that regularizes all the lines such that their start and end points and the total number of samples are consistent. Though not a perfect solution, this allows further processing of the data to be carried out in a much more efficient manner. This regularization means that samples could be moved laterally on the order 10 cm if necessary.

Data processing uncertainties arise primarily during migration; the data is acquired as a series of 2D lines and as such a 2D algorithm is implemented. This algorithm does not take into account the effects of side-swipe (i.e. reflections from out-of-the-plane of the survey). In essence, the data is migrated under the assumption of a 2D world. Another assumption applied during both NMO correction and migration of the data is that of a single velocity subsurface model, i.e. no lateral or vertical GPR velocity variation. This assumption is inherently inaccurate, but for the purposes of our investigation this assumption is an acceptable one to make especially in light of inferences from CMP velocity analysis. If the assumption was not reasonable, artifacts such as diffraction hyperbolas would remain in the data after migration. Such effects were minimal in the processed data, and so this single velocity model is considered an acceptable assumption to make.

Another source of error in the data is interference with cell phone frequencies. However, the interference from such devices does not tend to lie in the same frequency range as the acquisition signal and a simple bandpass filter can be used to remove most of this noise. In conclusion, the most important factor to consider for minimizing error and assumptions in GPR data acquisition is a fairly

even ground surface with minimal obstructions. Errors in processing such as migration are minimal compared to those in acquisition.

12.5 Interpretations

12.5.1 Dakota Bench

A GPR survey was acquired on a Dakota Sandstone outcrop approximately 200 m to the south of the hairpin turn with the dike outcrop (Figure 12.3). The survey covered a 12 x 25 m grid of 49 lines separated by 0.25 m. With a shot trigger spacing of 0.04 m, a total of 626 recordings were taken along each line. The acquisition started from the northwest corner with lines running west-east, and increasing inline numbers moving towards south.

The data was processed (H.2 Processing) using ProMAX using Ormsby bandpass filtering with parameters 50-150-700-1500 and Kirchoff post-stack time migration with a simple one-layer 0.12 m/ns velocity model.

Figure 12.3: Location of GPR surveys close to the hairpin dike

Interpretation of horizons in the data was carried out in ProMAX and exported to Surfer 8 to produce depth maps. One very prominent and laterally consistent horizon was identified at approximately 1.6 m depth, with a further two possible horizons also interpreted at 2.5 and 3.2 m depth respectively. It should be noted that these deeper horizons were not easily identified and appear to occur at the limit of GPR penetration depth at this location (3 m penetration depth is very good for GPR). Figure 12.6 shows a plain view of the three interpreted horizons to more clearly show the variation in depth for the boundaries of each layer (darker colours are deeper, deepest interpreted horizon on left and shallowest on right).

The interpretation of the data reveals sub-parallel bedding within the Dakota Sandstone, with bed thicknesses of approximately 1-1.5 m. The beds were proposed to correspond to sections of rock with variable weathering due to differing levels of exposure. This interpretation reveals fine structure which could be helpful in understanding preferential flow paths for fluids within the rock. Attempts were also made to track fractures visible on the surface into the subsurface by looking at un-migrated sections of data. In such sections, diffraction hyperbolas would be present at the locations of discontinuities within the rock. This proved difficult, and given the relatively shallow penetration depth, it would be hard to argue for continuation of fractures deep into the subsurface.
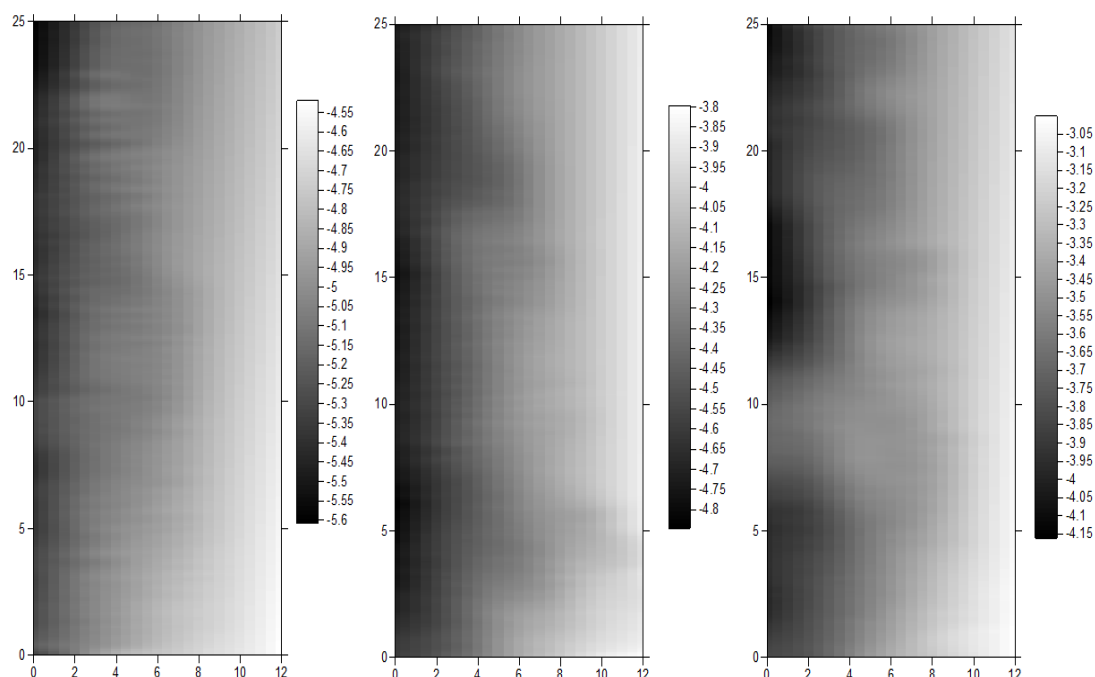
Figure 12.6: Plan view of the three interpreted horizons within the Dakota Sandstone. Left to right are the deepest to shallowest horizons.

12.5.2 Dakota Seismic

The "Dakota Seismic" GPR grid is located north-east of the recycling-center hairpin turn near seismic line in the northern field. The survey was a 30 x 30 m grid with 0.5 m line spacing oriented north-south. The grid had a slight dip towards the north-east (approximately 1-2 m for length of the grid). Basic data analysis showed that the data towards the beginning of the grid had higher attenuation, presumably an influence of different water content in the topsoil, and data toward the end of the grid (+20m) were much clearer.

The survey was designed to test the depth of GPR wave propagation from soil-water saturation and the depth of the weathering layer. These factors will affect the nature of the contact between soil and Dakota sandstone which in turn will affect the quality of imaging. GPR data was processed using the ProMAX software package to remove noise and other data artifacts resulting in better imaging of the shallow section of subsurface.

Based on the processed 3D GPR data grid, two horizons were interpreted as corresponding to the two strongest event/reflectors in the grid. These were related to the top of the Dakota Sandstone Group and its internal bedding.

The first horizon (Figure 12.7) possibly corresponds to the contact between soil and the Dakota Sandstone group. This was interpreted because 50 m to the south, the Dakota Sandstone group surface exposure was observed. This means that the thickness of formation above sandstone is not significant. The electromagnetic impedance contrast between the soil and Dakota Sandstone group should be very strong. Beneath this contact, similar responses were observed to those in the Dakota Bench GPR data, where measurements were obtained directly on the top of the Dakota Sandstone group. Interpretation of the Dakota seismic dataset extended from 0-15.5 m in X direction and from 13.08-30 m in Y direction (from 1 to 24 inline).

The second horizon (Figure 12.8) could be interpreted as an internal bed in the Dakota sandstone group as the average thickness of the Dakota Sandstone Group is around 60 m and the maximum depth of penetration of GPR data would be around 4. Interpretation extended from 0-6 m in X direction and from 14.5-30 m in Y direction (Figure 12.9).

Software limitations did not allow the interpretation of low amplitude reflections as they are not very correctable in the inline direction. A recommended option would be to load the data onto formal seismic interpretation software which will allow the use of all three dimensions of the data and additional interpretation techniques available only in seismic interpretation packages.

Analysis showed that the rest of the grid data quality are very low, no reflections corresponding to geological features are observed. This could be explained by high water saturation of the soil at this area which results in rapid signal attenuation.
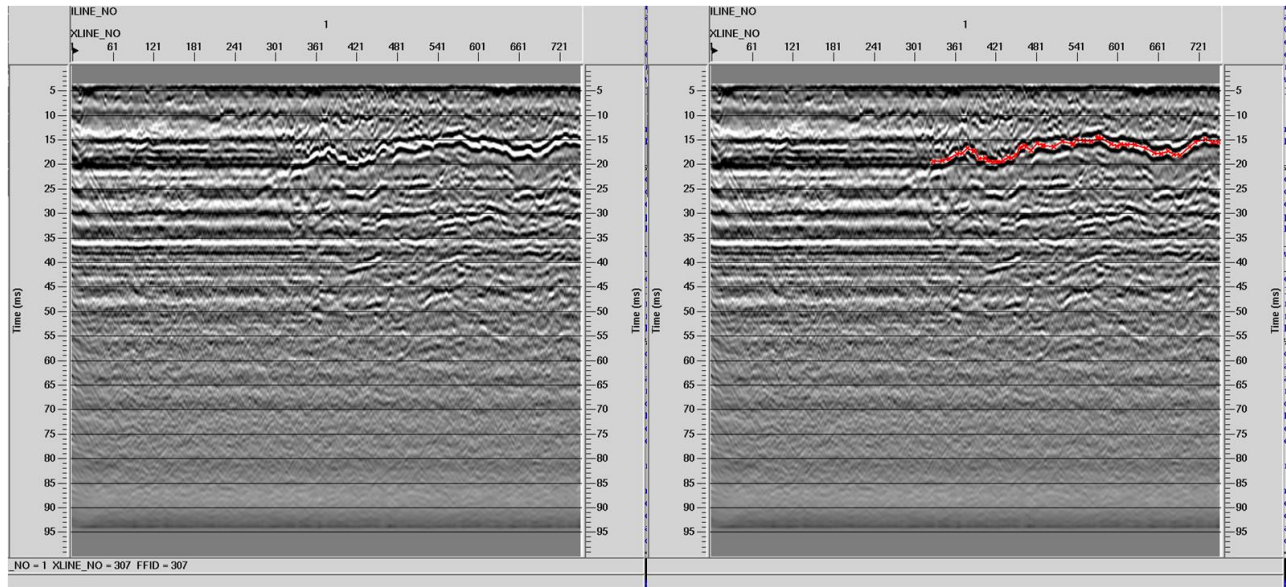
Figure 12.7: GPR "Dakota Seismic" Inline 1; Top Dakota Sandstone group.
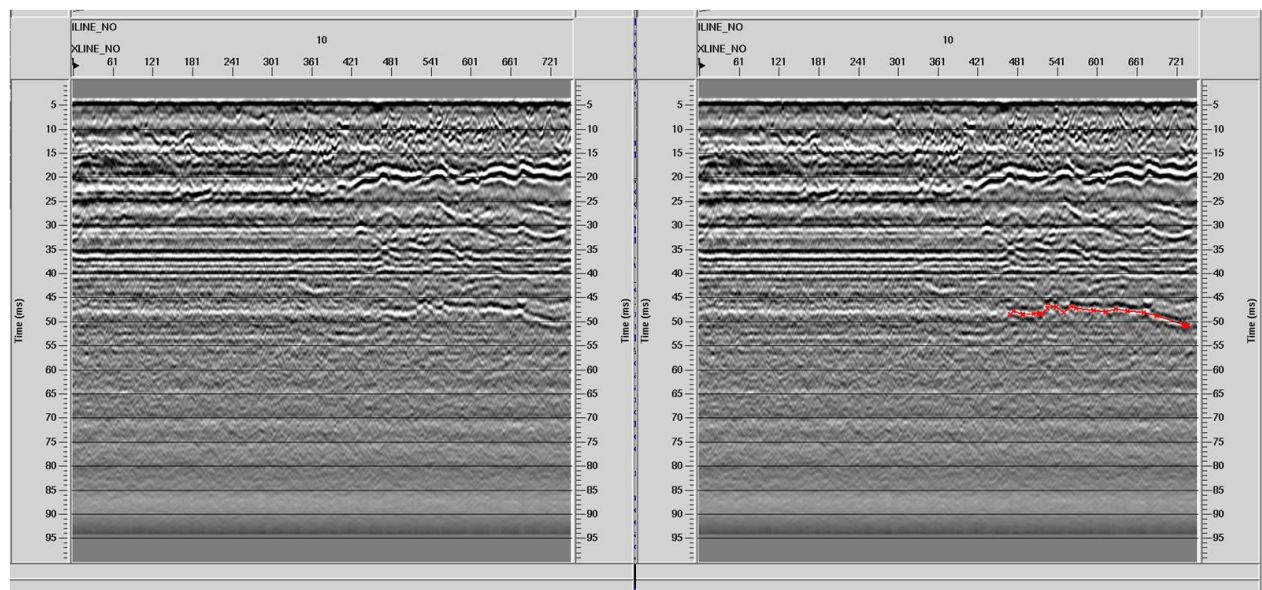
Figure 12.8: GPR "Dakota Seismic" Inline 10: Internal layer in Dakota Sandstone group
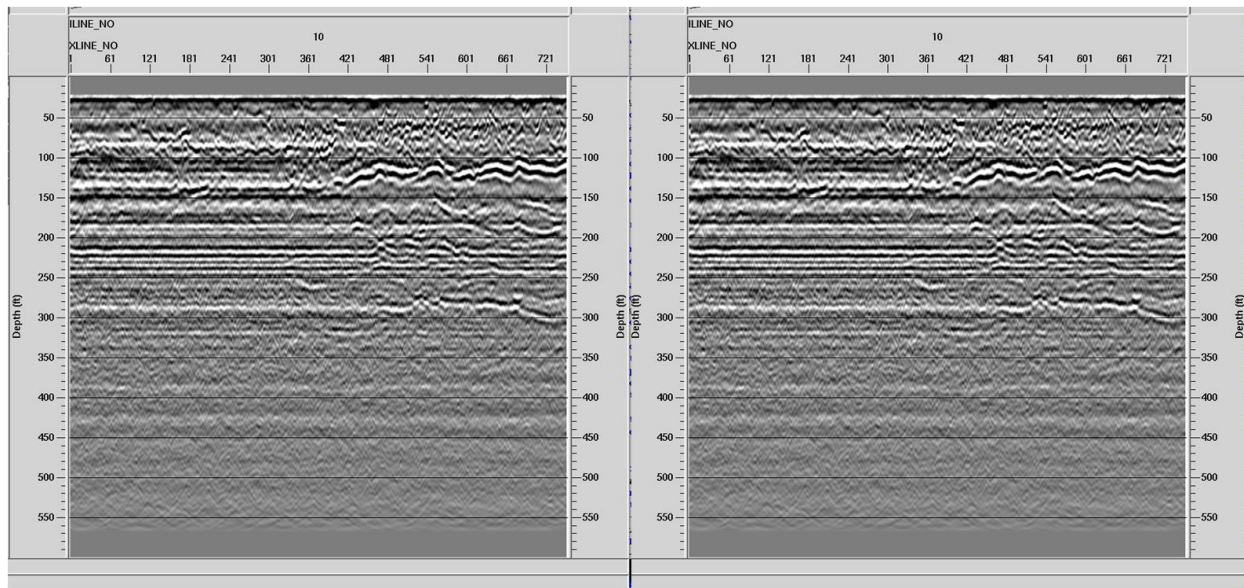
Figure 12.9: GPR "Dakota Seismic" Inline 10: Depth converted GPR cross section (constant velocity model - 0,12 m/ns)

12.5.3 Hairpin Dike

GPR surveys were performed in profiles crossing the exposure of the hairpin dike. The goal was to image the dike and surrounding structure and to measure the dip of bedding within the 'limey layer' (which is used in structural mapping as a proxy for the Dakota Sandstone). Rather than a grid, this survey used single line acquisitions, with surveys performed parallel to EM survey lines. A total of 5 lines were performed, but only the first three (Line 00, Line 01 and Line 02) are processed here. The remaining lines are CMP gathers but no useful observations could be made from these. Processing was performed in ProMAX with a GPR-standard workflow.

In this case, bandpass filtering, using an Ormsby filter with a frequency range of 50-350-700-1400 Hz had been used to filter ringing noise from the input data in order to obtain better signal/noise ratio. Constant velocity for RMS velocity was around 0.12 m/ns and was used to run the Kirchoff time migration.
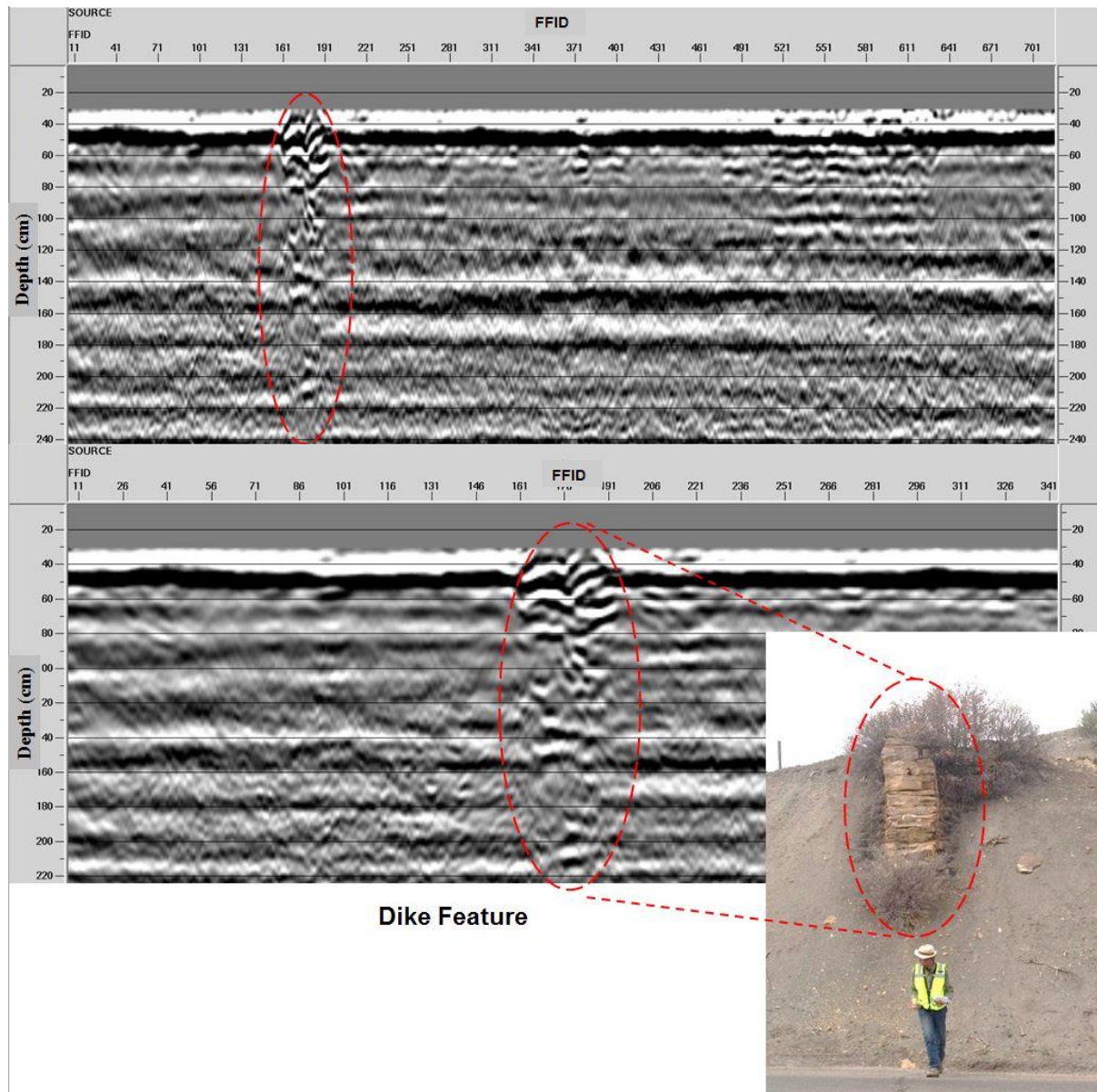
Figure 12.8: Line 00 GPR profile with west to east orientation, perpendicular with dike structure. The top image is the full scene, while the lower image is a subset with the dike anomaly.

Line 00 was acquired on the top of outcrop of the dike feature in hairpin turn road. The length of this line is 29.78 meter and consists of 725 traces. GPR profile of this line is shown as above (Figure 12.8) . Data is depth-converted.

After processing the data, the dike structure was clearly imaged in the GPR profile around trace number 181 (red line). The internal character of dike from the GPR profile is very similar to the internal character of the outcrop of dike feature in Pagosa Springs.

Line 01 was acquired parallel with line 00. The position of this line was to the north of line 00. The length of this line is 61.88 m and consists of 1,498 traces. The GPR profile of this line is shown as above (Figure 12.11).
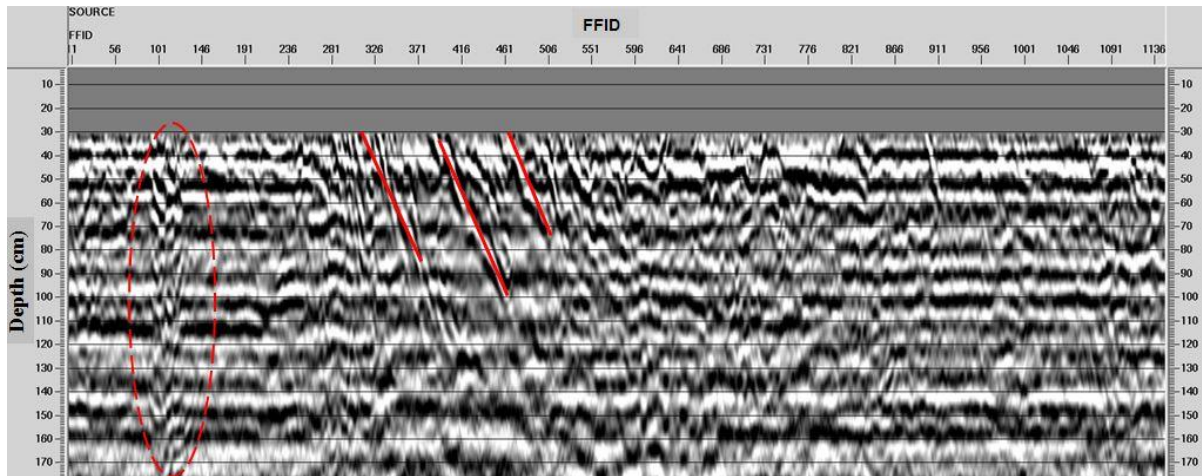
Figure 12.11: Line 01 GPR profile with west to east orientation, 10 meter distance to the north from line 00. The dike anomaly is circled, while the dipping layers thought to be the limey layer are delineated in red.

After processing the data, the dike again appears in the GPR profile. It appears around trace number 111 and there is a dipping event in the shallow section which corresponds to the dipping exposures of limey layer. This dipping lime layer was consistent with the dipping of the Dakota Sandstone, suggesting that the limey layer is indeed a suitable proxy for the Dakota Sandstone.

Line 02
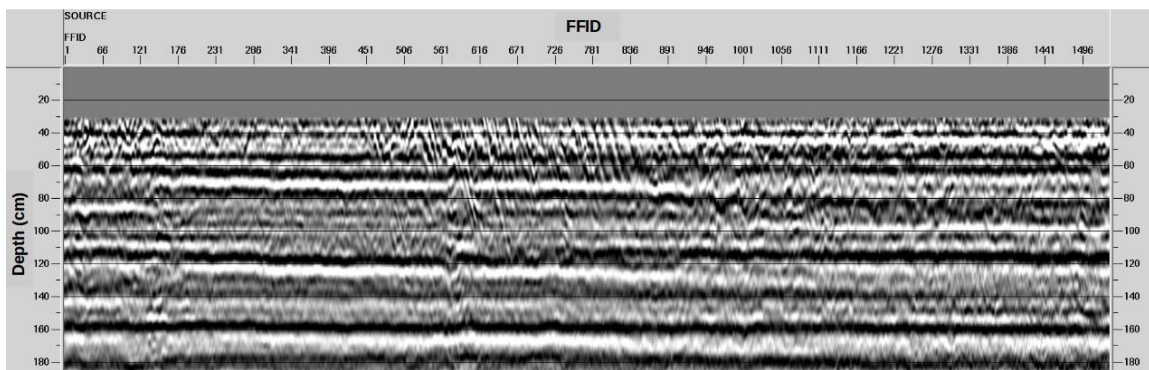
Figure 12. 12: Line 02 GPR profile with west to east orientation, 10 meter distance to the north from line 01.

Line 02 was acquired parallel to line 01. The position of this line was to the north of line 01. The length of this line is 94.03 meters and consists of 2,343 traces. The GPR profile of this line is shown as above (Figure 12. 12). In this line, the dipping limey layer is seen again in the shallow section of the GPR profile, at around trace number 500.

12.5.4 Travertine deposit at the mother spring

In the open field behind the mother spring, deposits of travertine have been observed. Travertine is usually formed from the precipitation of calcium carbonate and is associated with hot springs [81]. A 40x50 m survey grid was established over the travertine outcrop, although only 29.5 m of this was completed. This was due to the presence of large boulders at the end of the survey grid which did not allow the GPR equipment to be dragged across it. However, this range extended across the exposed travertine. The main aim of this survey was to determine the depth and extent of the travertine deposit and to understand its internal characteristics.

Standard processing procedures were carried out to improve the signal to noise ratio within the acquired dataset. A bandpass filter of 50-100-800-1600 Hz was applied and the final processing step was making the depth migration. This was applied with a constant velocity of 0.09 m/ns (determined from travel-time analysis of diffraction hyperbola in the dataset). The final migrated images have shown that the internal structure of the travertine is very chaotic and broken up. Through some of the migrated sections, a strong dome shape reflector is imaged (Figure 12.11) and this is seen correspondingly to a fairly horizontal strong reflector that could be the base of travertine. However, this reflector is not seen consistently throughout the dataset. The top of this dome shape structure is at a depth of about 1.8 m whereas the base horizontal reflectors are at depths of about 3.6 m so it is safe to assume that the travertine deposit are at least 3.6 m thick. The dome shape structure could represent the original vent which fed the former hot spring at this location.

GPR data acquired across the grid with top soil did not achieve the needed resolution due to attenuation within the conductive soil layer. The processed image does show strong reflectors that dip towards the section covered by top soil (Figure 12.12) and this is an indication that the travertine deposit extends laterally underneath the top soil layer. Therefore, the travertine deposit is probably more laterally extensive than implied by the extent of its outcrop. Imaging its full extent is probably beyond the capability of a 500 MHz GPR survey.
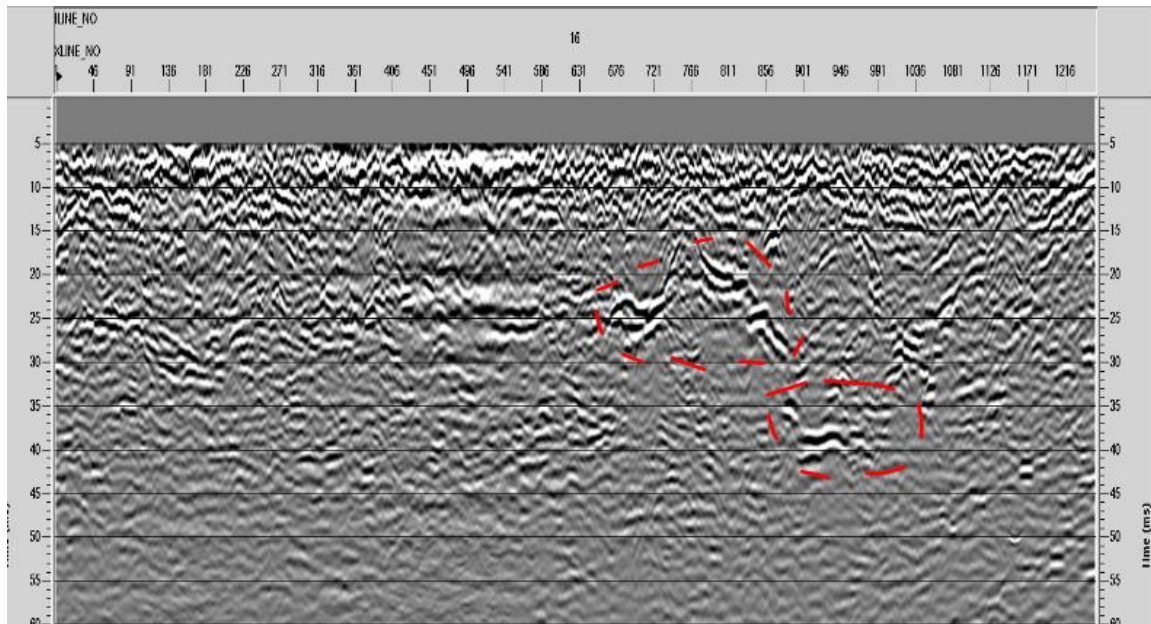
Figure 12.11: Strong dome shape reflectors and the corresponding reflector at the base highlighted by the red dashed circles.
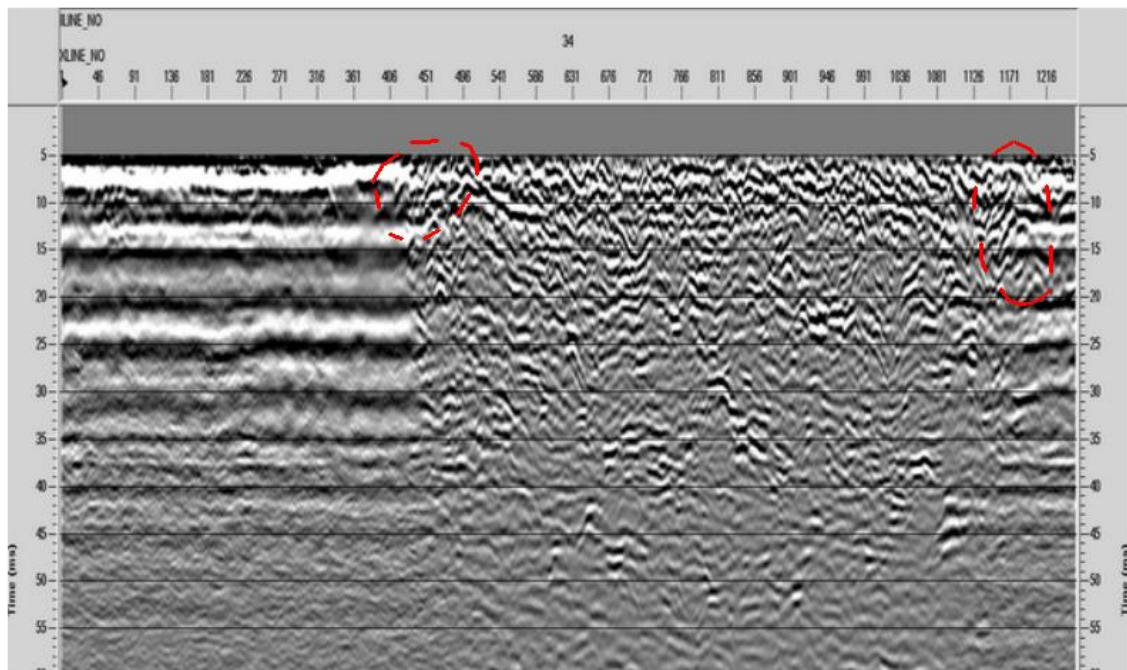
Figure 12.12: Highlighted by the red dashed circles are reflectors that dip towards and seems to extend underneath the top soil layer on either side.

190

12.5.5 White Patches

White patches of chemical precipitate were located on the ground surface near the San Juan river across from the Hairpin Dike. This was roughly 400-500 m north of the main seismic line. Topsoil overlying the Dakota Sandstone group was wet and there was a characteristic 'hot-springs' smell at the site. In places the ground is stained with crystalline deposits but these have no obvious source. GPR was applied at this site to investigate if the source of the precipitates is overland flow or a subsurface vent. The GPR survey was designed to be a 40x25m grid oriented north/south on the 40 m long side. Line spacing was 0.5 meters.

GPR data was processed and significantly improved due to filtering, static correction, NMO correction, and migration. The migration process was conducted using the velocity of 0.11 m/ns.The strongest and most visible event was picked. The visibility of this event correlates directly with the surface extent of the white patch. This reflection might therefore be explained as a contact between wet soil and underlying dry ground. There is no obvious and strong evidence of a subsurface water vent and it is still difficult to identify if white patches in this particular area are caused by terrestrial flow. Nevertheless it is likely to be that these chemical concretions are induced by surface water migration.

Signal energy in the remainder of the dataset is weak and difficult to pick. There are no geological patterns and structures. Despite the fact that the white patch presence is a result of water flow, it remains difficult to understand the origins of the surface water.

12.6   Conclusions and discussions

GPR surveys were carried out at various locations along the main seismic line, with particular emphasis on understanding the internal structure and properties of the main rock units involved in the geothermal system at Pagosa Springs. GPR is a low penetration depth technique and as such does not provide information on the large scale structure of the area like deep seismic imaging can. In areas covered with a layer of Mancos Shale, the penetration depth was effectively zero, and no imaging of rocks beneath this layer was achieved. This is due to the very high conductivity of the shale. Nevertheless, the various GPR studies helped to glean some important small-scale details.

The survey to the south of the dike protrusion known as the 'Dakota Bench' revealed horizons interpreted to be layering of sandstone with varying levels of weathering/consolidation within the upper Dakota Sandstone. The thickness of such beds was found to be approximately 1-1.5 m, which is in agreement with surveys carried out last year in Pagosa Springs. This information may be useful in trying to understand fluid migration pathways and preferential flow units within the sandstone reservoir that

services the geothermal system in the area. However, the depth of penetration was a limiting factor to gaining more information about bedding at greater depths (the deepest interpreted horizon lies at approximately 4 m below the surface).

The survey carried out to the north-east of the recycling center (just north of the main seismic line and therefore referred to here as 'Dakota Seismic') was designed to test the penetration depth of GPR as a function of water saturation and weathering. The results found that penetration through the water-saturated soil was minimal. However, some areas on the grid allowed imaging of what is interpreted to be the top of the Dakota Sandstone in addition to an internal layer. This was in agreement with the Dakota Bench survey.

Three parallel 2D lines were also acquired across the top of a known dike that protrudes from the ground. Imaging of the dike itself was very good, with some internal structure also visible in agreement with observations on the surface. This confirmed the extension of the dike to the north in the subsurface. In addition to the imaging the dike, the limey layer was also visible. Calculations revealed a dip of approximately 8º for this layer. This is consistent with the dip of the Dakota Sandstone in the vicinity of the dike and as such lends credibility to the use of the limey layer as a surrogate for the Dakota during geological mapping. There are suggestions from the magnetic surveys that the dike to the North of the outcrop could turn towards the North-East. Due to the exceptional results observed in this study, future GPR lines should be acquired in this area to the North of this year's dataset in an attempt to further map the dike's extent and direction in the subsurface.

A further survey was carried out near to the Mother Spring location on a Travertine deposit exposed at the surface. This purpose of this survey was to attempt to define the vertical extent of the Travertine and possibly image the vent that acted as the conduit for hot water in this location. The results of this survey exhibit a dome feature thought to possibly represent this conduit. Furthermore, a second horizon was identified which, though inconsistent across the survey due possibly to poor penetration, could represent the base of the Travertine deposit. These finding suggest a minimum thickness of the Travertine in this location of approximately 3.6 m. Imaging from within the deposit suggests a broken up internal structure. This could represent exposure and weathering at the surface, or possibly evidence for episodic venting of hot water and Travertine deposition interspersed with periods of non-deposition.

The survey carried out at on areas of chemical precipitation to the West of the San Juan River near to the dike (referred to as the 'white patches') in an attempt to identify a possible subsurface source of the

precipitate was inconclusive. The processed data revealed very little subsurface structure which is attributed to either very poor depth of penetration in the area or a lack of geological features in this location. One discontinuous horizon was interpreted but is proposed to mark the contact between dry and water-saturated soils only. The conclusion from this survey is that the most likely source of the chemical precipitate in this location is the evaporation of surface water.

13. Integrated Site Conclusions

The five sites that were the focus of the 2013 field camp were the main suvey line, the central survey line/hairpin dike area, Mill Creek, downtown Pagosa Springs, and Shahan's Ranch. The main suvey line had most methods conducted along it in order to image the geologic structure of the area. In addition to deep seismic along this line, there was DC, SP, and gravity that followed along the entire line. The central line was an area of focus as well since it was one of the areas closest to the town of Pagosa. This area also had several interesting features including new interpreted faults, which were confirmed between the surveys. The third location near the main seismic line was Mill Creek. The surveys that were focused in this area were DC, EM, and SP. These sets of data show that there is a thin layer of Mancos Shale, as well as a heavily saturated and fractured Dakota Sandstone that creates a great environment for fluid flow. Also, there is a correlation between the DC line and the deep seismic line that image a fault in the area.

Shahan's Ranch was the student site for this year meaning that all surveys were planned and conducted by the students. This site was chosen because of the free-flowing well and to gain a better context of the geothermal system in the area. The geological cross section along with the methods that were used here showed that the area was mainly Mancos Shale, with the Dakota underneath.

13.1 Main Survey Line
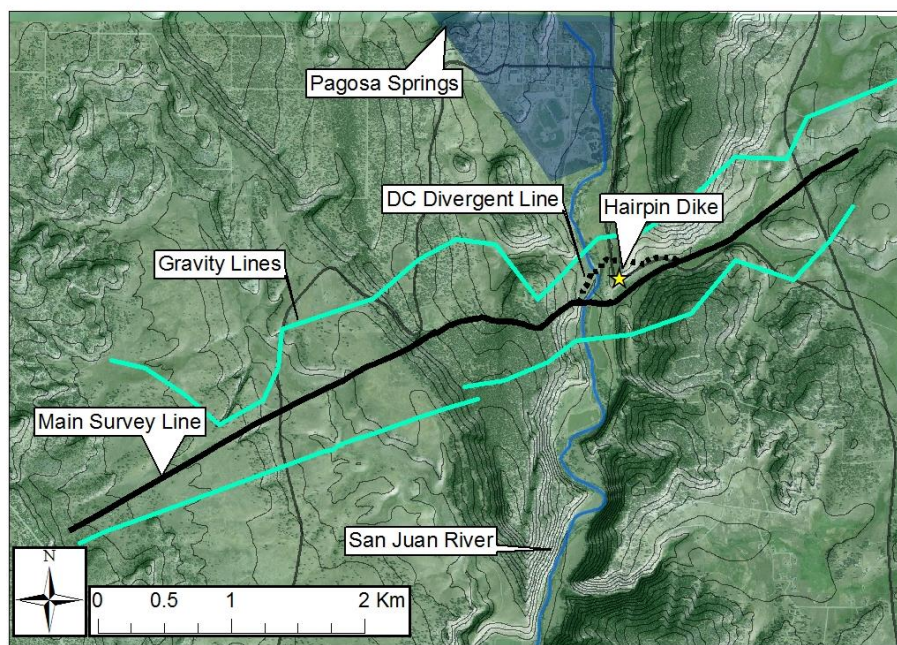
Figure 13.1.1: Surveys conducted around the main survey line

13.1.1 Deep Seismic

Deep Seismic is the most time consuming and most difficult method to acquire. Having deep seismic data provides a unique opportunity to image the geology of an area. This data can be used to confirm or alter interpretations made with other methods. Figure 13.1. 2 shows the final seismic migration developed by the 2013 field camp.
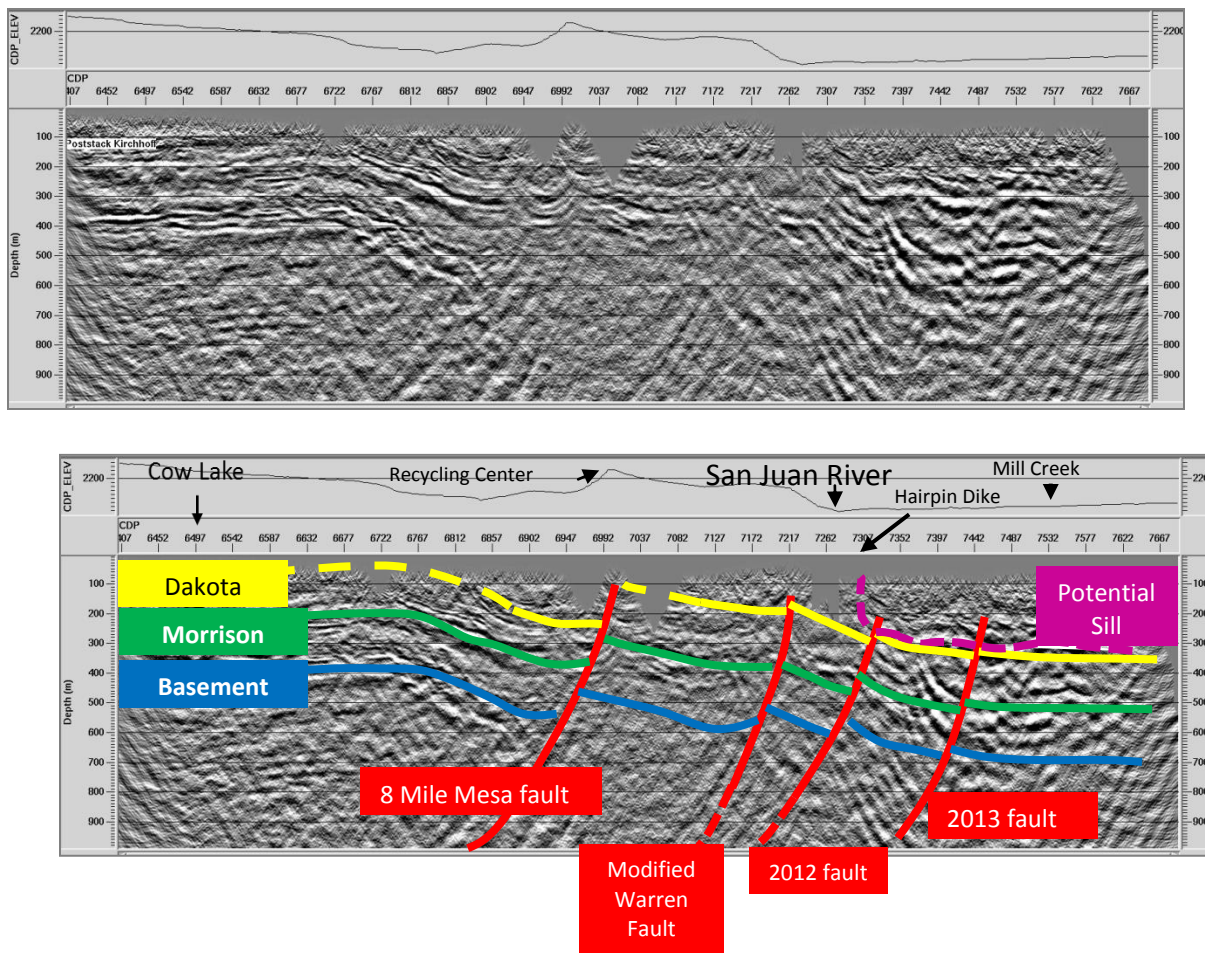
Figure 13.1. 2: Depth migrated deep seismic line. Without annotation (top)

Although this section is still rough, it can provide a confirmation for structural interpretations made with other methods. The seismic line above highlights four faults. The most prominent of these is the Eight Mile Mesa fault. The Warren fault was also very apparent, but when projected onto a map, it appeared on the other side of the river than it was originally thought to be located. When Warren proposed the fault in 1986, he had no seismic data, and drew the fault based off of surface observations. The actual location is not deferrable from the surface because of the river. On the right side of the data we see a reflector that

195

originates at the surface around the hairpin dike. This reflector follows the lithology of the area, and makes all the data below noisier. This feature has been interpreted as a sill, it has a much stronger reflection than the surrounding area. The data in several areas has a relatively low fold, making it harder to interpret. Some of the faults interpreted in the seismic line are clearer than others. Use of the methods below will help confirm their presence.

13.1.2 DC/SP

DC and SP are similar methods, although they are still far from the same. By interpreting them together, observations of conductivity and fluid movement can be combined in order to develop a model of the whole groundwater system. Figure 13.1. 3 below shows the results of the DC and the SP surveys stacked on top of each other.
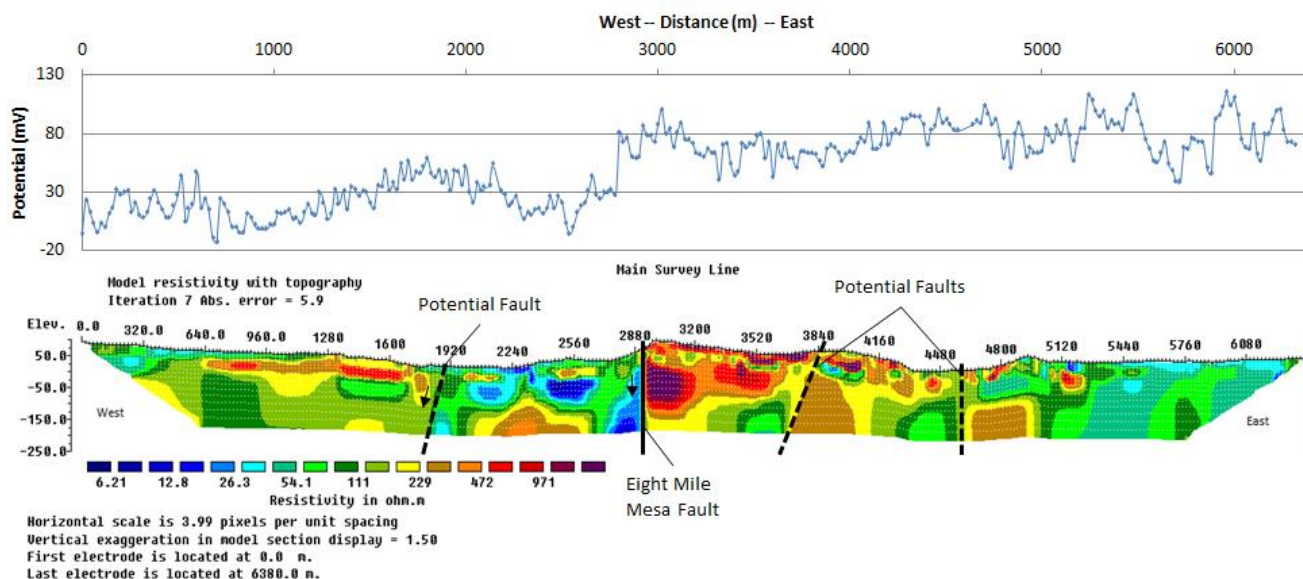
Figure 13.1. 3: SP (top) and DC (bottom) results along the main survey line

By combining these methods, the Eight Mile Mesa fault is clearly visible, and three others areas show potential to be faults. Faults are determined by dramatic contrasts in conductivity across a line. The SP data helps to determine whether or not water is flowing out of or into the faults seen in the DC data. These faults appear to have upwelling water. This water is likely coming from the Dakota sandstone, which is a reservoir for meteoric water that has filtered through the basement. The upwelling of water in each of the faults implies that the water is being recharged by a different method than one of these fault systems. The faults shown do not match the seismic faults drawn above. The correlation between the DC/SP lines and the main seismic line will be discussed in section 13.1.4 below.

13.1.3 Magnetics

Magnetics used on a large scale can help to determine general trends in the geology, as well as highlight anomalies across the survey line. Combined with other methods, this provides a more complete picture of the geology of the entire area. Figure 13.1. 4 shows the magnetic response across the main survey line.
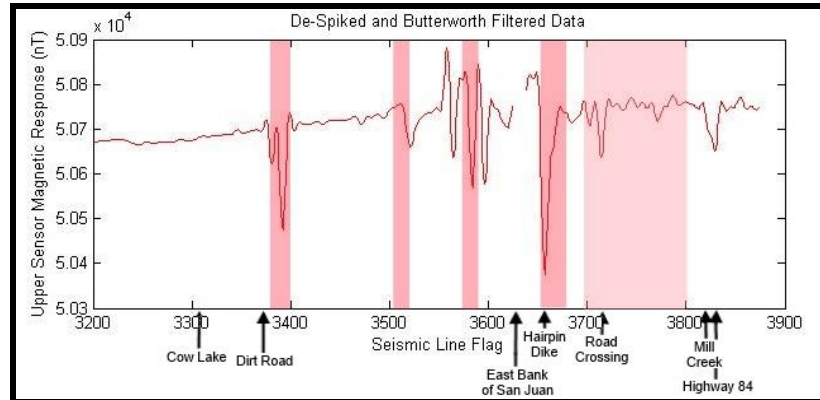
Figure 13.1. 4: Magnetic across entire survey line. Red areas are high noise area

On the west side of the line, there is a different overall trend than there is on the east side of the line. This shows that there is likely at least one fault in the central area, causing the general trend of the line to change. Much of the data is noise due to power lines, fences, and buried pipes throughout the survey. The hairpin dike appears to be visible, but is more likely to be the power lines that are present in the same area.

13.1.4 Gravity

Gravity is like SP and magnetics in that it is a one dimensional survey. Gravity gives a good overview of the area, showing general trends. This can be used to help determine faults and anomalies. Gravity alone has too many models to every set of data to make any interpretations. Combining gravity with the other methods however can help to confirm observations made in other data. Figure 13.1. 5 shows one of the many gravity models that can be made to fit this data.
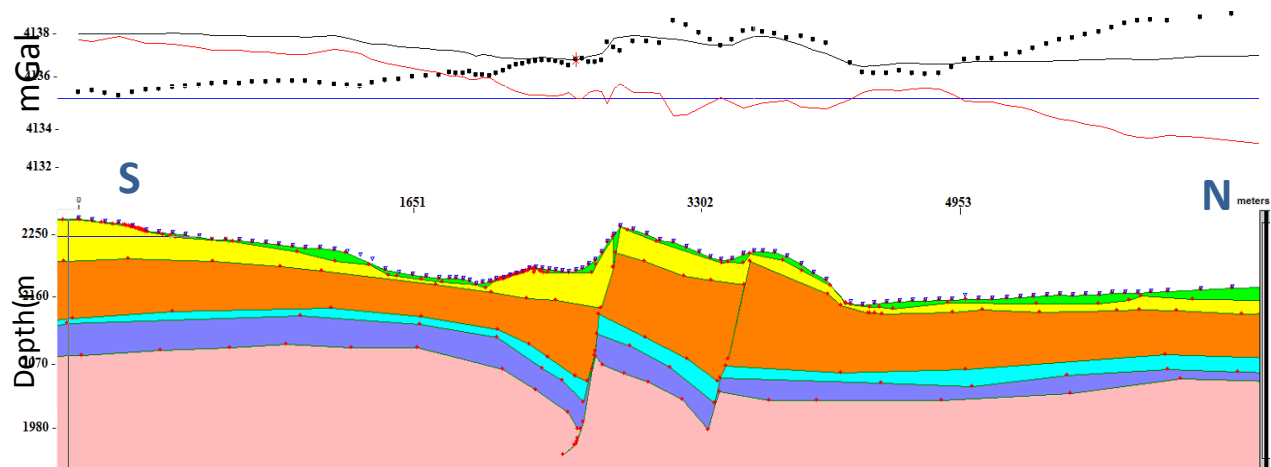
Figure 13.1. 5: Gravity interpretation along the main survey line

The gravity line above was created using the geologic cross section made before doing the survey. Using this supplemental data helps to eliminate some of the other possible models that fit the data collected over this line. The gravity model here shows the Eight Mile Mesa fault as well as the Warren fault. The model was created before the seismic line was interpreted, so none of those faults were included. The right side of the figure shows a positive gravity anomaly that was not described by the topography or stratigraphy. This could correlate to the sill that was possibly seen in the seismic data.

13.1.5 Main Survey Line Integrated Conclusion

None of the methods used on the main survey line are sensitive to the same earth properties. By combining them, a better interpretation of the area can be made. This combined interpretation not only used these methods to help confirm results, but also to obtain even more information about the area. The figures shown on the next page all cover the same line over the same horizontal scale. By viewing these simultaneously, several observations can be made.

Figure 13.1. 6 overlays all the methods used along the seismic line in order to get a more complete image of the geology in this area. The one fault that seems to be present in each survey is the Eight Mile Mesa fault. This isn't surprising, seeing as that fault is very visible at the surface. The Warren fault is apparent in the DC data, and the seismic data. This information was provided before the survey, and was therefore incorporated into the gravity line. Of the last two faults in the seismic migration, only one of them is seen in the DC inversion. The DC inversion is more sensitive to bigger faults, because they provide a larger contrast in resistivity. At least one of the faults outlined in the seismic migration is too small to make a significant difference in the DC inversion. The sill that is seen in the seismic interpretation is a good explanation for the higher gravity in that area. Neither of these methods provides definite evidence of a sill, but the east side of the DC line shows relatively low resistivity values, further confirming the presence of a sill. The SP data correlated to the known faults suggests that the faults are associated with

198

upwelling water. This is also the prediction for the mother spring in Pagosa Springs. The presence of so many faults upwelling water without any down welling faults suggests that the source of the meteoric water in the Dakota sandstone has a different source than faults. The final geologic cross section created from this information is shown in Figure 13.1. 7.

Figure 13.1. 6: Stacked methods across main survey line

200
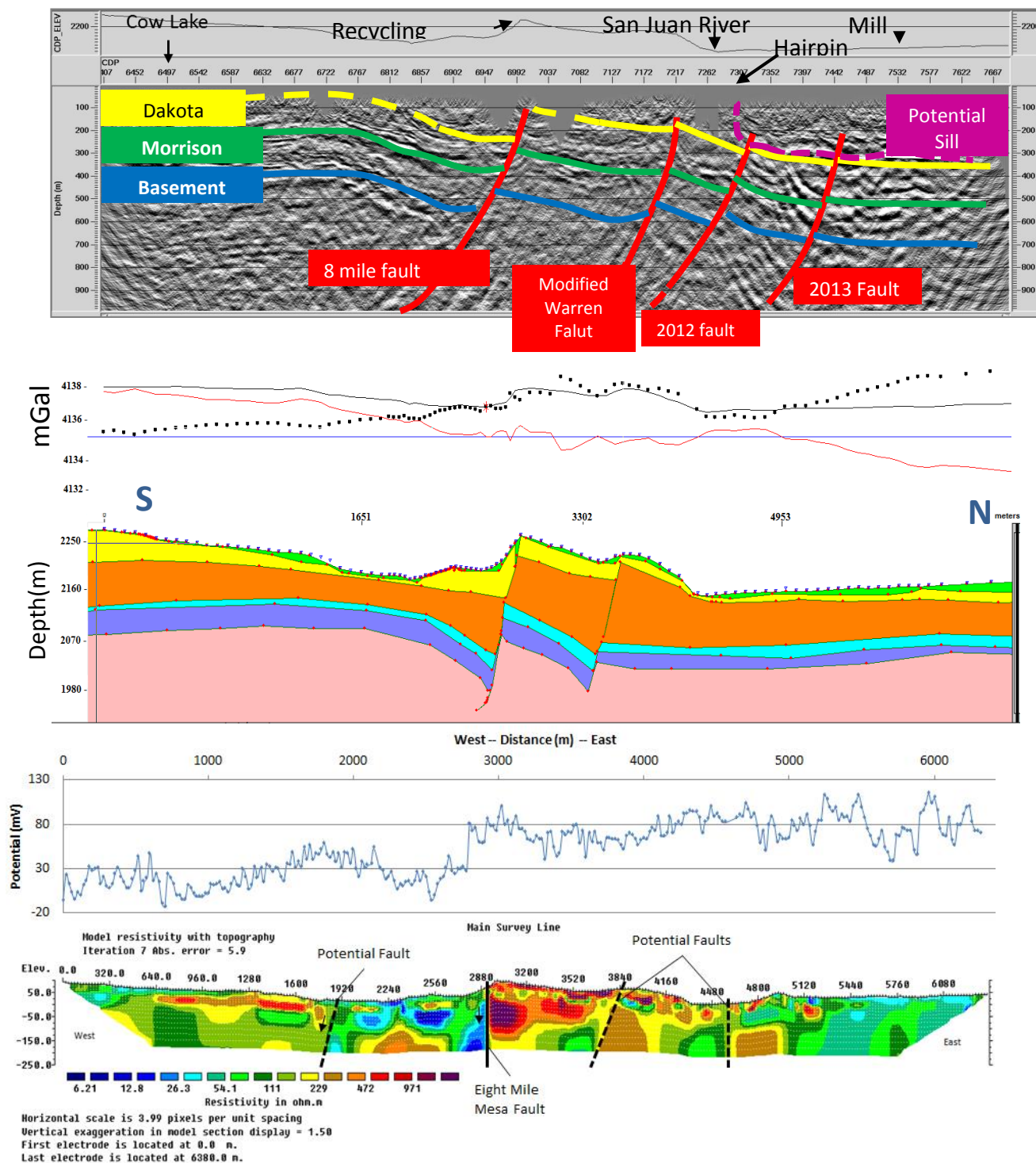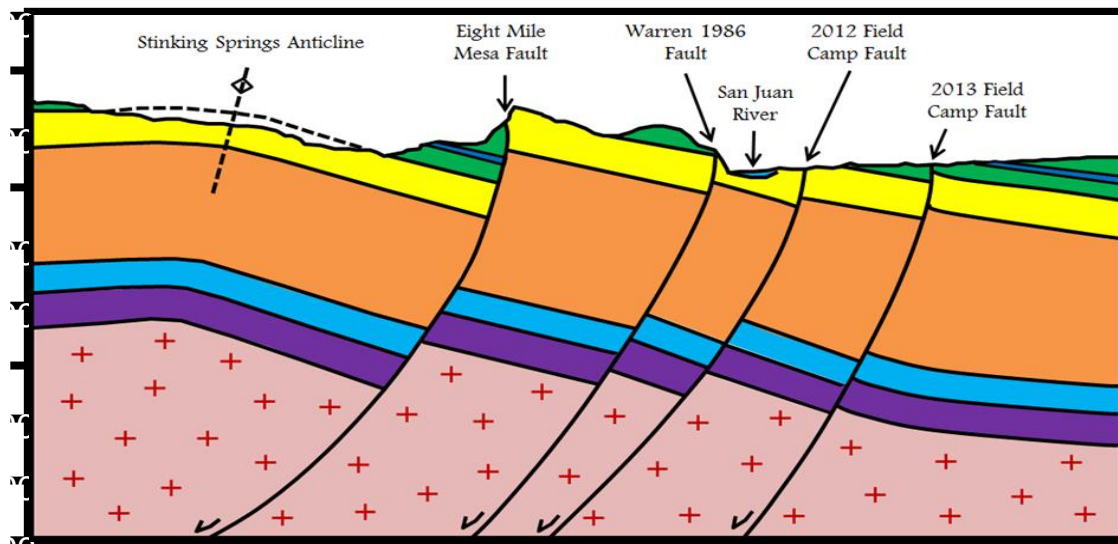
Figure 13.1. 7: Geologic cross section based on 2013 survey data

13.2 Central and Western Surveys
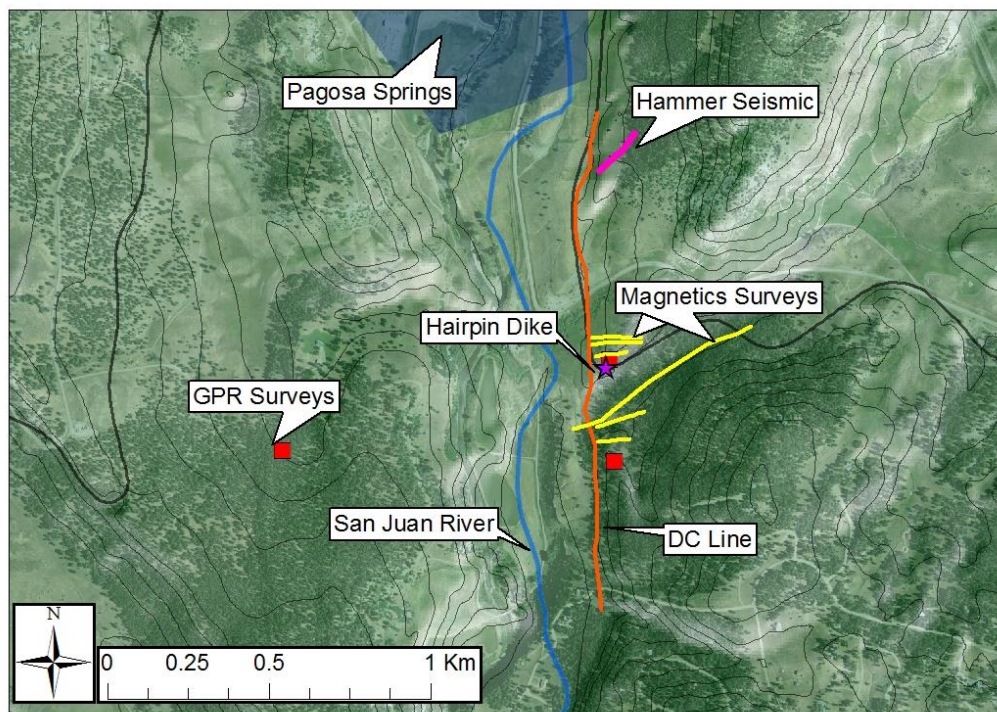
Figure 13.2. 1: Surveys conducted around the central portion of the seismic line

13.2.1 Magnetics

The magnetics data for central surveying focused mostly on the hairpin dike location. This data was not useful in determining depth of the contact between the Mancos shale and the Dakota sandstone. This contact is not detectable because there is no distinct difference in magnetic susceptibility between the two layers. From this data it was concluded were the location of the dike is based on anomalous data points in two of the surveyed lines. Figure 13.2. 2 shows two possible dike paths, these are based off of the surface expression of the dike, and anomalies that are possible associated with the dike. The two paths could be due to the split path of the dike, or coinciding noise in both surveys due to a buried pipe or cable.

Figure 13.2. 2: Map of Possible Dike Shape (red).

We see the dike generally trending NNW-SSE. The extent of the dike in terms of length and depth is difficult to interpret from the data collected. However, it is possible to interpret that the dike is at least 370 m long. From this interpreted dike, it may be possible to predict additional dikes with similar trending, but that will require further surveying. Although this dike does not appear to follow the path of any of the seismic detected faults, it has the same general orientation. This could show correlation

between the faulting system and the path that the dike took to the surface. Figure 13.2. 3 shows the orientation of the dike and close by faults.
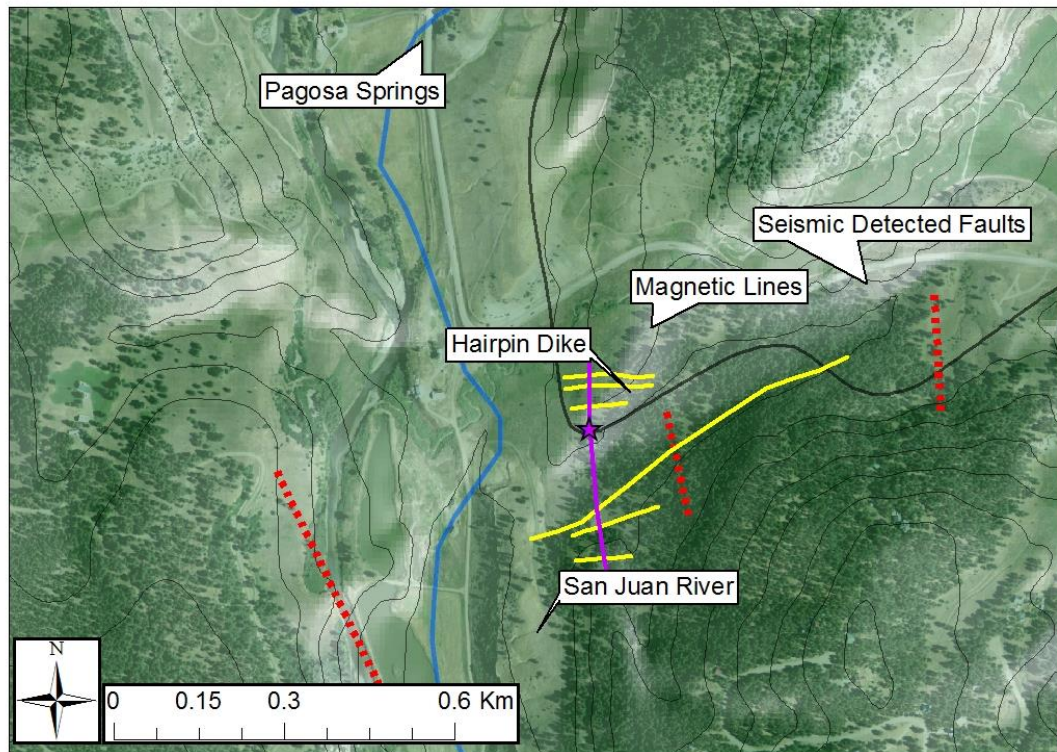
Figure 13.2. 3: Map of Possible Dike Shape (red).

13.2.2 DC Resistivity

The one DC Resistivity survey that was run in this area is a continuation of the PAGO 04 line that was run last year. Both of these results together can help draw the big picture of what is happening in the central area of the seismic line. The results from both lines are shown below in Figure 13.2. 4.
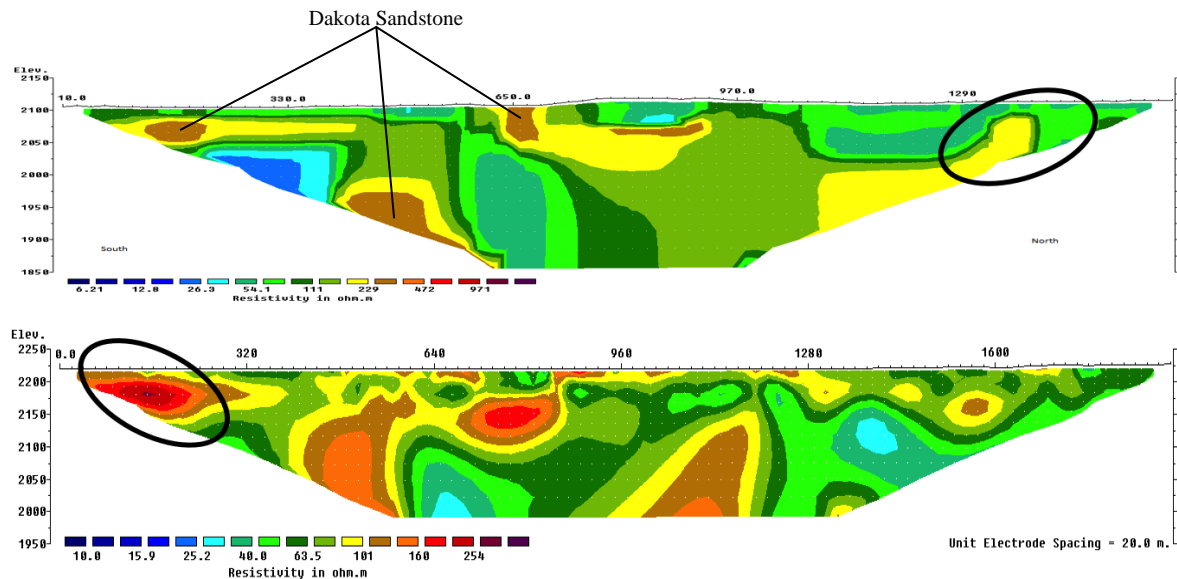
Figure 13.2. 4: Resistivity profiles for Hairpin Dike Line 1 (top) and PAGO 04 (bottom). Notice the area of high resistivity in both profiles indicated by the black circles

These results show what could be a highly resistive area. This probably represents the top of the Dakota. The top line shows a potential fault running through this area, and should be subject to further investigation. This line is separate enough from the other surveys, that it is the hardest to integrate into a comprehensive interpretation. It should be noted that areas of low resistivity under the Dakota could be interpreted as saturated Dakota. This is likely the source of the hot water.

13.2.3 Hammer Seismic

Hammer seismic method is used to develop seismic images on a small scale. These images are ideal for determining formation structure. Although it can be used to map faults, that isn't the most practical use of hammer seismic since it is at such a small scale. In this area it was used to image the Dakota sandstone. In the area where the hammer seismic was performed, there was an outcropping of the Niobrara layer. This would imply that the Dakota sandstone is about 30 meters below that location. Figure 13.2. 5 below shows the results of the hammer seismic survey performed.
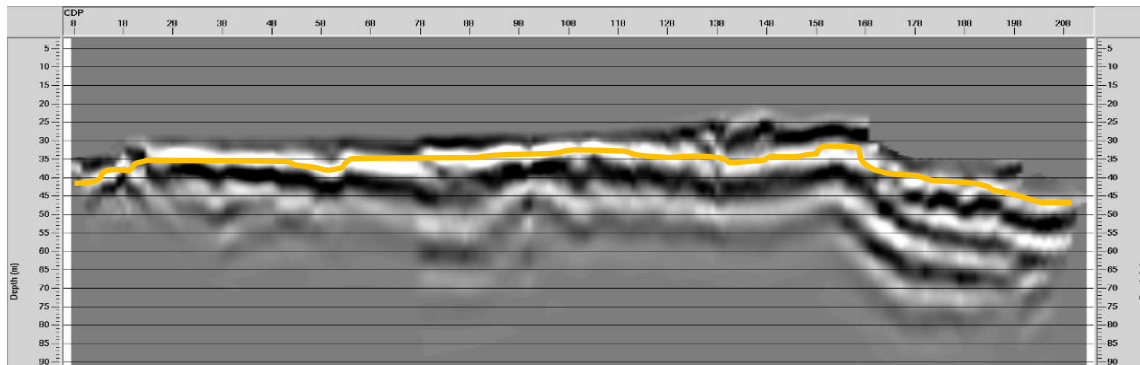
Figure 13.2. 5: Seismic migration at the bench location in the central survey area

The Dakota sandstone in the figure above is highlighted by a yellow line. This image shows a large amount of variation in the surface of the Dakota. This is likely due to heavy fracturing in the Dakota sandstone. This fact is important in the overall flow of water in this area. Although the Dakota sandstone isn't very permeable, the small fracture systems allow significant amounts of water to flow through it. This shallow seismic section helps to confirm that the fractures in the Dakota seen at the surface are present throughout the formation.

13.2.5 GPR

Several GPR surveys were run in this area. The first three surveys were used to confirm the location of the dike. One survey was located on top of a Dakota outcrop, and the last was located in a Mancos shale dominated area. Figure 13.2. 6 shows one of the surveys over the dike and the results.
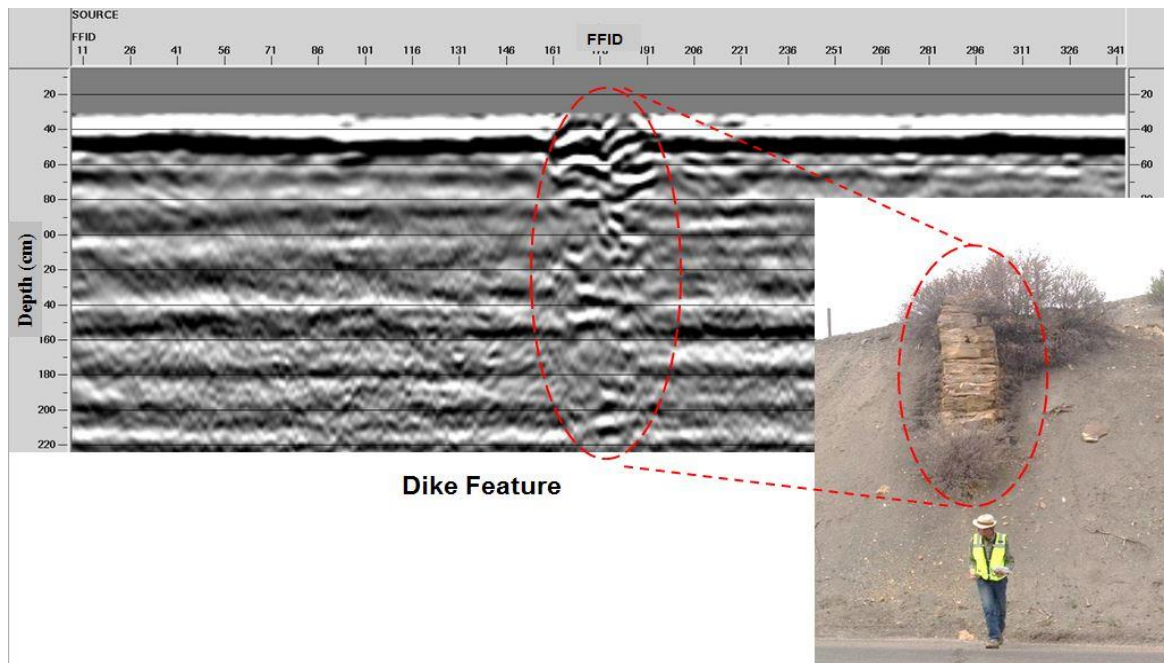
Figure 13.2. 6: GPR interpretation at the hairpin dike

205

Although this was conducted extremely close to the dike, this survey was also helpful in imaging the layers in the Mancos Shale. Although knowing the geology of the Mancos shale is interesting, knowing the geology of the Dakota sandstone is more beneficial in the understanding of the Pagosa Springs geothermal system. Figure 13.2.7 below shows the results of the GPR survey conducted on top of the Dakota sandstone just south of the hairpin dike.
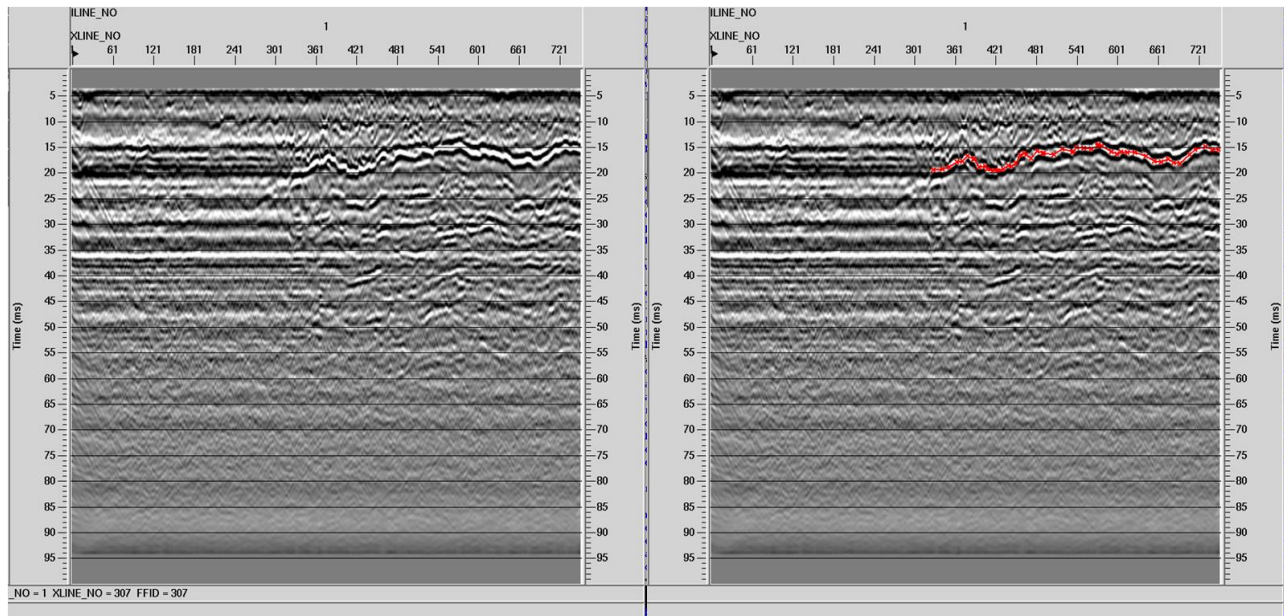
Figure 13.2.7: GPR on top of the Dakota sandstone

Similar to the shallow seismic interpretation, the GPR survey shows the rough surface of the Dakota sandstone. The heavily fractured structure is ideal for fluid movement.

13.2.5 Central Line Integrated Conclusion

Combining the interpretations for these surveys helps us to better understand the geology of this area. No specific faults were found in this area, although there are likely several small ones. The direction of the dike appears to follow the trend of surrounding faults as they were detected in the nearby mill creek area. It is very possible that the dike chose a fault scarp as the path of least resistance to the surface. The faulting in this area is also likely correlated to the rough shape and fracture systems in the Dakota sandstone. During one of the events that created the faults in this area, the Dakota sandstone was compressed to failure in fracture systems throughout the formation. These fractures are ideal for fluid movement, and make the Dakota sandstone the most likely hot water reservoir in the Pagosa Springs area. The DC line shows that there may in fact be saturated Dakota sandstone in this area.

13.3 Mill Creek Integrated Conclusion

13.3.1 EM Conclusion

All of the data sets collected at Mill Creek consisted of EM, DC, and SP. The interpretations of these data sets were combined to show a concise conclusion for the Mill Creek area. Figure 13.3.1 shows a map overlay of all the surveys conducted in at Mill Creek. The EM surveys were taken in the area denoted as a green square in Figure 13.3.1. EM34, EM47, and EM57 surveys were taken at this area. The EM section concluded that the Mancos Shale is a shallow resistive layer that overlays the saturated Dakota Sandstone. Two supporting EM inversion results from Mill Creek consist of those from the EM57 and EM47 shown in Figure 13.3.2 and Figure 13.3.3 respectively.
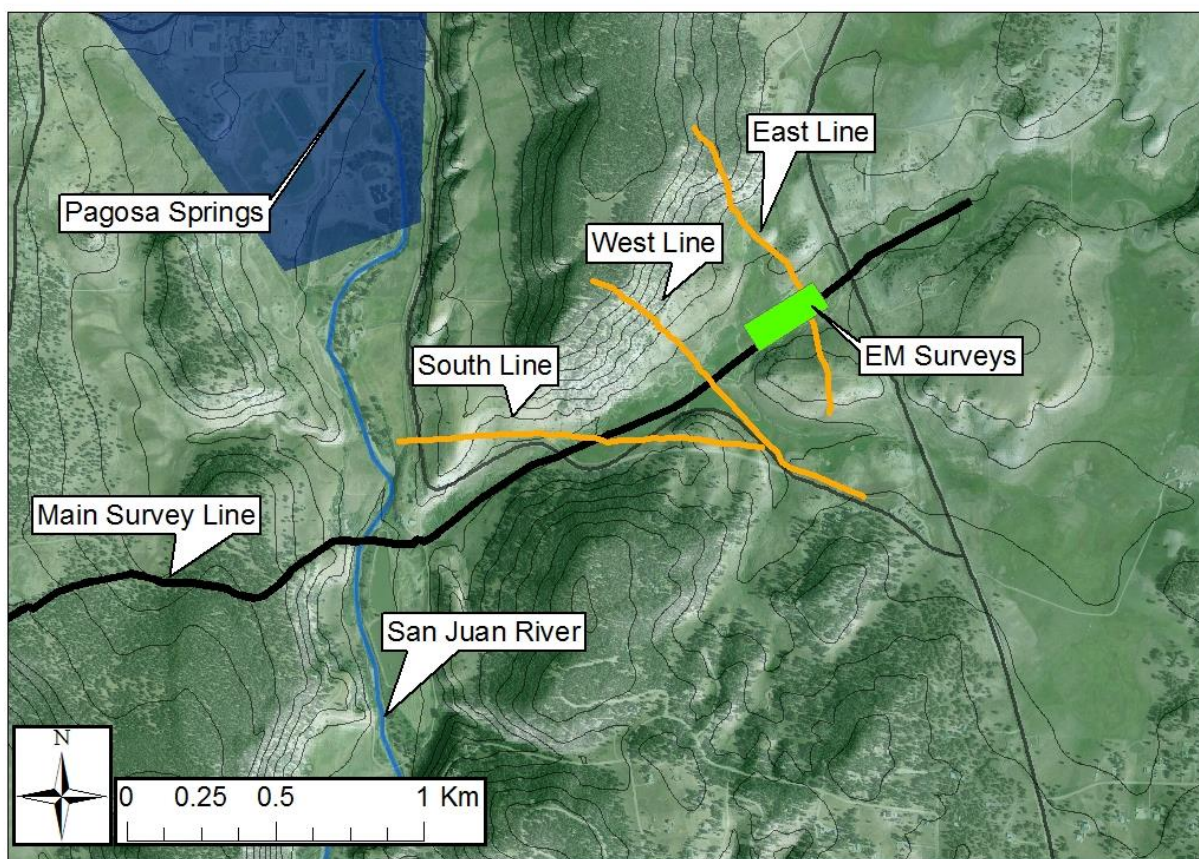
Figure 13.3.1: Shows the locations of all the surveys done in the Mill Creek area. These include surveys from EM, DC, and SP.
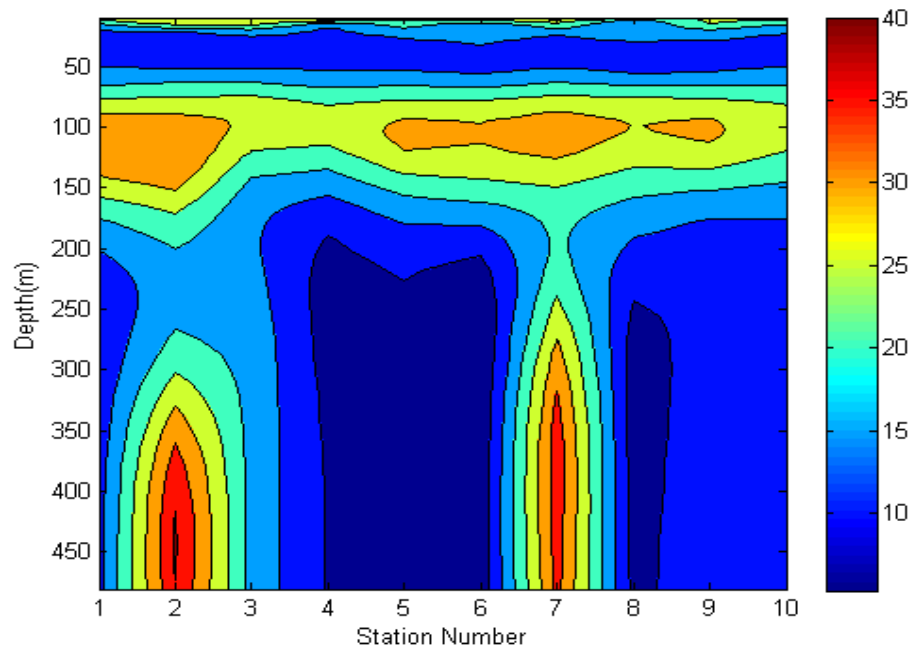
Figure 13.3.2: Shows the inverted results for the 30 Hz EM57 line 1903. The contour image shows results in resistivity (Ωm).
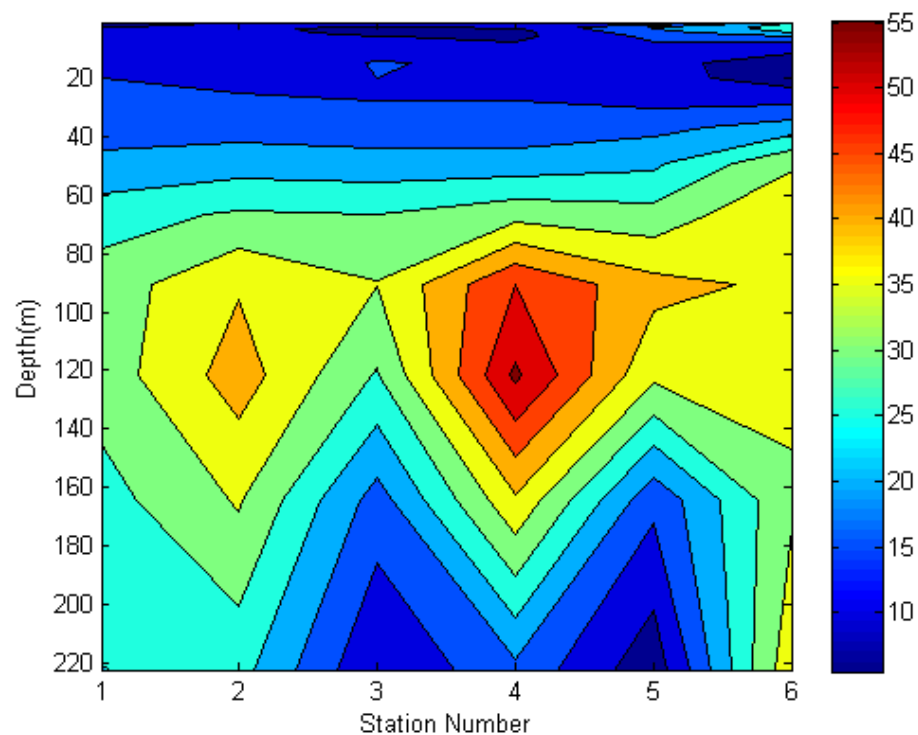
Figure 13.3.3: Shows the inverted results for the 75 Hz EM47 line 18. The contour image shows results in resistivity (Ωm).

Based on the geologic background discussed in the EM section, it can be concluded that thin resistive layer towards the top of the inverted results in Figure 13.3.2 is the Mancos Shale. This resistive layer was not present in the inverted EM47 results shown in Figure 13.3.3 because of the hypothesis that rain made the Mancos appear conductive. Below the Mancos Shale is the Dakota Sandstone and this is shown as the blue conductive unit in both of the EM sections. For the Dakota Sandstone to be conductive it is assumed that it is saturated and heavily fractured. The Dakota is shown to be about 50-60m thick which is consistent with the stratigraphic column generated from the P-1 well. The Morrison Formation is shown as the large resistive body in the middle of both sections. The main conclusion to take away is that the Dakota Sandstone is saturated and more conductive than the Mancos Shale in this area.

13.3.2 DC/SP Conclusion

DC resistivity and SP data were also collected at Mill Creek and the acquisition areas are shown in Figure 13.3.1 as the East, West, and South Line. Figure 13.3.4 shows the DC and SP data along the line denoted East Line in Figure 13.3.1. At the location of the EM surveys on Figure 13.3.4, the DC resistivity inversion matches the EM inversion results. There is a three layer system that is consistent with the EM47 and EM57 results: the top layer is the resistive Mancos Shale denoted as green, the second layer is the conductive Dakota Sandstone denoted as blue, and then the bottom layer is the resistive Morrison Formation. The SP data also shows something interesting about the Dakota Sandstone. Notice that between 300m and 800m along the SP line the data forms a trough. A trough in SP data corresponds to an aquifer flowing into or out of the page which would be east or west in this figure. This matches the DC inversion because below this area where the trough is present in the SP data there is a large conductive body which represents the saturated Dakota Sandstone. Due to Mill Creek flowing west it is reasonable to say that the water flowing in this area is flowing west as well because of topography. Since the blue conductive unit was determined to be Dakota Sandstone, the SP data also verifies that the Dakota is water saturated because it shows that fluids are moving in this unit. The accumulation of these three methods shows that the Dakota Sandstone is conductive, highly saturated, and is a conduit for water flow. All the SP results from the east, west, and south lines were combined to see the water flow in a 2D context and to connect the faults seen in the DC and seismic data. Figure 13.3.5 shows the 2D image of the SP data and the interpreted faults. The DC data from each of lines show that there are three different faults and they are denoted on the Figure 13.3.5 as red lines and these faults are supported by displaced values in the SP data. The 2D SP data also shows something interesting regarding the flow patterns in the Mill Creek area. The lowest readings are circled in red on Figure 13.3.5 because these are anomalous areas of interest. Recall that sharp negative anomalies in SP data correlate to a down welling of fluids. So the large blue region in the bottom portion of Figure 13.3.5 represents one of these areas. It is likely that the Dakota

Sandstone is highly fractured in this region and this allows for the water to percolate down. Three lines cross this area and they all show a significant negative anomaly, so this strengthens the interpretation if multiple data sets show the same anomaly. The same interpretation can be used to explain the other negative anomaly towards the top of the figure.
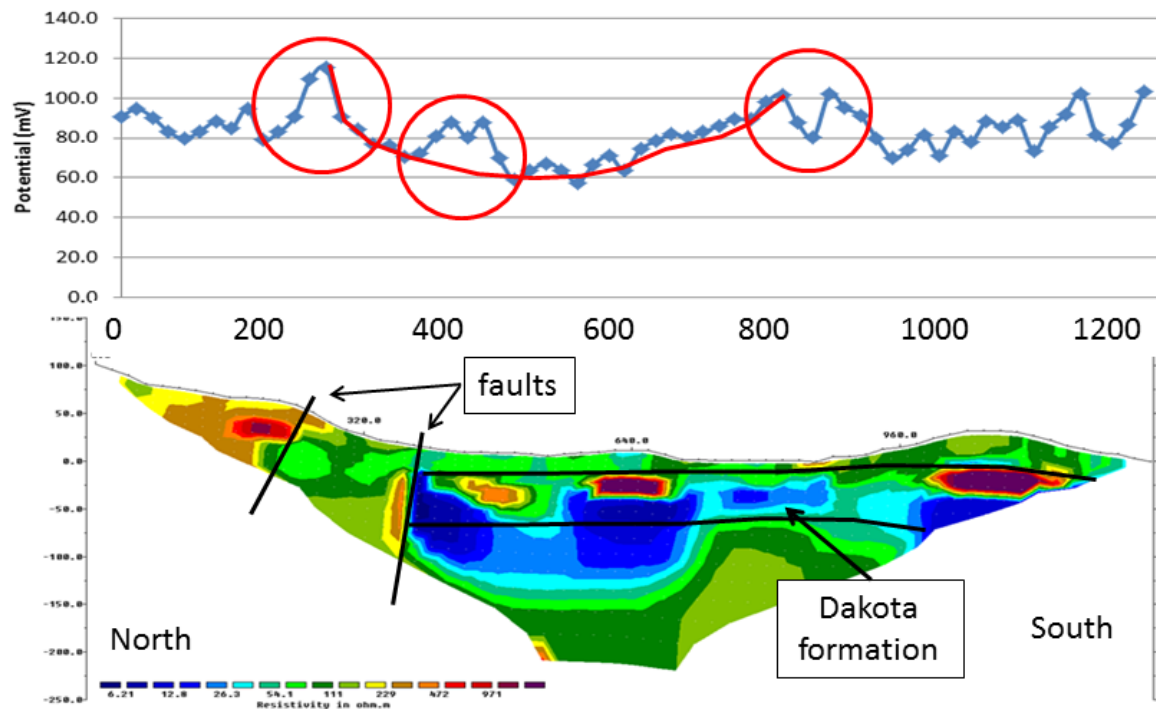
Figure 13.3.4: Shows the DC and SP results along the East Mill Creek line. An arrow denotes the location of the EM surveys.
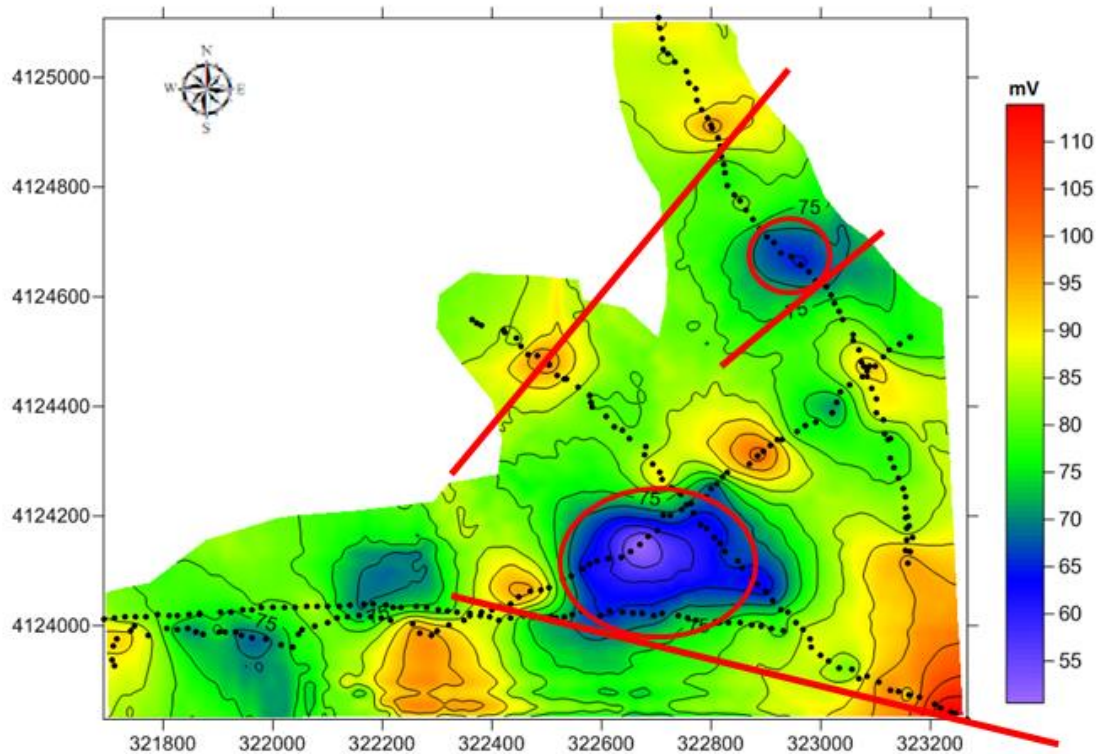
Figure 13.3.5: Shows a 2D plot of the SP results at Mill Creek. The data was extrapolated between the three lines.

13.3.3 Integrated Conclusion

Collectively, the integrated conclusion at Mill Creek states that the Dakota Sandstone is saturated, heavily fractured, and is a conduit for fluid flow. Each of the data sets in this area support the claim that the Dakota Sandstone is conductive, and the EM and DC results show that the Mancos Shale is relatively more resistive. In addition, correlation between the DC inversion results and the interpreted results from the main seismic line show that there is one fault at southern Mill Creek and the DC/SP results show there are two faults at northern Mill Creek. The northern-most fault is correlated between two DC sections and the eastern-most fault is only shown in one section so it is less reliable.

13.4 Downtown Pagosa Springs

13.4.1 Introduction

In the Downtown Pagosa Springs area two different geophysical methods were used for separate reasons. The first survey conducted near the mother spring area downtown (Figure 13.4. 1) was done using the ground penetrating radar (GPR) method and its main purpose was to determine the location of ancient subsurface travertine deposits. The second survey, conducted in the heart of downtown, was done using

the continuous wave electromagnetic method (CWEM) and was used to determine the location of leaks in the local pipe system.
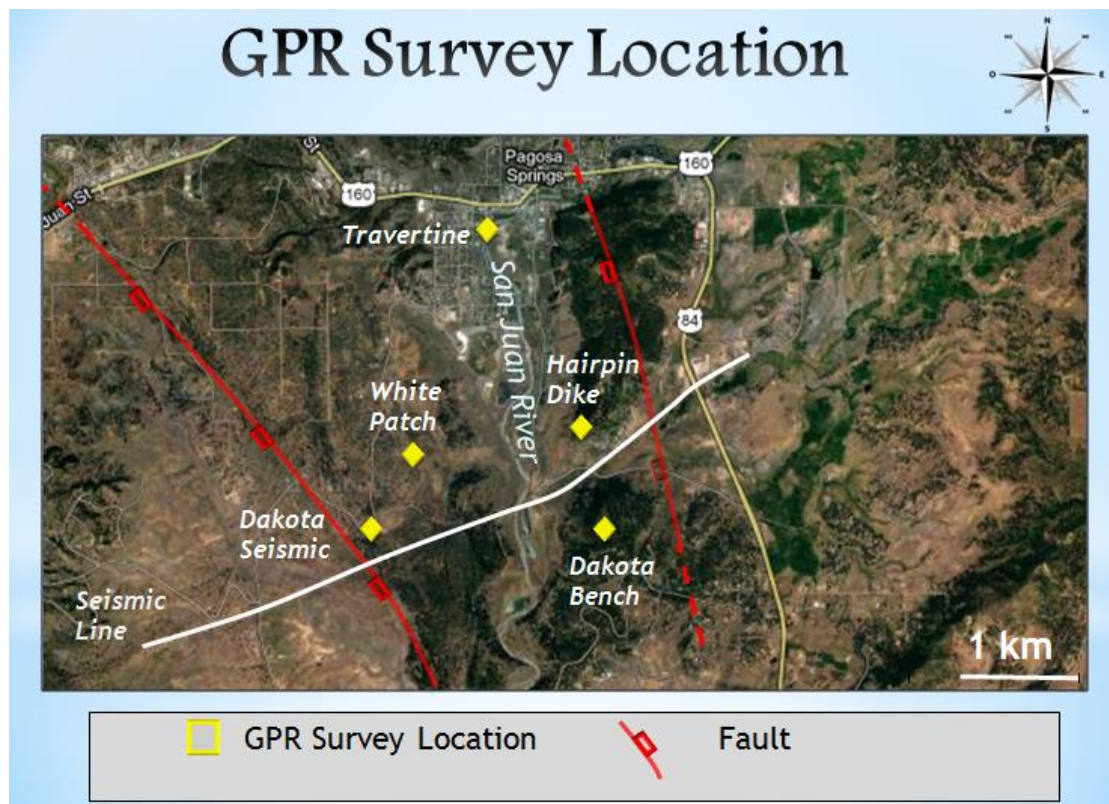
Figure 13.4. 1: A map of all the GPR survey locations. The yellow diamond labeled "Travertine" is the GPR survey conducted downtown.

13.4.2 GPR

The GPR surveys done in the downtown area of Pagosa Springs were focused on imaging the travertine deposits located behind the Mother Spring. As can be seen below, the tops of these deposits were imaged at a depth of approximately 1.8 m. The bottom of the travertine deposits were imaged at a depth of 3.6m, giving us an approximate thickness of at least 1.8m.

Figure 13.4. 2: The above Figure shows the migrated depth section of the GPR data collected at the survey site behind the mother spring.

Figure 13.4. 3: The above image shows the location of the CWEM survey line conducted in downtown Pagosa Springs.
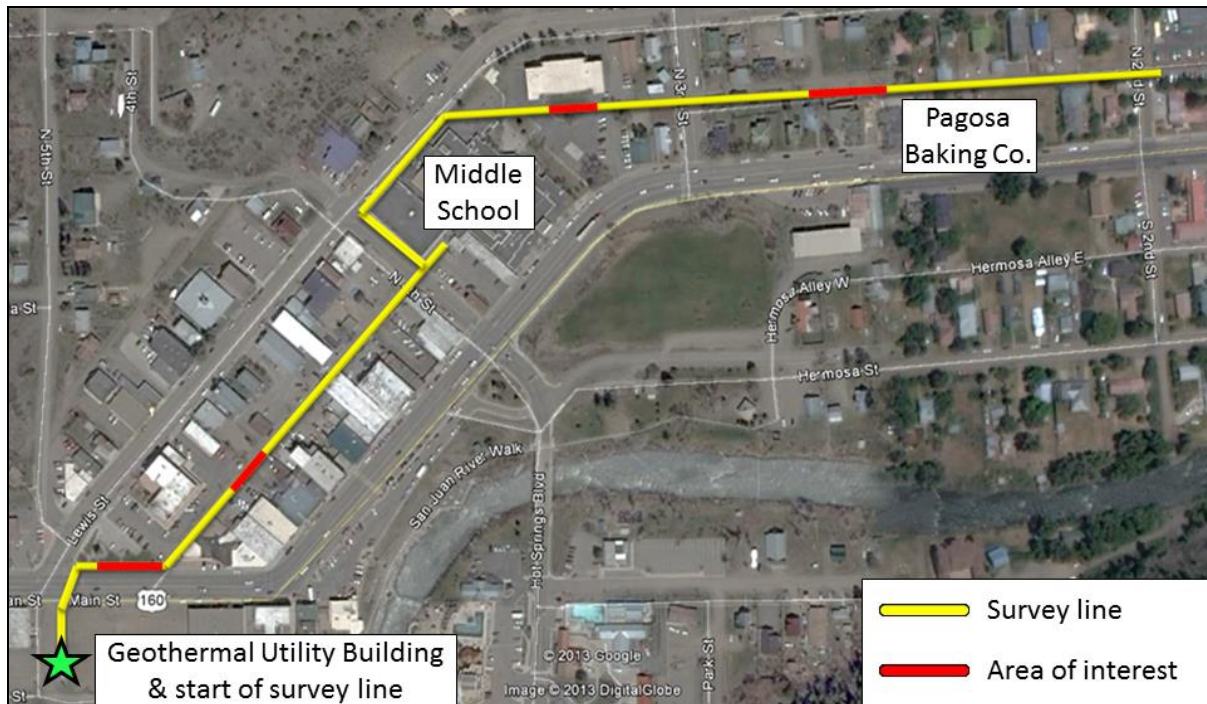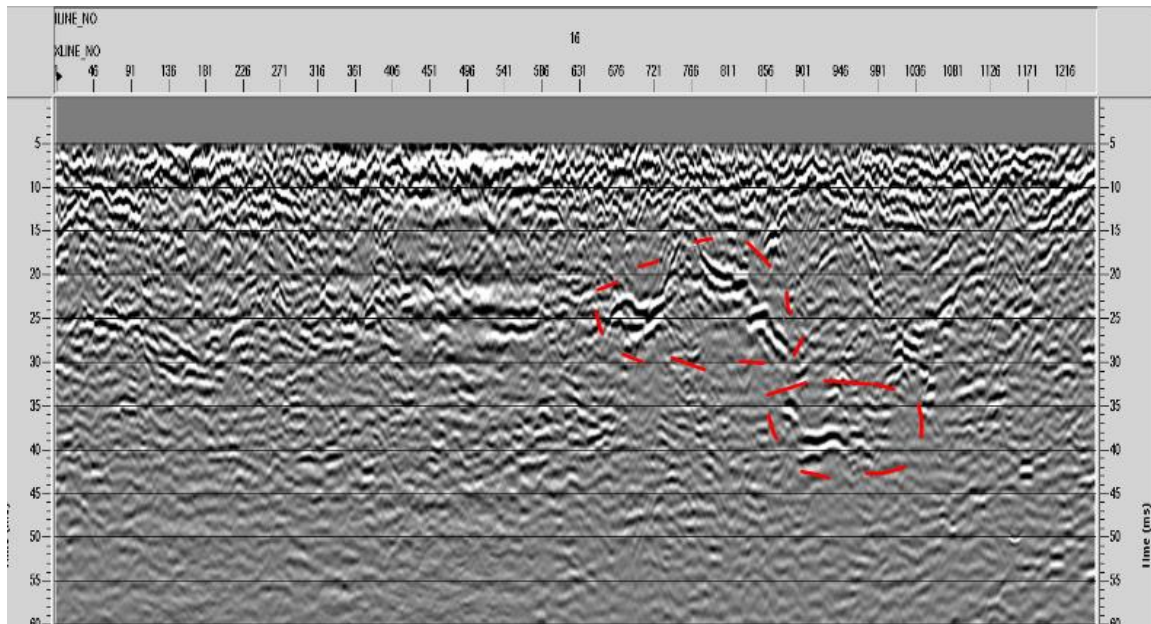
13.4.3 Continuous Wave Electromagnetics (EM – 31)

The CWEM method was employed in the downtown area in order to find the location of leaks in the downtown Pagosa Springs area. As the CWEM method is very good at detecting changes in near surface conductivity, it was chosen in order to determine the locations of these leaks in the pipes. While other methods could also be used to detect such changes in near surface conductivity, given the urban and noisy survey conditions, the CWEM method was the only one used for determining the locations of the leaks. Below in Figure 13.4. 4, the results of this survey are shown:
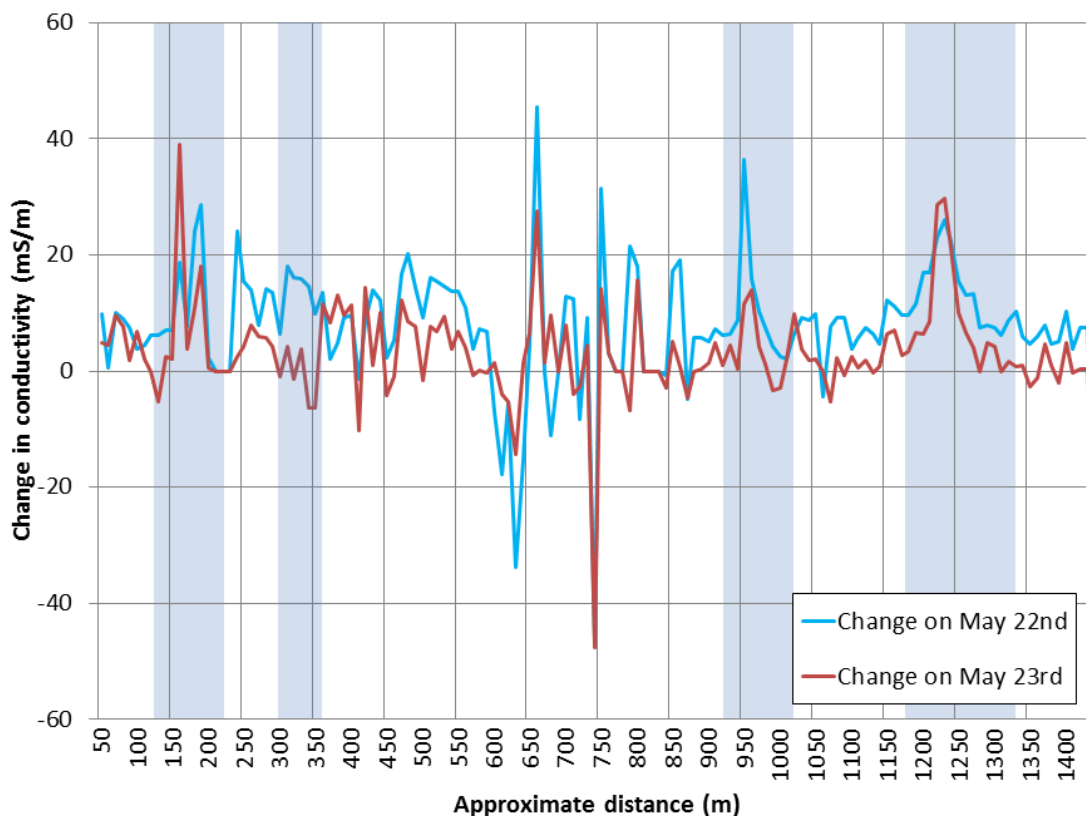
Figure 13.4. 4: The figure shown above displays the results obtained from the EM-31 survey done at the downtown Pagosa Springs location.

The two plotted data sets shown on the graph above correspond to surveys done on May 22 and May23. These data sets were selected out of all the measured data sets due to their high level of correlation. As can be easily observed in each plot, four anomalies were detected at the locations 140-200m, 300-350m, 940-1000, and 1170-1300. While at the location along 300-350 does not correspond to an anomaly for

both days, there was water detected at this location indicating a potential leak. As these findings do indicate the presence of potential leaks, the sources of these leaks is not fully known and further geophysical surveying will need to be done in order to best determine the cause of these anomalies.

13.5 Shahan's Ranch

13.5.1 Introduction

Shahan's Ranch was the field camp 2013 student site. The surveys ran at this site were all student designed and supervised. Shahan's ranch was chosen for a variety of reasons, the primary among them being that the site was the location of a previously drilled hot spring well. The goal in surveying the ranch was to gain context on a geothermal system and investigate the geothermal properties of the area. Furthermore, students also tried to determine the extent of leakage from the well as well as water runoff patterns in the area. Access to the ranch was graciously provided to us by the Shahan family who are the proprietors of the ranch.

13.5.2 DC/SP

In order to qualify the fluid flow in the area, a series of DC and SP surveys were ran in the immediate vicinity of the well. The survey lines are referenced in Figure 13.5. 1:
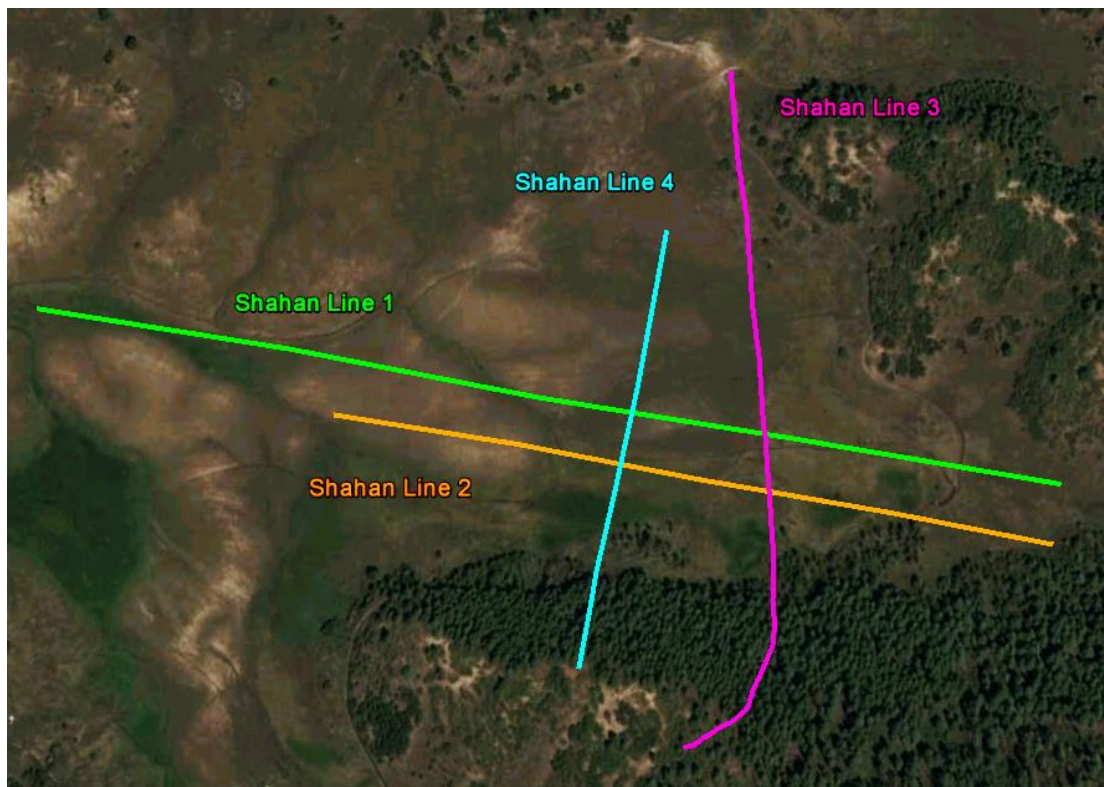
Figure 13.5. 1: Map of surveys conducted at Shahan's Ranch

The crossed pattern would allow us to do 3D analysis of the fluid flow in the area despite having 2D datasets. The Shahan Line 1 also runs directly over the well.
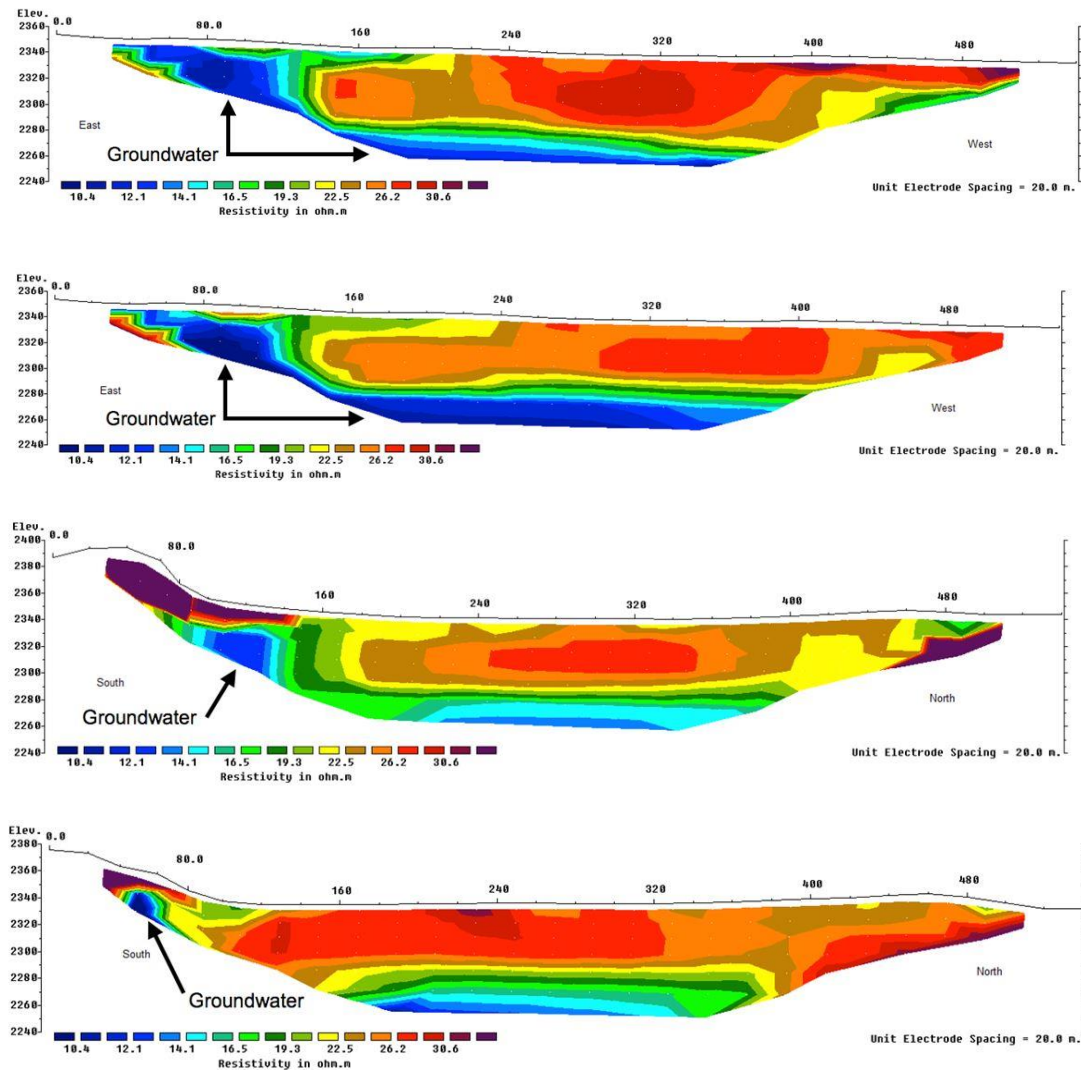
Figure 13.5. 2: DC Resistivity survey inversions.

As can be seen in Figure 13.5. 2, the Shahan Ranch lines show that in the area of the well there is groundwater located under the highly resistive layer that is on the surface. When using the geologic cross section created in the field, this layer is seen to be the Mancos Shale. The highly conductive, fluid filled layer underneath is then the Dakota sandstone. When SP data is compared to the DC data, the result is shown in Figure 13.5. 3.

216
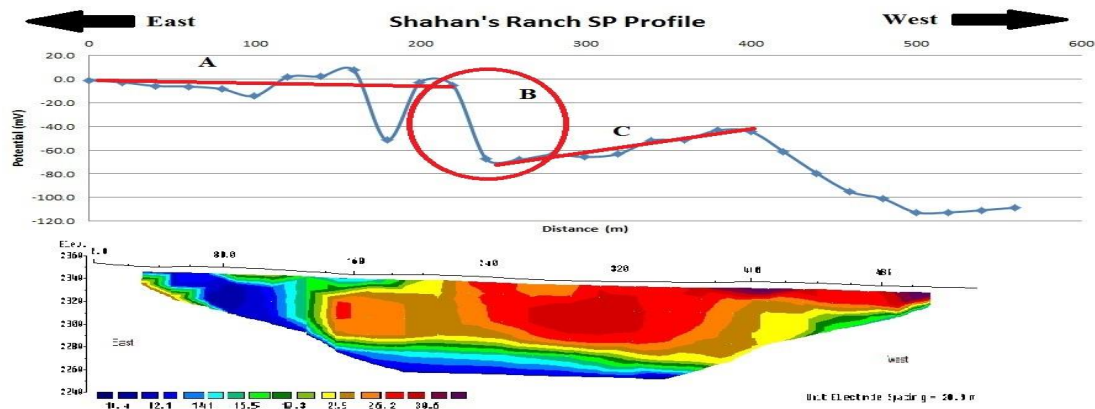
Figure 13.5. 3: DC compared to SP measurements

The sharp drop from segment A to segment C is seen as a reduction is flow. This is the result of wet saturated soils yielding to dry Mancos shale.

13.5.3 Shallow Seismic

The goals of the shallow seismic survey were to better image the Shahan Ranch area as well as determine the velocity for the Dakota sandstone. A lightning storm and human error prevented the data from being very useful, however there were some important results from Figure 13.5. 4.
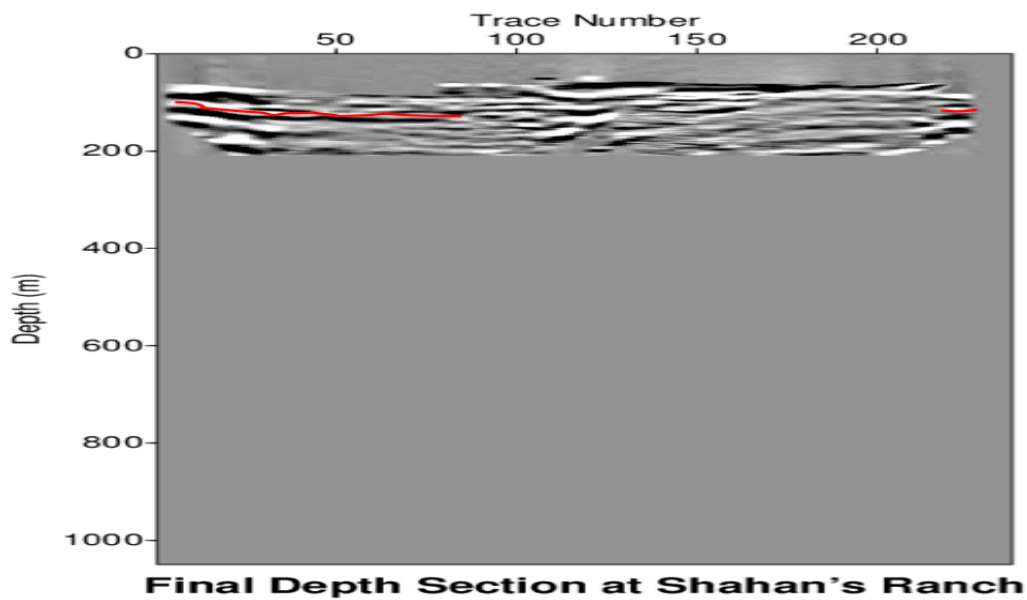
Figure 13.5. 4: Hammer Seismic section

The red outline shows a reflector between Mancos shale and Dakota sandstone. Because of surveying issues the rest of the data is not recoverable. However, it does show that the layering in the area is flat.

13.5.4 Gravity

A gravity survey was performed over the DC line Shahan Line 1. This was in order to qualify the structure of the subsurface underneath the well. The resulting gravity section can be seen in Figure 13.5. 5 and shows that the layers at Shahan's Ranch are relatively flat and continuous.
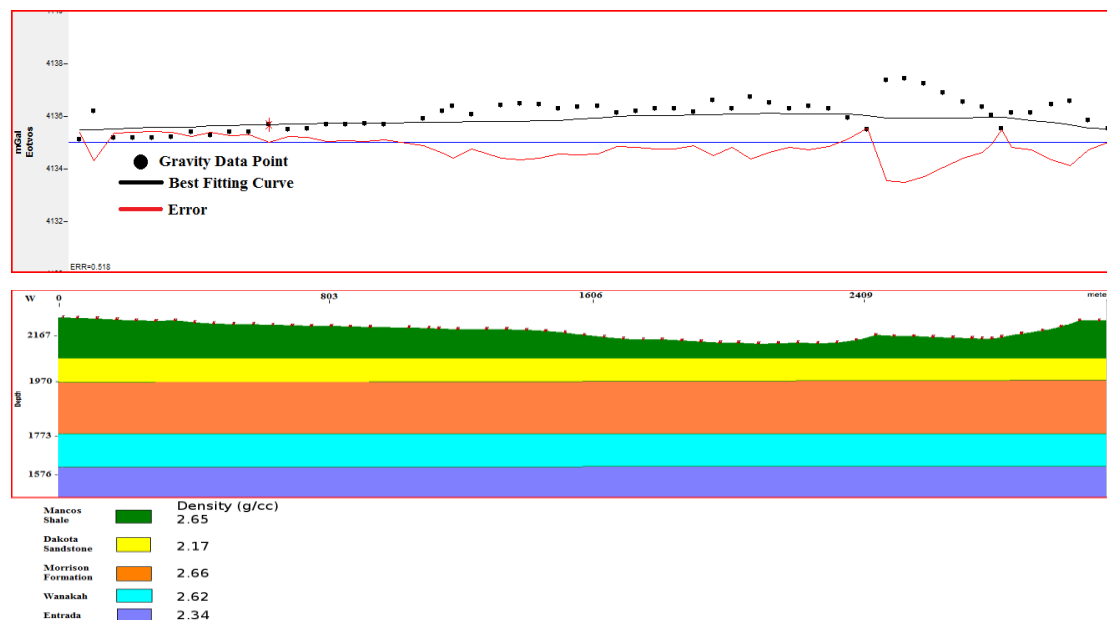
Figure 13.5. 5: Gravity interpretation of the area.

The modeled gravity section, while not perfect, encapsulates the trend in the area of horizontal bedding.

13.5.5 Electromagnetics

An EM 31 survey was performed in the area of the well. The goal of this survey was to qualify leaks from the well and its drainage. The results are shown in Figure 13.5. 6.
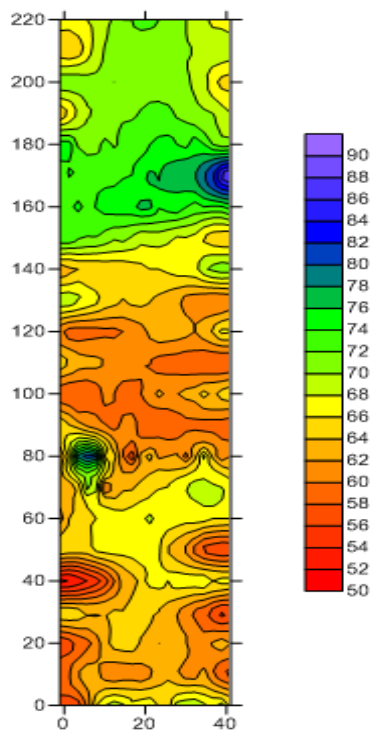
Figure 13.5. 6: EM31 measurements along the grid.

Possible drainage can be identified in the graph. In the section 60 meters to 80 meters as well as from 160 meters to 18 meters there is a conductivity change that can be associated with water drainage.

13.5.6 Conclusion

The geologic cross section seen in the gravity section (Figure X) shows the closest estimate to the geology of the area. The area is overlain by Mancos shale. This layer extends approximately 100 feet into the subsurface before transitioning to Dakota sandstone. This layer of Dakota sandstone is saturated with hot fluid from the subsurface.

On the surface, fluid is leaking away from the well. This is filtering through channels in the area, which affects the conductivity of the immediate subsurface.

14. Conclusion

The region of Pagosa Springs has been further characterized, especially along the main survey line. The Eightmile Fault, the 1986 Warren Fault, and the 2012 Field Camp Fault were all identified by seismic, DC, SP, and gravity methods, as well as geological observations this year. The 2013 Field Camp Fault was identified this year as a possible new fault by seismic, gravity, and geologic observations. This suggests that the Warren 1986 Fault and 2012 Field Camp Fault are major faults that strike North-South through this region. Based off of SP and DC data sets along the eastern side of the main survey line in Mill Creek and the surrounding area, further possible faults have been detected and are proposed to strike West-East. The EM and DC data indicated that in this region, the Dakota Sandstone is most likely saturated and would provide a recharge zone for the geothermal reservoir. Furthermore, based off of geochemical observations and geological studies, it is proposed that the source of the water from the geothermal system originates from rainfall in the Wolf Creek Pass volcanic system located in the San Juan Mountains to the east of Pagosa Springs. As shown in the geologic cross section (Figure 14. 1), the rainfall permeates through the subsurface in fractures until it hits the Precambrian crystalline basement. Here the water either travels along the Entrada Formation/Precambrian basement boundary or within shallow fractures in the basement. This groundwater continues westward until reaching the proposed modified Warren 1986 Fault where it then travels up the fault due to heating and pressure. This groundwater eventually reaches the surface and emerges at the mother spring or at small springs located around the Pagosa Springs area. This is the most probable geothermal system that can be derived from the data collected in the 2012 and 2013 field sessions.
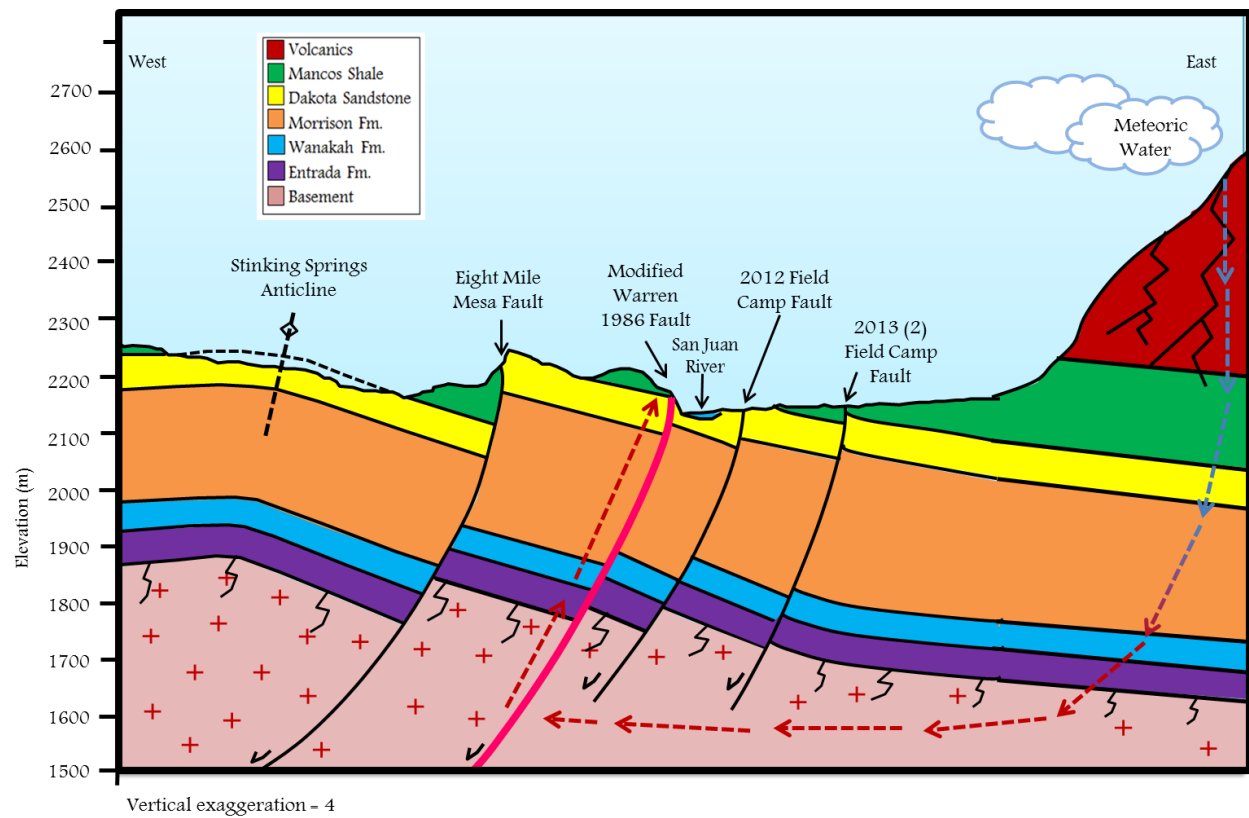
Figure 14. 1: Finalized geologic cross-section with proposed geothermal recharge system.

15.Recommendations

The Pagosa Springs geothermal system was further characterized in this geophysical investigation. However, further investigation is still required to fully understand the mechanisms controlling the geothermal reservoir.

In order to achieve further characterization, it would be beneficial to have more well data from the surrounding region, specifically geological and temperature information. These data would assist in characterizing the origin of the geothermal heat source, as well as the water's depth of origin. Further, depending on the location of the well, such data may indicate the original percolation method of the water source. More surveys will need to be run as well. The area north of Pagosa Springs has yet to be surveyed. Another survey line parallel and north of the main survey line run this year would also be extremely insightful to image the smaller faults in the eastern portion of the survey. Another survey that would provide insight and be fairly easy to obtain would be along the highway just south of the fairgrounds. Another possibly valuable region to survey would be the area north of our main survey line and west of the San Juan River. This area is relatively flat and has been untouched by surveys thus far. Regardless, future surveys should be built upon the findings of the past years' work.

Appendix A

A.1   Equipment

Two 12 ton Vibroseis trucks were used to generate the seismic source with a maximum frequency of 400 Hz. The trucks have a 3000 PSI operation pressure and a 30,000 PSI maximum pressure. The receivers were geophones with a cut frequency of 10 Hz.

A.2   Processing

A.2.1   Shot display

The shot display is the first step during seismic data processing. It is used for identifying features in the raw shot gathers that represent noise, bad traces, and everything else other than reflections. Bad shots were removed in the first step. Next, the dead channels of areas where geophones could not be deployed (for example, at the San Juan River) were subject to trace killing. Before the first arrival, there is energy present. This is potentially associated with aliased data, and so a top mute is applied to remove it.
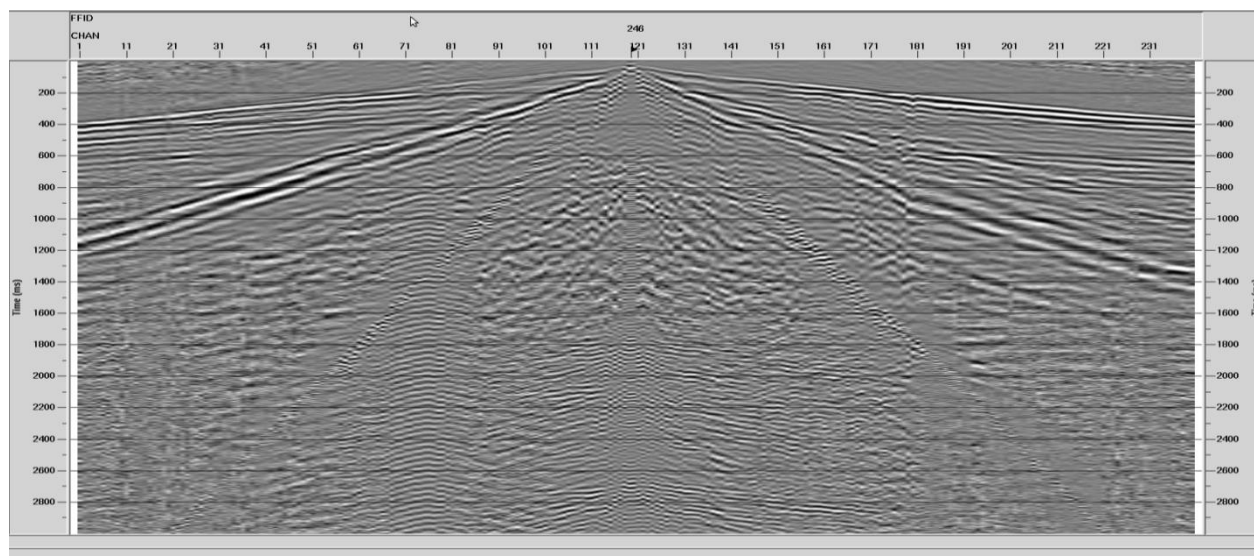
Figure A. 1: Raw shot record display with AGC.

A.2.2   Noise Attenuation

The features that represented noise in the dataset were ground roll, airwaves and refracted signals. In order to remove these, a combination of FK filters and trace mutes were applied. Trace mutes were targeted to the airwaves while FK filters (polygons and velocity filters) aided in removing the ground roll and linear noise (refractions). Figure A. 5 shows the comparison of

before and after noise removal. After these applications, the dataset appears much cleaner and a lot more signal (reflections) appear. The noise is not completely removed however , this was enough to increase the signal to noise ratio.
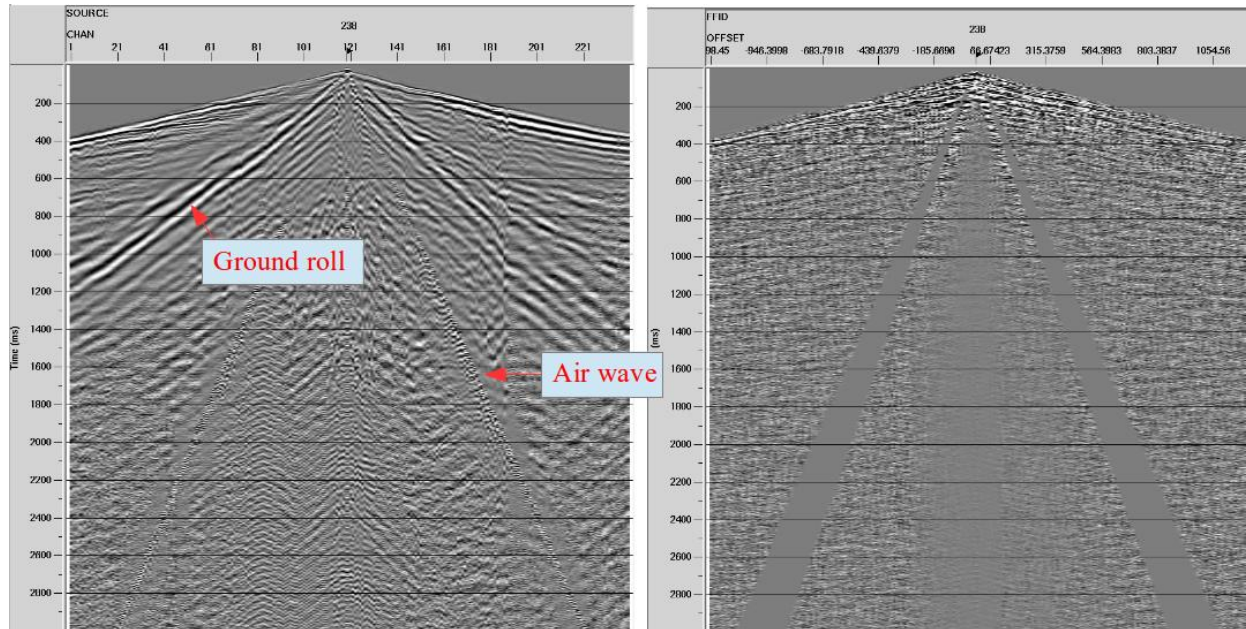
Figure A. 2: Shot gathers before Noise Removal on the left and after Noise Removal on the right.

A.2.3 Geometry

This step involves geometry assignment for source, receiver, and pattern coordinate information using the GPS survey data. The pattern information establishes the relationship between shots and geophones by specifying a particular receiver pattern for each shot. During acquisition, three different receiver patterns were used. The mid-point between each source and receiver is calculated, and the common depth-point (CDP) bin coordinate is computed for each trace in the data. Each CDP bin contains the mean of the midpoint coordinates of all the traces. The CDP bin number is computed by adding source and receiver station numbers. Thus, CDP index range from 6402 (first source and first receiver is at station 3201) to 7688 (last source is at station 3816 and last receiver is at 3872). The maximum CDP fold was 188. Fold is defined as the number of traces in a CDP gather that have a common reflection point.
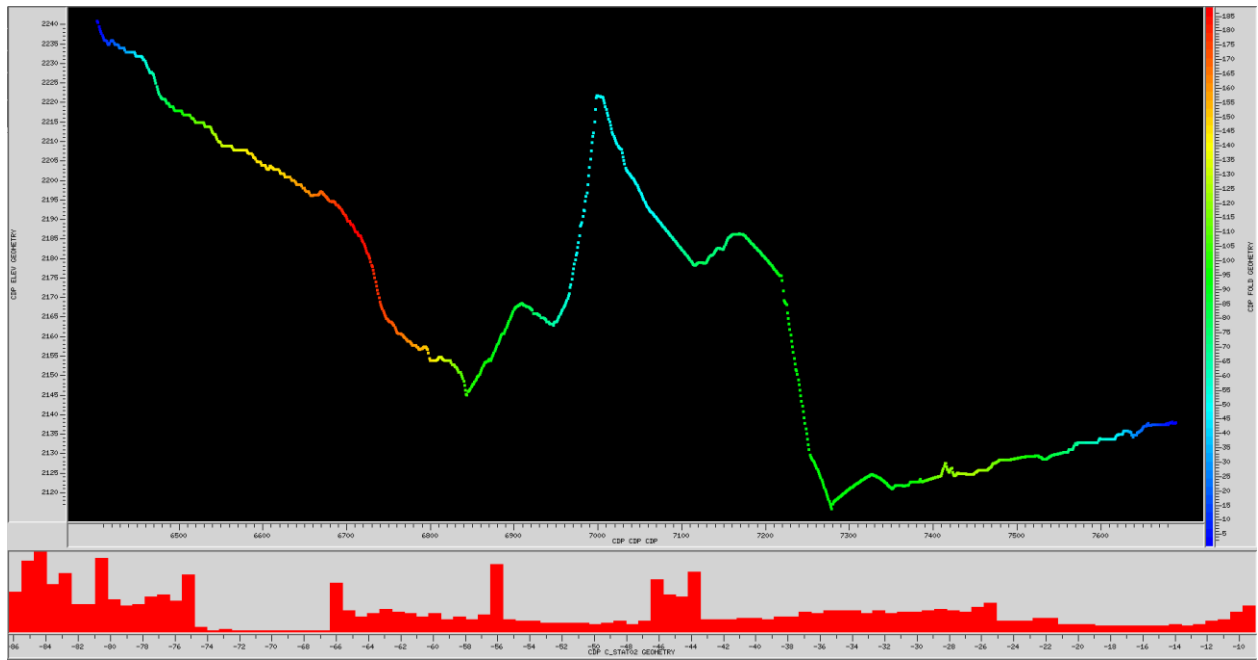
Figure A. 3: CDP fold.

A.2.4   Statics correction

Static corrections comprise of elevation, refraction, and residual statics. Firstly, elevation statics were done by applying a bulk shift of seismic traces in time to compensate the effect of topography as well as the elevation of sources and receivers. Variable topography was also incorporated. Datuming is a process to shift the data points to a constant depth level. 4 shows the topography before (in blue) and after datuming (in red). Elevation statics moves all CDP point to a constant depth of 2250 meters.
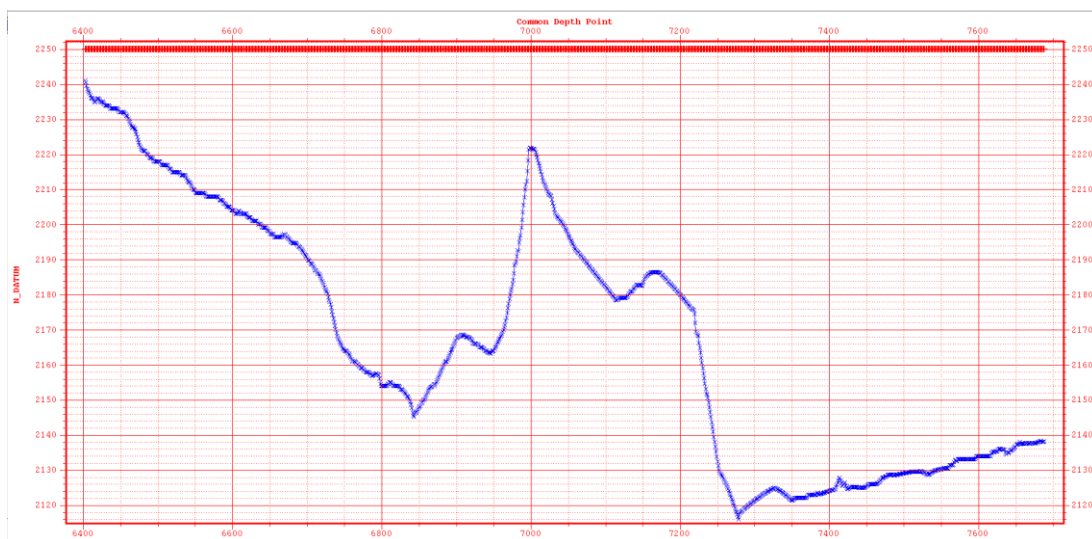
Figure A. 4: Constant datum level of 2250 m.

225

In refraction statics correction, the low-velocity layers in the near surface are targeted. This was carried out by a process called first break picking on each of the shot gathers. First breaks are essentially the first signal received at each trace and these commonly represent the base of weathered layers in the land seismic data. Figure A. shows an example of the shot gather where the blue line is the time window picked for first break calculation while red line is the picked first arrivals.
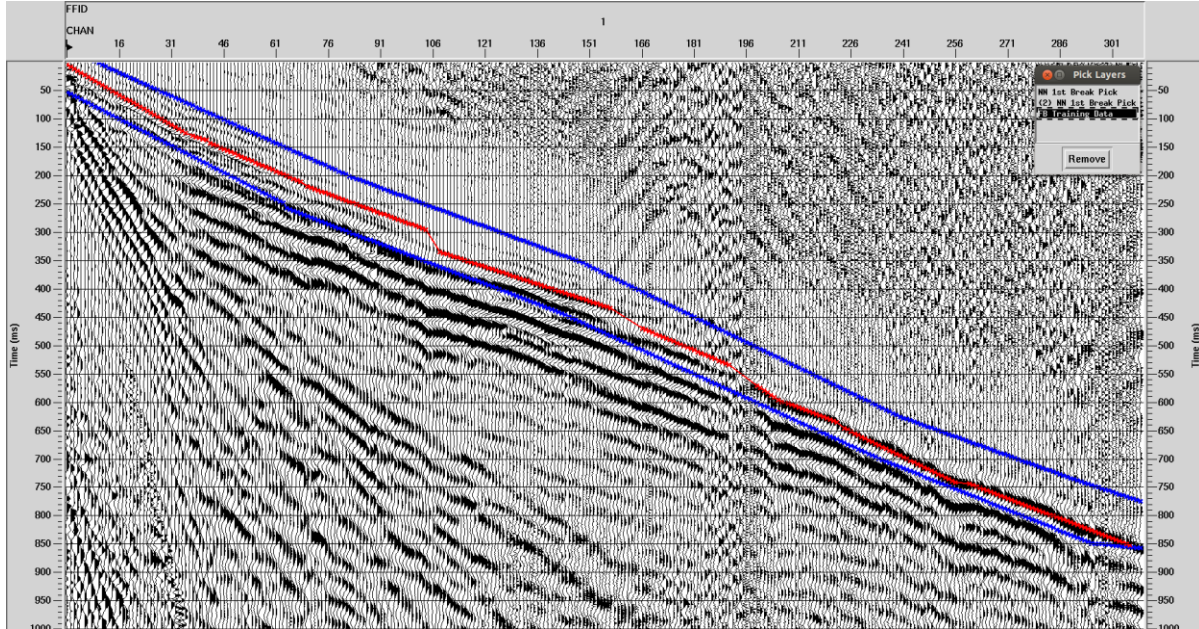
Figure A. 5: First-break picking shown on the shot gather.

A.3 Velocity analysis

NMO correction depends on the offset and velocity thus a correct velocity to flatten a reflection hyperbola is estimated by conduction velocity analysis.

The NMO equation (Equation A. 1) describes the behavior of the hyperbola in the x-t domain where t_0 is a two-way travel time for zero-offset geometry at a particular CDP location. The velocities (v^2) are found by fitting different hyperbolic curves and flattening the gathers.

$$t^2 = t_0^2 + \frac{x^2}{v^2}$$

Equation A.1: hyperbolic travel time (NMO) equation.

When the data is stacked, the horizontal reflectors for each gather are enhanced and the others are reduced thus intensifying the signal. Stacking assumes horizontal reflectors. Before stacking, a process called dip moveout (DMO) is conducted to account for dipping reflectors in the subsurface. This step is important as

if the reflector is near horizontal in one section and dipping in another, DMO will ensure that the signal is continuous across the reflector (see Chapter A. 4).

Figure A. 3 shows the velocity analysis function. The colorful plot is called the semblance plot where points of concentrated energy may represent a reflector. The right of the figure shows the shot gathers and so when velocity picking on the semblance plot, the shot gathers can be analyzed simultaneously to ensure they are flattened at that certain velocity. From picking the velocities, a velocity spectrum is produced after stacking the gathers. Figure A. 7 displays the velocity spectrum on the left and the plot of velocity vs two-way travel time on the right. The general trend is that velocity increases with time. Previous velocity picks against two-way travel time can be displayed for comparison.
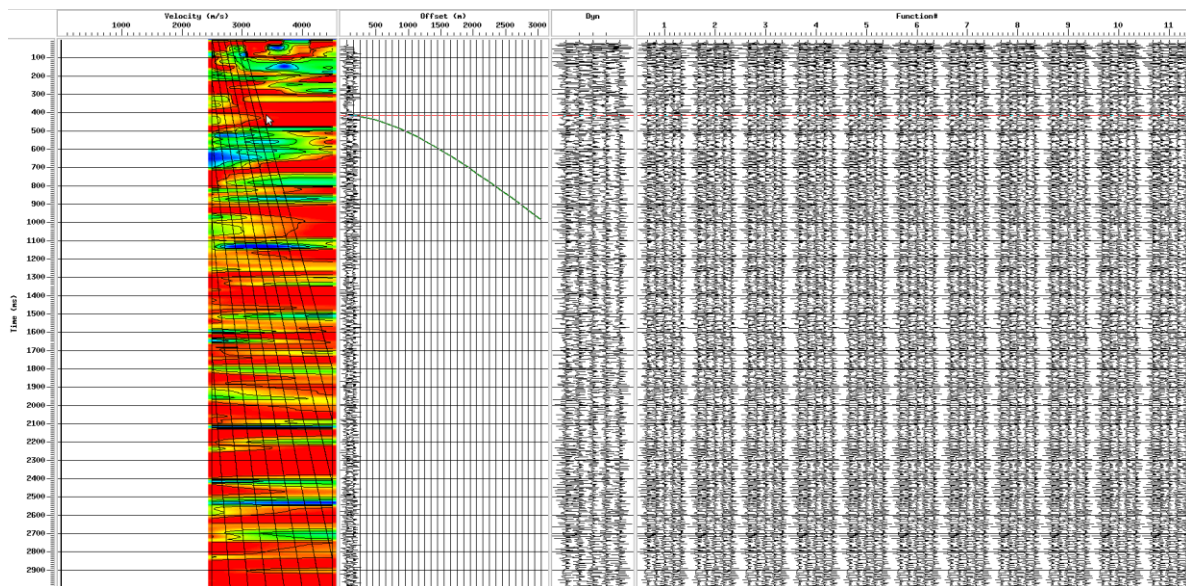
Figure A. 3: Velocity analysis window.
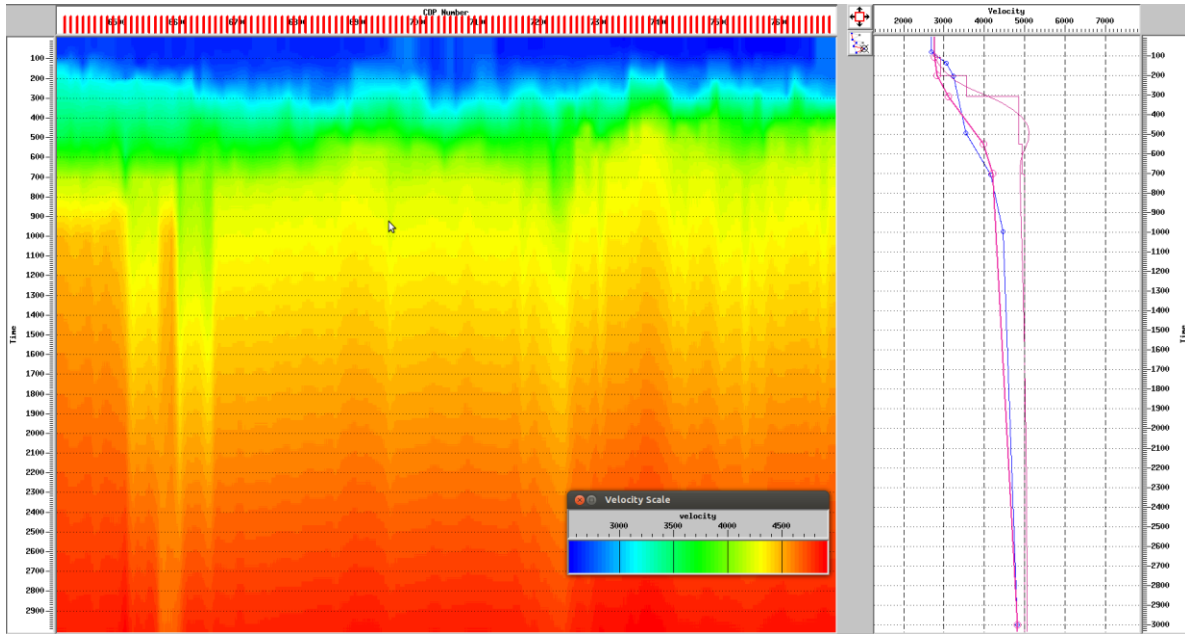
Figure A. 4: First pass velocity field display.

Several iterations in velocity picking are conducted along with NMO and stacking to correct for the wrong velocity picks. Figure A. 5 shows the velocity model we get after three iterations.
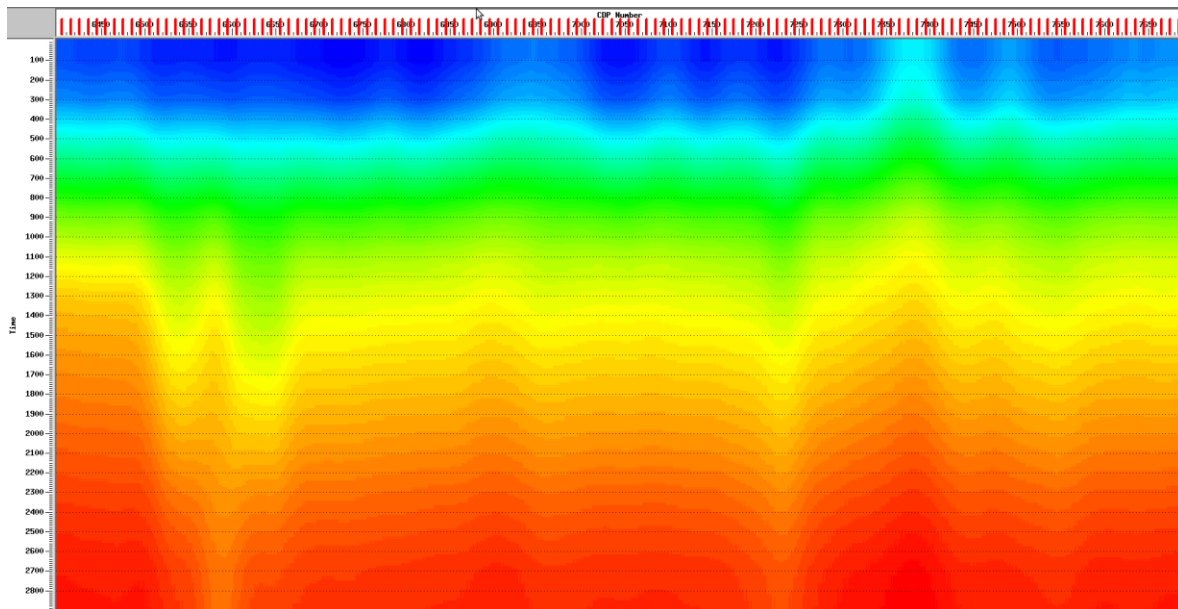
Figure A. 5: Smoothed velocity model.

A.4   DMO

Dip moveout (DMO) correction is necessary to account for dipping reflectors because the traces of common midpoint (CMP) gathers do not include a common reflection point (36).

When a reflector is tilted, the reflected ray paths will arrive at different times at two receivers (one receiver located at an offset up-dip with the second receiver at equal offset down-dip from the central shot point). DMO is set as the difference in travel time t_x (receiver 1) and t_{-x} (receiver 2) of the tilted reflector. DMO correction is used to calculate the reflection dip if the velocity is known. Nevertheless, the velocity can be derived by using normal move-out (NMO) calculations. (37)

In the Pagosa Springs dataset, DMO is applied to handle dipping reflectors such as the dipping Dakota sandstone layer.

A.5   Stacking

Data is sorted from shot to CMP gathers before stacking. Stacking is a process whereby traces are summed together after NMO and DMO corrections. This helps to improve the signal-to-noise (S/N) ratio as the signal portions of each shot add together whereas the noise (usually random) stacks out. Furthermore, stacking also attenuates multiples which is especially effective for long-period multiples. This is due to the differences in the NMO velocities being largest between primaries and long-period multiples. Figure A. 9 shows the stacked section. Features known as 'smiles' appear in the section and these can be removed after migration of the section (Chapter A.6).
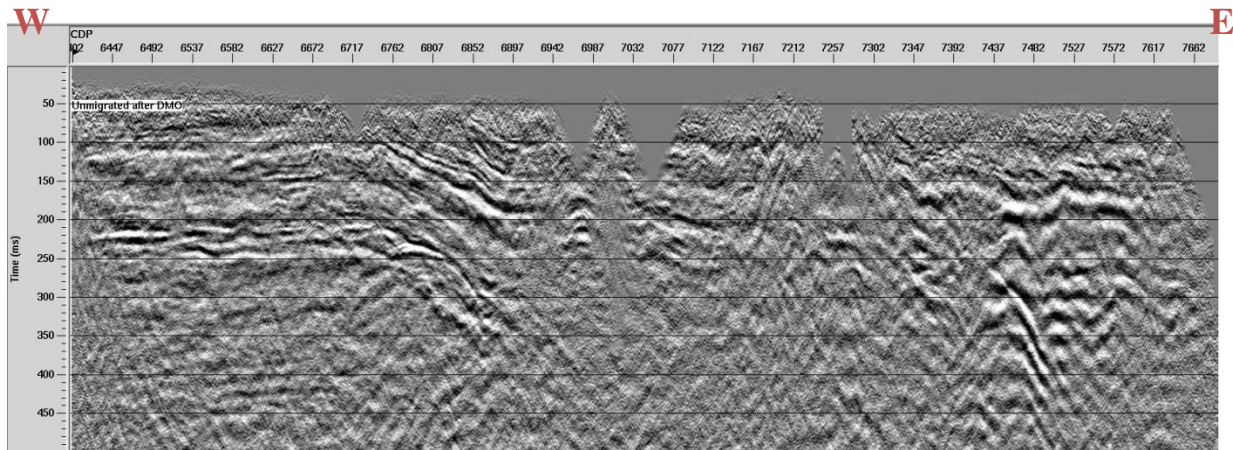
Figure A. 6: Stacked section after applying NMO and DMO.

A.6   Poststack migration

Migration is a seismic data processing technique which converts positions of reflection events in zero-offset to the true geological locations. It also collapses the diffraction patterns caused by point reflectors. After migration, dipping reflectors appear longer, at a greater dip, and move down-dip.

There is a variety of migration algorithms aimed at processing different seismic data. Two main categories are post-stack and pre-stack migration. Post-stack migration is an approach of migration in which the data is migrated after it has been stacked. Although the cost of post-stack migration is much less compared to the pre-stack migration, it can hardly yield clearer results compared to pre-stack migration. Pre-stack migration is another migration technique where seismic data is adjusted before stack. The most commonly used pre-stack migration is pre-stack depth migration.

In this 2D land seismic data processing, post-stack Kirchoff time migration method was adopted. Kirchhoff migration is a popular migration algorithm where data are decomposed into point reflections. It can handle various velocity variations, geometry, and structure. The post-stack time migration result can be seen in Figure A. 7.
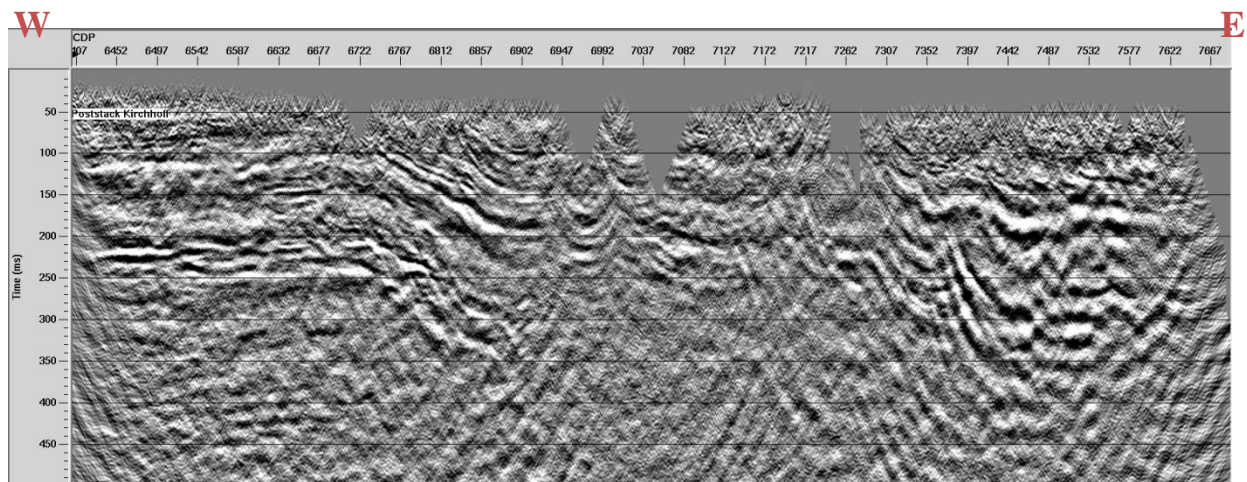
Figure A. 7: Post-stack Time Migrated seismic section.

Migration velocity is a critical factor that controls the quality of an image after migration. If the velocity is relatively smaller, the seismic data could be under-migrated and vice versa for when the velocity is larger. Larger velocities used for migration can result in the appearance of 'smiles' in the section. In this processing work flow, many 'smiles' swings can be observed in the deeper part of the seismic section as shown in Figure A. 8 below (red and orange circles). The red circles are probably due to single traces in the CDP gather. The reason for swings in orange circle is more complicated. One possible explanation is that this section has much lower velocity than expected. Another hypothesis is that there is an igneous intrusion through the Mancos shale that could distort the underlying reflections. The intrusion is of very high velocity.
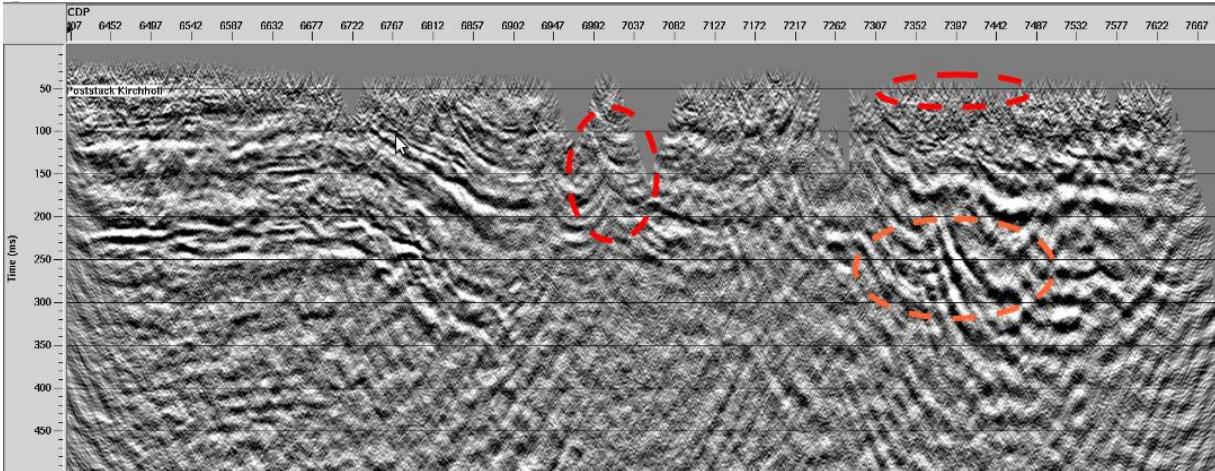
Figure A. 8: Post-stack Time Migrated seismic section highlighting noisy parts.

A.7   Time-depth conversion

There are three basic methods in the time-to-depth conversion process, namely the constant velocity (Vint) method, the layer-cake (Vo=Vint) method, and the variable velocity layer-cake (Vo+KZ) method. The Vint method converts the seismic data using a single velocity value assuming the whole section shares the same velocity. In the Vo=Vint method, the seismic section is defined into layers according to the horizons and each horizon has its own velocity value. Vo+KZ method is similar to the Vo=Vint method except that each layer now has a linear varying velocity function.

In this project, the Vo+KZ method is used by manipulating the NMO velocities. The NMO velocities are converted to the dix interval velocities and smoothed. The final result is shown in Figure A. 9.
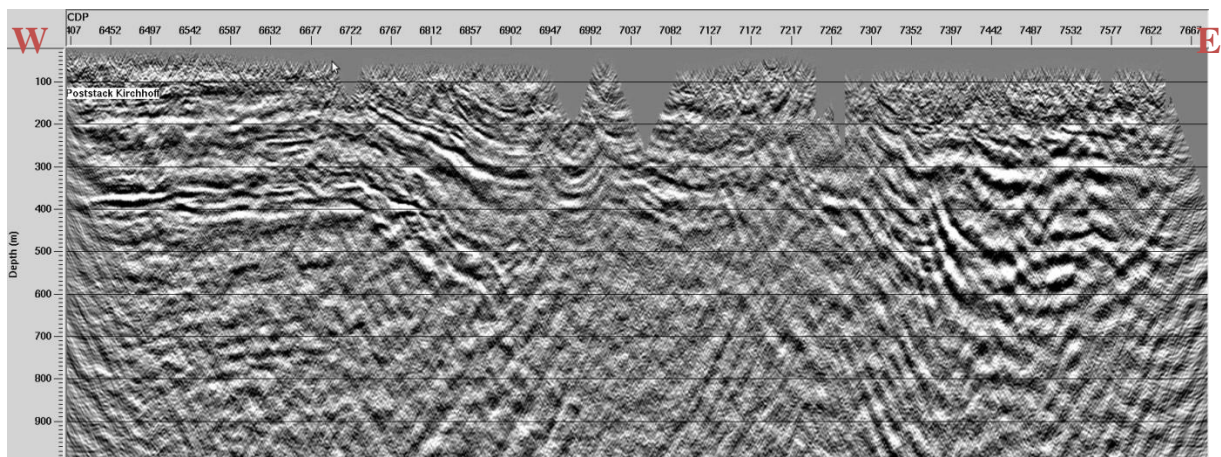
Figure A. 9: Depth converted time migrated seismic section.

Appendix B

B.1 Theory

Hammer seismic focuses on the near surface waves and reflections rather than the deep seismic which can go kilometers deep. Hammer seismic uses an impulse which, by itself does not yield great data, but when stacked multiple times can lead to data that is reasonable. For example, the group at the bench site took 3 hammer strikes per shot point and stacked the data on the site to save some time in the processing portion of the field session. Hammer seismic focuses on the reflections that it receives, which means that much of the data is usually cut out because there is a lot of noise in the data from ground roll, refractions, and noisy geophones.

B.2 Equipment

The hammer seismic crew used a standard sledgehammer with a plate to help propagate the waves consistently in the ground. The program that was used to acquire the data is called Multiple Geode Operating System (MGOS) from Geometrics which was able to stack the data in the field as well as organize all of the recordings into the field file identifications (FFID). The processing for the bench line and the well line used the program ProMAX which was recommended to do the processing. The Shahan's ranch used Seismic Unix (SU) to process their data.

Appendix C

C.1 Theory

The theory behind using gravity in geophysical exploration comes from the fact that buried dense objects can have a measurable effect on the Earth's gravitational field that can then be quantized to determine the existence of objects beneath the ground's surface. A common mistake is to associate gravity with the physical size of an object. The equations below show that it is indeed a mistake, since that gravity is only affected by the mass of an object—in turn determined by density and volume [47]. The more mass an object has, the more gravitational force it has. Gravitational acceleration (g) at the surface of the ground, seen in Equation C.1, is described by Newton's second law of motion and the universal law of gravitation. In Equation C.1, G is the Universal Gravitational Constant (Equation 7.1), m is the mass of the object in kilograms, and r is the distance between the center of mass the object and the center of mass of the Earth in meters [47].

$$g = G\frac{m}{r^2}$$

<div align="center">

Equation C.1: Gravitational acceleration.

</div>

When gravity meters are taking readings of the gravity acceleration in a location on the surface, only the component perpendicular to the surface (vertical) is measured. Mathematically, the gravitational acceleration of the vertical component is calculated by taking the derivative of the scalar gravitational potential field with respect to z, the vertical axis, as shown below in Equation C.2 [47]. Gravity meters can only record the vertical component of the gravity acceleration because the meter is essentially an accelerometer that uses a suspended mass attached to a spring. The machine then measures the vertical component of the gravity force acting on the suspended mass. Therefore, the vertical component of the gravitational acceleration of the dense objects in the subsurface can be measured using a gravity meter and will produce a positive anomaly, while the absence of mass or less dense objects will produce a negative anomaly [47]. Thus, since the vertical component is the one being measured it becomes essential that the gravity meter is level to ensure a correct gravity reading.

$$g_z = -\left(\frac{\partial U}{\partial z}\right) = G\int_x\int_y\int_z \left(\frac{z}{r^3}\right)dx\,dy\,dz$$

233

This method seems great theoretically but suffers from real world limitations. The environment where the gravitational acceleration readings are measured can prove to be an issue. Instruments such as the Scintrex CG-5 Autograv Gravity Meter can become a challenge to operate safely on steep ground, wet muddy ground, or in severe rain.

The gravity field of an object in the subsurface will depend on both the density and volume of the object and the distance between its center and the surface of the Earth. Equation C.1shows that the anomaly response of the gravitational acceleration will decrease proportionally by $\frac{1}{r^2}$ as the depth increases, where r is the distance from the center of the object to the surface of the Earth. Figure C.1 shows how the gravity anomaly response for a cylinder in the subsurface diminishes as the depth increases [58]. In this example, the cylinder is hollow, making it less dense than the material in the background. The gravity response of the cylinder must be negative in comparison with the surrounding material. As depth increases, the amplitude of the gravity anomaly response decreases while the width of the anomaly curve increases [58]. On the other hand, if the object was shallower and closer to the surface, the gravity anomaly response will have a larger amplitude and narrower width.
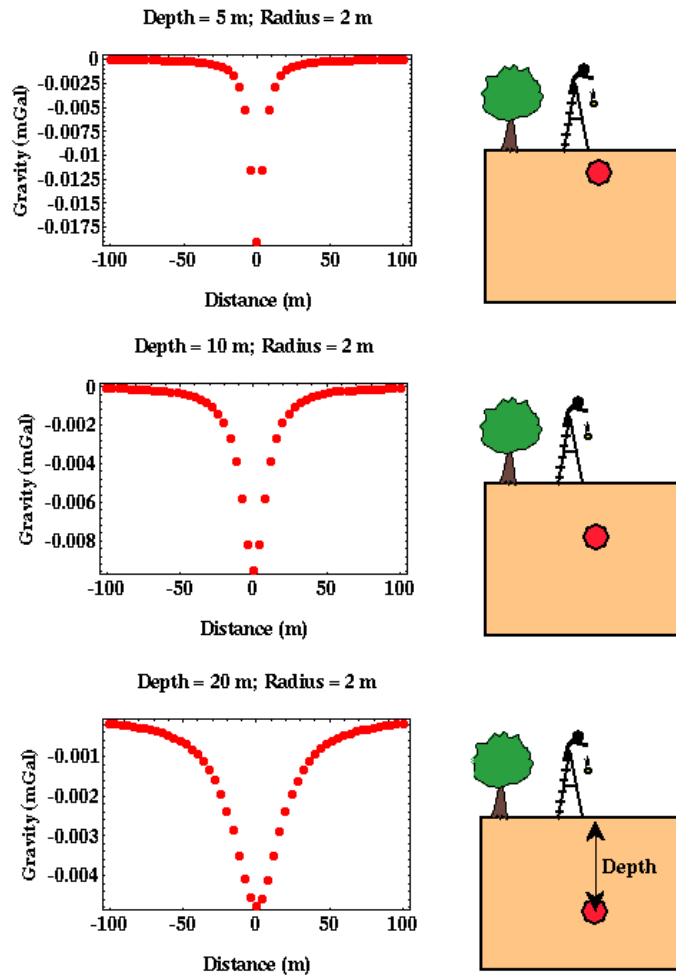
Figure C.1 Changes in gravity response with depth [58].

C.2 Equipment

The CG-5 was the primary instrument used in the field because it is relatively fast to setup, level, and operate in comparison to the LaCoste & Romberg gravity meter. This becomes advantageous when the gravity survey covers a long line such as the main seismic line because it allows the operator to take faster gravity readings and cover more stations between each loop. However, both the CG-5 and the L&R have their limitations. It is very difficult to use either of them on steep cliffs since it will be almost impossible to level the instruments. The CG-5 and L&R also experience different amounts of instrument drift. This necessitates the L&R making a base station reading about every 2 hours and the CG-5 about every 3-4 hours.

C.2.1 CG-5 Operation

1. Carefully remove the CG5 from its storage case and place it on the base plate, making sure to line the meter up with the corresponding grooves/notches on the leveling base platform.

2. Turn on the meter and press the "level" button. A diagram should appear on the digital display showing the current state of the meter and how the leveling screws should be turned in order to level the meter. Turn each of the three leveling screws according to the digital display until a smiley face appears on the digital display.

3. Once the parameters of the reading have been set (number and type of readings, station number, grid lines, etc.), navigate to the start menu using the keypad.

4. When it is time to take a reading, press the record button and walk quickly to a spot about 3 meters away. A blue light will shine from the side of the meter while the reading is in progress.

5. When the blue light goes off, return to the meter and record the relative gravity readings, the standard deviation for each reading, and the time each reading was taken.

6. After the data has been recorded, navigate back to the main screen and power the meter off. Place the meter back in its carrying case before moving to the next station.

C.2.2 L&R Operation

1. Carefully remove the LNR from the carrying case and place it on the stand.

2. Turn the meter on (switch on the right) and turn the locking knob counterclockwise to unlock it.

3. Level the meter by turning the leveling adjustment screws until the three leveling bubbles are perfectly centered.

4. Look through the eyepiece and turn the reading adjustment dial until the crosshair hits 2.6. Always approach from the same direction in order to get consistent readings.

5. Once the crosshair hits 2.6, the meter is ready to measure. The integer portion of the reading is the 4 digit number on the reading counter. To get the 2 digit decimal portion of the reading, look on the adjustment dial. Record the full reading (integer + decimal) and the time of the reading.

6. After the reading has been taken, lock the meter by turning the locking knob clockwise then turn the meter off. Place in carrying case before moving to next station.

The readings from the L&R must be converted into observed gravity readings using a table, seen in Table C.1. This table is specific to the L&R owned by the Colorado School of Mines Geophysics Department and should not be used to convert readings from any other L&R.

Table C.1: L&R conversion table [59].

TABLE 1

MILLIGAL VALUES FOR LACOSTE & ROMBERG, INC. MODEL G GRAVITY METER #G- 509

COUNTER READING*	VALUE IN MILLIGALS	FACTOR FOR INTERVAL	COUNTER READING*	VALUE IN MILLIGALS	FACTOR FOR INTERVAL
000	000.00	1.02510			
100	102.41	1.02385	3600	3681.92	1.02257
200	204.80	1.02365	3700	3784.17	1.02255
300	307.16	1.02349	3800	3886.43	1.02252
400	409.51	1.02335	3900	3988.68	1.02249
500	511.84	1.02323	4000	4090.93	1.02246
600	614.17	1.02311	4100	4193.18	1.02242
700	716.48	1.02302	4200	4295.42	1.02238
800	818.79	1.02293	4300	4397.66	1.02233
900	921.07	1.02286	4400	4499.89	1.02228
1000	1023.36	1.02280	4500	4602.12	1.02223
1100	1125.64	1.02273	4600	4704.34	1.02217
1200	1227.91	1.02268	4700	4806.56	1.02210
1300	1330.19	1.02261	4800	4908.77	1.02203
1400	1432.44	1.02260	4900	5010.97	1.02195
1500	1534.70	1.02255	5000	5113.16	1.02187
1600	1636.96	1.02250	5100	5215.35	1.02179
1700	1739.21	1.02247	5200	5317.53	1.02172
1800	1841.46	1.02243	5300	5419.70	1.02163
1900	1943.70	1.02240	5400	5521.87	1.02154
2000	2045.94	1.02238	5500	5624.02	1.02143
2100	2148.18	1.02237	5600	5726.16	1.02132
2200	2250.41	1.02235	5700	5828.29	1.02119
2300	2352.65	1.02236	5800	5930.41	1.02105
2400	2454.88	1.02238	5900	6032.52	1.02096
2500	2557.12	1.02242	6000	6134.60	1.02066
2600	2659.36	1.02245	6100	6236.67	1.02045
2700	2761.61	1.02248	6200	6338.72	1.02022
2800	2863.86	1.02251	6300	6440.74	1.01999
2900	2966.11	1.02255	6400	6542.74	1.01974
3000	3068.36	1.02256	6500	6644.71	1.01966
3100	3170.62	1.02258	6600	6746.66	1.01914
3200	3272.88	1.02260	6700	6848.57	1.01981
3300	3375.14	1.02260	6800	6950.45	1.01947
3400	3477.40	1.02260	6900	7052.30	1.01812
3500	3579.66	1.02259	7000	7154.11	

* Note: Right-hand wheel on counter indicates approximately 0.1 milligal.

7-12-78
CR

237

Appendix D

D.1   Theory

The Earth has a continuous magnetic field created by the rotation of the planet's core. This field is primarily dipolar in shape and direction, with the field traveling from the South Pole to the North Pole (Figure D.1). While the field flows primarily from south to north, its strength and exact direction vary. Due to the dipolar shape of the field the direction of the field changes at different locations on the Earth. The direction of the field is measured in two ways, inclination and declination. The inclination is the angle in the vertical direction with respect to the horizontal, whereas the declination is the horizontal angle with respect to north.

Diurnal and seasonal variations can be seen in this field throughout the course of a year. These changes are monitored by the base station in surveys lasting more than an hour. Additionally the local magnetic field can be disturbed by local occurrences, electrical storms, and solar activity. For these reasons the magnetic field in an area can have significant variations which must be accounted for via a base station recording the field in a static area over time, so that changes in the field are not interpreted as survey anomalies.

When the Earth's magnetic field reaches a target with magnetic susceptibility a secondary field is generated. This field is the anomalous magnetic field which is added to the primary magnetic field of the Earth to form the total magnetic field (Figure D.1). Like the primary field the secondary field is also generated in the shape of a dipole. This dipole is the sum of many smaller dipoles contained within the target and the sum total of these dipoles represents the larger total dipole of the anomaly which can be seen in the magnetic survey. While in most situations the dipole is situated parallel to the primary magnetic field, this is not the case in remnant magnetization where the dipoles of the target have been previously positioned in the presence of the primary field. In remnant magnetization the target maintains this dipole direction as it is rotated or moved within the subsurface, thereby resulting in its dipole response no longer aligning with the primary field.

Due to the strength of the primary magnetic field often being several orders of magnitude the response of the anomalous magnetic field the anomalous field is not measured alone but as a variation of the primary magnetic field [62]. In order to predict how the total field is changed by an anomaly the anomalous field is projected onto the total field through the use of a dot product (Figure D 2).

The primary material property detected in a magnetic survey is that of magnetic susceptibility. This property determines the strength of the magnetic response of an anomaly within the presence of a magnetic field. Situations where the magnetic susceptibility of a target is significantly higher than the surrounding half space generate a strong target dipole in comparison with the regional anomalous field, thereby creating a strong response during a survey that can be used to define the location of a target. A common example of this situation is an igneous intrusion within a sedimentary host rock as shown in Figure D.1.

While geologic targets and anomalies generate magnetic responses a significant number of other sources generate magnetic responses as well. These noise sources create a significant problem in magnetic interpretation. While the sources vary (Figure D 2) any external source of metallic nature can create a significant problem for magnetic surveys. As these sources tend to be near or on the surface where the survey is being conducted and have a very high level of magnetic susceptibility they can significantly overcome the responses of geologic backgrounds and anomalies.
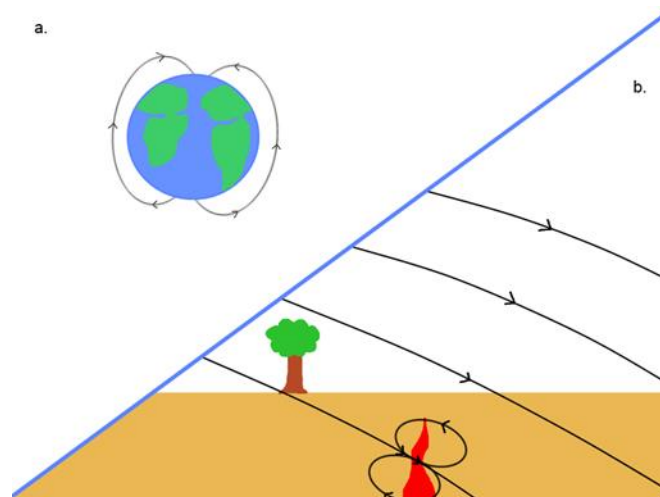
Figure D.1 - (a) Earth's primary field (b) primary field in northern hemisphere with an igneous intrusion
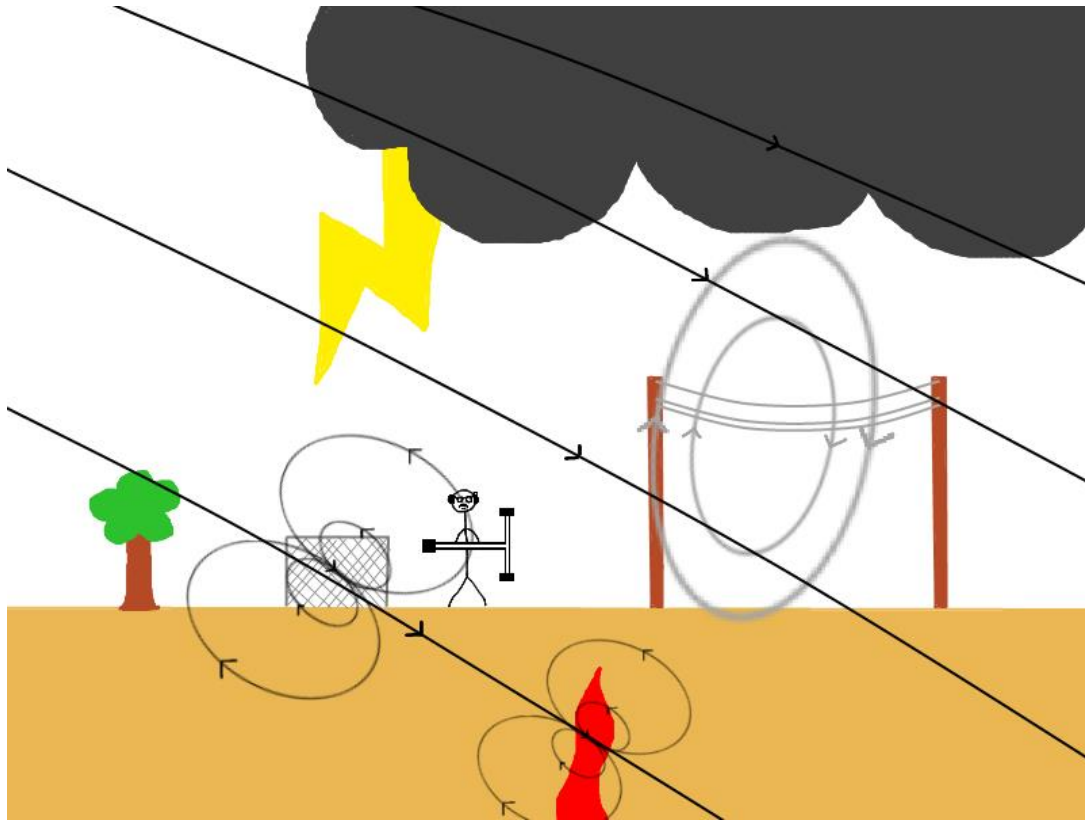
Figure D 2 - Magnetic noise sources compared to signal from magmatic dike.

$$B_{Total} = B_0 + B_a$$

[D1]

$$Total\ Field = B_a \cdot B_0$$

[D2]

$$M = k * H = \frac{m}{V}$$

[D3][60]

D.2   Equipment

Figure D 3 - Proton Precession Magnetometer [63, p. 143]
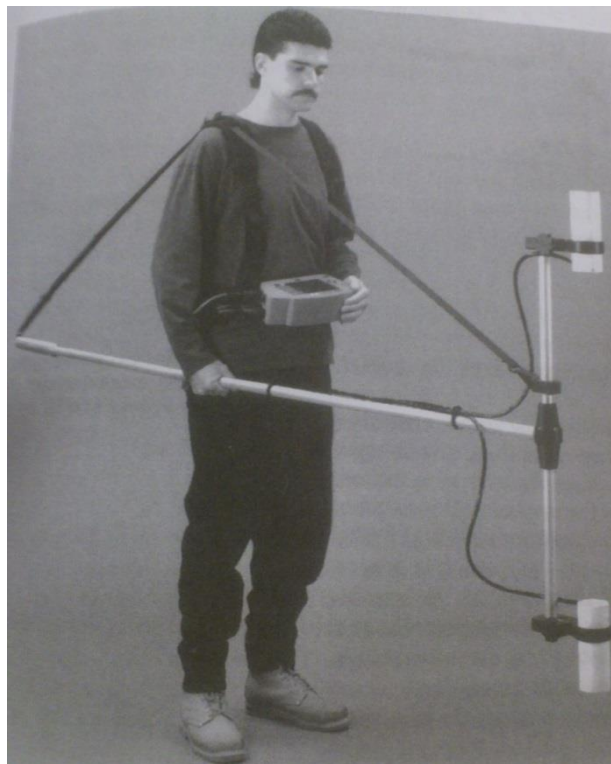
Figure D 4 - Reference image for Cesium magnetometer. [64, p. 143]

Two magnetometers were used in order to acquire magnetic data. The first was a proton precession magnetometer G-856 AX and the second was a cesium magnetometer G-858 MagMapper. With the exception of two surveys made on the first day of magnetic data acquisition the proton precession magnetometer was used as a base station to correct for diurnal variations. While performing base station readings the proton precession magnetometer was set in a single location and set to continually read the magnetic field every five seconds during the entire period of the magnetic survey. It was a scalar instrument and recorded only the strength of the magnetic field and not the direction of the field.

The cesium magnetometer was used as the survey magnetometer and was carried throughout all of the survey lines to acquire magnetic field data. Like the proton precession magnetometer, the cesium magnetometer only measured total field strength and not the direction of the field. However instead of a single sensor, the cesium magnetometer consists of two sensors with a one meter vertical offset. The result of this is that in addition to providing magnetic field data at two different heights with the higher sensor providing a less noisy but less detailed information set than the lower sensor. The cesium magnetometer also can deliver a vertical gradient for the magnetic field.

Appendix E

E.1 Theory

Models of the subsurface used during the inversion of EM data display two limiting characteristics, firstly the situation of a discrete conductive anomaly buried within insulating material. In such a case the eddy currents induced and detected yield evidence of the body's location and conductivity. The other limit is that of a conductive semi-infinite half space overlain and underlain by insulating material, whereby horizontal currents are induced and may be interpreted in terms of apparent conductivity [EM1]. Physical field examples of course seldom exhibit the properties of these simple limiting cases and will typically involve far greater subtlety and complexity.

The transient response of the magnetic field during the central loop configuration method of EM data acquisition is readily defined and may be used as a first pass indicator of conductivity variations with depth. For a homogenous subsurface, the curve will trend towards $\frac{\partial B}{\partial t} = -t^{\frac{5}{2}}$ where 'B' is magnetic flux density. A two layered earth model with the upper layer more resistive than the lower will decay slower than this simple model; a more rapid decay occurs when the upper layer is less resistive than the other, as shown in Figure E.1 [EM2].
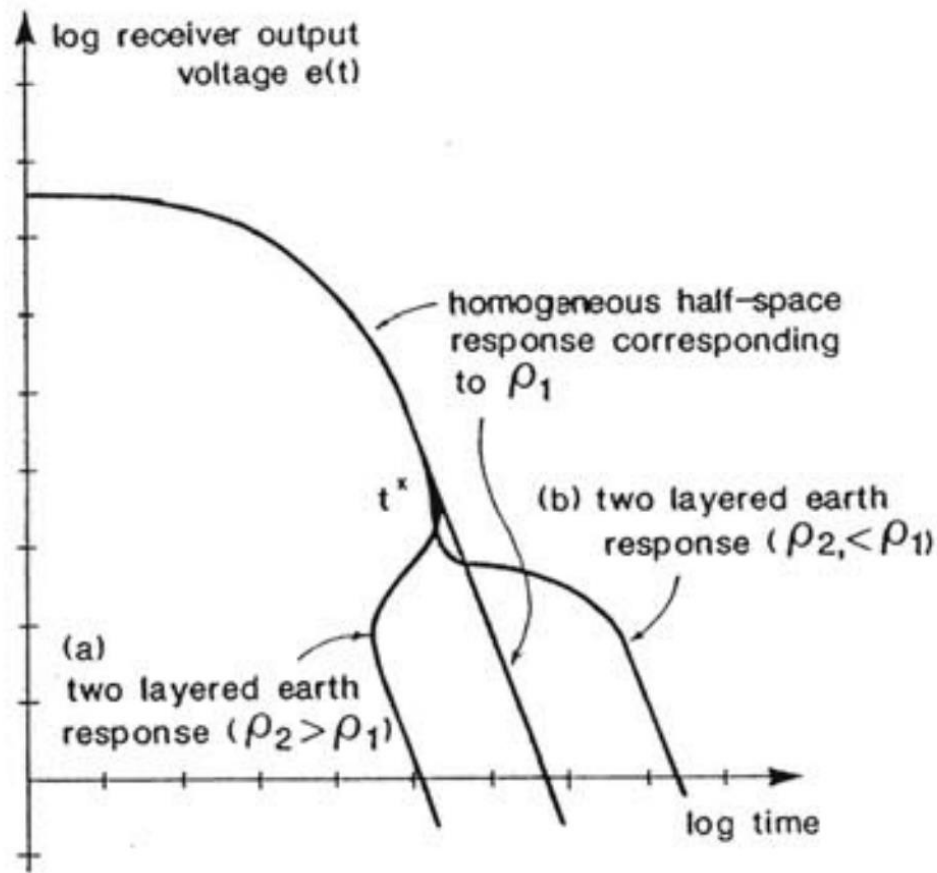
E.2 Equipment

E.2.1 EM31 Instrument

For frequency-domain EM, the first instrument used at Pagosa Springs was the EM31-MK2 (Figure E.2) manufactured by Geonics. The EM31 used in the field operated at 9.8 kHz, with a fixed internal coil spacing at 3.66m [68]. The depth of investigation is highly dependent on the spacing of the coils. For horizontal coplanar mode (HCP) the EM31 has a depth of investigation of about 1.5 x coil separation which is close to 6.0m. The benefits of this instrument are that it can be operated with a single person carrying the device while walking at a constant pace through a survey area providing a large degree of mobility. There are two different types of recording modes for the EM31: continuous and discontinuous. The continuous mode records data at a given time interval until the survey is stopped. The instrument is measuring the field at all times during the discontinuous mode, but the EM31 only records the data when an orange button is pressed to usually denote a station. The discontinuous mode was used for the pipe survey in the town of Pagosa Springs and at the student site in Shahan's Ranch. The EM31 is effective at mapping near surface geological variations and groundwater contaminants [68]. The EM31 is more

244

effective at locating these near surface anomalies because these surveys can be conducted quickly and contrary to DC resistivity no ground contact or electrodes are required [68]. There are some limitations to the EM31 system; for example, fixed coil spacing and depth of investigation, a limited dynamic range, and the complexity of distinguishing the source and anomalous field in FEM.

Figure E.2: A picture illustrating the EM31 during setup.

E.2.2 EM34 Instrument

The second FEM instrument used at Pagosa Springs was the EM34-3 (Figure E.3) manufactured by Geonics. This instrument implements the same induction method as the EM31. This instrument consists of two coils – one as the receiver coil and one as the transmitter coil. The EM34 can be operated using two different modes: horizontal coplanar mode and vertical coplanar mode. Horizontal coplanar mode is a transmitter and receiver coil orientation where the coils are lying flat on the ground and this orientation results in a vertical dipole. The vertical dipole mode is very sensitive to vertical geological anomalies and is able to locate groundwater in fractured bedrock zones. Vertical coplanar mode is good for lateral variations within the subsurface. Both methods were used in the EM34 surveys. The EM34 has an advantage over the EM31 in that the coil spacing can be varied. This allows for different depths of investigation potentially allowing for the characterization of different layers.

Calibration of the EM34 is required before use. In order to accomplish this, the EM34 had to be taken to an area with minimal interference and calibrated to either Horizontal or Vertical Coplanar Mode depending on which method was being used for the survey. Once calibrated, measurements could then be taken along the survey using the method that the instrument was calibrated too.

Figure E.3: A picture showing all of the EM34 components laid on the ground.

E.2.3 EM47 Instrument

The first time-domain EM instrument utilized at Pagosa Springs was the Geonics Protem EM-47 instrument. Time-domain electromagnetics is different than the frequency domain method because in TEM the current in the transmitter loop is instantaneously shut off rather than the current oscillating like a sinusoid. This instrument uses a square transmitter loop (usually fairly large, i.e. 50m x 50m) and has a multicomponent receiver coil. This receiver coil takes measurements in the x, y, and z direction. A figure showing what the three-component receiver looks like is shown in Figure E.4.

A 12-volt battery is connected to the transmitter box in order to power and control the current flowing through the transmitter loop. This square transmitter loop consists of a conductive wire that current is

injected into. When the primary current shuts off in the square transmitter, a large change in primary flux results and causes secondary currents to generate in conductive targets. This induced current causes a magnetic field and this field decays quickly over time due to resistance. If the target is more conductive the secondary magnetic field will decay slower compared to when the target is resistive.

Figure E.4: Three component EM 47 receiver.

The receiver coil measures this decaying secondary magnetic field by taking readings over closely spaced time intervals. These time intervals are called time gates, and typically there are about 20-30 time gates for a measurement in a single location.

This process of turning on and off the current in the square transmitter loop happens repeatedly at a certain frequency and this is called the repetition rate. Common repetition rates for the EM47 are 285 Hz and 75 Hz. The readings are stacking during this process to increase the signal to noise ratio. All the readings for a certain frequency at a particular station are called a sounding. When all the data is recorded for a particular frequency at a station, the three-component receiver is moved to another station and the process is repeated.

E.2.4 EM57 Instrument

The second time domain electromagnetics instrument utilized at Pagosa Springs was the Geonics Protem EM57-MK2. The EM57 is very similar to the EM47 except a few parameters are different. This instrument still has a large transmitter loop consisting of a conductive wire (i.e. a 50m x 50m loop). One main difference the EM57 has compared to the EM47 is the EM57 receiver coil (Figure E.5) measures only one component, the z (or vertical) component. This instrument induces a current in the square transmitter loop that is significantly higher than that of the EM47. The EM57 transmitter box can be powered by multiple 12V batteries or can be powered by a gas generator. Powering the transmitter box with the generator was the source of power used for this instrument in Pagosa Springs. This high power source was used to create a steady current of 20A in the transmitter loop. Then similar to the EM47, the current is shut on and off in accordance to the repetition rate. The repetition rates used for the EM57 were 30 Hz and 7.5 Hz. Similar to the EM47, the EM57 transmitter shuts the current off almost instantaneously to create a change in flux from the primary loop. This results in a secondary current and decaying secondary magnetic field that is measured using the receiver at a specific set of times, or time gates. All this data is recorded on the Protem box and when the data is finished collecting at one station the single component receiver was moved to the next station to complete the process.

Figure E.5: An image depicting the EM57's receiver loop in action.

Appendix F

F.1 Theory

F.1.1 DC Resistivity

DC resistivity falls into the category of active geophysical methods. This is due to the electrical current injected into the ground through two electrodes along the line. Potential measurements are taken between two other electrodes. The depth of penetration increases as current electrodes are spread apart; voltage measurements in different locations at each depth will result in a 2D pseudo-section of apparent resistivities (see F.1.2 Apparent Resistivity).

In the past, these data were acquired manually for each point in the resulting pseudo-section. However, modern acquisition systems utilize long cables with many electrical takeouts, each connected to an electrode planted in the ground. The cables are connected to each other, to a power source, and to the controller box. The controller box automatically runs through a specified (via the user interface) array to collect apparent resistivity data using the electrodes along the line as needed. This saves time, and allows many different array types (Wenner, Dipole-Dipole, etc.) to be used from the same electrode configuration.

F.1.2 Apparent Resistivity

The property of resistivity defines a material's resistance to the flow of electricity. When applied to materials in the Earth's subsurface, various characteristics can affect resistivity, such as fluid saturation, rock porosity, fluid types, temperature, and inter-grain properties. These factors make DC resistivity a powerful tool in groundwater imaging. The actual apparent resistivity value measured is the total resistivity of the subsurface between electrodes plus the electrode contact resistance. Apparent resistivity values are ingrained with the assumption that the earth is homogeneous, and inversion techniques are required to process the data into real resistivity. This method uses the basic physical relationships expressed by Ohm's Law (Equation F.1) and the apparent resistivity equation (Equation F.2):

$$V = IR$$

Equation F.1: Ohm's Law

$$R_a = \frac{V}{I}\left(\frac{1}{AM} - \frac{1}{AN} - \frac{1}{BM} + \frac{1}{BN}\right)^{-1}$$

Equation F.2: Apparent Resistivity [74]

Where V is voltage, I is current, R is resistance, R_a is apparent resistivity, and $\left(\frac{1}{AM} - \frac{1}{AN} - \frac{1}{BM} + \frac{1}{BN}\right)^{-1}$ is a geometric scaling factor specific to each point collected along a DC array setup.

F.1.3 Induced Polarization

With Induced Polarization (IP) methods, a time varying square wave of current is injected into the subsurface. Then, measurements are taken of the change in potential of the decay of this current as it swaps polarities (Figure F.1). This measurement is related to the property of chargeability.
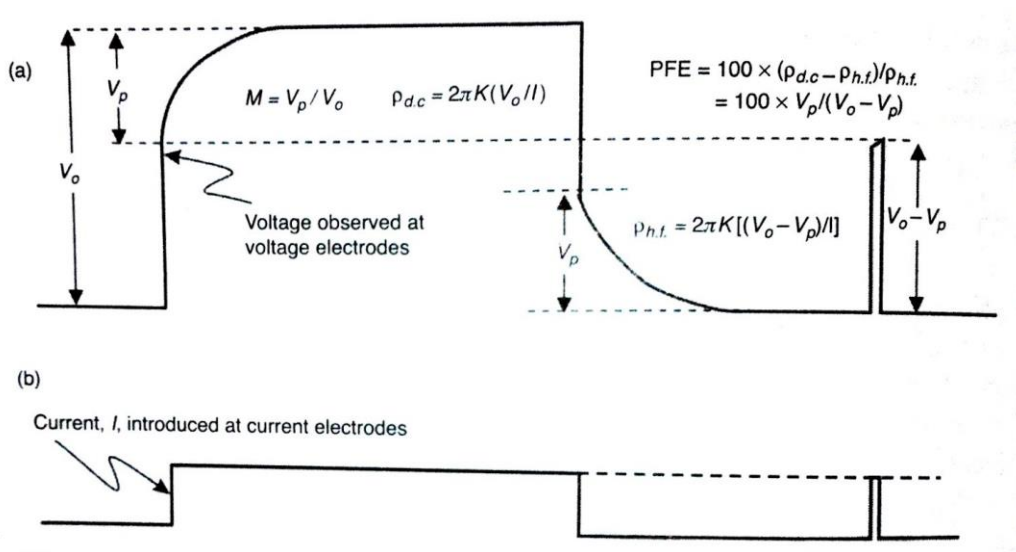
Figure F.1: (a) Induced polarization decay (b) Injected current signal [70]

A material's chargeability is defined by its resistance to charge polarization as current decays in the subsurface. This can help to understand the geology of an area, as different rock types have distinct chargeabilities. For example, most clays will have a high chargeability and most sandstones will have a low chargeability. The inversion of the data acquired will produce an IP model and a resistivity profile. These are then used to calculate and plot normalized chargeability.

F.2   Equipment

F.2.1   ABEM

Setup and Acquisition

The ABEM Terrameter uses reels of cable connected in series with 8 takeouts per reel. The ABEM then runs through predefined electrode arrays to inject current into the ground and measure voltages at the

surface. Once acquisition is complete, reels can be rolled over to extend the line—and the resulting resistivity section—horizontally.

Figure F.2: ABEM (orange) with cables, electrodes, cable connectors, and flags

Data Formatting

The ABEM produces data in .s4k format, which can then be converted using the SAS4000 software. Data is first transferred to a computer directly from the ABEM, and SAS4000 converts the data to formats such as .dat that the inversion software res2Dinv can read.

F.2.2   SuperSting

Setup and Acquisition

The SuperSting, like the ABEM, uses cables with seven takeouts for electrodes, and multiple cables can be connected to increase survey length. Electrode tests, like the ones done in ABEM, must be run before acquiring data to check coupling and cable connections.

Data Formatting

Data files are generated in .stg format that contain x, y, and z coordinates for each of the A, B, M, and N electrodes. As the inversion software res2Dinv reads .dat files, the SuperSting data must be converted to this format manually in order to process the data.

F.3 Array Types

F.3.1 Wenner

The Wenner array is the primary configuration for most DC resistivity surveys conducted in Pagosa Springs. This array consists of two current electrodes, named A and B and two potential electrodes, named M and N, between them. The spacing between electrodes A and M, M and N, and N and B will all be the same (Figure F.4). During acquisition, this array setup is moved laterally to provide same-depth measurements along the survey line. AB separation is then increased to increase depth of investigation, and the process repeats. This array provides a high signal to noise ratio, and images horizontal structures well.

Wenner

$$\rho_\alpha = 2\pi a \frac{V}{I}$$
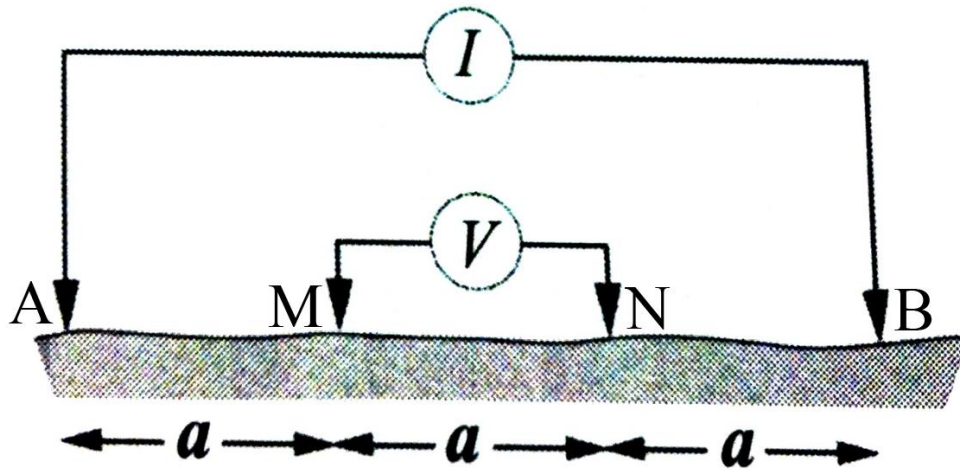
Figure F.4: Wenner array layout [72]

F.3.2 Dipole-Dipole

Dipole-Dipole arrays follow the same naming convention as Wenner arrays, with current electrodes A and B, and potential electrodes M and N. However, the distance between electrodes is only fixed for the AB and MN pairs. Therefore, the M and N electrodes are placed outside A and B, and are usually separated by a multiple of the AB/MN pair spacing (Figure F.5). This configuration can be moved laterally for constant-depth measurements, and the spacing between AB and MN can be increased to increase depth of investigation. As opposed to the Wenner array, the Dipole-Dipole setup is better at imaging vertical features such as faults and dikes. The trade-off is a low signal to noise ratio.

Dipole-dipole

$$\rho_\alpha = \pi n(n+1)(n+2)\, a\frac{V}{I}$$

Figure F.5: Dipole-Dipole array layout [72]

Appendix G

G.1 Theory

The self-potential (SP) method was devised in 1830 by Robert Fox. It is a passive method detecting differences in natural ground potentials between any two points on the ground surface [78]. A pair of electrodes were used via being connected by a long wire and a voltmeter to measure the potential difference, Figure G1.
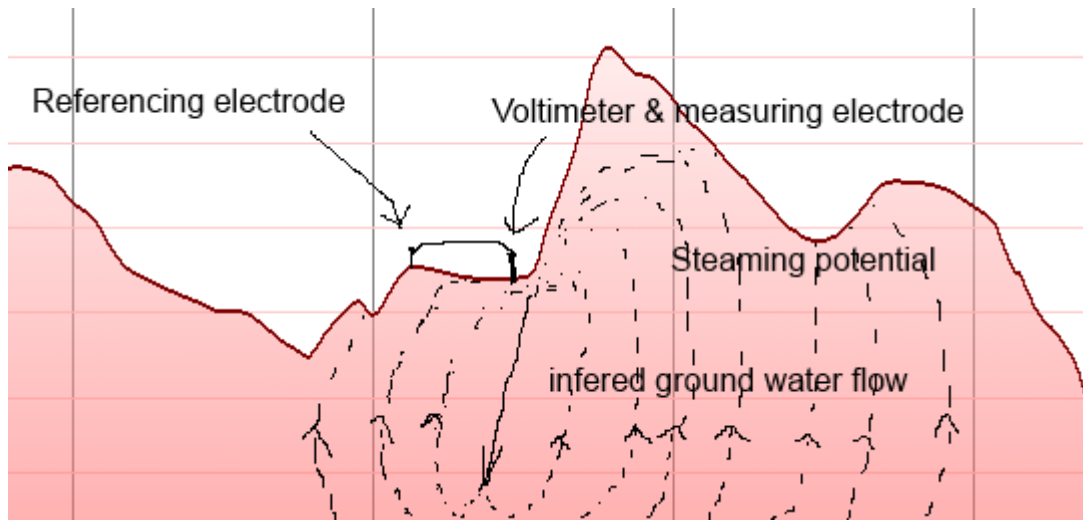
Figure G1: The self-potential method

The natural ground potentials are governed by the Poisson's equation for a given natural source and subsurface resistivity distribution:

$$\nabla \cdot \sigma(x)\nabla V(x) = I\delta(x - x_s)$$

Equation G1: The Poisson's equation for a given natural source and subsurface resistivity distribution:

Here σ is the conductivity of the Earth, V is the electric potential, I is a point current located at x_s and δ is

a Dirac delta function. This dataset contains the measured electric potential difference $V(x_1) - V(x_2)$

with location x_1 and x_2 typically from GPS.

Here it is also assumed that the Earth is homogeneous with conductivity σ and tying to interpret possible

sources for the electric potential differences is possible.

G.1.1 Sources of Self-Potential

In Table G1 sources exist that could contribute to the potential differences measured.

Electrical potential generated	Source	Energy type	Magnitude	Wavelength
Streaming potential	The transport of counterions along with the pressure-driven fluid flow	Electro-kinetic	Depends on Darcy velocity of the groundwater $\geq -100\text{mV}, \leq 100\text{mV}$	Possibly Long, depends on large scale groundwater flow
Diffusion potential	The diffusion of different species of ion with different speed.	Electro-chemical	Depends on the relative speeds of the ions	Short, depends on local heterogeneities of groundwater ion species
Mineral potential	Massive sulphide orebodies (positive), pyrite and chalcopyrite and other conductor minerals (negative)	Undetermined	$\geq -\text{hundreds of mV}, \leq \text{tens of mV}$	Depends on the scale of minerals
Redox potential	oxidation-reduction reactions in rocks, biomasses	Electro-chemical	$\geq -300\text{mV}, \leq 300\text{mV}$	Short

Hydro-Thermo related potential	Thermal diffusion caused by a temperature gradient that moves counterions with fluid flow	Electro-kinetic	Depends on Darcy velocity of the groundwater $\geq -100mV \leq 100mV$	Possibly Long, depends on large-scale thermal gradient
Man-made interference	Power line, cell phones etc.	Electric	Varied	Varied

It is possible to find pressure and temperature gradient driven streaming potentials which might be responsible for long wavelength SP data.

G.1.2 Kriging of the SP data

The kriging interpolation method is used to create an optimal prediction of the data distribution over a specific region using the acquired data at known locations. Within the kriging method, variograms are used to express spatial distribution and variations and thus minimizes the errors of the interpolated values. Note that there is an interest in the regional trend of the data. This step is done by assuming probability distribution of every finite set of electrical potentials at position $(x_1, \dots, x_k)$ is multivariate Gaussian with zero mean and the covariance governed by a symmetric semi-variogram $\gamma(h)$. Here h is the correlation length.

The explicit form of $\gamma(h)$ is fitted from SP data using Surfer11. Over-fitting the variograms on the data would result in local variations of the acquired data and thus, failure on showing the regional context of the data.

G.2 Equipment

The equipment for SP surveys consists of a pair of electrodes, a voltmeter, and a spool of cable. One electrode is used as the reference electrode and is buried at the beginning of each profile. This reference electrode is connected using the cable to the voltmeter, which is then connected to the second electrode.

258

The second electrode is moved to different locations and the voltmeter is used to measure the electric potential between the electrodes. Each measurement is recorded manually. For longer surveys, multiple references are necessary. With multiple references, all measurements must be corrected to a single reference, so that measurements made with different references can be combined.

Appendix H

H.1 Theory

Ground penetrating radar (also known as GPR) uses electromagnetic waves to image the subsurface with frequency ranges from 1 MHz to 1.5 GHz (79) (Figure H.1). GPR frequencies propagate above a certain frequency known as the transition frequency (f_T); this is usually above 10 MHz (Figure 12. 16). f_T is dependent upon the electrical conductivity and dielectric permittivity given by the formula below (Figure H.1); these quantities affect GPR velocity and attenuation.
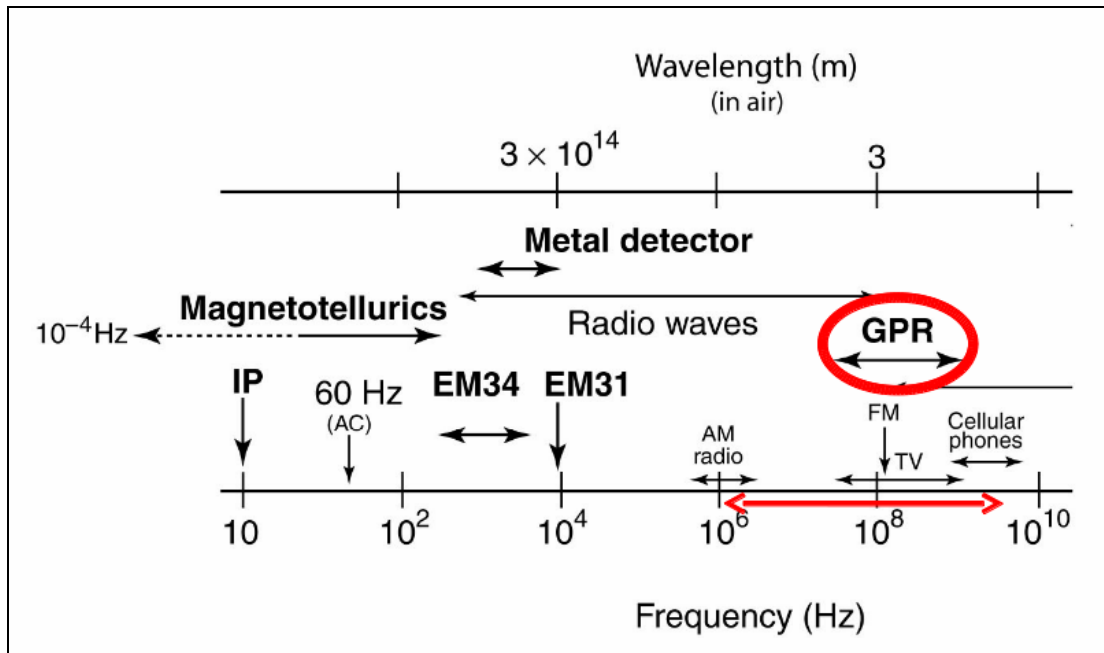
Figure H.1: Typical ranges of electromagnetic waves used in GPR data acquisition.

$$f_T = \frac{\sigma}{2\pi\varepsilon}$$

Equation H.1: Transmission Frequency.

where σ = electrical conductivity

ε = dielectric permittivity

f_T = transition frequency
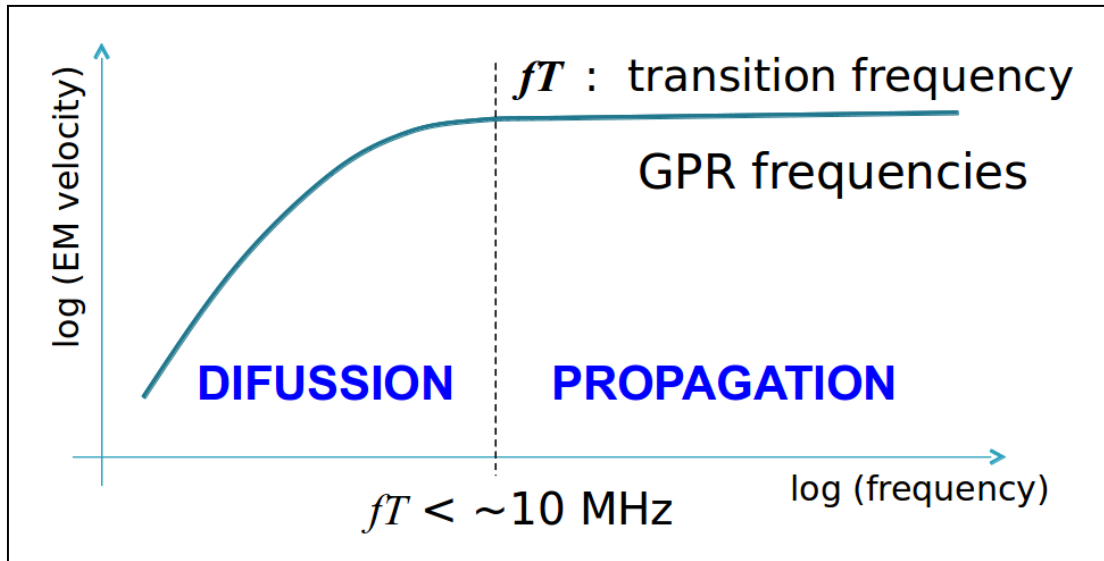
Figure H. 2: Schematic diagram showing the transition frequency above which EM wave propagates.

GPR Velocity

GPR velocity is simplified down to the following equation (Equation H.2) which is dependent upon the changes in relative dielectric permittivity. Different materials have different relative dielectric permittivity. Table H.1 shows some typical ranges of relative dielectric permittivity and its corresponding velocities for a range of common materials.

The geothermal water at Pagosa Springs has a high sodium content (about 790 milligrams per liter) that is comparable to the salinity in sea water (Pagosa Springs, geothermal department). It is important to take into account that the lithology within most of the survey areas is comprised of shale and sandstones.

$$v = \frac{c}{\sqrt{\varepsilon_r}}$$

Equation H.2: GPR Velocity.

where   c = speed of light in vacuum = 0.3 m/ns

ε_r = relative dielectric permittivity

Material	Rel. Dielectric Permittivity	Velocity (m/ns)
Air	1	0.300
Fresh water	80	0.033
Saline water	80	0.033
Ice	3-4	0.160-0.170
Granite	4-6	0.130-0.135
Limestone	4-8	0.120-0.130
Salt	5-6	0.125-0.130
Sandy soil	3-30	0.055-0.170
Clay soil	3-15	0.086-0.170
'Average' soil	16	0.075

Table H.1: List of different materials and their relative dielectric permittivity and velocities.

GPR Attenuation

Attenuation is one of the main factors that affect the GPR wave propagation and resulting image resolution. GPR attenuation is given by the following formula (Equation H.3) and the attenuation coefficient is directly proportional to frequency. Also, this equation is mainly controlled by the dielectric permittivity and magnetic permeability. The higher the electric conductivity within a material relates to a higher attenuation coefficient as it is related by the loss factor (P) equation.

$$\propto = 2\pi f \left\{ \frac{\mu\varepsilon}{2} \left[\sqrt{1 + P^2} - 1 \right] \right\}^{1/2}$$

Equation H.3: GPR Attenuation.

where ε = dielectric permittivity

μ = magnetic permeability

c = speed of light in vacuum

P = loss factor = $\frac{\sigma}{2\pi f \varepsilon}$

Material	Electrical conductivity (mS/m)	Attenuation coefficient (dB/m)
Air	0	0
Fresh water	0.01	0.002
Saline water	3000	103
Ice	0.01	0.002
Granite	0.01-1	0.01-1
Limestone	0.5-2	0.4-1
Salt	0.01-1	0.01-1
Sandy soil	0.01-10	0.01-3
Clay soil	2-1000	1-300
'Average' soil	0.2-5	0.2-2.5

Table H.2: List of different materials, their electrical conductivity and corresponding attenuation coefficient.

Table H.2 shows the typical ranges of electrical conductivity and corresponding attenuation coefficient for different types of materials. Hence, any GPR survey carried out over clay rich soil or saline water will be highly attenuated and a loss in resolution and depth penetration will occur. This is especially true for clay rich soil as clay minerals have a high cation exchange capacity which store the GPR pulse instead of allowing it to propagate (79).

GPR reflection and diffraction

GPR energy also reflects and diffracts when there is a contrast in electromagnetic energy between boundaries. This is similar to seismic waves but instead of reflection or diffracting due to a change in acoustic impedance, GPR energy reflects due to a change in dielectric contrasts.

In summary, GPR data is very useful for high resolution near surface imaging. Under the right conditions (dry, non-saline lithologies), vertical and lateral resolution down to centimeter scale is achievable.

H.2 Processing

GPR data processing is conceptually similar to seismic data processing. The processing software used here is ProMAX, which is principally designed for seismic data processing. Some adaptations and

adjustments had to be made in terms of the data input. The main purpose for GPR data processing is to improve the signal to noise by filtering, gain application, and migration. The following processing sequence has been applied to all the GPR data acquired in Pagosa Springs.

1) 'De-wow' filter

The initial processing step is always to apply a 'de-wow' filter; these act as low-cut filters to remove the 'wow' noise. 'Wow' is a non-linear, low frequency noise which results from cross talk between the antennas and limitations in instrument frequency response (79).

During data acquisition, the radar frequency used is 500 MHz. While processing data care is taken to preserve this frequency and remove all other spurious noise. Within ProMAX, the module used to remove 'wow' noise is 'trace dc removal' and it removes the mean of the 'wow' noise from the dataset.

2) Bandpass filter

Bandpass filter allows users to design a filter that retains specific ranges of frequencies; it is defined by F1-F2-F3-F4 (Figure H. 3) where F1 and F4 are known as 'corner frequencies' that act as tapers to prevent ringing artifacts (also known as Gibbs phenomenon). F2 and F3 are the main frequency ranges to retain. For the GPR data, bandpass filters are designed to remove the noise spikes.
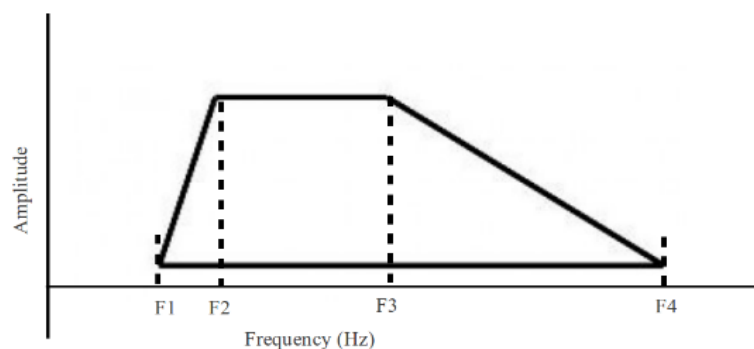

Figure H. 3: Schematic diagram of bandpass filter.

3) Static correction

In order to record the whole waveform, the transmitted wavelet is delayed for each trace. The start time was over-recorded during the data acquisition so it must be shifted at each trace. This time lag contributes to image the subsurface data.

This shift should be considered in data acquisition. However it is better to remove extra time in pre-processing step because the wavelet has to have the correct time section. The first break can be identified from the wavelet data. GPR waves travel with the speed of light (0.3 m/ns). Knowing this speed and antenna separation of 0.23 m it is possible to calculate time for the wave to reach the receiver in the air. This was calculated to be 0.767 ns. This value is subtracted from first break time and the obtained result is a static time which is applied to the whole dataset.

4) Trace muting

Muting is essentially a procedure which 'zeroes-out' the amplitude of the selected data. Within the GPR dataset, the main noise components are the direct air and ground waves. This noise energy has higher amplitude that masks the weaker reflection signal. Trace muting will only help to balance the energy distribution within the trace and prepare it for gain application.

GPR air waves are direct-wave energy that travels through the air from the transmitter antenna to the receiver antenna, rather than through the subsurface. Ground wave energy is analogous to the seismic direct wave; it travels directly from transmitter to receiver through the ground. The ground wave energy has no reflection from deeper boundaries. Since neither has reflections, both air and ground waves are considered noise that masks the weaker reflection signals.

5) Automatic Gain Control (AGC)

Once the noise is removed, automatic gain control (AGC) is used to compensate for the decrease in signal amplitude with depth. By application of AGC the weaker signals will be enhanced by multiplying each sample by a scalar to balance the power within the specified window around it. The main disadvantage of AGC is that it destroys all true amplitude variations (82) but this is not pertinent to the analysis and interpretation that is considered here.

Velocity Analysis and Migration

GPR data resolution and depth penetration is dependent upon the type of material the EM waves propagate through. Within the different survey locations, a 500 MHz transmission frequency has achieved an optimal depth penetration of 4 m. Within such a shallow change in depth, the velocity of the layer does not change very much. Hence constant velocity models were used to carry out migration of the GPR data.

265

Migration is the final step in processing to correctly position the reflectors within the subsurface and arrive at an accurate image. A constant root-mean-square (RMS) velocity has been used to migrate the data and collapse the diffractions. There are various different types of migration algorithms that are based on the integral method or the wave equation method. Kirchoff time migration is an integral method algorithm. It was applied to the GPR dataset as it is efficient in handling geometry and structure.

References

[1] Galloway, M.J., "Hydrogeologic and Geothermal Investigation of Pagosa Springs, Colorado." Colorado Geological Survey, Department of Natural Resources, Denver, CO, 1980.

[2] Goff, F., and J. Tully. "Geothermal Assessment of Archuleta County and the Pagosa Springs Aquifer, Colorado." Geothermal Resources Council Transactions, vol. 18, 1994.

[3] Google Earth V 7.0.3.854 (2013): http://earth.google.com (May 2013).

[4] Kelley, V. C., 1950. "Regional Structure of the San Juan Basin." Guidebook of the San Juan Basin- New Mexico and Colorado- First Field Conference, New Mexico Geological Society, New Mexico Bureau of Mines and Mineral Resources, p 101-108.

[5] Kelley, V.C., 1950. "Pre-Cambrian Rocks of the San Juan Basin." Guidebook of the San Juan Basin- New Mexico and Colorado- First Field Conference, New Mexico Geological Society, New Mexico Bureau of Mines and Mineral Resources, p. 53-55.

[6] Beaumont, E. C. and Read, C. B., 1950. "Geologic History of the San Juan Basin Area." Guidebook of the San Juan Basin- New Mexico and Colorado- First Field Conference, New Mexico Geological Society, New Mexico Bureau of Mines and Mineral Resources, p.49-54.

[7] Galloway, M. J., 1980. "Hydrogeologic and Geothermal Investigation of Pagosa Springs, Colorado." Colorado Geological Survey Department of Natural Resources, Denver CO, 109 p.

[8] Warren, W. J., 1986. A Geothermal Exploration Project in Pagosa Springs, Colorado [M. S. thesis]: Colorado School of Mines, 127 p.

[9] University of Calgary Geoscience Department, 1996, Geological Time Scale: http://www.geo.ucalgary.ca/~macrae/timescale/ (May 2013).

[10] Field Camp Attendees, 2012, Geophysical Characterization of the Geothermal System in Pagosa Springs Area, Upper San Juan Basin, Archuleta County, Colorado: Colorado School of Mines, 323 p.

[11] US Geological Society, 1984. Oak Brush Hill Topographic Map, Ref. Code 37107-B1-TF-024, Printed by Maptech, Inc. 1997.

[12] Global CCS Institute, 2013. Borrow Area Characterization Well: http://www.globalccsinstitute.com/publications/co2-storage-report/online/55976 (May 2013).

[13] Sheehan, A., Abets, G.A., Jones, C.H., and Lerner-Lam, A.L., 1995, Crustal thickness variations across the Colorado Rocky, Mountains from Teleseismic Receiver Functions: Journal of Geophysical Research, Vol 100, No B10, Pages 20, 391-200, 404.

[14] Raynolds, R. GPGN 486. Class Lecture, Topic: "Geology of the Pagosa Springs area." Pagosa Springs, Colorado. May 13, 2013.

[15] Barrett, J. K. and Pearl, R. H., 1994. "Hydrogeochemical Data of Thermal Springs and Wells in Colorado." Colorado Geological Survey Department of Natural Resources, Denver CO.

[16] Homma, A. and Tsukahara, H., 2008. "Chemical Characteristics of Hot Spring Water and Geological Environment in the Northernmost Area of the Itoigawa Shizuoka Tectonic Line" [M. S. thesis]: Shinshu University, p. 217-225.

[17] Hyder, D., 2013, Bolack San Juan Basin Flora Project: http://www.sanjuancollege.edu/pages/989.asp (May 2013).

[18] Morgan, P. GPGN486. Personal Interview, Topic: Heat flow and thermal buoyancy. Golden, Colorado. May 28th, 2013.

[19] Railsback, B., 2011, Heat flow, geothermal gradient, and the thermal conductivity of sedimentary rocks: http://www.gly.uga.edu/railsback/PGSG/ThermalCond&Geothermal01.pdf (May 2013).

[20] Density of Fluids – Changing Pressure and Temperature: http://www.engineeringtookbox.com/fluid-density-temperature-pressure-d_309.html

[21] Galloway, M., (1980), Hydrogeologic and Geothermal Investigation of Pagosa Springs, Colorado, 97.

[22] Warren, W.J., (1986), A geothermal exploration project in Pagosa Springs, Colorado, 36.

[23] ASTER webpage (2004), asterweb.jpl.nasa.gov/instrument.asp, accessed on 5/31/2013.

[24] Andrews-Hannah, J. GPGN 470. Class Lecture, Topic: "Thermal Infrared
Remote Sensing." Geophysics Department, Colorado School of Mines, Golden, Colorado, February 27th
2013.

[25] Coolbaugh M. F., C. Kratt, A. Fallacaro, W. M. Calvin, and J. V. Taranik (2006),
Detection of geothermal anomalies using Advanced Spaceborne Thermal Emission and Reflection
Radiometer (ASTER) thermal infrared images at Brady's Hot Springs, Nevada, USA, *Remote Sensing of
Environment, 106,* 350-359.

[26] Andrews-Hannah, J. (2013), "Lab4: Prospecting from Space-Detecting, Delineation,
and Classification". Geophysics Department, Colorado School of Mines, Golden, Colorado, February 15th
2013.

[27] "What is GPS?", http://www8.garmin.com/aboutGPS/ Accessed May 29, 2013.

[28] "Augmentation Systems", http://www.gps.gov/systems/augmentations/ Accessed May 30, 2013

[29] Federal Aviation Administration, 2001, Specification for the Wide Area Augmentation System
(WAAS): Department of Transportation.

[30] Kee, Changdon, Parkinson, Bradford W., Axelrad, Penina, "WIDE AREA DIFFERENTIAL
GPS",*NAVIGATION*, Vol. 38, No. 2, Summer 1991, pp. 123-146.

[31] CGG, Seismic Overview: http://www.cgg.com/default.aspx?cid=24&lang=1

[32] Tsvankin, I., 1995, Seismic Wavefields in Layered Isotropic Media, Samizdat Press

[33] Pagosa Springs Field Camp Final Report:
http://geophysics.mines.edu/UserFiles/File/geophysics/fieldcamp/Pagosa_Springs_Field_Camp_2012_Fi
nal_Report%202.pdf (June 2012)

[34] Schuster, G., Basic Processing Steps: Static Corrections to Remove Elevation and Near-Surface
Heterogeneities: http://utam.gg.utah.edu/stanford/node17.html (July 1998)

[35] Ventosa, S., Rabeson, H., Duval L., 2011, Coherent noise removal in seismic data with redundant multiscale directional filters, in 19th European Signal Processing Conference, Barcelona, Spain, ISSN 2076-1465, p.1150-1154

[36] Sheriff, R.E., 1991, Encyclopedic Dictionary of Exploration Geophysics: Soc. of Expl. Geophys.

[37] Universidade Fernando Pessoa, Seismic-Sequential Stratigraphy: http://homepage.ufp.pt/biblioteca/Seismic/Pages/Page7.htm (April, 2007)

[38] Aki, K. and Richards, P.G., 2002, Quantitative Seismology, University Science Books, Sausalito, CA.

[39] Sheriff, R.E. and Geldart, L.P., 1995, Exploration Seismology, Cambridge University Press.

[40] Yilmaz, O., 2001, Seismic Data Processing, Society of Exploration Geophysicists, Tulsa.

[41] Galloway, M.J., 1980, Hydrogeology and Geothermal Investigation of Pagosa Springs, Colorado, Colorado Geologic Survey Department of Natural Resources.

[42] Larson, 2010, Illinois State Geological Survey: Seismic Reflection: http://www.isgs.illinois.edu/sections/geophys/seisref.shtml (November 2010).

[43] Zonge Geosciences, Inc.,1-800 Geophysics.com: Seismic Refraction Technique: http://www.microgeo.com/detailed_discussions/dm1.html.

[44] US Department of Defense, Environmental Security Technology Certification Program performance report, 1999, Resolution Resources International: Seismic Surveys: http:// www.rri-seismic.com/Frame%20Pages/Tech%20Pages/Seismic/seismic.htm (October 1999).

[45] Lowrie, W, 2002, Fundamentals of Geophysics: Cambridge, United Kingdom, Cambridge University Press, p. 144.

[46] Stark, A, 2008, Seismic Methods and Applications: Boca Raton, Florida, U.S. Brown Walker Press, p. 156.

[47] Telford, W.M., Geldart, L.P., Sheriff, R.E., Applied Geophysics, Second ed., Cambridge:Cambridge University Press, 1990 (May 2013).

[48] The geoid, http://planetearth.nerc.ac.uk/images/uploaded/custom/geoid-c2.jpg (May 2013).

[49] European Space Agency, Earth's Gravity, http://www.esa.int/Our_Activities/Observing_the_Earth/GOCE/Earth_s_gravity_revealed_in_un precedented_detail (May 2013).

[50] Basic accelerometer, http://www.data-acquisition.us/images/10_116.jpg (May 2013).

[51] L&R, http://www.mat.ucm.es/~fuensant/hierro/3proyecto/instrumentacion/lacoste1.jpg (May 2013).

[52] CG-5, http://seongwooinst.com/index/data/cheditor/0811/cg5.jpg (May 2013).

[53] Krahenbuhl, R., Class notes (2012).

[54] Wiens, D., 2009, Gravity Survey Corrections: http://epsc.wustl.edu/~epsc454/grav-corrections.html (May 2013).

[55] Keller, R. G., Using and Understanding Gravity Data: http://research.utep.edu/Default.aspx?PageContentID=3946&tabid=38186 (May 2013).

[56] Ander, M., 2002, Gravity Error Budgets in Exploration Geophysics, http://www.eos.ubc.ca/courses/eosc454/content/Gravity%202.1%20Survey%20errors.pdf (May 2013).

[57] Scintrex, CG-5 Autograv Gravity Meter,
http://scintrexltd.com/dat/content/file/Scintrex_CG5-DIGITAL-Brochure-R1.pdf (May 2013).

[58] Boyd, T. M., 2003, Sources of the Local and Regional Gravity Anomalies,
http://galitzin.mines.edu/INTROGP/notes_template.jsp?url=GRAV%2FNOTES%2Frlsource.ht
ml&page=Gravity%3A%20Notes%3A%20Geologic%20Sources (June 2013).

[59] LaCoste & Romberg, L&R conversion table (May 2013).

[60] Griffiths, D., 2012. An Introduction to Electrodynamics. Addison Wesley. Boston, MA.Geomatrix
Earth Science LTD, 2013. G-856AX Portable Magnetometer. [Webpage] Available:
http://www.geomatrix.co.uk/g-856ax.php

[61] 2013. GEOALERT SIDC: Solar Influences Data Analysis Center RWC Product Archive.
http://sidc.oma.be/archive

[62] Drahor, M. G., Meriç A. Berge, Geophysical investigations of the Seferihisar geothermal area,
Western Anatolia, Turkey, Geothermics, Volume 35, Issue 3, June 2006, Pages 302-320, ISSN 0375-
6505, 10.1016/j.geothermics.2006.04.001.
(http://www.sciencedirect.com/science/article/pii/S0375650506000290)

[63] Reynolds, J.M., 1997. An Introduction to Applied and Environmental Geophysics. Geo-Sciences
Ltd, UK. Vol. 12 Issue 180.

[64] Mariita, N.O., 2007. The Magnetic Method. Kenya Electricity Generating Company Ltd. Short
Course II on Surface Exploration for Geothermal Resources. (http://www.os.is/gogn/unu-gtp-sc/UNU-
GTP-SC-05-18b.pdf)

[65] Milsom, J., and A. Eriksen, (2011). Field Geophysics. Chichester: John Wiley and Sons Ltd.

[66] McNeill, J. D. (1994). TN-27 Principles and Application of Time Domain Electromagnetic
Techniques for Resistivity Sounding. Ontario: Geonics Limited.

[67] Klein, J., & Lajoie, J. (1980). Electromagnetic Prospecting for Minerals, Practical Geophysics for the Exploration Geologist. Spokane, WA: Northwest Mining Association.

[68] Hayashi, M. (2004). Temperature-electrical Conductivity Relation of Water for Environmental Monitoring and Geophysical Data Inversion. Env. Monitoring and Assessment. 96: 119-128.

[69] Keynes, Milton. "Sales Products :: Electromagnetic Geonics EM31-MK2." Sales Products :: Electromagnetic. Geomatrix Earth Science Ltd, 2010. Web. 05 June 2013.

[70] Milsom, J., and A. Eriksen, "7.2.4 Frequency effects," in *Field Geophysics*, 4th ed., Wiley, 2011, pp. 141-142.

[71] AGI, "AGI USA," 26 March 2012. [Online]. Available: http://www.agiusa.com/agicatalog.shtml. [Accessed 5 June 2012].

[72] Milsom, J., and A. Erikson, "6.1.3 Array Descriptions," in Field Gephysics, 4th ed., Wiley, 2011, pp. 111-114.

[73] Archie, G. (1942), The electrical resistivity log as an aid in determining some reservoir characteristics, Transactions of the American Institute of Mining, Metallurgical, and Petroleum Engineers, 146, 54–62.

[74] Revil, a., M. Karaoulis, T. Johnson, and a. Kemna (2012), Review: Some low-frequency electrical methods for subsurface characterization and monitoring in hydrogeology, Hydrogeology Journal, 20(4), 617–658, doi:10.1007/s10040-011-0819-x.

[75] Milsom, J., and A. Eriksen, 2011, Field Geophysics

[76] K. Richards, A. Revil, A. Jardani, F. Henderson, M. Batzle, A. Haas, 2010, Journal of Volcanology and Geothermal Research, v. 198, p. 226.

[77] Barde-Cabusson, S., and Finizola, A., Version: 10 April 2012, Tutorial for Self Potential data processing

[78] Reynolds, J. M. *An introduction to applied and environmental geophysics*. Wiley, 2011.

[79] Booth, A. GPGN 486. Class Lecture, Topic: "Ground Penetrating Radar." Pagosa Springs, Colorado. 2013

[80] Sensoft, 2013, PulseEKKO Pro: http://www.sensoft.ca/Products/pulseEKKO-PRO/Configurations.aspx (June 2013)

 [81] Monroe, W.H., 1970, A glossary of karst terminology. Geological Survey Water-Supply Paper 1899-K, U.S. Gov. Print. Off., Washington. http://pubs.usgs.gov/wsp/1899k/report.pdf

[82] Jakubowicz, H. 2013. Advanced Seismic Processing lecture series, Imperial College London.

[83] Pagosa Springs, (accessed June 2013), Geothermal department. http://www.pagosasprings.co.gov/index.asp?Type=B_BASIC&SEC={E4D74380-5C86-4626-972B-C735CE3280D9}